UNSTEADY THREE-DIMENSIONAL COMPRESSIBLE VORTEX FLOWS

James Oliver Reeves

A dissertation submitted to the Faculty of Engineering and the Built Environment, University of the Witwatersrand, in fulfillment of the requirements for the Degree of Master of Science in Engineering.

Johannesburg, 2010

Declaration

I declare that this dissertation is my own, unaided work, except where otherwise acknowledged. It is being submitted for the degree of Master of Science in Engineering in the University of the Witwatersrand, Johannesburg. It has not been submitted before for any degree or examination at any other university.

Signed on this the _____ day of _____ _____

_____

James Oliver Reeves

Abstract

Vortex flows are fundamental to nature and technology. In this dissertation, the results of an experimental and numerical investigation into the behaviour of the free vortex generated by shock diffraction over edges yawed to the incident shock wave are presented. The objectives of this study were to explore the behaviour of the free vortex in three dimensions, with a particular focus on the distortions caused to the vortex by the presence of a solid boundary, or wall. Three-dimensional numerical simulations and experimentally obtained schlieren photographs reveal significant distortion and bending of the free vortex in regions near the boundary of the flow domain, so as to meet it at a right angle. Experimentation was performed in a shock tube for incident shock Mach numbers of 1.32, 1.42, and 1.65, with four test models, two incorporating straight diffraction edges, and two incorporating curved diffracting edges. Numerical simulation was performed with Fluent 6.3.26 software. The numerical solutions were validated against the experimental results through pictorial comparison, and despite relatively coarse meshes being used, were found to mimic the experimental results very well. The numerical results are used here to investigate and explain the various features of the resultant flow fields, with particular emphasis placed on the behaviour and properties of the free vortex. The effects of bending on the structure of the vortex and on the flow properties with the vortex are examined. The rate of circulation production for the three-dimensional diffraction cases was calculated, and the trends observed correlated with those for the much published two-dimensional diffraction case. Also investigated is the three-dimensional shock diffraction case, where it was found that the shape of the diffracted shock wave differed slightly from the two-dimensional case in the region near the boundaries of the domain.

Acknowledgements

I would like to thank my supervisor, Professor B. W. Skews, for his guidance and advice, and for allowing me the opportunity of presenting this work at an international conference.

I would also like to thank the National Aerospace Centre of Excellence (NACoE) for funding my studies.

Table of Contents

List of Figures

List of Tables

List of Symbols

ρ	Density
V	Volume
p	Pressure
h	Enthalpy
M	Mach number
M_s	Incident shock Mach number
a	Speed of sound
R	Universal gas constant
T	Temperature
γ	Ratio of specific heats
δ	Wedge/corner angle
Γ	Circulation
Γ'	Normalised circulation
ω	Vorticity
u	Velocity
s	Entropy
g	Gravitational acceleration
t	Time (usually specified in μs)
t_0	Time instant that incident shock wave begins to diffract over any portion the diffracting edge. Future times are usually given referenced from this time.
ξ	Optical roll angle
ζ	Edge incline angle (angle between diffracting edge and incident shock wave)
d	Edge depth
α_w	Edge-wall angle
δt	Time step between successive images or data points
α	Quantity by which diffracted shock shape is normalised ($\alpha=at$)

Subscripts:

1	Region in front of incident shock wave
2	Region behind incident shock wave
0	The quantity referred to is a stagnation quantity
∞	The quantity referred to is at reference or ambient conditions

1 Introduction

Recently, the study of vortices and vortex motion has received much attention as a result of problems arising in physics, engineering and mathematics (Saffman, 1997). Numerous studies on the subject of vortices have been undertaken and published. However, only a very small proportion of these publications deal with the subject of compressible vortices, and even fewer deal with the three-dimensional behaviour and dynamics of any type of vortex. With the recent advances in computer technology and experimental techniques, work of a much more detailed nature is now possible.

The formation of a spiral vortex during the diffraction of a shock wave over a convex corner has been noted and observed for many decades, and a wealth of published literature exists detailing the basic flow features (Howard & Matthews (1956), Skews (1967a, 1967b), along with publications by many others). However, until recently, very little work has been undertaken with specific aims of attempting to quantify the parameters evident in such vortex flows. Work that has been published to date has been limited to two-dimensional studies.

This can be attributed to a number of factors. The main reason is that it has only become practical to obtain numerical solutions of sufficient resolution to the governing equations of such flows using the modern and high powered computer equipment and software that has become available over the past 5 years or so.

Numerical simulations are vital to any attempt made in studying complex flow phenomena, as it is impractical, and in most cases impossible, to obtain useful quantitative data (specifically, accurate velocity and density measurements) from physical experiments. Physical experimentation is nevertheless extremely important in any study, as observations gathered from physical experiments are typically used to validate the results of numerical simulation. This is usually achieved through means of a pictorial comparison. The photographs that are taken during the physical experiment, using an appropriate optical technique, are compared to the numerical data obtained. There are few laboratories that are equipped to undertake such work.

Vortex flows are fundamental to nature and technology, from weather phenomena such as hurricanes and tornadoes, to being necessary for the generation of aerodynamic lift. A physical understanding of them is thus important, and the topic of three-dimensional compressible vortices is virtually unexplored in the literature.

This Masters dissertation explores the shock wave diffraction process over three-dimensional wedges of various profiles, whereas work published to date in the literature is limited to two-dimensional cases. In this work, the shock diffraction process, in addition to being analysed itself, is used to generate compressible three-dimensional vortices of arbitrary profiles, the investigation and analysis of which form the bulk of the work presented.

Section 2 of this dissertation provides an introduction to shock waves and the process of shock wave diffraction, as well as a literature review and critique of previous research in the field. This is followed by an introduction to compressible vortices, and a theory and literature review of the topic. Finally, an introduction to the optical techniques used to visualise the flow fields analysed in this dissertation is given. The objectives of this study are summarised in section 3.

Section 4 gives a brief account of the apparatus used to perform the experiments, and details and specifications of the test pieces that were designed and used. Section 5 gives an account of the methods used in performing both the physical and numerical experiments, and a brief introduction to the analysis tools and techniques used.

The numerical and experimental results are presented in section 6. Analysis of the various vortices investigated is given first. The section concludes with an investigation into the three-dimensional shock diffraction cases. Section 7 concludes by reiterating the primary conclusions of the research.

2 Literature Review

2.1 Shock Waves

A shock wave is a discontinuous change in the flow properties of pressure, density, and temperature in a region of fluid, manifested as a wave front. A shock wave propagates faster than the signal speed of the medium (the speed of sound), and the faster it propagates, the stronger the shock wave is said to be. The present study deals with normal shock waves propagating through an ideal gas, and the diffraction process that occurs when a normal shock wave propagates over a corner or edge. A brief discussion of shock waves and the relations pertinent to this study is given in the sub-sections that follow, along with a discussion of the shock tube; a means of generating shock waves for study in a laboratory.

2.1.1 Normal shock wave theory

A normal shock wave is a discontinuity front aligned at 90° to the flow direction. These kinds of waves are a common case study in one-dimensional compressible flow problems, and are common in fluid flow in pipes. The creation of a normal shock wave in laboratory situations is in fact analogous to one-dimensional fluid pipe flow, and is typically achieved through the use of a shock tube, discussed in §2.1.2. Here, a disturbance is created in what is effectively a pipe, containing still gas. This disturbance forms a shock wave that propagates through the originally

still gas. The pipe section of the shock tube usually terminates in a test section, where the shock wave propagates over a test specimen or measurement apparatus.

The formation of a normal shock wave can be described as follows: After a disturbance (for example, the acceleration of a piston into a stationary gas), a succession of compression waves are created that travel at the local speed of sound into the stationary gas ahead of the piston. The disturbance can be viewed as a series of small impulsive steps, with a compression wave created at each step, which moves into the gas at sonic velocity. The gas behind the compression wave will be compressed, heated, and accelerated to the velocity the piston has at the end of the first step. For a second step, the second compression wave that is created will move into the gas in front of the piston at sonic velocity (which is now higher than that of the first step, since the gas in front of the piston and behind the earlier compression wave is heated). As the gas immediately ahead of the piston is moving at the same velocity as the piston, this second compression wave will have an absolute velocity of that of the gas immediately in front of the piston, added to the sonic velocity at the second step. Thus, the absolute velocity of each successive compression wave will be greater than that of any preceding wave. Due to this, the later waves eventually catch up to the earlier waves, and form a large discontinuity; the normal shock wave (Skews, 2007). Similar explanations can be found in most compressible gas dynamics text books, for example, Thompson (1972).

A brief review of the normal shock wave theory and relations pertinent to the present study is given below. These relations can be found in any standard gas dynamics text book. Derivations of the relations given below can be found in Zucrow & Hoffman (1976). These hold for frictionless adiabatic flow across a constant area shock wave, for the case when the reference frame is fixed on the shock wave. A schematic of the situation is given in Figure 2.1.

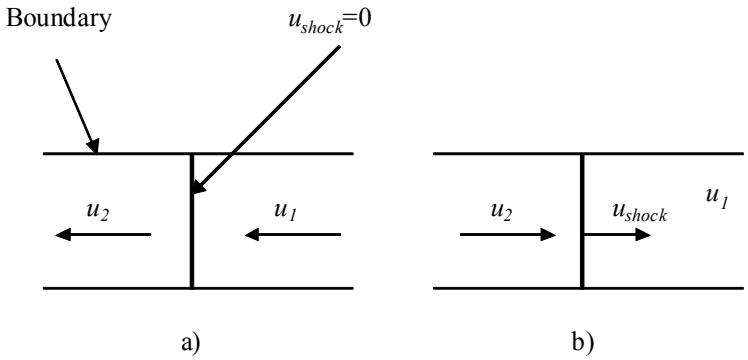

Figure 2.1: Normal shock wave. a) reference frame fixed on shock wave. b) stationary reference frame

The equations for the conservation of continuity, momentum, and energy for such a case are given below. Subscript 1 refers to the gas state prior to the shock wave, and subscript 2 refers to the gas state after the shock wave.

Continuity: $$\rho_1 u_1 = \rho_2 u_2 \tag{2.1}$$

Momentum: $$\rho_1 u_1^{\,2} + p_1 = \rho_2 u_2^{\,2} + p_2 \tag{2.2}$$

Energy: $$h_1 + \frac{u_1^{\,2}}{2} = h_2 + \frac{u_2^{\,2}}{2} \tag{2.3}$$

In addition, the Mach number (M) and local speed of sound (a) are defined as follows. Other useful expressions, the enthalpy (h), and ideal gas equation are also given.

$$M = \frac{u}{a} \tag{2.4}$$

$$a = \sqrt{\gamma RT} \tag{2.5}$$

$$h = \frac{\gamma}{\gamma - 1} RT \tag{2.6}$$

$$p = \rho RT \tag{2.7}$$

After combining and manipulating the above equations, the following results are obtained.

$$\frac{p_2}{p_1} = \frac{\left(1 + \gamma M_1^{\,2}\right)}{\left(1 + \gamma M_2^{\,2}\right)} \tag{2.8}$$

$$\frac{T_2}{T_1} = \frac{\left(1 + \frac{\gamma - 1}{2} M_1^{\,2}\right)}{\left(1 + \frac{\gamma - 1}{2} M_2^{\,2}\right)} \tag{2.9}$$

$$M_2 = \left(\frac{\frac{2}{\gamma - 1} + M_1^{\,2}}{\frac{2\gamma}{\gamma - 1} M_1^{\,2} - 1} \right)^{1/2} \tag{2.10}$$

The following equations, relating the stagnation pressure and density to the flow properties are also useful.

$$\frac{p}{p_0} = \left(1 + \frac{\gamma - 1}{2} M^2 \right)^{\frac{\gamma}{\gamma - 1}} \tag{2.11}$$

$$\frac{\rho}{\rho_0} = \left(1 + \frac{\gamma - 1}{2} M^2 \right)^{\frac{1}{1 - \gamma}} \tag{2.12}$$

The equations given relate to the case for a stationary shock wave, Figure 2.1 a). In order to treat the case of a stationary observer and moving shock wave, a reference velocity is applied to the stationary shock case. The static properties of pressure, temperature and density will remain the same in the new reference frame, however, the stagnation properties will differ, depending on the reference frame that is used. In fact, it can be shown that all the terms, save for the velocities, hold for the change in reference frame.

2.1.2 The shock tube

A shock tube is a device used for generating high speed gas flows of short durations. A typical shock tube consists of a tube of constant cross-section, in which two regions of gas, a low

pressure and a high pressure region, are separated by a diaphragm. It is typical to use thin plastic film or metal sheet as a diaphragm. Removal, or bursting of the diaphragm, causes a shock wave to propagate into the gas at a lower pressure, and a rarefaction (or expansion) wave to propagate into the gas at a higher pressure (Glass, 1959). Figure 2.2 gives a schematic overview of the basic operation of a shock tube. A contact discontinuity, referred to as the contact surface, exists in the flow behind the normal shock wave, across which the pressure is constant, but the temperature and density usually differ. The contact surface propagates in the same direction as the shock wave, though some distance behind it, and exists due to the different thermodynamic histories in the two regions of gas. The first documented use of a shock tube in scientific study was by Vieille in 1899, and shock tubes have been used over the past century or so to study areas such as shock wave physics and diffraction, unsteady boundary layers, physical effects in gases at high temperatures, as aerodynamic test facilities for a wide range of test speeds, and many other subjects (Glass, 1959).

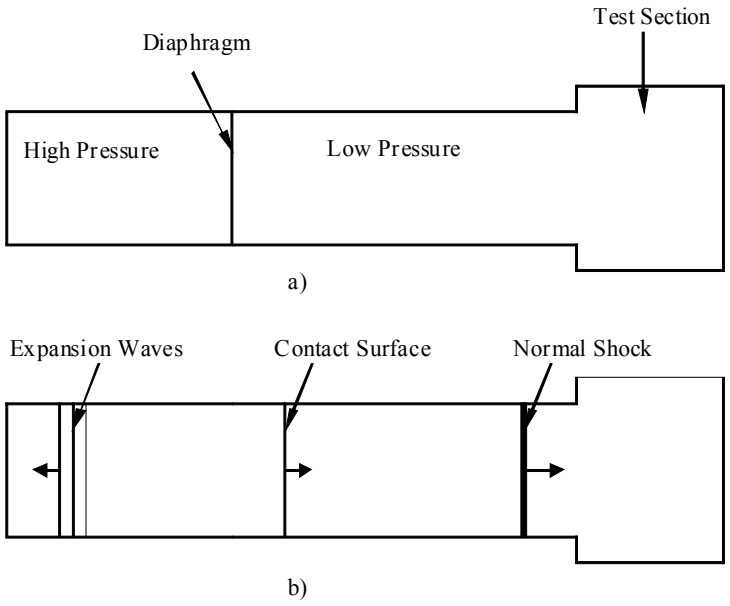

Figure 2.2: Typical shock tube. a) prior to diaphragm rupture. b) after rupture.

An appropriate test section and measurement apparatus are usually fitted to the low pressure section of the tube. This allows normal shock wave and induced quasi-steady flow behind the

shock wave to be used in the study of shock wave physics, or as a short duration high speed wind tunnel. The strength of the normal shock wave generated is proportional to the initial pressure ratio across the high and low pressure gases prior to diaphragm rupture. The standard compressible flow equations, given in §2.1.1, can be used to determine the resultant flow properties, and the pressure ratio required to produce a shock wave of given strength. A complete mathematical and theoretical description of the operation of the shock tube is given by Glass (1959).

2.2 Shock Wave Diffraction & Vortices Generated By Shock Wave Diffraction

2.2.1 Background

The flow features associated with planar shock wave diffraction around a convex edge are explained and discussed in this section.

Shock wave diffraction refers to the phenomena that occur when a shock wave encounters an obstacle. Typically, and as referenced in the present study, this refers to the process of a propagating shock wave traversing a sharp corner, or edge. The flow fields that result are characteristic of the starting process of flow over a boundary with an edge, for example, an aircraft wing (Bershader, 1995).

The solution of two-dimensional flow fields resulting from the diffraction of plane shock waves around corners made up of two planar walls has become a standard gas dynamics test case,

particularly for modern numerical methods. Studies published in the literature concerning this case date back to the 1950s, where the work of Howard & Matthews (1956), and the later work of Skews (1967a, 1967b), described the basic flow features present.

A wealth of published literature exists detailing the shock wave diffraction process. Skews (1967a, 1967b) described the shape of the diffracted wave, and the perturbed region behind a shock wave (for $1 \leq M_s \leq 5$) diffracting around corners of various angles (between 15° and 165°). The present study deals with incident shock Mach numbers in the region of $1.3 \leq M_s \leq 1.7$, diffracting around a corner of angle 165°. Thus, this section focuses on phenomena that are pertinent to these flow cases.

Early studies into shock diffraction were conducted experimentally, through the use of shock tubes, with schlieren and shadowgraph optical techniques used to obtain photographs of the process. Equipment of sufficient resolution, that would allow for physical measurements of the flow properties during the diffraction process did not exist then, and still does not exist today. Even if it did, it would be impossible to obtain such measurements without causing large disruptions to the flow field. The advent of modern computing and numerical methods has allowed for the numerical solution of the diffraction process. Such numerical solutions provide a wealth of data regarding the flow properties. Much of the published work of the late 1980s and early 1990s focused on the comparison, and verification, of the solutions of various numerical schemes, or codes, against the experimental work of earlier authors, and investigation into the finer flow features that the numerical solutions revealed. More recent work has looked at quantifying and explaining the physical processes that occur, and has only become possible due to the rapid advancement of computer technology. Much, if not all, of the recently published work has been purely numerical in nature. Physical experimentation seems to have lost popularity among researchers, probably due the expensive equipment required to perform it, and the fact that modern numerical schemes have matured, and are reputed to give highly accurate predictions of the physical flow features. The inability of physical experimentation to provide accurate data pertaining to the flow velocities and densities further compounds this. The lack of physical evidence can, in some cases, raise questions about the validity of certain numerical results.

All of this work touched upon above dealt with two-dimensional cases, and despite all of the advances made, no published work exists detailing the diffraction of shock waves over three-dimensional edges, and the three-dimensional compressible vortices formed as a result.

The basic two-dimensional flow field for a shock wave diffracting over a convex edge is shown in Figure 2.3. The figure and explanations thereof are derived from the work of Skews (1967b) and Sun & Takayama (2003a). For shock Mach numbers of less than approximately 1.6, the diffraction pattern is typically that shown in Figure 2.3 a). For shock Mach numbers of greater than around 1.6, a pattern similar to that shown in Figure 2.3 b) is evident. The two cases are similar, save for the appearance of a few additional flow features as the incident shock Mach number is increased. The features of the flow are discussed below.

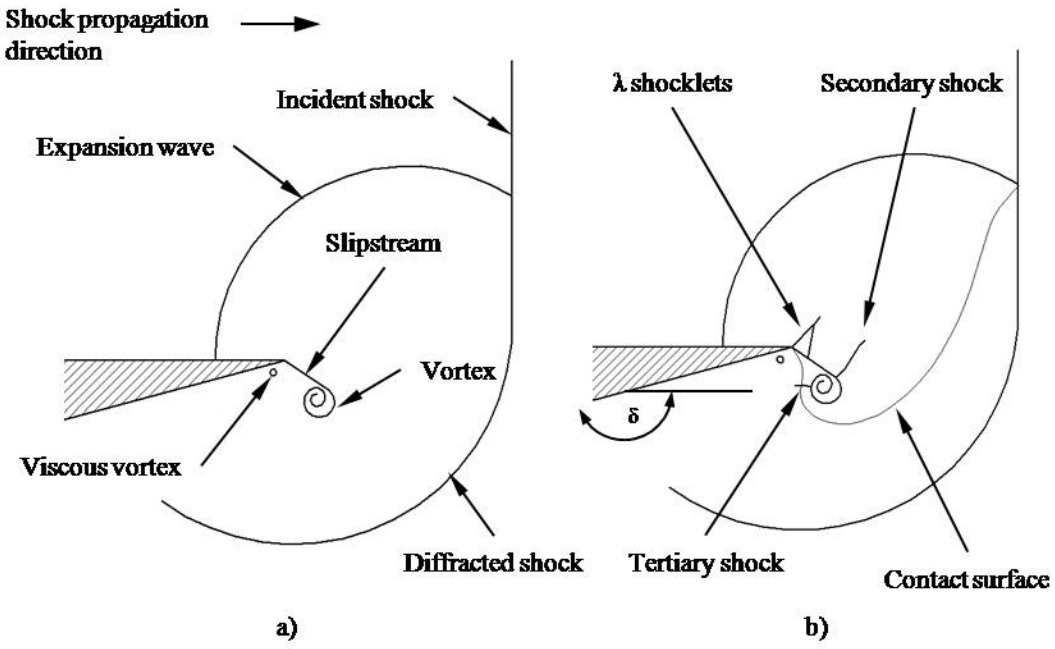

Figure 2.3: Features of shock diffraction, a) M_s~1.3 b) M_s~1.6

When the plane shock wave reaches the corner, it diffracts around the edge, a process which results in the curved shock profile, as can be seen in Figure 2.3. The slipstream is formed due to the inability of the high speed gas behind the shock wave to negotiate the corner. This is a narrow flow region in which the high-velocity gas behind the shock wave interacts with the essentially stationary gas below the edge. This forms a vortex sheet, a narrow region across which there is a discontinuity in tangential velocity, which rolls up to form the free vortex.

The reflected wave represents the reflected sound wave generated due the initial diffraction effects, and indicates the limit of the region of flow that has been affected by the diffraction process.

For incident shock Mach numbers of greater than 1.33 the flow above the slipstream becomes locally supersonic (Sun & Takayama, 2003a), and as such, secondary shocklets begin to appear on the slipstream, in order to decelerate and guide the flow over the slipstream and around the vortex. The velocity of the flow above the slipstream increases with increasing shock Mach number, resulting in stronger, and more apparent, secondary shocklets, and causing them to move further along the slipstream. These shocklets represent the initial stages in the formation of the secondary shock wave, which can be seen in Figure 2.3 b). This becomes fully defined for an incident shock Mach number of approximately 1.6. Additionally, for incident shock Mach numbers of around 1.6 and upwards, a tertiary shock wave appears between the vortex and the wall, as indicated in Figure 2.3 b). This strong compression, or ‘tertiary shock’, forms to decelerate the reverse-flowing gas, and guide it around the vortex.

The development of the lambda-shaped secondary shocklets was explained by Kliene et al. (1995) as follows. The flow above the slipstream is analogous to the flow patterns observed in stationary transonic flows of solid boundaries. For the slightly supersonic flow over the corner, the convex curvature requires a deceleration of the flow, which is established by a weak, almost normal shock. This shock interacts with the boundary layer, inducing a local flow separation. For a laminar boundary layer, this separation region can develop in front of the shock, causing an

oblique shock, the front leg of the lambda configuration, to develop. This front shock is usually weak, and gradually disappears as the flow Mach number increases. It vanishes when the boundary layer becomes turbulent. Kleine et al. (1995) validated their observations through experimental and numerical solutions to the Euler equations. All flow features were in excellent agreement with the experimental results, aside for the development of the front leg of the lambda shock, which was not present. This is expected, as its formation mechanism cannot be modeled by an Euler solver. It would be expected that solutions to the Navier-Stokes equations would predict the front leg shock of the lambda configuration. Sun & Takayama (2003b) showed that numerical solution of the laminar Navier-Stokes equations does in fact accurately predict the formation of all the components of the lambda shock configuration.

The free vortex, which is of primary interest to the present study, is initially formed due to roll up of the slipstream, and is well defined for the regime of shock Mach numbers ($1.3 \leq M_s \leq 1.7$) investigated (Skews, 1967b). It is a well known fact that the evolution of this free vortex with time is a self similar process for the two-dimensional diffraction case (Skews (1967b) and Bershader (1995)). The vortex starts as a vortex sheet in a spiral pattern, the curled end of the slipstream. This sheet tightens and is consolidated into an homogenous vortex through the action of viscous diffusion (Bershader, 1995).

As the Mach number of the incident shock wave is increased, so the diffracted flow pattern spreads. Images detailing this can be found in Sun & Takayama (2003a). The secondary and tertiary shocklets appear, and the slipstream is lengthened. The vortex becomes more elliptical in definition and stronger.

The strength of the free vortex was quantified by Sun & Takayama (2003a) for solution of the two-dimensional Euler equations. This was given in terms of the circulation (Γ), a measure of the total vorticity in the flow field, and a rate of circulation production. They reported that the rate of circulation production was constant during the diffraction process, except for at very early time instances as the vorex was still forming. The rate of circulation production was found to increase

with increasing incident shock Mach number, and for increasing wedge angle (δ). The effect of wedge angle was only significant for angles less than 90°. For angles greater than 90°, the rate of circulation production was found to depend only on the incident shock strength.

Tseng & Yang (2006) performed similar experiments to those of Sun & Takayama (2003a) for solution of the laminar Navier-Stokes equations. The inclusion of viscosity in the simulations yielded very little difference to the results of Sun & Takayama (2003a), aside from a small amount of vorticity being present prior to, and produced during, the diffraction process, due to the wall boundary layers.

According to Bershader (1995), for inviscid compressible flow that is not homentropic (the flow behind a curved or diffracted shock wave), the existence of an entropy gradient will produce vorticity at a rate given by equation (2.13).

$$\rho \frac{D}{Dt}\frac{\boldsymbol{\omega}}{\rho} = \left(\boldsymbol{\omega}\cdot\nabla\right)\mathbf{u} + \nabla\boldsymbol{T}\times\nabla\boldsymbol{s} \tag{2.13}$$

This vorticity production will occur even if the flow was initially irrotational. For the case of the present study, the entropy gradient, and hence rotation in the flow, are introduced through the shock diffraction process. Thus, vorticity is generated by baroclinic effects, or a baroclinic torque, which arises from the abovementioned entropy gradient. This process is typical of the flows behind curved shock waves, as is mentioned by Bershader (1995).

A recent study by Sun & Takayama (2003a) found that the vorticity produced by the slipstream contributed a large proportion to the vorticity production in shock wave diffraction, and that the slipstream was a more important source of vorticity than the baroclinic effects mentioned above.

They go on to mention that it is has been common practice for the vorticity to be ascribed entirely to baroclinic effects, whereas their results show that this is incorrect. Their results show that the slipstream actually represents a larger portion of the vorticity produced, and that baroclinic effects are in fact negligible in the formation of the free vortex. This vorticity production arises from the tangential velocity jump across the slipstream. The presence of the contact surface between the diffracted shock wave and the free vortex (see Figure 2.3) confirms this, as this represents the boundary of the region of non-isentropic flow (the region between the diffracted shock and the contact surface). Thus, the non-zero entropy gradient would not affect the free vortex. For further details, the reader is referred Sun & Takayama (2003a).

As mentioned previously, Sun & Takayama (2003a) attribute the generation of vorticity in such flow fields to the slipstream. They go on to explain that the origin of the slipstream is a singular point in the flow field, and that equation (2.13) does not include vorticity that originates from singularities. Work published since has adopted and fallen in line with the thinking and observations set forth by Sun & Takayama (2003a).

The viscous vortex (or secondary vortex) as illustrated in Figure 2.3, is formed due to viscous effects. Yang, Takayama, & Han (1997) proposed that this vortex was formed due to boundary layer flow induced on the wall under the diffracting edge by the free vortex. The particles in this boundary layer are forced to separate from the wall due to the positive pressure gradient, forming a shear layer which rolls up to form a vortex that rotates in the opposite sense to that of the free vortex. As the secondary vortex arises due to viscous effects, numerical simulations solving Euler codes do not predict it. Solution of the Navier-Stokes equations however does satisfactorily predict the secondary vortex. There are numerous publications in the literature concerning these topics, for example Sun & Takayama (2003b) and Tseng & Yang (2006).

Skews (1967b) described the trajectory of the two-dimensional free vortex in terms of angular position (measured relative the diffracting edge) and a vortex velocity. It was expected that the vortex would move along a straight path below the slipstream, which the results, despite

including inaccuracies which arose due to difficulties in locating the centre of the vortex accurately and consistently, tended to confirm.

The results of numerous studies, in particular those by Bershader (1995), on the free vortex behaviour have shown that a free vortex propagates downstream at a velocity approximately equal to the fluid velocity behind the shock wave, which can be easily calculated using the compressible flow relations for simple flow geometries. However, the fluid velocity in the region affected by the diffraction process is highly non-uniform, and can only be obtained through numerical simulation.

From the results of the experiments performed by Bershader (1995), a density drop of over 70% was found at the core of the free vortex. A similar change in pressure profile was also reported, with a drop of around 66% occurring at the vortex core.

It should be noted that the discussion and all studies referred to in this section dealt with two-dimensional flow fields. To the knowledge of the author, no published work exists on shock diffraction in three dimensions, over edges yawed to the incident shock direction, and the vortices generated in the three-dimensional flow fields that result. Brief consideration of the three-dimensional effects on these phenomena is given in §2.2.2.

A detailed discussion on compressible vortices is given in §2.3.

2.2.2 Three-dimensional effects on shock wave diffraction and vortices formed

Preliminary work was conducted in the form of an exploratory study (Skews & Crosbie, 2008) into three-dimensional vortices generated by shock diffraction in 2005 at the School of Mechanical, Industrial, and Aeronautical Engineering, at the University of the Witwatersrand. This study focused on the free vortex formed as a result of shock wave diffraction over a convex corner at the trailing edge of a wedge inclined to the shock propagation direction. Limited numerical and experimental work was undertaken and fair agreement was found between the two sets of results. A brief discussion of the results is given below.

It was shown that the vortex bends so as to meet the wall (or solid boundary) at a right angle. These effects were well captured by the numerical solutions, despite the coarseness of the simulations performed. It was found that even though the vortex had a conical three-dimensional envelope, it appeared as though the flow properties in the region free from the effects of the wall mimicked those of the two-dimensional flow case. However, no quantitative data was obtained, and little was said about the bending behaviour of the vortex near the walls, save for the observation that these effects were mirrored to some extent in the numerical work.

The study highlighted two areas of interest recommended for further study:

- The meeting of two vortices at an angle.
- The case of a vortex with an axis that is not perpendicular to a surface bending so as to meet that surface at a right angle.

This dissertation aims to expand upon the initial exploratory study that was performed.

2.2.3 On the use of numerical methods to simulate shock diffraction and vortex behaviour

As mentioned previously, it is practically impossible to obtain accurate experimental data for the flow velocities and densities. Thus, typical investigations into vortex dynamics make use of numerical simulations to obtain the relevant data. Practical, experimental results are nevertheless vital, and are usually used to validate the numerical simulations by means of pictorial comparison.

Numerical schemes used in the solution of compressible flow problems have reached a level of maturity, and advances in computer technology over the past decade have allowed for the investigation of increasingly complex flow phenomena that was previously not thought possible. The results of numerous studies have confirmed that numerical solution of the unsteady Euler equations precisely replicate shock propagation, reflections from walls, and interactions with bodies. It has also been shown in numerous studies that the difference between experimental photographs and numerical solution of these equations can be so small as to fall within the uncertainty present in conventional shock tube measurements (Sun & Takayama, 2003b). However, in areas where viscous effects are prominent, such as flows near a sharp corner, the difference between the two becomes noticeable (Sun & Takayama, 2003b).

A major difference between Euler solutions of shock wave diffraction and actual experimental results is that the secondary vortex (viscous vortex), see Figure 2.3, is not captured in the Euler solution. This is of course intuitive, as it is well known that the secondary vortex forms primarily due to viscous effects, and Euler solutions are inherently inviscid solutions. One would expect that the Navier-Stokes equations, which are an extension of the Euler equations to include viscosity modeling, would predict the secondary vortex. Numerous studies have been published

in the literature that confirm that this is in fact the case, for example, Sun & Takayama (2003b) and Tseng & Yang (2006).

Viscosity is known to have non-negligible effects in the core of a free vortex, as is explained by Bershader (1995). Work by Mayer & Powell (1992) showed that including viscosity in the calculation enhanced the coupling of the core to the external flow field. They show that viscosity, combined with compressibility effects, produce very low densities, pressures, and temperatures on the core axis. Thus, in order to fully explore the flow behaviour in the core of a vortex, it is expected that solution of the Navier-Stokes equations would be required. However, viscosity has a negligible effect on the flow field away from the core.

The presence of the secondary vortex and viscous effects in the solution of the Navier-Stokes equations has very little effect on the development and evolution of the free vortex. Numerous studies have shown this to be the case. Bershader (1995) confirmed that viscosity does not play a major role in the behaviour of the free vortex. Additionally, work by Takayama & Inoue (1991) showed that various numerical solutions of the Euler and Navier-Stokes equations, for adaptive and non-adaptive grid techniques, showed little variation, aside from the prediction of the secondary vortex. It can be concluded from these studies that Euler codes are extremely successful in modeling the perturbed region behind a diffracting shock wave, and that there are no significant differences between Euler, Navier-Stokes, and experimental results. The vast body of work published in the literature on the subject confirms that the formation and evolution of the free vortex behind a diffracting shock wave are primarily inviscid phenomena, and that numerical solution of the Euler equations provides excellent predictions of these flow phenomena.

2.3 Vortices

Most people have a general idea of what a vortex is; they are prevalent in a large variety of guises in everyday life. It is perhaps not surprising then, that there appear to be as many definitions as there are guises of them. As the present study is concerned with vortices from a fluid dynamics point of view, only a few of them are of any particular relevance. Lugt (1983) defined a vortex as the "rotating motion of a multitude of particles around a common centre." Green (1995) defines a vortex as "any region of concentrated vorticity". There are many others, but the definition proposed by Green will be implemented for the present study.

The compressible vortex, referred to in the title of this work, is simply a vortex flow in which compressibility is included, or in which variations of the density of the fluid in which the vortex occurs, are present. The typical free vortex formed during shock diffraction exhibits a density drop of around 70% at the core (Bershader, 1995), and is thus a highly compressible flow phenomenon. Most vortices that occur in air, for example the wing tip vortices generated by aircraft and tornados, have non-negligible density variations throughout them, and are thus termed compressible vortices.

Very few published studies concerning three-dimensional vortices exist, most of these being concerned with tornados. There are also very few publications that deal with compressible vortices in general, let alone three-dimensional cases. This is perhaps due to the fact that obtaining quantitative data from vortices, such as tornados, is practically impossible under field or laboratory conditions. As mentioned in previous discussion, the computer technology required to perform such complex three-dimensional simulations has only very recently become available.

The vorticity in a flow is defined as

$$\vec{\omega} = \nabla \times \vec{u} \tag{2.14}$$

and has the dimensions of frequency. The vorticity vector is the curl of the velocity vector, and is proportional to the rate of rotation of a small fluid element about its own axes (Green, 1995). The circulation, a property closely related to the vorticity, is defined for a closed contour, *C*, as

$$\Gamma = \oint_C \vec{u} \cdot d\vec{l} \tag{2.15}$$

This can also be written as

$$\Gamma = \int_S \vec{\omega} \cdot \vec{n} dS$$

where *S* is an arbitrary curved surface. Circulation is a scalar quantity which is equal to the integrated component of vorticity normal to the surface *S* (Green, 1995).

A comprehensive account of vortex theory can found in Green (1995), along with accounts of various studies conducted on vortices and vorticity.

The present study is concerned with the free vortex (often referred to as the spiral vortex) generated by shock wave diffraction over a convex edge. This vortex is a highly complex, highly compressible flow phenomenon. The three-dimensional behaviour of this vortex is to be studied, a problem of which the solution is only suited to numerical schemes run on modern high powered computers. A summary of compressible vortex theory will be given in the following sub-sections.

2.3.1 Compressible vortices

A brief overview of the equations governing compressible vortex flow is given below. More detailed derivations are contained in Bershader (1995), where a summary of the experimental and theoretical work performed at Stanford University is given. This work was concerned with two-dimensional flow fields, however, the theoretical relations derived are still applicable to the three-dimensional flow fields that are the subject of the present study.

Some of the important conclusions on compressible vortices according to the abovementioned study are:

- A free compressible vortex exhibits a steep density and pressure profile (depending on vortex strength) with a strong partial vacuum around the centre.
- The time-dependence shows a decreasing depth of the density profile with only a small increase in vortex size.
- The temperature profile shows a fairly steep gradient in the core with a maximum at the core boundary. Some non-negligible viscous shear and heat transfer may take place at this boundary.

The general vorticity equations are derived by Green (1995). The result for the time rate of change of the vorticity following a particular fluid element is given by equation (2.16),

$$\frac{D\vec{\omega}}{Dt} = -\vec{\omega}\left(\nabla\cdot\vec{u}\right) + \left(\vec{\omega}\cdot\nabla\right)\vec{u} + \frac{1}{\rho}\nabla\rho\times\left(g - \frac{Du}{Dt}\right) + \frac{1}{\rho}\nabla\times\left(\nabla\cdot\vec{T}\right) + \nabla\times\vec{g} \tag{2.16}$$

In theory, it is possible to solve equation (2.16), (2.14), and the continuity equation (equation (2.1)) for the vorticity field. An expression equivalent to equation (2.16) is given by Bershader (1995), and derived by Thompson (1972), and is obtained by taking the curl of the extended Crocco-Vaszonyi equation (see Bershader (1995) for details)

$$\begin{aligned}\frac{D\vec{\omega}}{Dt} = {} & \left(\vec{\omega}\cdot\nabla\right)\vec{u} - \vec{\omega}\nabla\cdot\vec{u} + \nabla\vec{T}\times\nabla s + \frac{4}{3}\mu\left[\nabla\left(\frac{1}{\rho}\right)\times\nabla\left(\nabla\cdot\vec{u}\right)\right] \\ & + \mu\left[\frac{1}{\rho}\nabla^2\vec{\omega} - \nabla\left(\frac{1}{\rho}\right)\times\left(\nabla\times\vec{\omega}\right)\right]\end{aligned} \tag{2.17}$$

The cross product of temperature and entropy in equation (2.17) can be written in terms of pressure and specific volume

$$\nabla T\times\nabla s = \left[\left(\frac{\delta T}{\delta p}\right)_v\left(\frac{\delta s}{\delta v}\right)_p - \left(\frac{\delta T}{\delta v}\right)_p\left(\frac{\delta s}{\delta p}\right)_v\right]\frac{\nabla\rho}{\rho^2}\times\nabla\rho \tag{2.18}$$

The above implies a production of vorticity when ∇p and $\nabla\rho$ are not parallel. This is known as "baroclinic torque". This effect was mentioned in §2.2.2, where the role it plays in the formation of the free vortex formed during shock diffraction was discussed.

A simplified form of the above vorticity equation, applicable to inviscid compressible flow, is given by equation (2.19) (Bershader, 1995).

$$\rho \frac{D}{Dt}\left(\frac{\omega}{\rho}\right) = (\boldsymbol{\omega} \cdot \nabla)\boldsymbol{u} + \nabla \boldsymbol{T} \times \nabla \boldsymbol{s} \tag{2.19}$$

Whilst it is practically impossible to solve the above, and previously mentioned, equations for an arbitrary flow field, they do nevertheless provide some physical explanation as to what one observes in such vortex flows.

Equation (2.19) describes the rate of change of vorticity for a fluid element. The first term on the right hand side states that, in lay-man's terms, if a vortex line is stretched, the rate of vorticity production will increase, or that vorticity will be produced. This term is obviously zero for two-dimensional flows. The second term on the right-hand side describes an increase in vorticity if a non-zero entropy gradient is present. This is the 'baroclinic' effect mentioned previously.

The structure of a compressible vortex is summarised by Lee & Bershader (1994), and explained below with the aid of Figure 2.4. Note that this describes the structure of a two-dimensional vortex. A vortex can be divided into four distinct regions:

1. The core. This region undergoes solid body rotation, with the circulation being proportional to the square of the distance from the centre.
2. A logarithmic region adjacent to the core region. The tangential velocity reaches a maximum in this region, and the circulation is proportional to the logarithm of the distance from the centre.

3. A transition region to an outer inviscid region. Many relationships have been provided relating the circulation to position, these are summarised by Lee & Bershader (1994). However, according to Lee & Bershader (1994), measured data generally does not fit any of these curves.

4. The outer irrotational region, where circulation is constant.

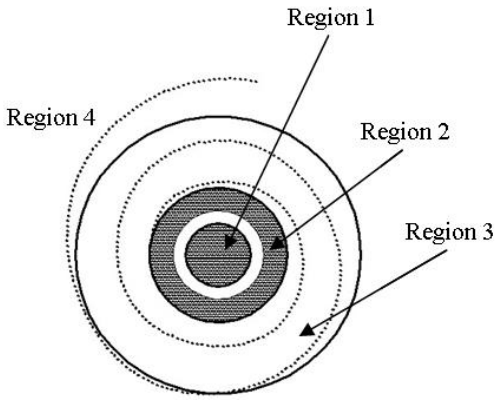

Figure 2.4: Structure of a compressible vortex (derived from Lee & Bershader (1994))

For the case of a three-dimensional vortex, this structure would extend out of the plane of the page. The same basic regions are present. The one major difference between the two-dimensional and three-dimensional case is the presence of axial flow through the vortex in three-dimensional cases. In the present study, the flow velocity inside the three-dimensional vortex is described on planes taken perpendicular to the vortex axis. The velocity is given in terms of tangential (positive counter-clockwise) and radial (positive away in the direction away from the vortex core) components in the plane, and an updraft velocity component parallel to the vortex axis/core.

Little work exists on the structure of three-dimensional vortices, and as was mentioned previously, the majority that does exist is concerned with tornados. Most of the work on the

structure of a tornado-like vortex results from axisymmetric, incompressible numerical simulations, for example Nolan & Farrel (1998).

The structure of a tornado-like vortex can be characterised by the arrangement of axial flow in the core. A single-celled vortex exhibits an updraft near the core, whereas a two-celled vortex exhibits a downward recirculation in the core. Here, there is downdraft region at the centre of the core, surrounded by an updraft region (Nolan & Farrel, 1998).

2.3.2 Hemholtz's Laws

The three laws of vortex motion were proposed by Hemholtz in 1858. These can be expressed as follows (Saffman, 1997):

- Fluid particles originally free of vorticity remain free of vorticity.
- Fluid particles on a vortex line at any instant will be on a vortex line at all subsequent times.
- The strength of a vortex tube does not vary with time during the motion of the fluid.

Although these laws are for inviscid fluids, they do still hold true for fluids where viscosity has negligible effects. For further details or mathematical derivations of the above, the reader is referred to Saffman (1997), or any other of the many texts on vorticity.

An important result of the Hemholtz laws, applicable to the current study, is that the circulation around a vortex tube is constant. A vortex tube is defined as the closed surface, or tube, made up

of the vortex lines passing through every point of a given closed curve. A vortex line is a curve that is everywhere tangent to the vorticity vector.

This result implies that the vorticity flux through a vortex tube is constant, or in other words, that the sum of the vorticity taken on a plane perpendicular to the vortex axis inside the vortex tube is constant along the vortex axis. As such, if a vortex tube is to terminate at a solid boundary, the vortex axis would have to meet that boundary at a right angle.

This result also ties in with the first term on the right-hand side of equation (2.19), in that if a vortex tube is stretched, it will contract, and to conserve angular momentum, the rotational rate will increase. One would also expect to find a local maximum of the vorticity vector at the waist, or region of greatest contraction.

2.4 Schlieren Imaging

Schlieren imaging is a common technique used to translate phase differences in light to amplitude differences that the human eye can see (Settles, 2001). This phase difference arises from variations in the refractive index of a medium, for the purposes of this study, air. The refractive index of a gas depends upon the gas composition, temperature and density, and wavelength of illumination (Settles, 2001).

The temperature and density in a compressible flow lead to disturbances in the gas that refract light, and thus the schlieren technique is commonly used to visualise them. The mathematical relations and theories fundamental to the schlieren technique can be found in the book by Settles

(2001). What follows in this section is a brief discussion of the technique, and its implementation in the present study.

The Z-type arrangement show in Figure 2.5 is one of the most popular and practical implementations of the schlieren technique. The first slit is used to generate a point light source. The light from this source is reflected off of a parabolic mirror, so as to form parallel light, which is passed through a test region. Schlieren techniques employ the use of a knife edge to cut off the refracted light after it has passed through the test region. Adjusting the amount of light cut off by this knife edge adjusts the sensitivity of the system. The illuminance level in a schlieren image responds to the first spatial derivative of the refractive index in the medium. As such, a schlieren image displays the deflection angle of the light rays passing through the medium. This allows for variations in density of transparent medium to be visualised.

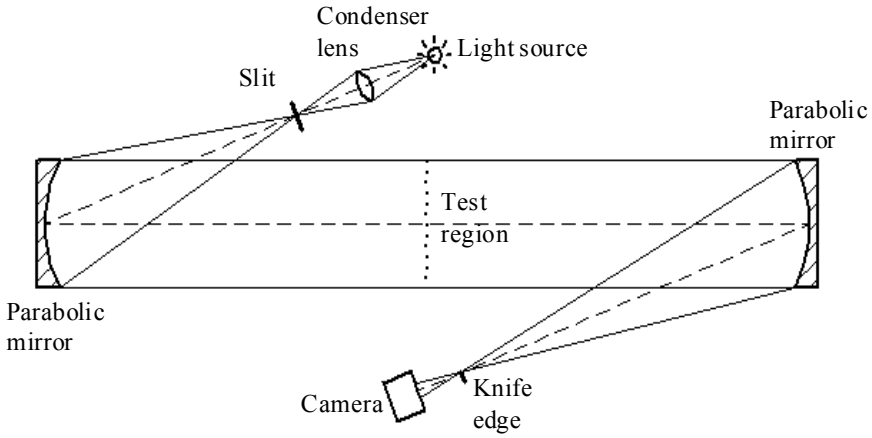

Figure 2.5: Typical schlieren set up

3 Objectives

The objectives of this study are:

- To perform physical and numerical experiments to aid in developing a physical understanding of the evolution, and bending, of the free vortex in three-dimensional flow fields.
- To expand upon the work conducted previously (Skews & Crosbie, 2008), providing a quantitative set of results for the meeting of two vortices at an angle, and the bending of a vortex with axis at an angle to a surface so as to meet that surface at a right angle.
- To investigate the applicability, and accuracy, of modern numerical solution schemes in the abovementioned areas.

4 Apparatus

Discussions of the various apparatus used during the study are given here. Descriptions of the Seitz shock tube, its operation, and its instrumentation are given in §4.1 through §4.3. Section 4.4 gives an overview of the schlieren optics system used. An account of the test models used is given in §4.5.

4.1 The Seitz Shock Tube

The Seitz shock tube is an automated shock tube located in the Engineering laboratory of the School of Mechanical, Industrial, and Aeronautical Engineering, at the University of the Witwatersrand, and was designed and built in partial fulfillment of Seitz (2001) Ph.D during the 1990s. Photographs of the tube are given in Figure 4.1.

The tube uses a double diaphragm technique and normal bursting to generate the shock wave used for testing. A maximum shock Mach number of around 1.84 is attainable with the low pressure (driven section) at atmospheric pressure (approximately 0.83 bar in Johannesburg). A schematic indicating the basic dimensions of the shock tube is given in Figure 4.2. The driver is comprised of the compression and intermediate chambers.

a) b)

Figure 4.1: Photographs of Seitz shock tube, a) driver, b) expansion chamber and test section

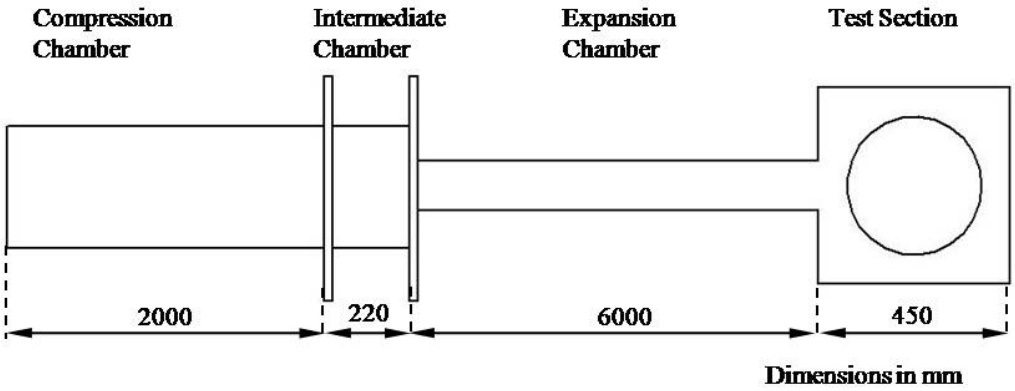

Figure 4.2: Schematic of Seitz shock tube

The test section has a rectangular cross section of 180mm x 76mm, and is 450mm long, with schlieren quality optical viewing windows of diameter of 300mm on both sides. The top, bottom, and back walls of the test section are lined with pressure transducer ports, which can be used for locating pressure transducers, or for mounting test models. The sides of the test section open quickly and easily, and so facilitate cleaning of the section between each test. The length of the expansion chamber is 6m.

There are also numerous pressure ports upstream of the test section. Two high speed pressure transducers are fitted in these ports, and are responsible for measuring the test shock Mach number. Various other sensors are fitted in various locations in the tube and driver section, so as to facilitate the measurement of temperature and other pressures critical to the operation of the tube (see §4.3 for more details).

The driver section of the tube consists of the main compression chamber, and an intermediate chamber. The driver incorporates a two-stage contraction geometry, the first transforming the circular cross-section of the main pressure vessel to a section of 180mm x 180mm. The second, which takes place in the intermediate pressure chamber, reduces this cross section further to 180mm x 76mm. The first diaphragm is placed between the main and intermediate pressure vessels, and the second between the intermediate pressure vessel and the expansion chamber. A schematic of the shock tube driver section is given in Figure 4.3. The pressure vessels are rated to a maximum safe operating pressure of 20 bar, however, the maximum pressure of the air supply available in the laboratory is 15 bar. Opening and closing of the driver section is achieved through the use of a hydraulic motor, which is controlled by the computer control software.

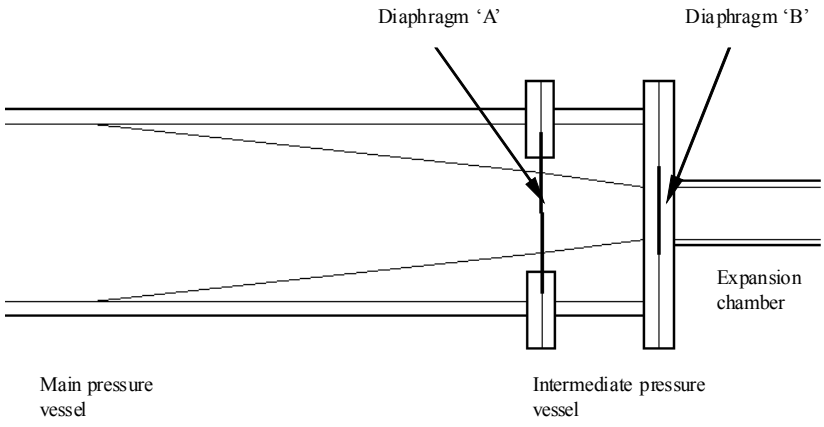

Figure 4.3: Seitz tube driver schematic

The diaphragm that is inserted between the main and intermediate pressure vessels is referred to as diaphragm ‘A’, and that which is inserted between the intermediate pressure vessel and the expansion chamber as diaphragm ‘B’ in this dissertation. For the purposes of this study, polyester films of various thicknesses were used as the diaphragm material. The control software determines the thickness of diaphragm required at each station based on calibration data, for a user specified shock strength.

Shock tube operation and experimental results gathering is fully automated, aside from the cleaning of the test section between tests, and the insertion of the diaphragm material. It should be noted that the electronics and data acquisition systems have been refurbished, and the software program rewritten, since the original design was commissioned. As such, the original documentation, and the information contained in Seitz (2001) Ph.D thesis concerning these aspects, is not correct. A brief summary of the shock tube operation can be found in §4.2.

The shock tube was calibrated for different incident shock Mach numbers prior to testing. Table 4.1 gives the Mach number and corresponding diaphragm arrangements for the Mach numbers used during testing (Mach 1.32, 1.42, 1.65). These Mach numbers were used as they yielded the most consistent and repeatable results, whilst spanning the desired range of Mach numbers. The number and thickness of the polyester film used at each location is given in the table.

Table 4.1: Mach number diaphragm calibration

Mach Number	Diaphragm 'A'	Diaphragm 'B'
1.32	25µm	25µm
1.42	50µm	2x25µm
1.65	2x100µm	25µm & 50µm

4.2 Shock Tube Operation

As mentioned previously, the operation of the shock tube is automatic, and controlled through its own software program. The program makes use of a simple GUI, and the vast majority of its commands are self explanatory. This software program provides means to test the various sensors and functions of the tube, as well as to calibrate them and to calibrate the pressurising procedure to different diaphragm thicknesses and required shock Mach numbers. Details of the testing procedure are given in §5.1.2.

4.3 Instrumentation

4.3.1 Data acquisition system

The data acquisition system consists of a personal computer fitted with data acquisition cards, and is run through the custom Seitz shock tube software program, developed by TLC Software cc. Two National Instruments PCI-6110 data acquisition cards are used. These provide eight 12-bit, analogue input ports with a sample rate of 5 million samples per second for each channel (National Instruments Corporation, 2009a). These cards are used in the acquisition of the various temperature and pressure values that are required for operation of and testing using the shock tube. A National Instruments PCI-6224 data acquisition card is also used. This provides a combined total of 48 inputs or outputs, and has digital triggering capabilities (National Instruments Corporation, 2009b). This card is mainly used to trigger the various operations of the shock tube, such as the operation of the hydraulic motor and the opening or closing of the tube, and triggering the light source during testing. The majority of these commands are issued

automatically by the shock tube software program, but can be issued manually for troubleshooting purposes.

4.3.2 Pressure and temperature sensors

Ambient pressure and temperature are measured and processed by the shock tube software program. A pressure and a temperature sensor are mounted in the shock tube laboratory for this purpose. The temperature sensor has an accuracy of 0.25 °C, and the pressure sensor an accuracy of 0.4 mbar (Seitz, 2001).

High-pressure transducers with a range of 0-20 bar (gauge) measure the pressure in the compression and intermediate chambers. These transducers are designed to withstand any rapid pressure changes such as those caused by a diaphragm burst.

The pressure measurements inside the shock tube are measured using fast response PCB piezoelectric pressure transducers. The signals are processed by the data acquisition software, and are used to determine the speed of the shock wave and the timing of the light source trigger.

4.4 Optics Set Up

A brief overview of the schlieren technique was given in §2.4. The system employed for the current study was based on the z-type arrangement depicted in Figure 2.5, and again in Figure 4.4 below.

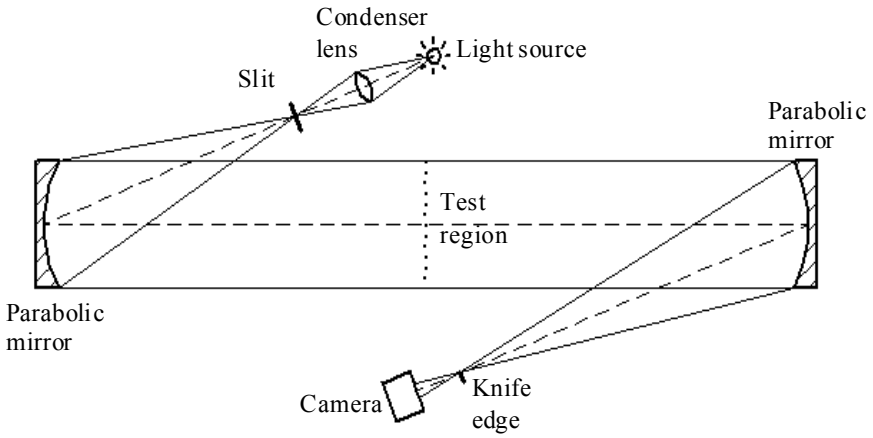

Figure 4.4: Experimental schlieren layout

A Xenon flash lamp was used as the light source. This was triggered by the shock tube software program at a delay time specified by the user. The light from the source is passed through a converging/condensing lens and then through an adjustable slit. The condensing lens and slit are used to produce a well defined, and effectively point light source. These items are mounted on custom built rail guides, so as to facilitate easy alignment and positioning.

The two parabolic mirrors of 254 mm diameter (f/6), mounted on fully adjustable stands, were used. These were used to generate the parallel light that is passed through the test section, and then bring it to focus again at the camera. A knife edge is positioned at the focal point before the camera, and is used to cut off portions of the light. By adjusting the amount of light cut off, the sensitivity of the image to changes in the refractive index gradient of the test medium can be altered.

A Fujifilm FinePix S3 Pro digital camera was used to take experimental photographs. This could take photographs at a maximum resolution of 12 megapixels. A focusing lens was positioned just in front of the camera.

For the purposes of the present study, it was necessary to obtain experimental photographs with the optical axis perpendicular to the test section, and with the optical axis rolled about the test section, so as to look down through the test section. This is illustrated in Figure 4.5. The oblique axis schlieren requires much more careful set up and alignment than the perpendicular set up, so as to prevent distortions in the resultant images. In practice, roll angles of greater than 30° are hard to achieve without introducing significant distortions to the image. Due to space limitations, the maximum roll angle achievable was around 10° for the present study. Modifications were made to the optics set up so as to allow for images at an optical roll of 10° to be taken.

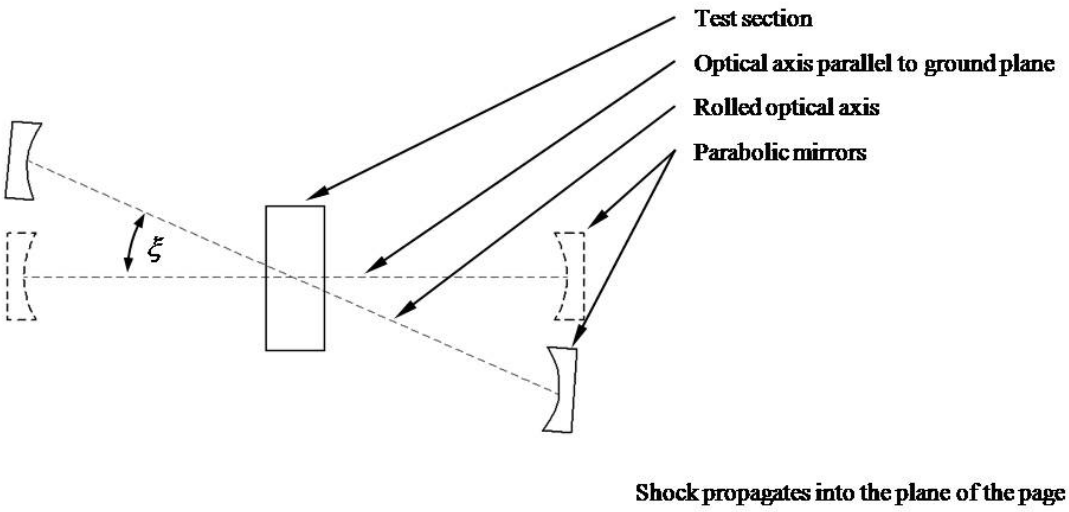

Figure 4.5: Optical axis illustration

4.4.1 Precautions and considerations

It was necessary to take great care when aligning the optics equipment, so as to ensure that the parallel light was perpendicular to the test section, so as to minimise any distortions in the photographs taken. For the purposes of this study, it was necessary to roll the optical set up, so as

to obtain images looking down through the test section at an elevation of 10°. Again, great care had to be taken to make sure the set up was accurately aligned.

4.5 Test Models

4.5.1 Overview

A generic mount, used to cut the incident shock wave produced by the shock tube, was used to mount various test specimens in the shock tube, and direct a planar shock wave over them. This mount is shown in Figure 4.6. It was mounted to the roof of the test section of the shock tube, and the test wedges were mounted to the back of it, as indicated in the figure. The sharp leading edge of the mount sliced the incident shock wave in two, the upper portion of which passed over the test piece mounted at the back.

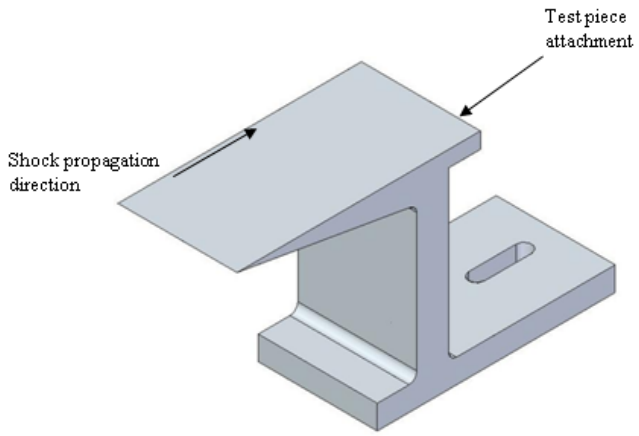

Figure 4.6: Wedge mount

This study investigated the diffraction of a shock wave over edges yawed to the direction of propagation of the incident shock wave. Two wedges with edges yawed at 45° to the shock wave were used. These specimens were used in the exploratory study by Skews & Crosbie (2008), and were repaired for use in the present study. Shock diffraction and free vortex behaviour over curved edges was also to be examined. To this end, new test pieces were manufactured. A discussion of the test pieces is given in the sections to follow. All wedge angles (corner angle) were 165°. Definitions and nomenclature are given in Figure 4.7.

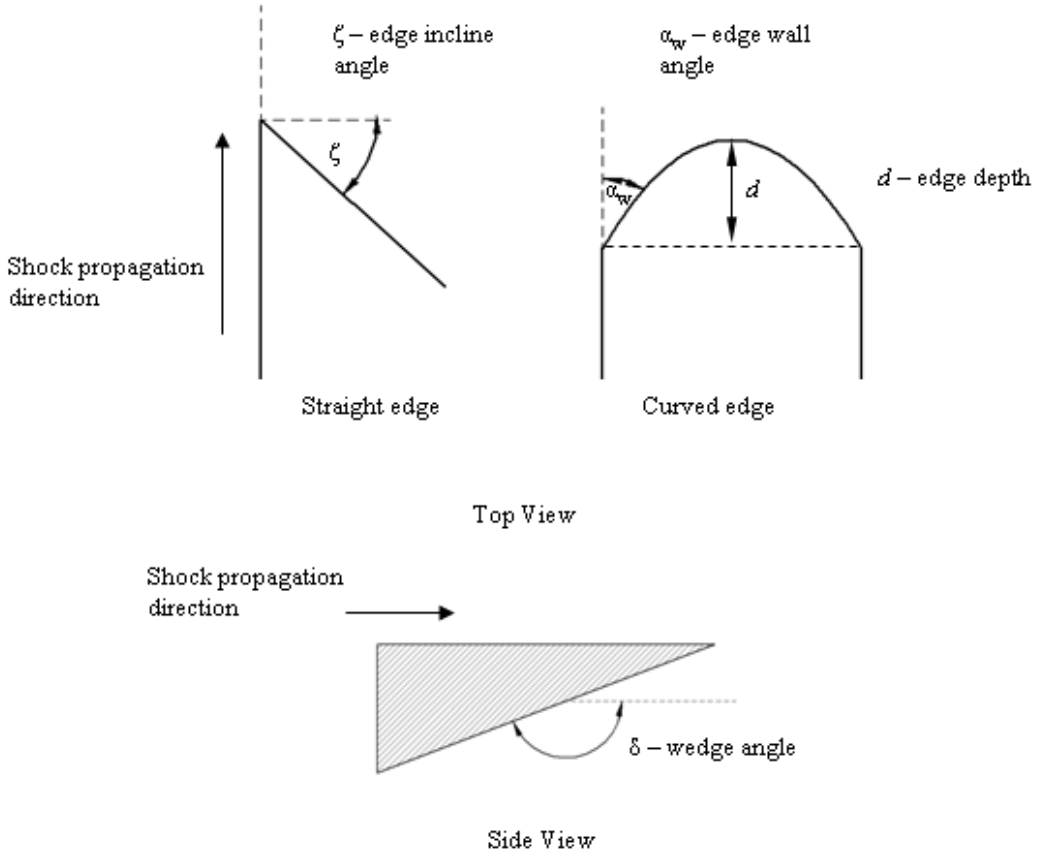

Figure 4.7: Test piece nomenclature

4.5.2 Straight edged test models

Two attachments with straight edges were used on the wedge mount. These two attachments were used to build either a 'V' on 'inverted-V' wedge, with the edge angles inclined at 45° to the incident shock wave. As mentioned previously, the wedge angle δ was 165°. The two edge arrangements are shown in Figure 4.8 a) and b).

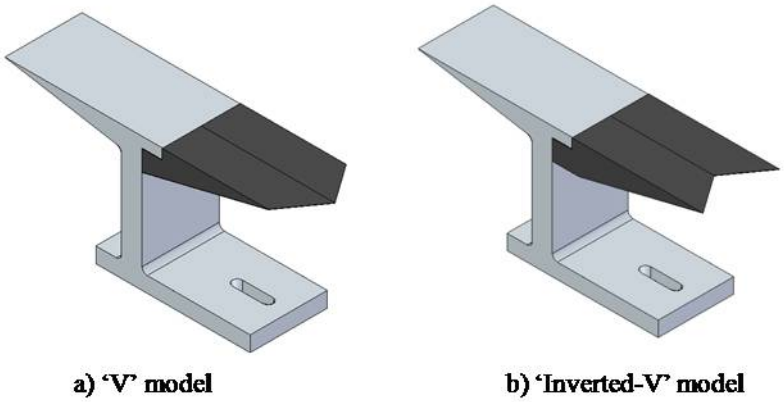

Figure 4.8: Straight edge test specimens

Tape was placed on the side of the models so as to create a seal with the test section window, so as to prevent any flow leakage between the model and the window. The width of the models was 75 mm, which allowed for a small amount of clearance between the models and the test section window for sealing and to prevent scratching the window. The critical dimensions of the two models are summarised in Figure 4.9.

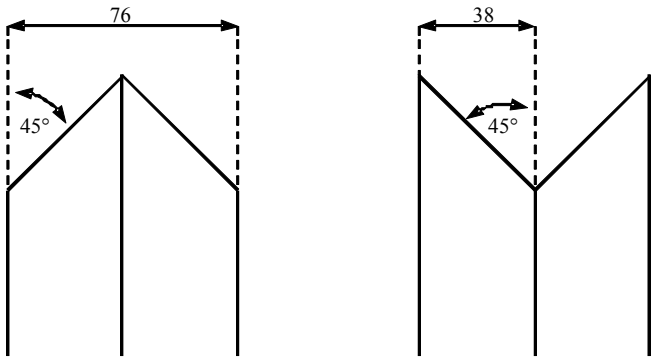

Figure 4.9: Straight edge dimensions

The edge arrangement of the two models allowed for the interface between the model and the window to be the initial ('V' model) and final ('inverted-V' model) point of shock diffraction. Additionally, the merger of the two spiral vortices created from the shock diffraction could be studied from the 'V' edge model.

4.5.3 Curved edge test specimens

Two further test specimens, incorporating a curved diffraction edge, were designed for use on the wedge mount. A similar arrangement to the 'V' and 'inverted-V' models was made, with a parabolic edge profile on one model, and the inverse of that parabolic profile used for the second model. These two models are shown in Figure 4.10.

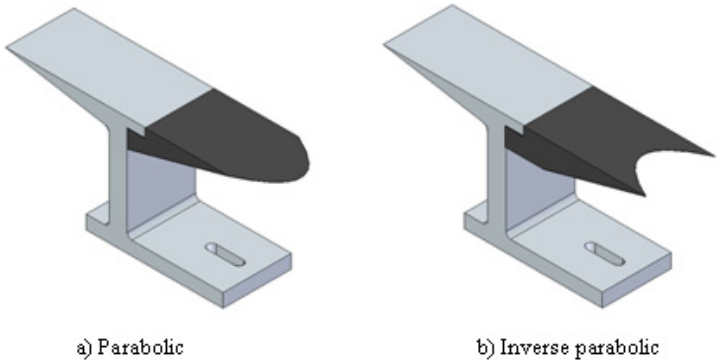

Figure 4.10: Parabolic models

The parabolic edge was defined by the equation

$$y = 0.0285x^2$$

again, the wedge angle δ was 165°.

A parabolic curve profile was chosen, as it would provide a larger edge-wall angle than a circular arc, and larger edge depth (see Figure 4.7). The edge-wall angle for the parabolic model is 25°, and for the inverted parabolic model it is 155°.

5 Experimental and Computational Procedures

Overviews of the experimental and computational procedures are presented in this section. A summary of the experimental testing procedure is given in §5.1, and a summary of the numerical modeling procedure is given in §5.2.

5.1 Seitz Tube Testing Procedure

5.1.1 Overview

All experimental testing was performed using the Seitz shock tube in the Mechanical Engineering laboratory at the University of the Witwatersrand. A brief discussion of the procedure followed during testing is given in this section.

In order to study the evolution of the flow fields with time, experimental photographs were to be taken at successive time steps during a test. Due to the lack of a high-speed camera of sufficiently high resolution, a standard digital camera was used to take a single frame for each test performed. The specific test was then reset, a slightly longer delay applied to the light source trigger, and then the test rerun. Following this procedure, a set of still images was obtained for each test

model geometry and optical arrangement, usually requiring around 10 individual experimental runs to obtain. A delay step of 25μs between successive images was used during the present study.

Prior to testing, it is necessary to make sure that all instrumentation is turned on and functioning correctly. The shock tube software provides a function for monitoring pressure and temperature inputs. It is also ideal to test the optical system frequently, as settling and minor bumps can cause large errors and deviations. The model should be checked frequently so as to ensure that it is securely mounted in the test section. The tube should be cleaned by blowing high pressure air down the expansion chamber between each test run. Optical equipment, such as mirrors and the camera, also require frequent cleaning.

5.1.2 Testing procedure

Much of the operation of the shock tube is controlled by the software program. The program also prompts for numerous checks to be made when a test is initiated, as a guard against errors and unsafe operation. A brief summary of the operating procedure of the shock tube is given below.

- The shock tube draws air from the laboratory's main 15 bar receiver. It is necessary to make sure that enough pressure is present prior to testing, and if not, pressurise the receiver. Pressurization may take a few hours.

- All instrumentation must be switched on and checked to make sure that it is functioning correctly. The software program provides numerous monitors that allow for this. Additionally, if there is a major problem with the apparatus, an error message will be displayed, informing the user, and operation of the tube will not be permitted.

- Clean the test section and check that the model is securely mounted, then close and bolt the test section doors securely.
- The test program is initiated from the software program, whereupon the user will be prompted to specify the desired shock Mach number, and other parameters.
- Based on calibration data, the diaphragm configuration required for the specified shock number will be displayed, and the user prompted to confirm that the diaphragm has been loaded correctly.
- The user will then be prompted for the light source trigger delay time.
- The program will then prompt the user to check that the pressure regulator governing the supply pressure to the shock tube is set correctly.
- Numerous other prompts are presented, and once confirmed, the test will commence and complete automatically.

5.1.3 Repeatability considerations

As mentioned previously, a separate test had to be run to obtain each image in an image set. Some inconsistencies arose during this procedure, as ambient temperature and pressure variations would occur over the course of obtaining all of the images in one set. As a result of these factors, and various other inaccuracies inherent in the shock tube control and sensor systems, incident shock Mach number variations of approximately ± 0.01 about the specified test Mach number were unavoidable. Whilst much care was taken during testing to eliminate as many inconsistencies as possible, and numerous tests were repeated so as to obtain images for incident shock Mach numbers falling into the abovementioned range, these effects are noticeable in a few of the experimental image sets. These effects manifest themselves as an apparent inconsistent time step between the images within a set. They have little effect on the validity of the results however, as can be seen by inspecting the consistency of the flow features throughout the image sets, and through comparison with the numerical results.

Due to the effort required in rearranging the optical set up between the 0° and 10° optical roll tests, all the tests for an optical roll of 10° were performed in one test session, at a later time in the year than those at 0° optical roll. The ambient temperature was between 1°C and 2°C warmer for these tests, when compared to those tests performed at 0° optical roll. This had a similar effect to that mentioned above; apparently introducing a slight delay offset between the images taken at 0° and 10° optical roll.

All numerical simulations were run at a constant ambient temperature of 23°C (295K).

5.2 Numerical Modeling

Numerical results were obtained through the use of the commercially available Ansys Fluent (versions 6.3.26 & 12) computational fluid dynamics code. Ansys Gambit was used as a pre-processor for geometric modeling and generating an initial unstructured mesh. Tecplot 360 (2008 & 2009 versions) was used to process the numerical results obtained from Fluent. A brief discussion of the procedure adopted for the numerical modeling is given in this section, along with a description of the models and parameters used.

5.2.1 Introduction

Initially, two-dimensional shock diffraction cases were modeled. These were used as reference cases to validate the solver settings against previous experimental work, and to test various mesh adaption schemes. Inviscid Euler and Navier-Stokes solutions were generated. No noticeable

difference in the free vortex behaviour and its evolution was present between the two cases. As mentioned in §2.2, numerous studies have been performed and published in the literature, that demonstrate that the inviscid solution displays negligible differences when compared to the viscous solution, with regards to the free vortex.

An explicit density-based solver, incorporating an explicit unsteady time formulation was used. A dynamic grid adaption scheme based on pressure gradients was used, and was found to track the free vortex satisfactorily. The results obtained were compared against previous work by Skews (1967a, 1967b), Skews & Crosbie (2008), and Sun & Takayama (2003a, 2003b), among others, and displayed good agreement with them. The same basic solver settings were then used in the three-dimensional modeling.

Solutions to the three-dimensional inviscid Euler equations are presented. Additional solutions to the Navier-Stokes equations are also presented in this dissertation.

5.2.2 Three-dimensional modeling

The three-dimensional models were divided into three regions, so as to obtain the best mesh quality in the most important regions of the flow (a face perpendicular to the oncoming flow, so as to allow for initiation of the incident shock wave, and the region where the flow would diffract over the edge). An example, representative of the initial unstructured meshes used for all models is given in Figure 5.1, and shows the mesh used for the parabolic edged model.

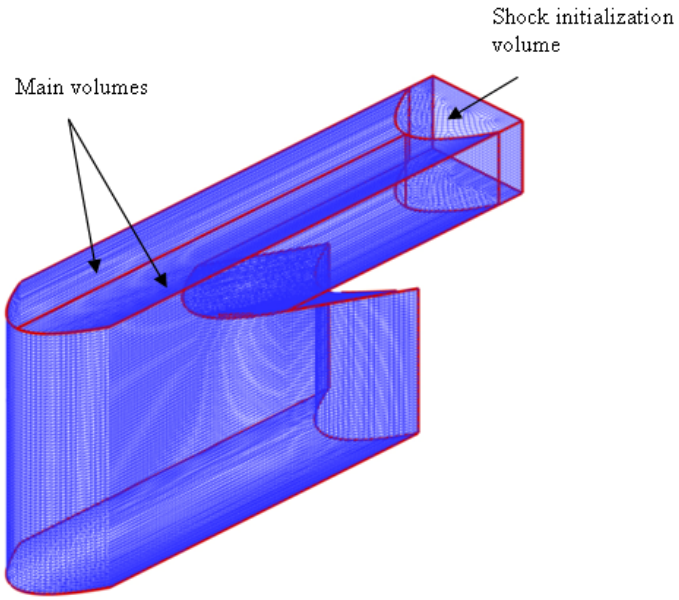

Figure 5.1: Mesh illustration

The mesh in the two main volumes was swept from the diffracting edge, so as to obtain the best quality mesh at the edge. This resulted in a face upstream that was not perpendicular to the oncoming flow. Thus, a shock initialization volume was added, so as to provide a face perpendicular to the flow direction to allow for a shock initialization, and transition to the rest of the mesh.

An initial unstructured mesh of approximately 450 000 cells was used on all models, however, with the mesh adaption scheme the maximum number of cells increased to 3.5 million. This number was limited by the memory available in the machines used. The same settings mentioned previously for the two-dimensional models were used. The smallest cells in the refined grid were approximately 0.13mm cubes. An illustration of the unrefined and refined meshes is given in Figure 5.2 for a plane taken through the flow domain. The initial unstructured mesh was generated with cells as close to 1mm x 1mm x 1mm cubes as possible.

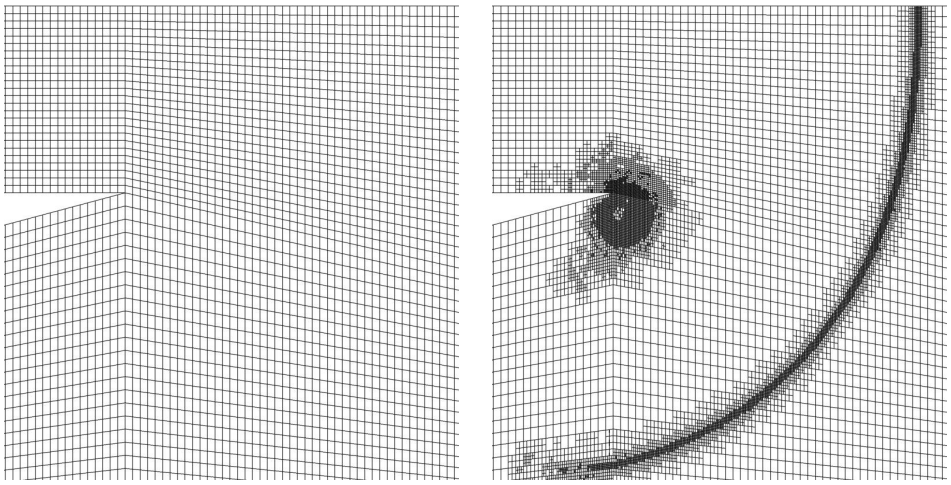

a) Unrefined mesh b) Refined mesh

Figure 5.2: Mesh adaption scheme illustration

Despite this, the meshes used in the simulations documented in this dissertation were relatively coarse when compared to those presented in the works of Sun & Takayama (2003a, 2003b), among others, for two-dimensional flow cases. Mesh densities comparable to those used by Sun & Takayama (2003b) would be impossible to attain in three dimensions with the computer equipment used in the present study. For example, the refined cell edge length in a typical two-dimensional simulation (performed by the author in validating the solver settings against work published in the literature) was 0.06mm. The minimum cell edge length obtained in the three-dimensional simulations was in the order of 0.25mm. Thus, part of the aims of this investigation were to investigate whether numerical simulation, using these relatively coarse three-dimensional grids, run on fairly high-level but non-specialised computer equipment, could accurately capture the features of these highly complex three-dimensional flows. It was thus probable, and expected, that the accuracy of solutions generated and presented in this dissertation would not match that of the many two-dimensional studies published in the literature.

Numerical simulations were run on a personal computer, incorporating an Intel Quad Core 2.4GHz processor, and 4Gb of memory. A typical simulation, using grid adaption and a mesh refinement level of 4 would take between 1 and 2 months to solve.

6 Presentation and Discussion of Numerical and Experimental Results

6.1 Overview

The numerical and experimental results obtained during this investigation are presented here. The experimental results were used as a means of validating the numerical results obtained, and as such, the two sets of results are presented together wherever logical, and are not compartmentalized.

Flow fields for incident shock Mach numbers of 1.32, 1.42, and 1.65 were investigated in this study. All numerical simulations were run at an atmospheric pressure of 85000 Pa (0.839 bar), a value representative of the atmospheric pressure in Johannesburg. Solutions to the Euler equations are presented for all models tested. Solutions of the laminar Navier-Stokes equations are presented for the 'V' model as well.

The results are presented and discussed in the sub-sections that follow, with each test model the subject of a separate section. The 'V' and 'inverted-V' models are dealt with in §6.2 and §6.3 respectively, and the parabolic and inverted parabolic models in §6.4 and §6.5 respectively. The basic flow features and associated discussion thereof are common between all models tested, and in order to avoid large sections of repetition, these are only discussed in detail in §6.2 for the 'V' model. Discussion in the sections regarding the other models is mainly aimed at reinforcing that

contained in §6.2, and demonstrating the similarities and differences in the flow fields over the different geometries.

These sections start with a general description of the flow field, using the experimental and numerical results to show its structure. This is followed by an analysis of the free vortex, using the numerical results. This makes up the bulk of the rest of these sections.

The results for the vorticity production and diffracted shock shape for all the models are combined into a single section for each topic. The vorticity production is dealt with in §6.6, and the diffracted shock shape in §6.7.

Due to the unsteady and three-dimensional nature of the numerical simulations performed, vast quantities of data were produced. Practically limitless areas of interest and methods of presenting the data exist. It would be impractical, for example, to provide plots of the properties of the vortex along its entire length for one time instant, let alone for the hundreds of time instants and numerous incident shock Mach numbers and model configurations considered, in this dissertation. The results that are presented in the following sections only represent a small portion of the amount of data considered, and those that are presented were chosen so as to highlight the most important regions and effects in the flow field, and how they evolve with time.

6.2 'V' Model Tests

The M_s=1.42 case is dealt with in §6.2.1 through §6.2.4. A brief overview and discussion of the flow field and general arrangement of the flow field are given, followed by a more detailed investigation into the structure of the flow field, specifically of the free vortex. A discussion of

vorticity in the flow field and a brief introduction to vorticity production are then given. A discussion of the Navier-Stokes solution follows.

A discussion of the M_s=1.65 and M_s=1.32 cases is given in §6.2.5.

6.2.1 General description of the flow field

Schlieren images at sequential time steps (of δt =25μs) were taken for an optical roll of 0° and 10°. The delay time given in the following sections is that specified as the light source trigger delay. A corresponding delay time, giving the equivalent instant in the numerical simulations was calculated, based on the lengths and shock Mach number.

Schlieren images showing the evolution of the free vortex for 0° optical roll are given in Figure 6.1. Image a) is at a time delay of 1700μs from the diaphragm bursting. Image k) represents a total time of 1950μs.

The diffracting shock wave is clearly visible in the earlier images, it then moves out of the shot. The vortex appears to retain a fairly consistent profile from images c) through i). In the last two images, j) and k), the vortex appears to be less well defined. It is also evident that the vortex profile expands as it propagates downstream. It should be noted that in order to obtain images showing the features of the free vortex, a relatively low schlieren system sensitivity had to be used. As such, flow features, such as the slipstream, are not well defined in these images.

Figure 6.2 shows the same test for an optical roll of 10°. The top row of images are schlieren photographs obtained from experiment, and the bottom row the results of the numerical

simulation at corresponding time intervals. These images are more useful than those presented in Figure 6.1 (for 0° optical roll) in highlighting the incident shock wave structure, and the bending of the free vortex at the window. The numerical data plots show a surface of constant density (0.8 kg/m^3), and line plots on slices parallel to the centre line of the model, showing lines of constant density. Two slices, showing these constant density lines, are present in the images contained in Figure 6.2, one at the near side window, and the other on the centre line of the model. In the last two numerical results images of Figure 6.2 (images g) and h)), the shock wave has reflected off of the model geometry, and has begun to propagate back upstream. This effect is obviously not present in the corresponding schlieren images.

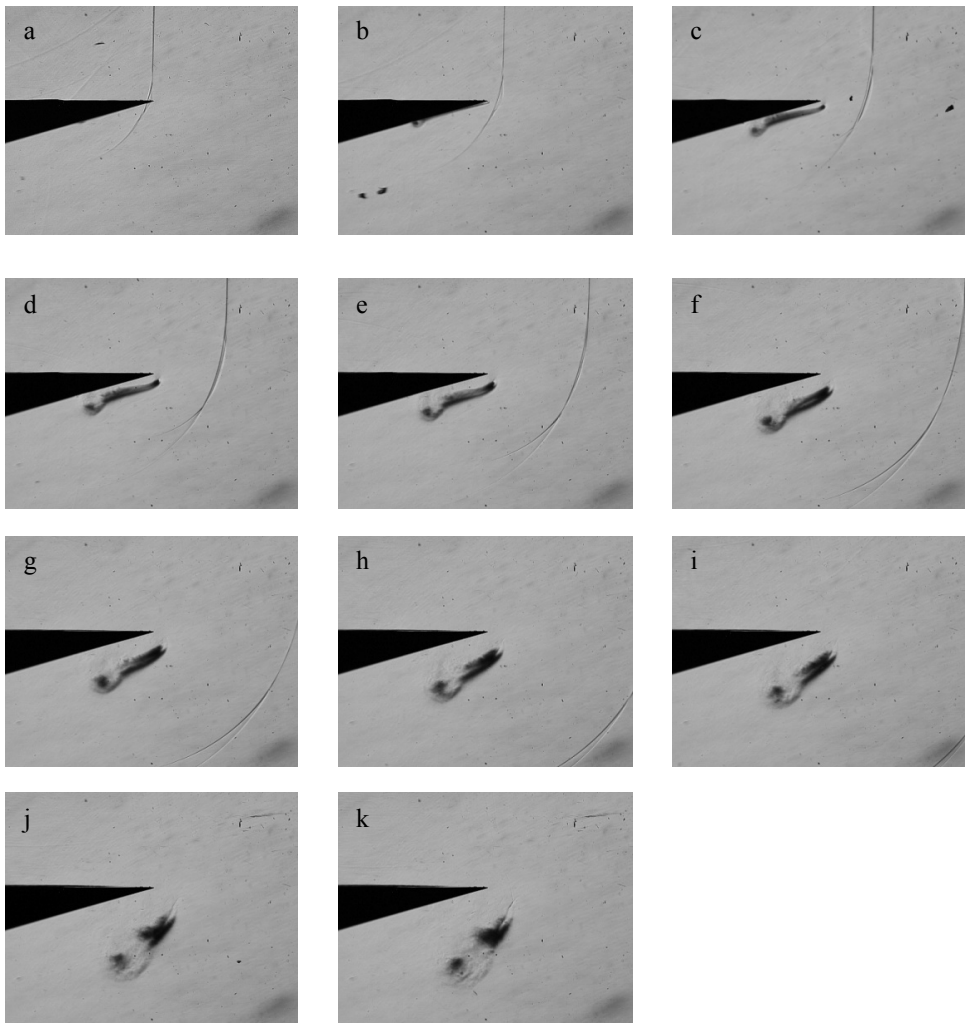

Figure 6.1: 'V' model schlieren images, 0° optical roll. Image a) at 1700μs, δt =25μs

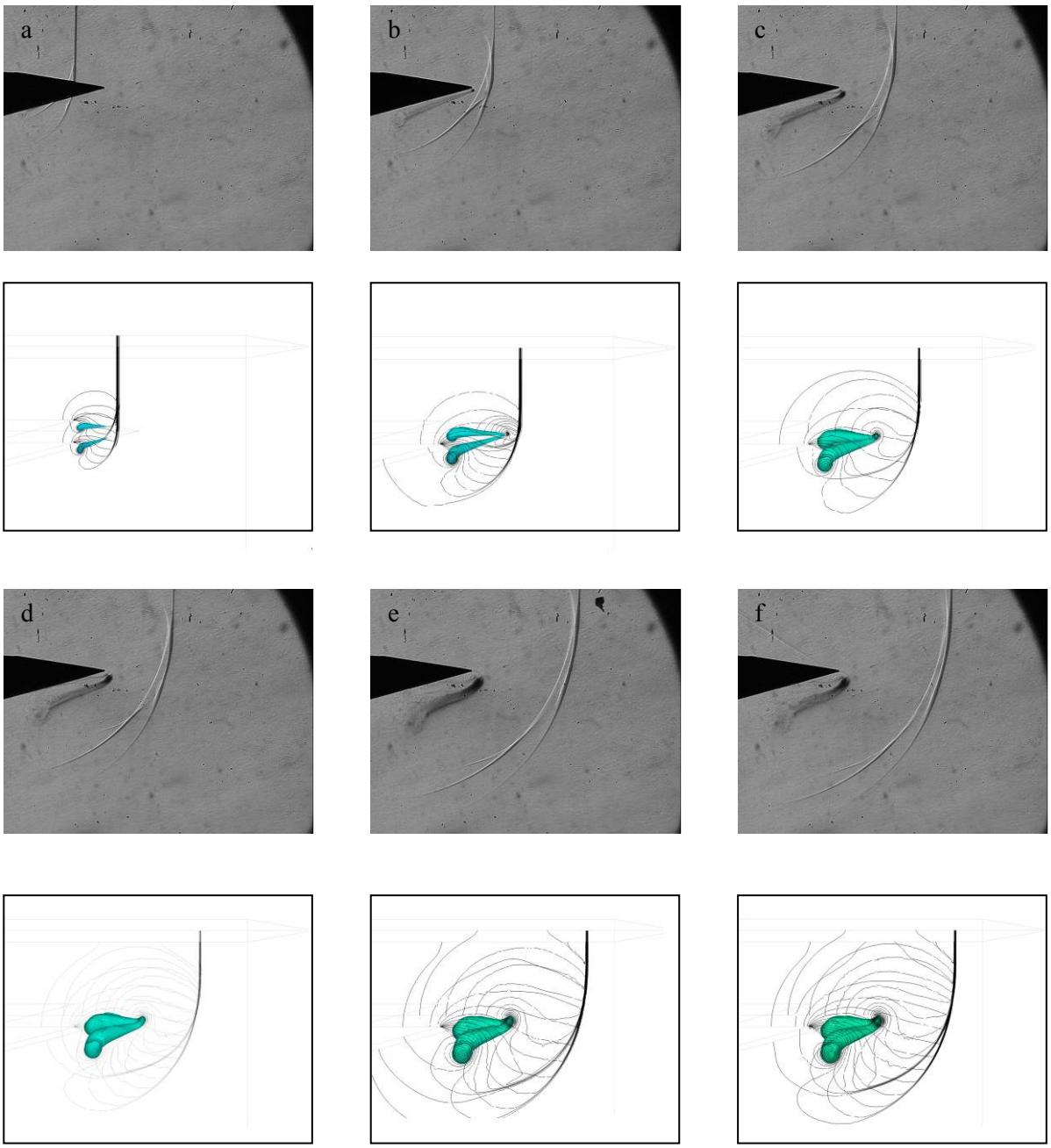
a
b
c
d
e
f

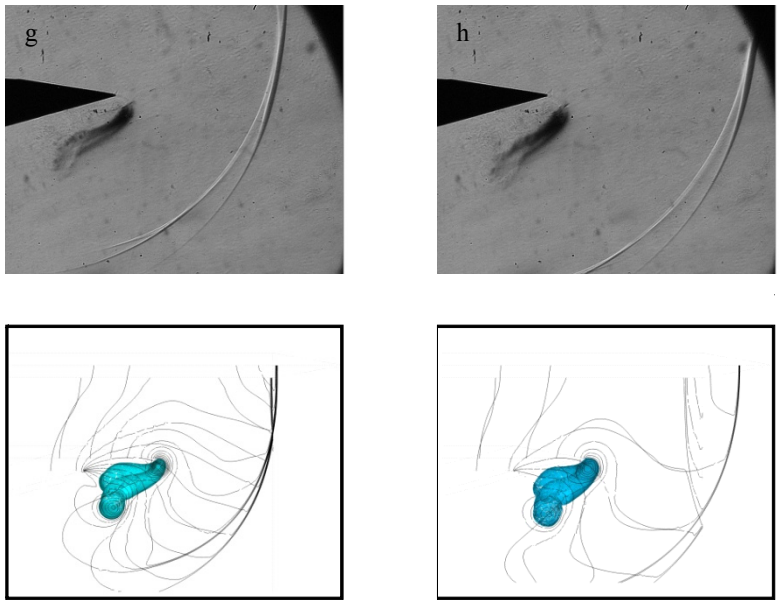

Figure 6.2: 'V' model schlieren and CFD images, 10° optical roll. Density contour (ρ=0.8 kg/m^3), lines of constant density indicated. Image a) at 1675μs, δt =25μs

The above sequence of images provides a visual means of verifying the accuracy with which the numerical solutions mimic the actual experimental behaviour. The correlation between the two sets of results is striking, and is perhaps better displayed by an overlay of the numerical and experimental images, as is given in Figure 6.3. Here, two surfaces of constant density are plotted.

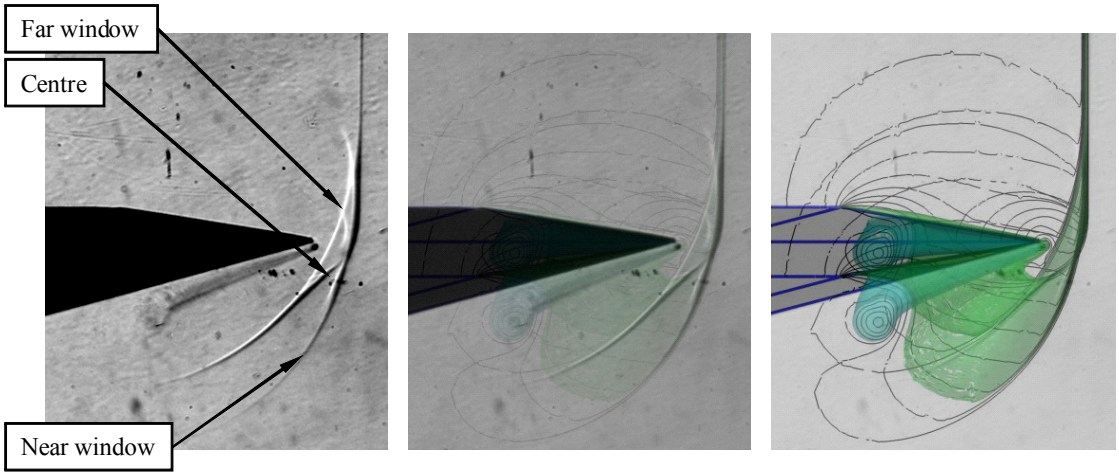

Figure 6.3: Overlay of numerical results on experimental image. (Image b) from figure 6.2)

An initial simple check of the correctness of the numerical simulations can be performed by checking the flow conditions behind the shock wave against those expected for theoretical relations (equations (2.8) through (2.12)). Table 6.1 gives a summary of flow parameters obtained theoretically and numerically for the present case of an incident shock wave travelling at Mach 1.42. It should be noted that numerical simulations were performed at ambient pressures and temperatures of 85 000Pa and 295K respectively.

Table 6.1: 'V' model M_s=1.42 theoretical and numerical comparison at delay of 1800μs

	Pressure Behind Shock (Pa)	Temperature Behind Shock (K)	Velocity Behind Shock (m/s)
Theoretical Values	185793	373	205.5
Numerical Values	184360	372	204

A brief discussion of the flow features illustrated in Figure 6.2 and Figure 6.3 will now follow.

From the schlieren images in Figure 6.2 and Figure 6.3, the diffracted shock wave structure can be seen as the shock evolves with time. The lower shock profile corresponds to the near shock wave window interface. The upper (and less clearly defined) shock profile corresponds to the interface between the shock wave and the far side window. Additionally, the profile of the shock wave at the centre of the test section can be seen. This generally falls between the two window profiles in the images at an optical roll of 10°. The components of the shock wave are labeled in Figure 6.3. It should be noted that only the near side window and centre shock profiles are shown in the numerical images in Figure 6.2.

From Figure 6.2 and Figure 6.3, it is evident that the vortex exhibits significant distortion close to the window, and near the centre, where the two vortices from either side of the diffracting edges meet. Furthermore, it appears from the images, that the distortion where these two vortices meet

becomes more pronounced with time, while appearing negligible in Figure 6.3 (Figure 6.2 b). The bending of the vortex to meet the window at a right angle appears to have been accurately reproduced in the numerical simulations. The distortion of the vortex will be discussed in more detail in the sections to follow.

Obviously, the regions affected by this distortion would not exhibit a self-similar evolution with time. However, it appears that the region between the two vortex distortions is uniform, and may exhibit properties of self similar vortex evolution. It does appear however, that by image e) in Figure 6.2, the entire vortex has been bent, showing significant distortion throughout its length. These phenomena will be discussed, for the current test model, in the sub-sections that follow.

Shock diffraction

Obviously, the diffraction profile for the present three-dimensional case varies from the two-dimensional case. The location of the vortex varies across the flow domain, this is discussed further in the sub-sections that follow. A study of the shape of the diffracting shock wave is given in §6.7.

Summary

In the sections that follow, the various regions of the flow field are explored in greater detail. A view of the flow field, generated from a set of numerical results, showing its typical arrangement is given in Figure 6.4. The important parts of the flow field are labeled on the figure and a general description of each part and how it evolves with time is given below.

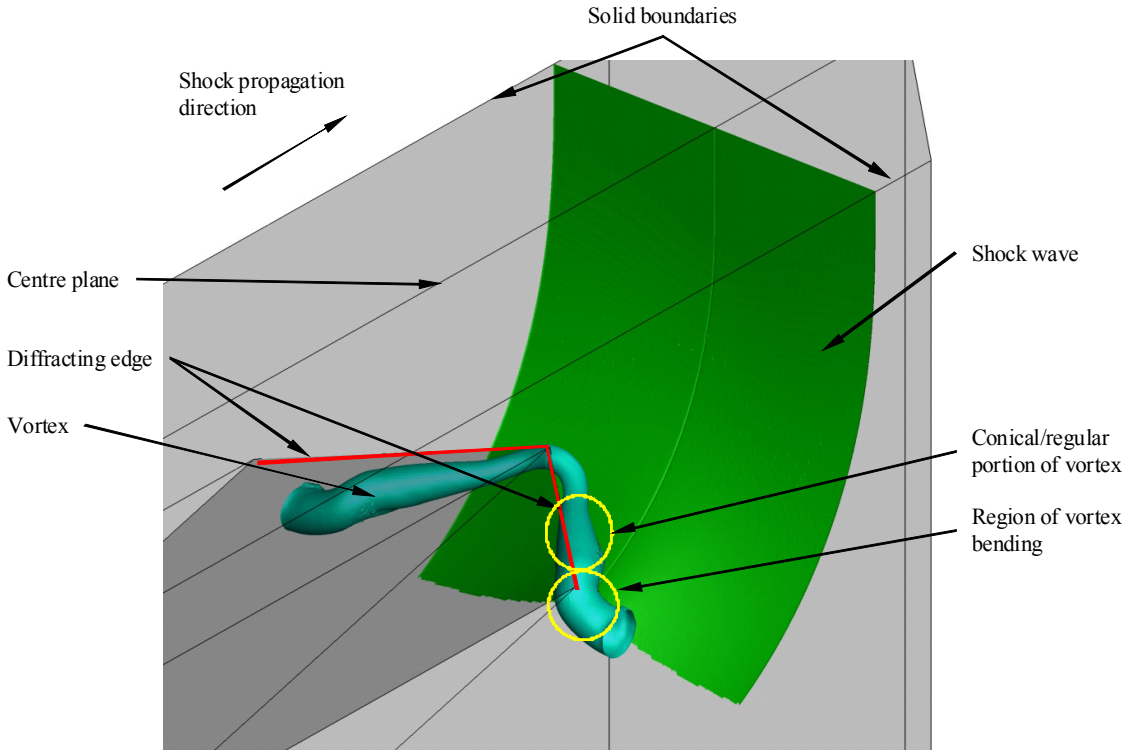

Figure 6.4: Illustration of typical flow field

The incident shock wave undergoes a diffraction process consistent with that of two-dimensional cases. Analysis of the shape of the diffracted shock wave is presented in §6.7.

Figure 6.4 clearly illustrates the bending of the free vortex in the regions close to the solid boundary, and at the centre of the flow domain. In between these two 'bend' regions, a region exhibiting a conical envelope (labeled as the regular region for the parabolic models) that is apparently free from the distortions caused by the bends exists. As time evolves, this region becomes smaller, until the whole vortex appears bent.

The flow field was studied for around 300μs after the shock wave reached the outer extremities of the diffracting edge, for M_s=1.42. The instant that the shock starts to diffract is referred to as t_0.

6.2.2 Structure of the flow field

The bending of the free vortex

Top views showing the evolution of the free vortex are given in Figure 6.6. Again, a density surface of 0.8kg/m^3 is plotted. The core of the vortex was extracted using Tecplot, and is indicated on the images as a black line. The vortex core is calculated by considering the eigenvalues and eigenvectors of the velocity gradient tensor. The algorithm used does have some slight difficulties extracting cores, particularly when the axis aligns with grid lines. As such, some portions of the core are not continuous in the images that follow. The first image occurs 55μs after t_0. There is an interval of 20μs between each successive image. A non-dimensional scale is given so as to allow for comparison of the extent of the vortex distortion between different test cases. The total length of the scale corresponds to 38mm. 0 on the scale represents the centre plane.

The behaviour of the vortex can be seen from this sequence of images. The vortex core has bent so as to meet the wall at a right angle, and at the centre of the domain, or tip of the 'V', the cores of the two vortices on either side of the edge bend so as to join and form a continuous curve. In between these two curved regions a linear portion of the core exists, where the vortex exhibits a conical envelope. The core assumes a complicated profile in the region of the bends, where a point of inflection is apparent as the core bends so as to meet the wall, and the core from the vortex on the other side of the edge, at a 90° angle. The behaviour at both the centre and near the wall appears very similar.

The vortex appears to remain relatively stationary with time when viewed from the top, aside from the region close to the wall, which propagates in the direction of the incident shock wave. The motion of the vortex would obviously depend on the velocity field under the diffracting edge,

which in itself is very complicated. The velocity vector under the diffracting edge generally points downwards, or into the page in the images shown in Figure 6.6.

It is evident that as the vortex evolves, so the distortion (caused both by the wall, and by the meeting of the two vortices in the middle) propagates along the vortex core. In images a) and b), before the two vortices have met, the vortex core forms a straight line away from the area affected by the walls, with the density surface forming a cone, and appears to exhibit a self-similar evolution along its length. However, once the shock wave has passed the tip of the edge and the two vortices have met, a significant distortion in the vortex occurs. This can be seen in image c), and as the vortex evolves with time, its effects can be seen to propagate along the vortex axis, until, in image h), the entire vortex appears affected, with the core exhibiting variable curvature along its entire length.

It appears from these images that the vortex core is further back and closer to the diffracting tip than it is in the two-dimensional case. This result is mirrored in the experimental results. Through close examination of the schlieren image given in Figure 6.5, one can see the spiraling of the slip stream on the centre plane. Also indicated on the figure is the approximate location of the vortex core on the centre plane.

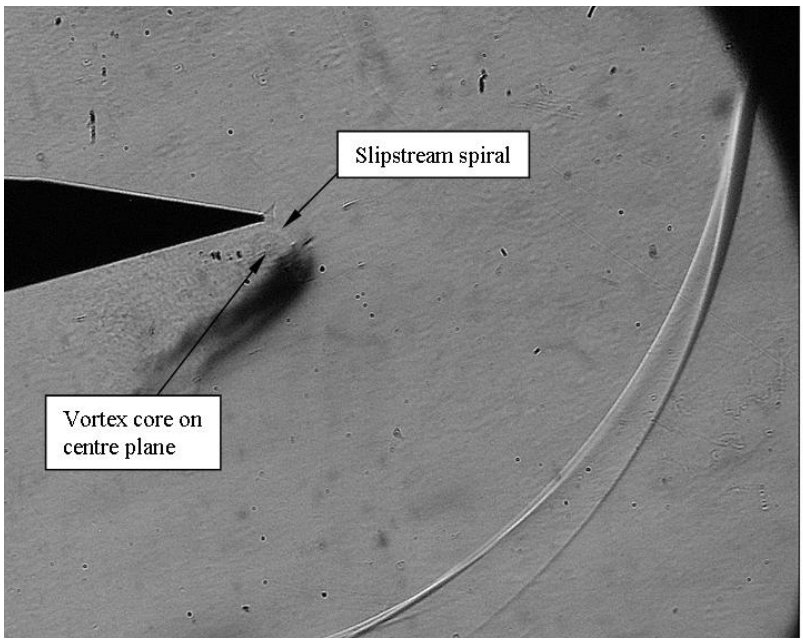

Figure 6.5: 'V' model, 10° optical roll, M_s=1.42, centre plane illustration

It can be seen in Figure 6.6 that a kink appears in the density surface towards the centre of curvature of the bend in the region of the window (seen in images f) through h)). In this region, the vortex is found to contract radially. The implication of this, referring to equation (2.19), is that the vortex has been 'stretched'. Thus it would be expected that a local maximum of the vorticity vector would be present in the region of contraction, so as to satisfy Hemholtz's laws. This is exactly what occurs. Further discussion is given in the sub-section on the structure of the free vortex.

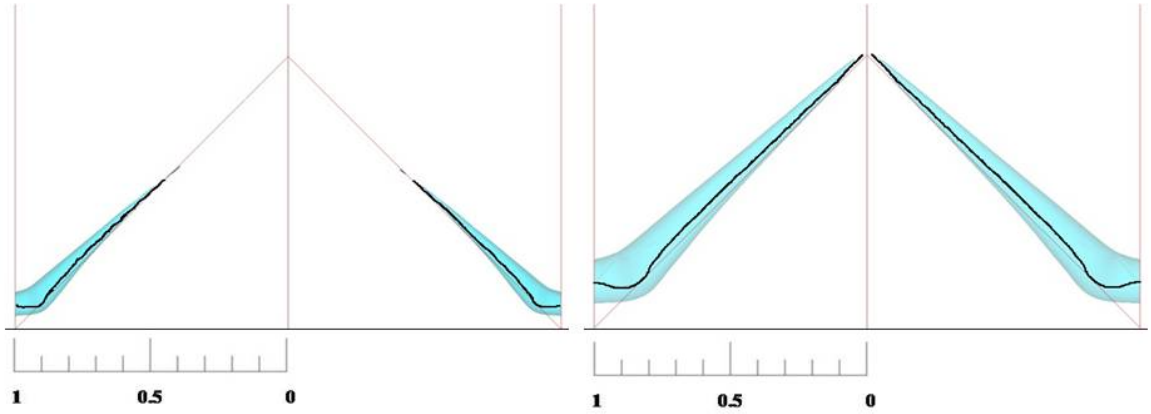

a) t=55μs b) t=75μs

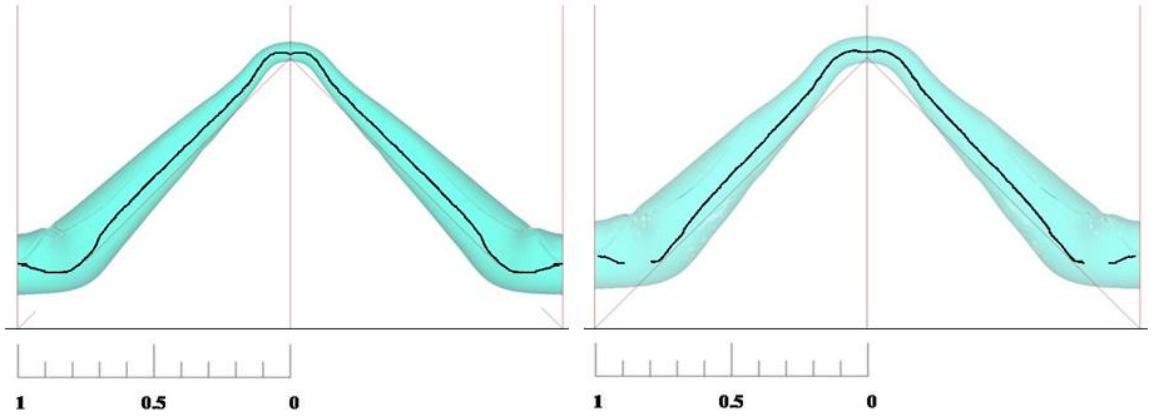

c) t=95μs d) t=105μs

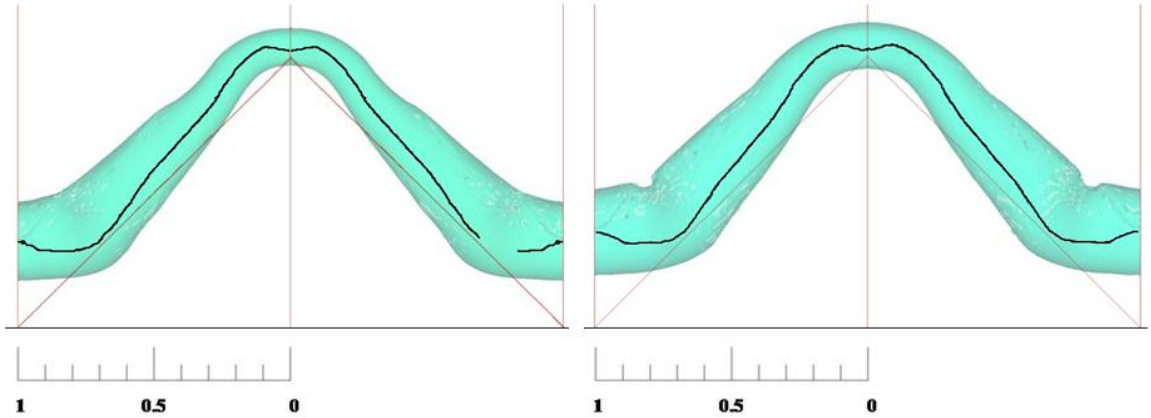

e) t=125μs f) t=145μs

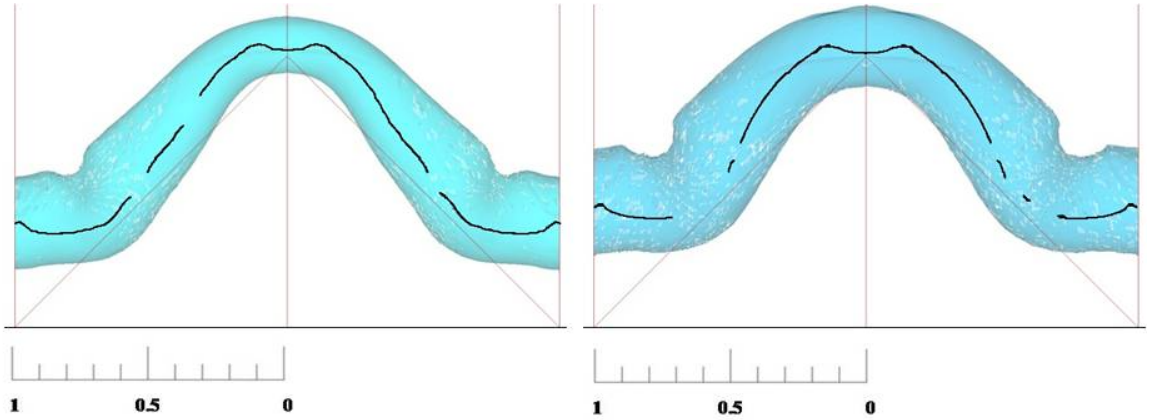

Figure 6.6: Top View of Vortex Bending ('V' M_s=1.42), surfaces of constant density (0.8kg/m^3) shown

The sequence of plots in Figure 6.7 contains vertical slices at a delay of 75μs (image b) in Figure 6.2). The captions give the distance that the slice was taken away from the centre line.

Figure 6.8 contains vertical slices at a delay of 155μs (image f) in Figure 6.2). These images show the bending of the vortex to meet the window, and its bending to meet up with the vortex on the other side of the wedge. The slip stream, mentioned previously, is more clearly visible in these images. Significant distortions to the vortex can be seen between 20 mm and 28 mm (0.52 and 0.74 on the scale in Figure 6.6) from the centre line, as the vortex undergoes significant bending in this region, so as to meet the window at 90°. The top view of this case can be seen in Figure 6.6 f), where it can be seen that a slight indent starts to appear in the vortex at this stage of its evolution. This can be seen in images d) and e) of Figure 6.8, where the vortex appears to have a circular profile in image d), whereas it is more ovular in image e). The slice in d) is prior to the indent, while the slice in e) is taken at a point inside the indent, and corresponds to 0.79 on the scale shown in image f) in Figure 6.6. It must be borne in mind here that the plots are not taken on planes that are perpendicular to the vortex axis, and so the true profile of the vortex is distorted in these images. This is done in the section on the structure of the free vortex below.

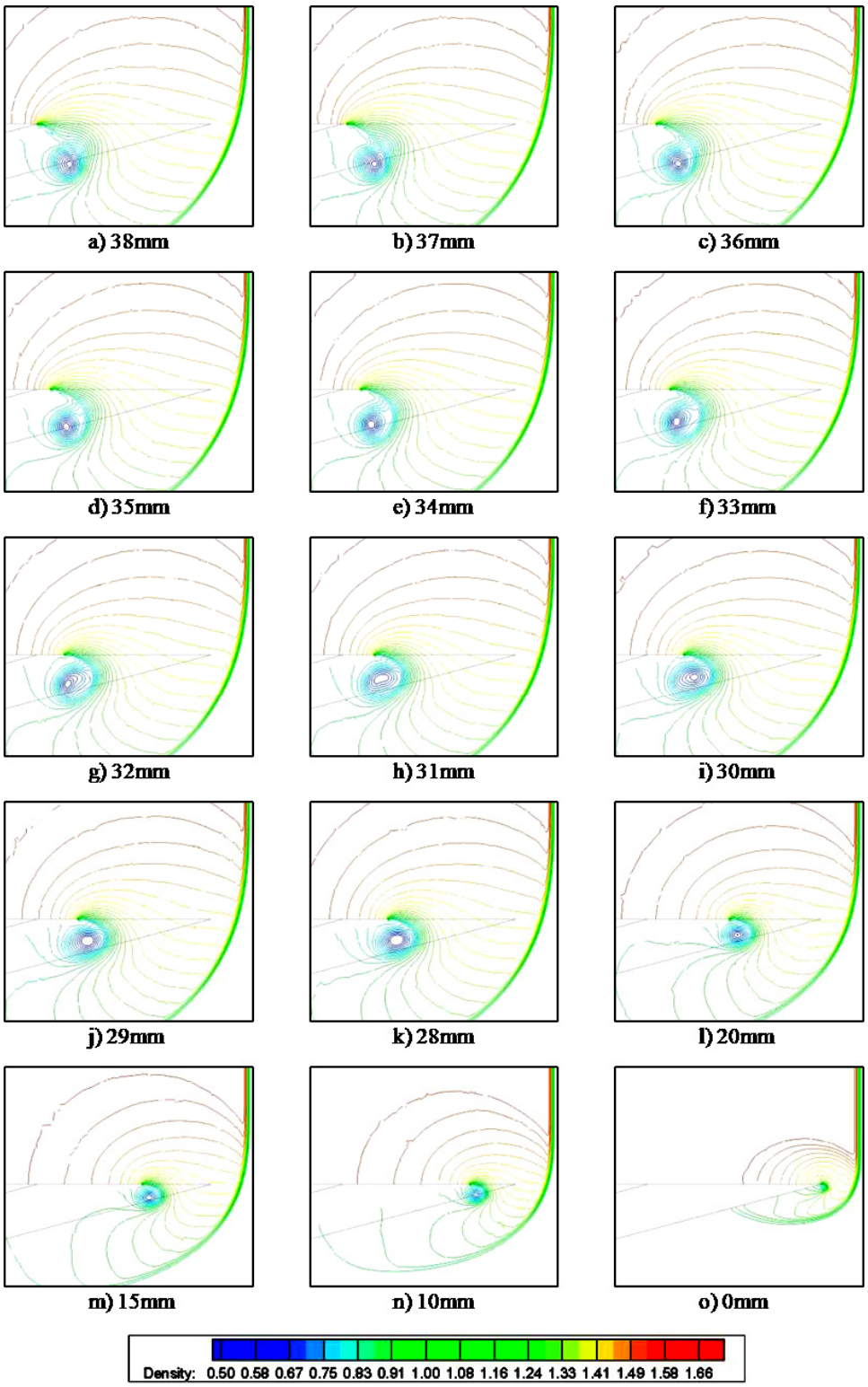

Figure 6.7: Vertical Slices Density Contours ('V' model, M_s=1.42, t=75μs)

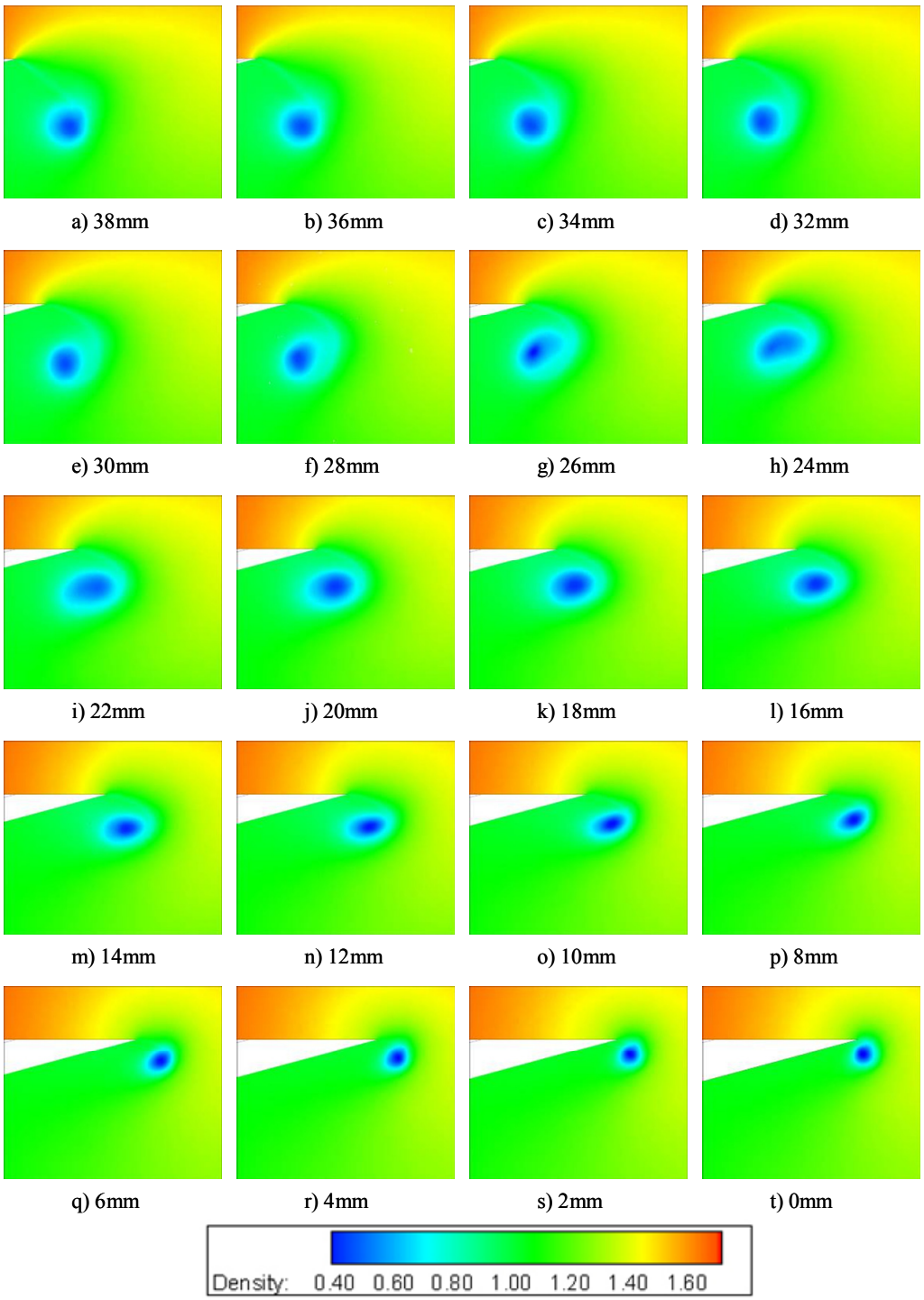

Figure 6.8: Vertical Slice Flood Density Contours ('V' model, M_s=1.42, t=155μs)

Figure 6.9 gives a top view with stream lines, indicating the general behaviour of the flow behind the incident shock wave over the edge. This is a complicated problem that varies with time, and is not analysed in any further detail. It does however serve to illustrate that the flow over the edge, in general, curves around the vortex and slightly towards the centre of the flow domain.

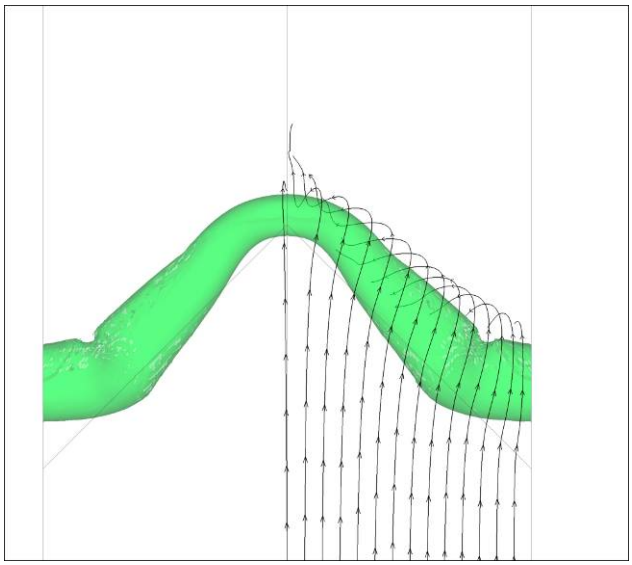

Figure 6.9: Streamlines indicating flow over the diffracting edge

The structure of the free vortex

In this section, the properties of the vortex are investigated on the two planes shown in Figure 6.10. Although limitless scope exists for the selection of this data, it is believed that the two locations chosen demonstrate the most important aspects of the flow. The first, plane I, is taken through the section of the vortex exhibiting a conical structure, and the second, plane II, through the region of the bend at the solid boundary. The planes extend directly into the page, their normals parallel to the top surface of the diffracting edge, and are taken perpendicular to the vortex cores from the top view. The velocity data presented is transposed however, so that the updraft component is parallel to the vortex core at the location being considered. Data is taken at various time instances in an effort to show the evolution of the structure with time. The aim of

this section is to show the structure of the vortex, and the effects that bending have on it. The self similarity of the vortex evolution in the 'conical' region is also investigated, and demonstrated in the results presented.

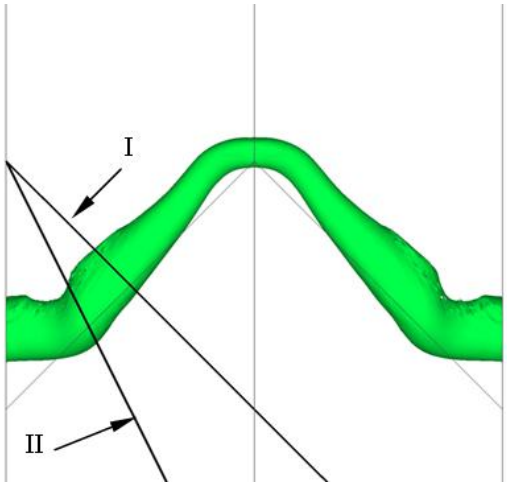

Figure 6.10: Vortex Slice Definitions (M_s=1.42)

Figure 6.11 shows the profile of the vortex taken on plane I for t=155µs. Data is given for t=100µs and t=155µs. The profile of the vortex at the two time instances appears very similar, this is demonstrated by the plots that follow.

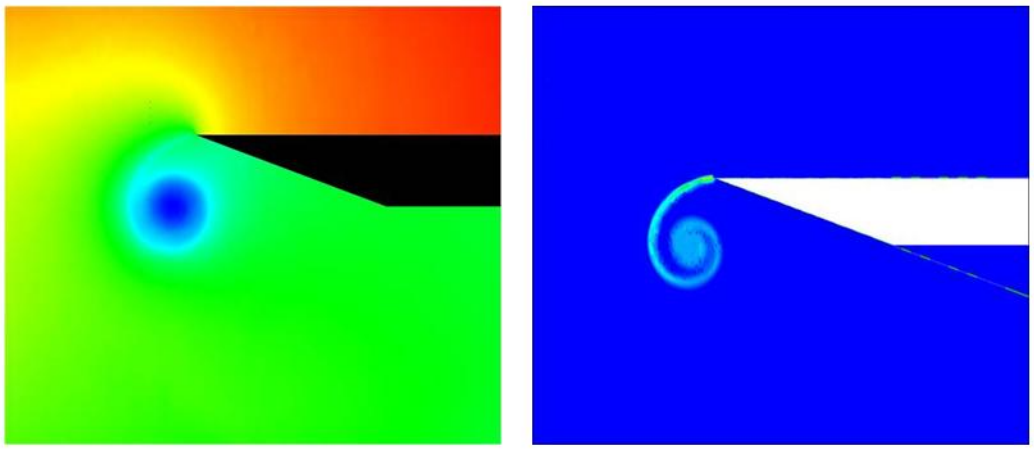

a) Density b) Vorticity Magnitude

Figure 6.11: Vortex Profile M_s=1.42, t=155µs

The plots given in Figure 6.12 through 6.15 below contain data taken on a horizontal line through the vortex core. The data is taken prior to the slipstream, and the spirals of the slipstream can clearly be identified in the plots. The first set of data is for t=100μs, and another at a later time t=155μs is also given.

Figure 6.12 gives a plot of the tangential velocity profile (positive counter-clockwise in the images) on a horizontal slice taken through the vortex core. Note that the extent of the slice was such that the data represented starts to the left of slipstream (refer to Figure 6.11 b)). The zero distance point is arbitrary, and was merely chosen as such so as to include the vortex and the flow immediately around the vortex in the plot.

Considering the data set for t=100μs in Figure 6.12, the first peak, corresponding to approximately 4.5 on the x-axis, is the outer spiral of the slipstream (the left-hand side in Figure 6.11 b)). The second peak is the beginning of the region of continuous vorticity magnitude that lies inside the slipstream spiral. The trough between the two peaks represents the region between the slipstream spirals. The apex of the trough thereafter is the vortex core, which is located at approximately 10.5 mm. The change in gradient at 11.5 mm corresponds to the region between the free vortex and the right-most portion of the slipstream. The final peak is the rightmost portion of the slipstream.

The tangential velocity profile approximates that of a Rankine vortex, i.e. the tangential velocity is proportional to distance away from the core, near the core of the vortex. This is clearly evident in Figure 6.12, however, the slipstream disturbs this by introducing variations in the tangential velocity, as was discussed above.

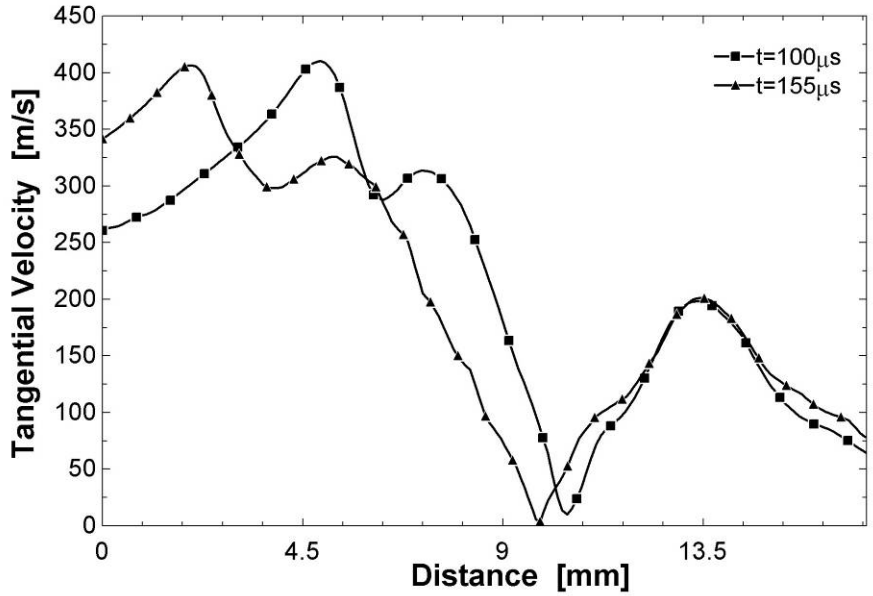

Figure 6.12: Tangential velocity profile, conical section, M_s=1.42

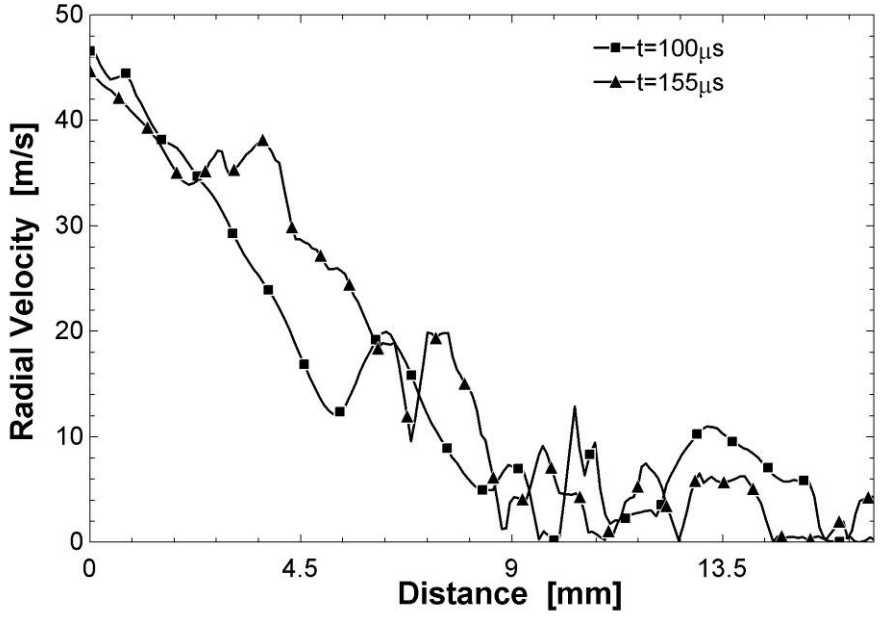

Figure 6.13: Radial velocity profile, conical section, M_s=1.42

The spiral nature of the vortex can clearly be seen in Figure 6.11 b), and from the tangential velocity plot. Again, referring to the data set for t=100μs, one can see that the vortex occupies the region from approximately 4.5mm to 13.5mm on the x-axis. The tangential velocity is greatest just above the left-most spiral of the slipstream. It can be seen that the maximum tangential velocity is approximately 400m/s at this time instant. The maximum tangential velocity at the right most portion of the vortex is around 200m/s, and the resulting tangential velocity profile is a highly complicated structure, that would be impossible to describe through a set of mathematical equations. The vortex regions, as discussed in §2.3.1, are still identifiable. A decay region that loosely corresponds to the data presented by Lee & Bershader (1994) is present between 0 and 4.5mm, and again on the right hand side of the vortex (see Figure 2.4 for an illustration of the regions comprising a vortex). The transition from the core region to the decay region corresponds with the data presented by Lee & Bershader (1994) for the logarithmic region, however, the presence of the slipstream on the left hand side has lead to the forming of two peaks in tangential velocity. This is not seen in isolated 'equilibrium' vortices that do not incorparate a slipstream as part of their structure. As this vortex is not isolated in an ideal flow field, the outer regions would obviously not correlate with the structure mentioned previously and in the literature.

There is quite clearly a strong similarity between the data sets for the two time instants presented in Figure 6.12. This would imply a degree of self similarity in the evolution of the vortex with time in the region that is currently being considered. There are obviously some slight discrepancies between the two data sets, caused by the presence of the solid boundaries and the fact that this is a highly complicated three-dimensional flow field.

Figure 6.13 gives the radial velocity, positive in the radial direction away from the core. In regions close to the vortex core, the magnitude of this value is typically a few percent of the magnitude of the tangential velocity. This small radial velocity is described in the experiments by Bershader (1995) for two-dimensional cases, and is typically appreciably larger than that

predicted by theory (Bershader, 1995). The data appears rather erratic, there is however a degree of similarity between the data sets of the two time instances presented.

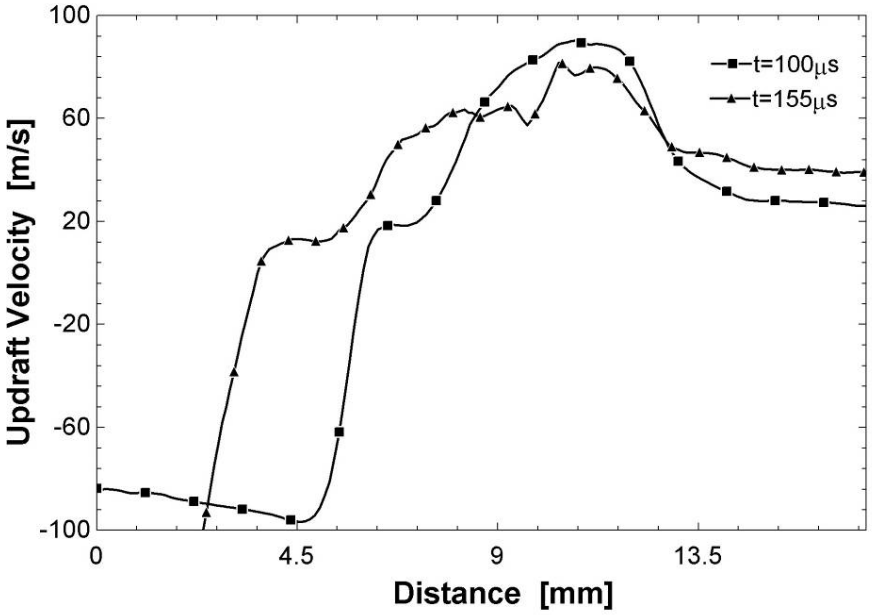

Figure 6.14: Updraft velocity profile, conical section, M_s=1.42

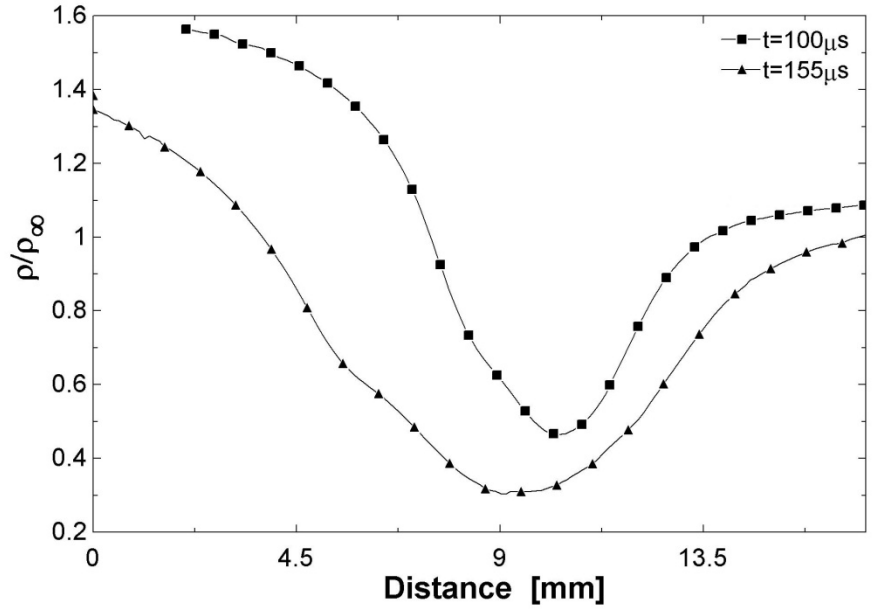

Figure 6.15: Pressure profile, conical section, M_s=1.42

Figure 6.14 plots the updraft velocity on plane I. A positive value indicates that flow is towards the wall in the direction of the core, and a negative value towards the centre plane of the flow domain. It can be seen that a maximum of approximately 90m/s occurs at the vortex core for t=100μs. This value represents a large percentage of the tangential velocity, and represents a major difference between the two and three-dimensional shock diffraction and free vortex cases.

Considering the t=100μs case, and moving from left to right in Figure 6.14, the updraft velocity is initially negative. A large, apparently discontinuous jump occurs in its value as one moves through the outer spiral arm of the slipstream. The vortex occupies the region between 6.3mm and 13.5mm on the x axis of the plot. The updraft velocity is greatest at the core and positive across the region which the vortex occupies, indicating that there is a significant updraft present throughout the vortex. This indicates that this vortex is single-celled, its core structure differing from that of a typical tornado, which is two-celled, and exhibits a downdraft region at the core, surrounded by a large updraft region. As with the tangential velocity plot, there is good similarity between the plots of the two different time instances. To the knowledge of the author, no literature exists detailing the updraft velocity profile in a typical three dimensional vortex.

Figure 6.15 gives a plot of the pressure, normalised by the reference pressure (85000 Pa). Again the various components of the flow field, mentioned previously, can be identified from the peaks and troughs in the data. Considering the data for t=100μs, the pressure value at the core is approximately 0.5. The pressure trend correlates quite closely with those published in the literature (see Lee & Bershader (1994) for two-dimensional vortices. Again, a good degree of similarity is present between the two data sets plotted.

Figure 6.14 shows the structure of the vortex taken through plane II at t=175μs. Data for the ‘bend’ section is presented for t=175μs and t=250μs, in a similar to manner to the above.

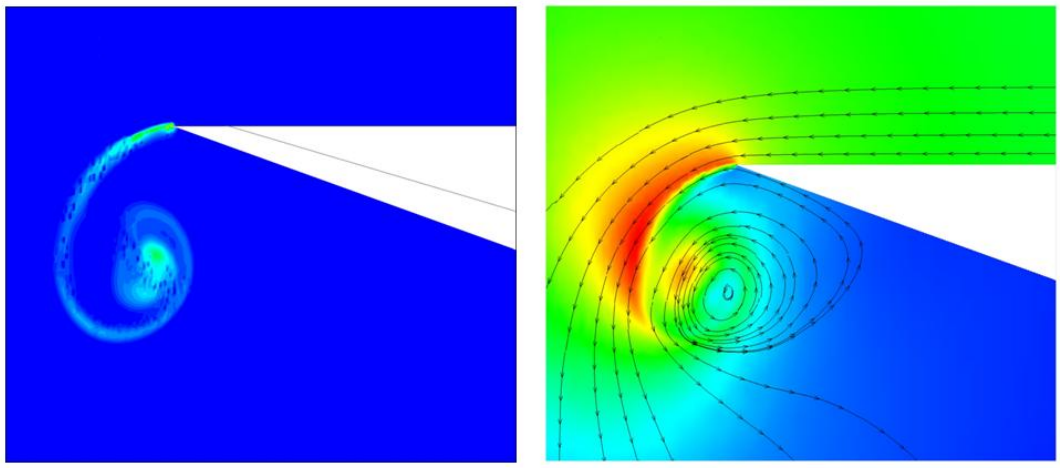

a) Vorticity magnitude b) Velocity magnitude with streamlines

Figure 6.16: Vortex profile, 'bend' section, M_s=1.42, t=175μs

One can see in Figure 6.16 a) the distortion caused to the vortex profile by the bend, when compared to the profile given in Figure 6.11 b), which is regular along the 'conical' section. A region of higher vorticity magnitude in the region of the bend is apparent, as can be seen by comparing the two images. This result reinforces the previous discussion; that the vortex appears to contract in the region of the bend, and hence, in order to satisfy Hemholtz's laws, a local maximum of the vorticity vector is found in this region.

The centre of curvature of the bend lies to the left in the images in Figure 6.16. Image a) shows that the slipstream is distorted, and that a larger gap exists between the outer portion of the spiral and the central core region when compared to Figure 6.11 for the 'conical' section. Image b), which shows the velocity magnitude, seems to indicate that a region of higher velocity magnitude exists in this region. This is evidenced by the red region just to the left of the core. The large red region on the left in the image is the flow above the slipstream. The vortex core lies at the centre of the circular slipstream pattern. It can be seen that there is a region of relatively low flow velocity around the core.

Similar plots to those given above are presented in Figure 6.17 through 6.20 for the slice taken through the bend in the vortex. Much of the discussion given above applies here, and will not be repeated, for the sake of brevity.

Figure 6.17 is a plot of the tangential velocity on plane II, at the two time instants considered here (t=175μs and t=250μs). The general trend of the two curves is quite similar to each other, and also to those for the conical section given in Figure 6.12. The distance between the two peaks in tangential velocity on either side of the vortex core is greater in the bend section, with rightmost peak (the outside of the bend) showing a lower velocity magnitude than for the data pertaining to the 'conical' section of the vortex. The presence of the bend has caused the almost linear portion of the curve between the second peak on the left and the core in the results from the 'conical' section to become distorted here. This is particularly evident in the data for t=250μs.

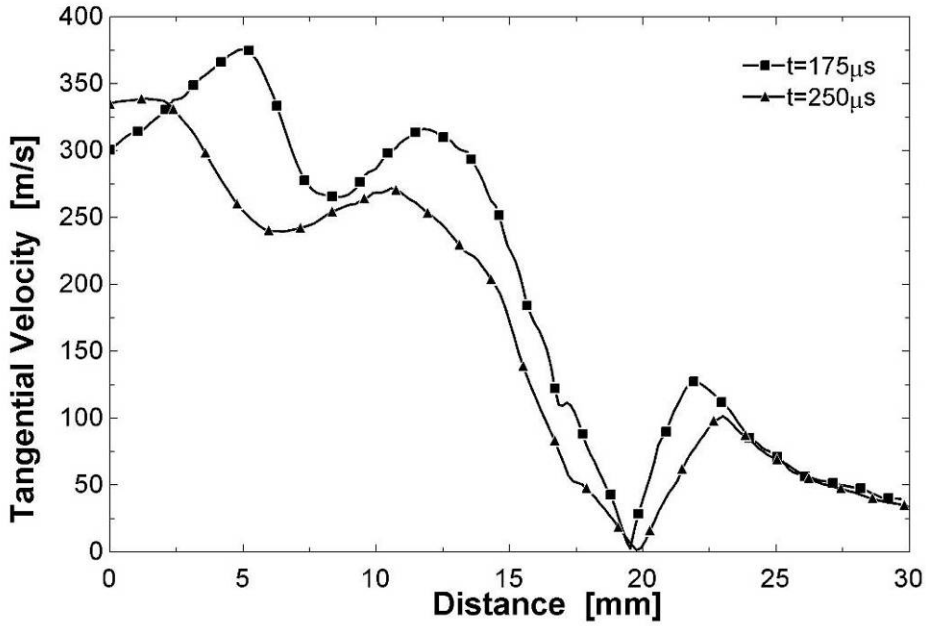

Figure 6.17: Tangential velocity profile, bend section, M_s=1.42

Figure 6.18 gives a plot of the radial velocity. Plots of the updraft velocity and the normalised pressure profile are given by Figure 6.19 and Figure 6.20 respectively.

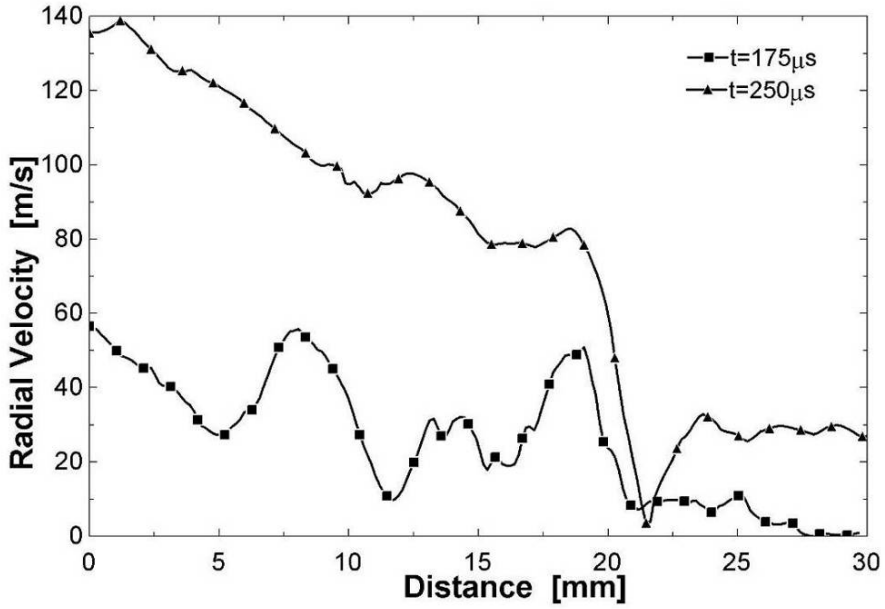

Figure 6.18: Radial velocity profile, bend section, M_s=1.42

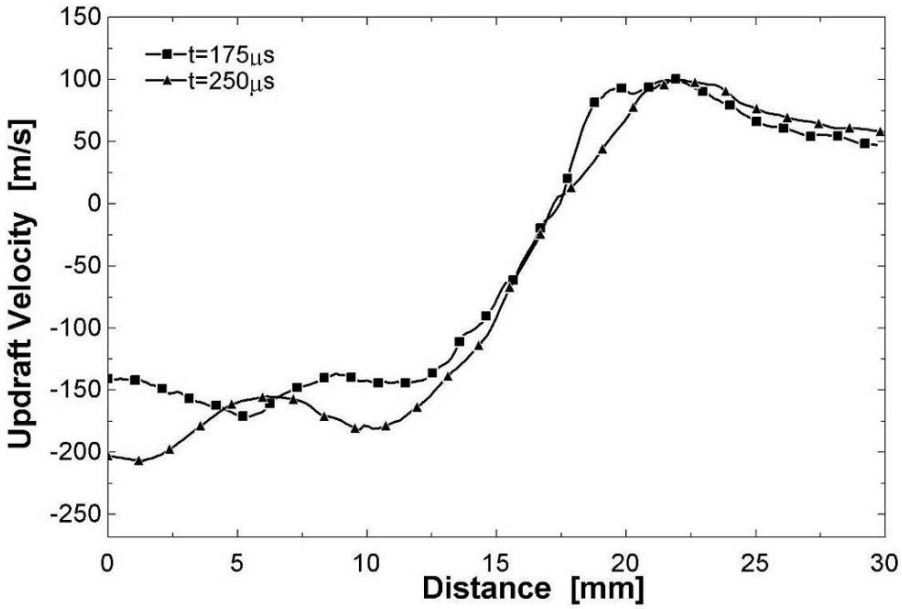

Figure 6.19: Updraft velocity profile, bend section, M_s=1.42

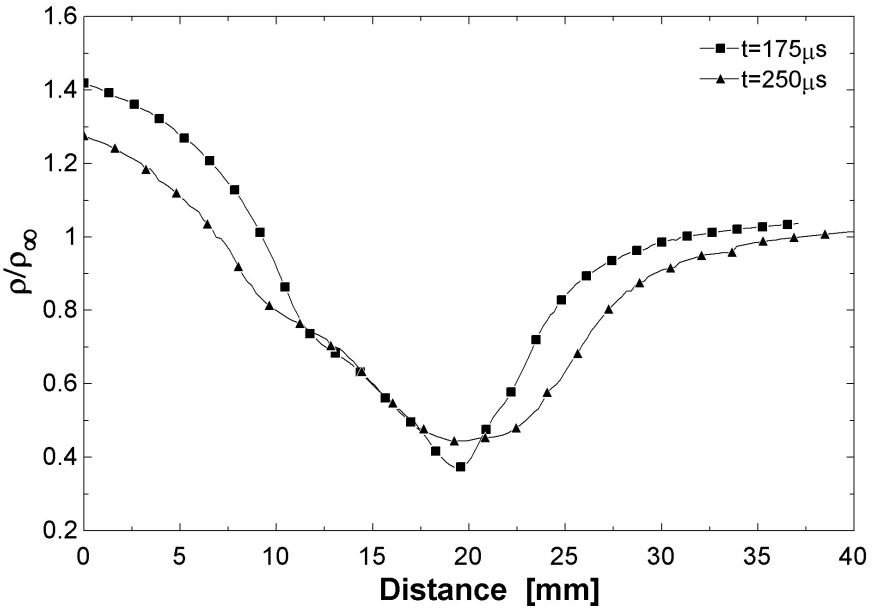

Figure 6.20: Pressure profile, bend section, M_s=1.42

The bending of the vortex has distorted the pressure profile slightly. It appears slightly stretched on the left of the core when compared with the data for the 'conical' section. The pressure value at the second peak on the left in the data is larger relative to that on the right hand side of the vortex than for the 'conical' section. The value of normalised pressure is around 0.35 for t=175μs and 0.45 for t=250μs at the core, compared with 0.5 for the 'conical' section.

The plots of radial velocity show little correlation between the two time instances plotted. The plots of updraft velocity do however, with the two curves appearing very similar. From Figure 6.19 it is seen that a large velocity into the plane illustrated in Figure 6.16, or towards the centre of the flow domain, is present in the vortex between the two peaks of the slipstream on the left. Considering the data for t=175μs, the updraft is approximately -150m/s on the left hand side of the vortex, and increases to approximately 100m/s on the right hand side. The value is approximately 90m/s at the core.

6.2.3 Vorticity

The vorticity in a flow is calculated using equation (2.14), which yields a vector quantity. The magnitude of the vorticity vector is plotted at various slices parallel to the centre plane for t=155μs in Figure 6.21. From these images, it can be seen that the slipstream is clearly a large contributor to the total vorticity, as is explained by Sun & Takayama (2003a). The variation of the magnitude of vorticity can be seen through the length of the vortex. Where the vortex distorts and bends, it can be seen that there is a region of greater magnitude of vorticity. This can be seen in image g), which corresponds to a value of 0.68 on the scale in Figure 6.6 f), a region where significant vortex bending is taking place. A similar region of greater magnitude in the vorticity vector can be seen in images i) through n). Again, by referring to Figure 6.6 f), it can be seen that the slices shown in images i) through o) correspond to a region of significant vortex bending, near the centre of the flow domain. Between the two regions of bending, the slip stream pattern appears self similar.

More detailed discussion on the vorticity and vorticity production is given in §6.6.

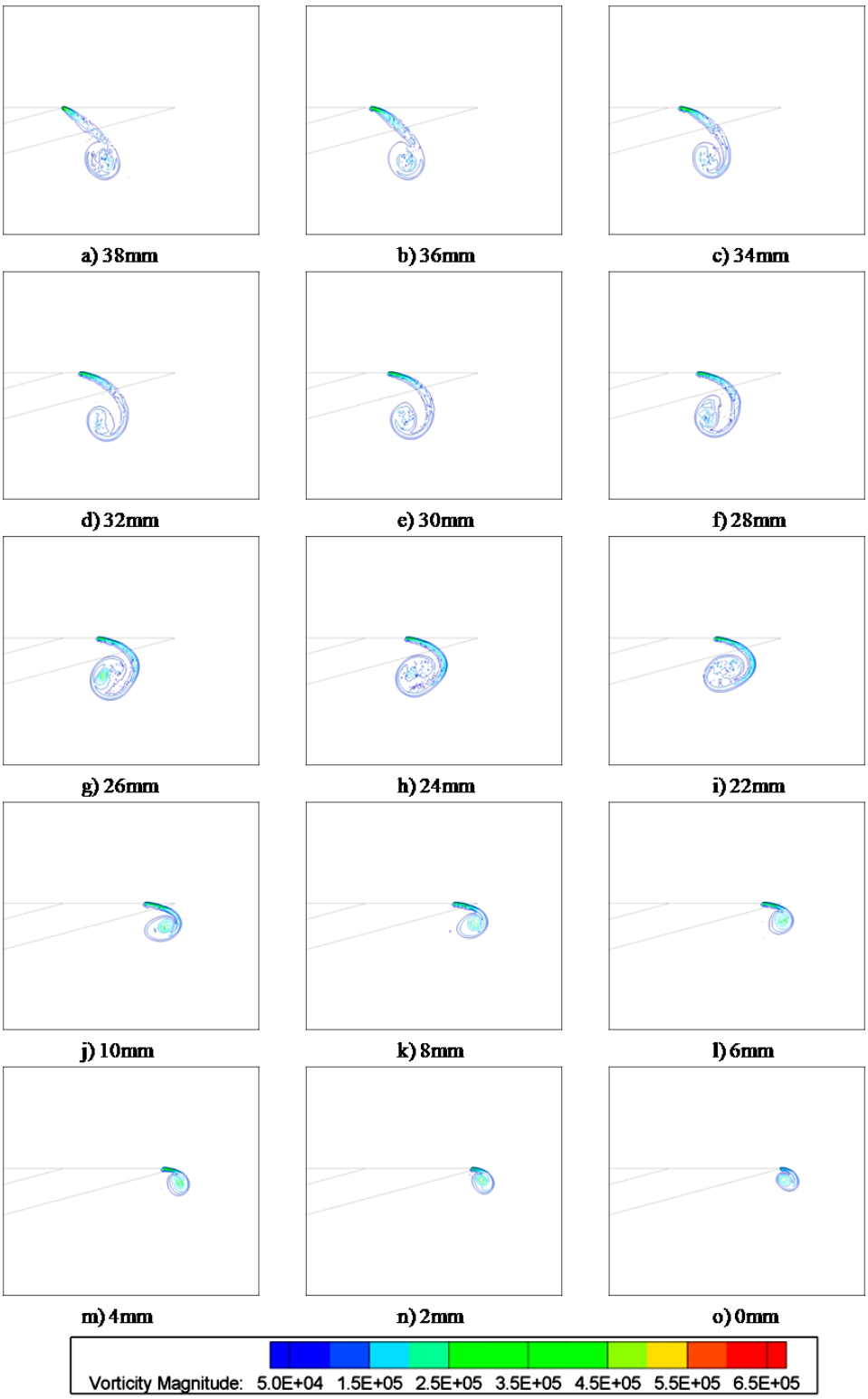

Figure 6.21: Vorticity Magnitude Contours ('V' model, M_s=1.42 t=155μs)

6.2.4 Navier-Stokes solution

Solutions of the laminar Navier-Stokes equations were computed for the 'V'-edged model for an incident shock Mach number of 1.42. The same mesh adaption scheme, boundary conditions, and parameter settings as used in the Euler solutions were used for the Navier-Stokes solutions.

The laminar Navier-Stokes solution showed little difference to the Euler solution. Plots of the tangential and updraft velocities, and normalised pressure are given in Figure 6.22 through 6.25. These are taken on plane I in Figure 6.10. The Euler data set is taken at t=155μs and the Navier-Stokes set at t=152μs.

As viscous effects play a role in the consolidation of the spiral slipstream, and in the behaviour of the core (Bershader, 1995), it was thought that the Navier-Stokes solution would exhibit some difference to the Euler solution. Investigation of the results yielded no appreciable difference between the two solutions. It is suspected that the relative coarseness of the meshes used would have prevented any more detail from being captured in the numerical solution.

The modeling of the boundary layer flow behind the incident shock wave was investigated. This had the effect of appreciably coarsening the mesh in the region of the vortex, as much finer mesh resolution was needed near the walls in order to model this. The maximum number of cells was limited by the computer power available.

The results of this study suggest that considerably greater computer power would be required to perform these calculations to any satisfactory degree of accuracy.

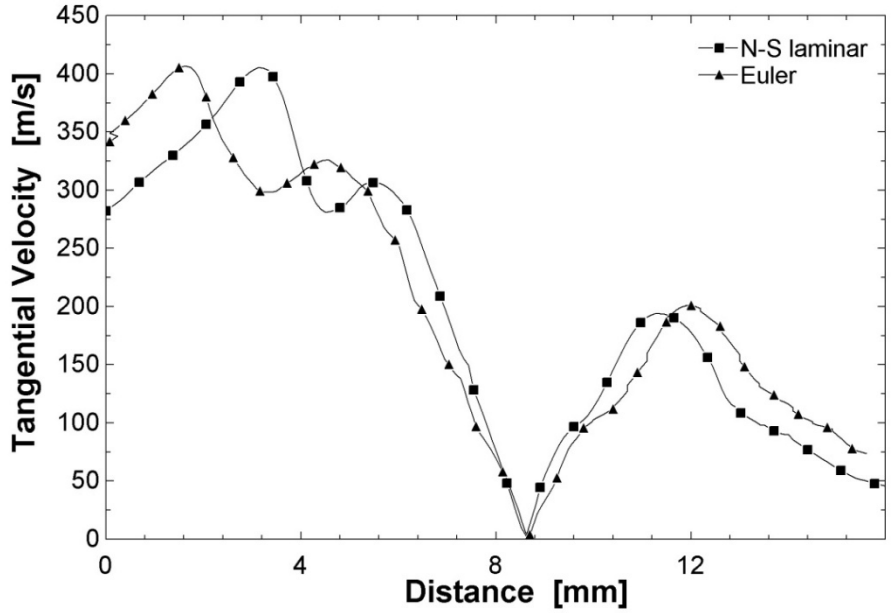

Figure 6.22: Tangential velocity profile 'V'-model, M_s=1.42, plane I, Euler & Navier-Stokes comparison

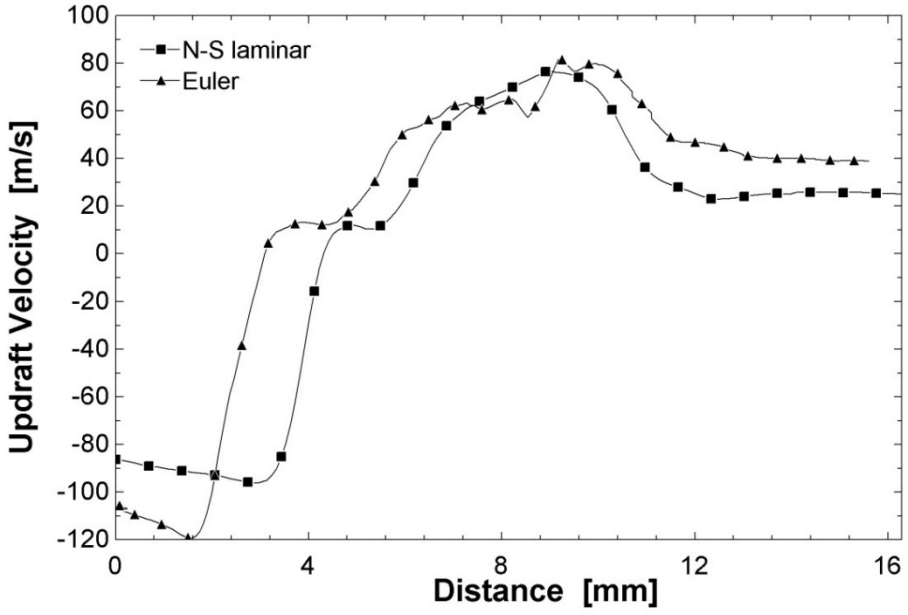

Figure 6.23: Updraft velocity profile 'V'-model, M_s=1.42, plane I, Euler & Navier-Stokes comparison

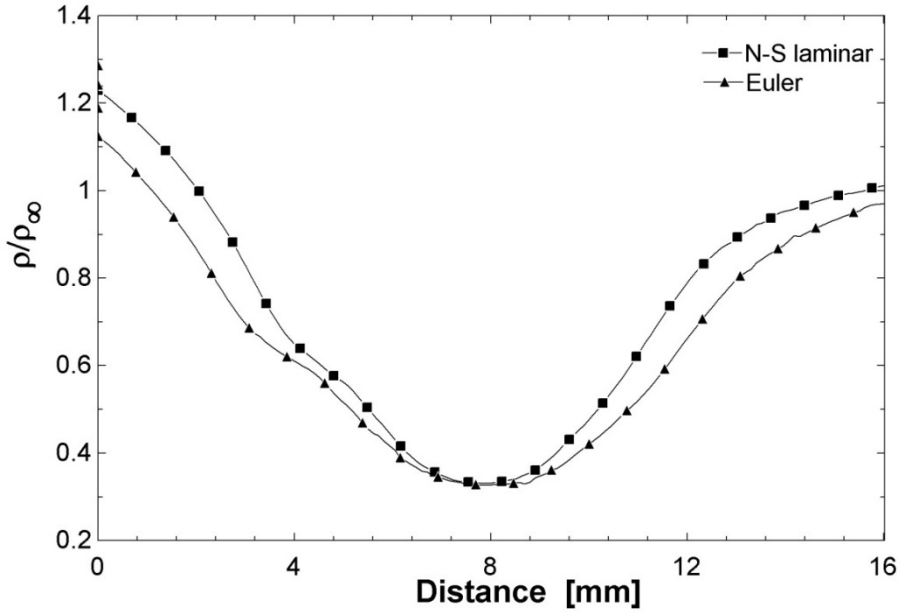

Figure 6.24: Pressure profile 'V'-model, M_s=1.42, plane I, Euler & Navier-Stokes comparison

Further investigation of the vortex dynamics and core behaviour revealed no discernable difference between the Navier-Stokes solution and the Euler solution, shown in Figure 6.6.

A discussion of the vorticity and vorticity production for the Navier-Stokes solution is given in §6.6.

6.2.5 Further 'V' model tests for other Mach numbers

Further numerical and experimental studies were performed for the 'V' model geometry, for incident shock Mach numbers of 1.32 and 1.65. The experimental and numerical results are presented and the resulting flow fields discussed in this sub-section.

M_s=1.65

As mentioned in §2.2, a secondary and tertiary shock wave develop in the flow field for diffraction of a shock wave of strength greater than approximately Mach 1.5 over a convex corner. It is thus expected some slight differences would be prevalent in the flow field for an incident shock Mach number of 1.65, when compared to the previous case of an incident shock Mach number of 1.42.

Figure 6.25 shows a sequence of schlieren images for an incident shock wave of Mach 1.65, taken with an optical roll of 0°. Figure 6.26 shows the same sequence of schlieren images those in Figure 6.25, except that the images were taken at an optical roll of 10°. The secondary shock wave is more clearly depicted against the far window in Figure 6.26. The basic features of the flow are indicated in Figure 6.27.

As one would expect, based on the published literature on shock wave diffraction, the secondary and tertiary shocks are apparent in the flow field for an incident shock Mach number of 1.65. However, to the knowledge of the author, there is no published literature concerning the appearance and behaviour of these shocks, or for that matter the general shock diffraction and free vortex behaviour, in such highly three-dimensional flows, as is presented here. It is thus interesting to examine the flow field in more depth with the aid of the numerical results, in order to investigate further the behaviour of these secondary and tertiary shocks, and the effects that they have on the free vortex.

Manifestations of the secondary and tertiary shocks can be seen in the sequence of images in Figures 6.25 and 6.26. For the sequence of images taken at 0° optical roll (Figure 6.25) these two shocks are clearly apparent near the centre plane. Referring to image h), the tertiary shock can clearly be seen between the vortex and the tip of the diffracting edge. The secondary shock can be

seen above the right-most portion of the vortex in image h). These shocks become more apparent and larger with time.

The secondary shock is also apparent against the windows, these are more clearly visible in the images taken at 10° optical roll (Figure 6.26). However, there appears to be no evidence of the tertiary shock against the windows. It is impossible to discern the extent to which these shocks are apparent along the length of the vortex from these images, as the shock surface is inclined to the optical axis, and hence not visible in the images. They are however visible where the shocks strike the windows, and where the shock surface aligns with the optical axis, on the centre plane. It is unclear as to whether the distortion to the vortex interferes with or delays the formation of these shocks, or whether the formation of the shocks forces additional distortion to the arrangement that the vortex core assumes across the flow domain. Further light is shed on these questions below, through examination of the numerical results.

The lambda shock configuration that develops on the slip stream is apparent in both sequences of images (Figure 6.25 and Figure 6.26), this is due to these flow features being slightly stronger here than in the M_s=1.42. It is more clearly visible in the images taken at 10° optical roll (Figure 6.26).

The lambda configuration apparent in the images appears to occur on the centre line of the model. As was mentioned previously in the discussion of the appearance of the secondary and tertiary shocks, it is impossible to confirm the appearance of the lambda shock configuration at other locations across the test section for the same reasons, and whether the distortion to the shock diffraction and free vortex profile interferes with its formation. In order to verify its appearance and perform a more in depth analysis of the lambda shock configuration, numerical solutions of the Navier-Stokes equations are required. Aside from the presence of these secondary and tertiary shocks and lambda shock configuration, the general arrangement and evolution of the flow field with time is consistent with that presented in the previous section for M_s=1.42.

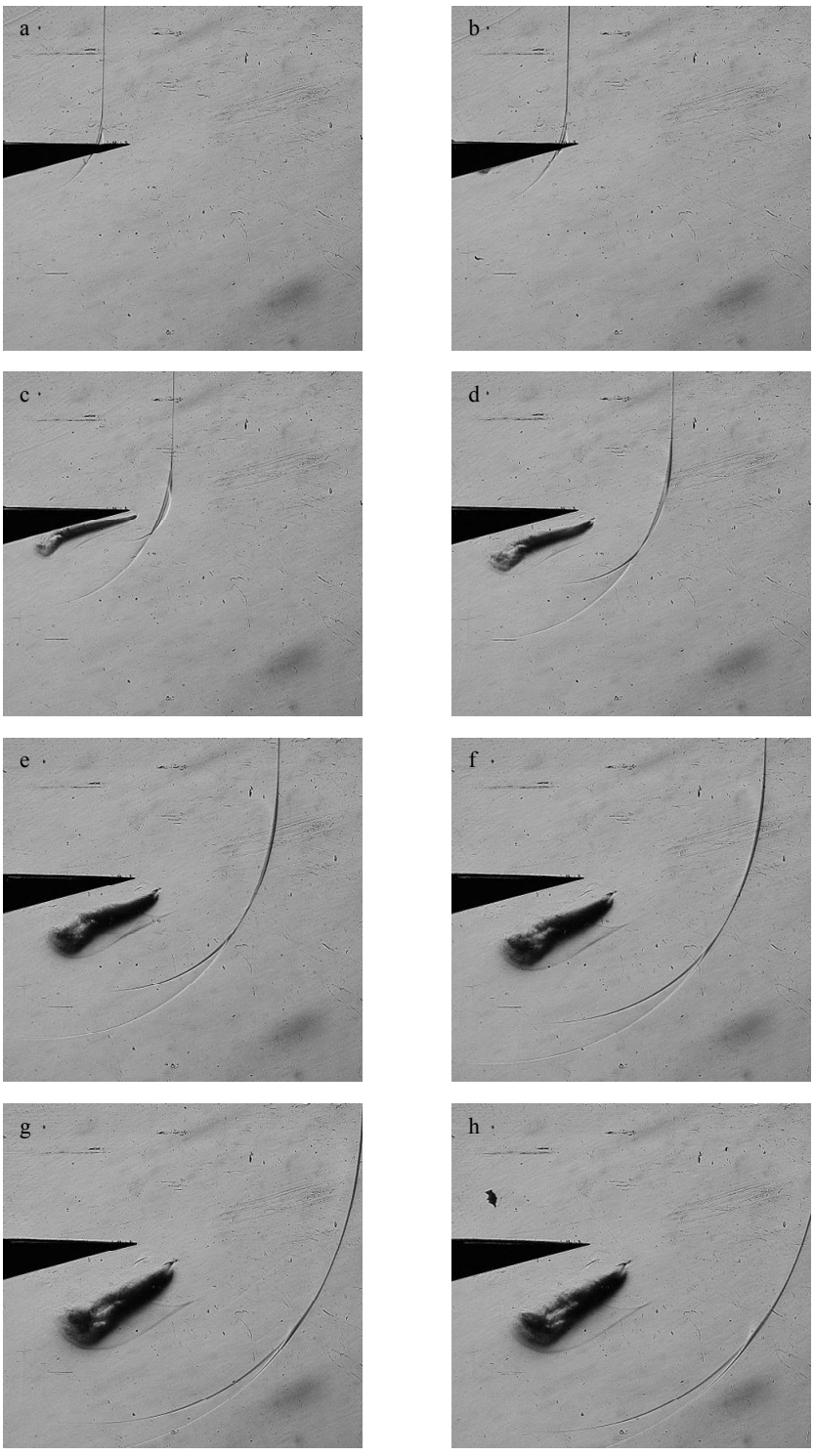

Figure 6.25: 'V' model schlieren images, M_s=1.65, δt=25μs, image a) at t=1425μs

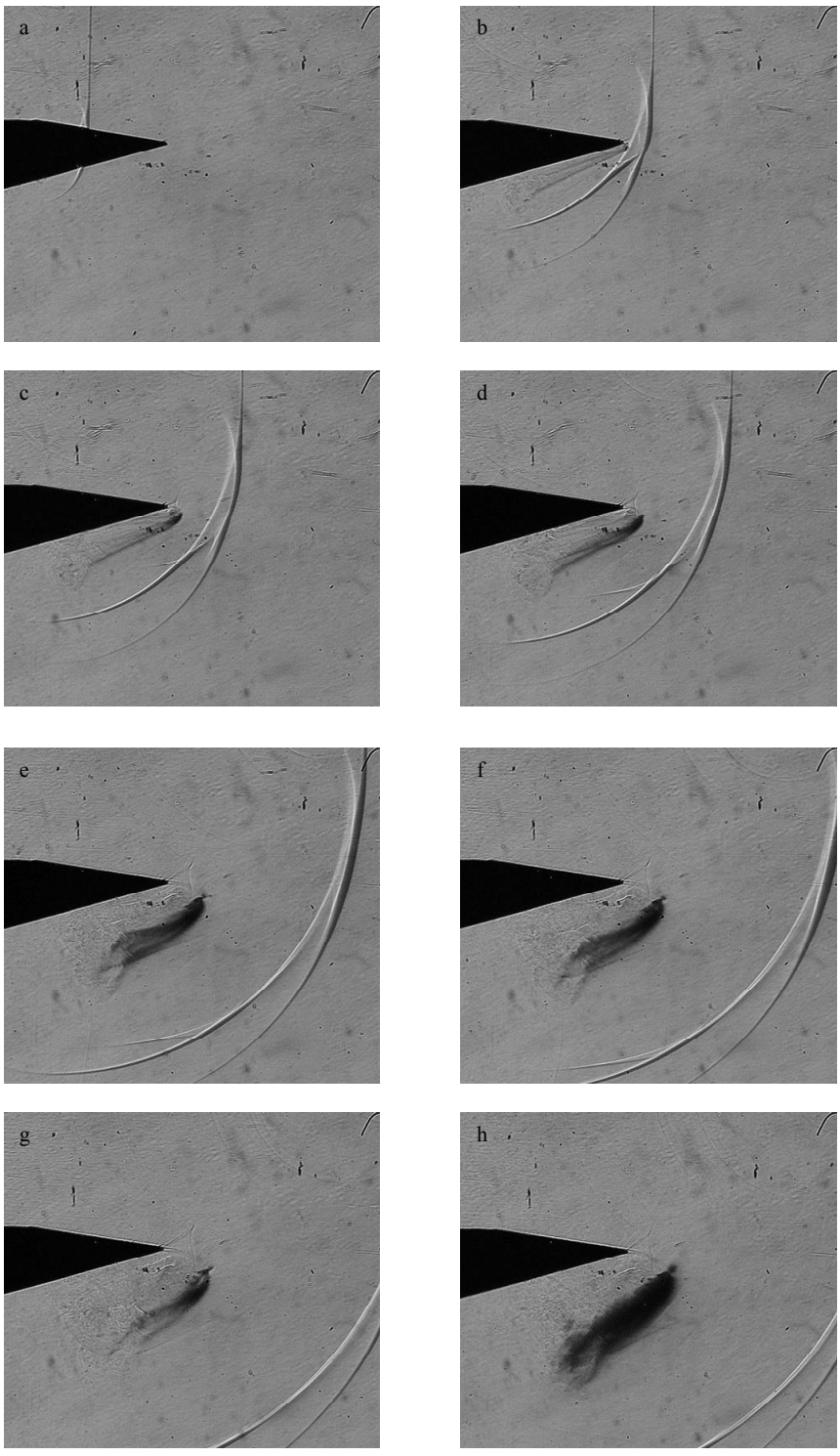

Figure 6.26: 'V' model schlieren images, M_s=1.65, δt =25μs, optical roll 10°, image a) at t=1425μs

Figure 6.27 is an enlarged view of image g) in Figure 6.26. The basic features of the flow field are indicated on the figure.

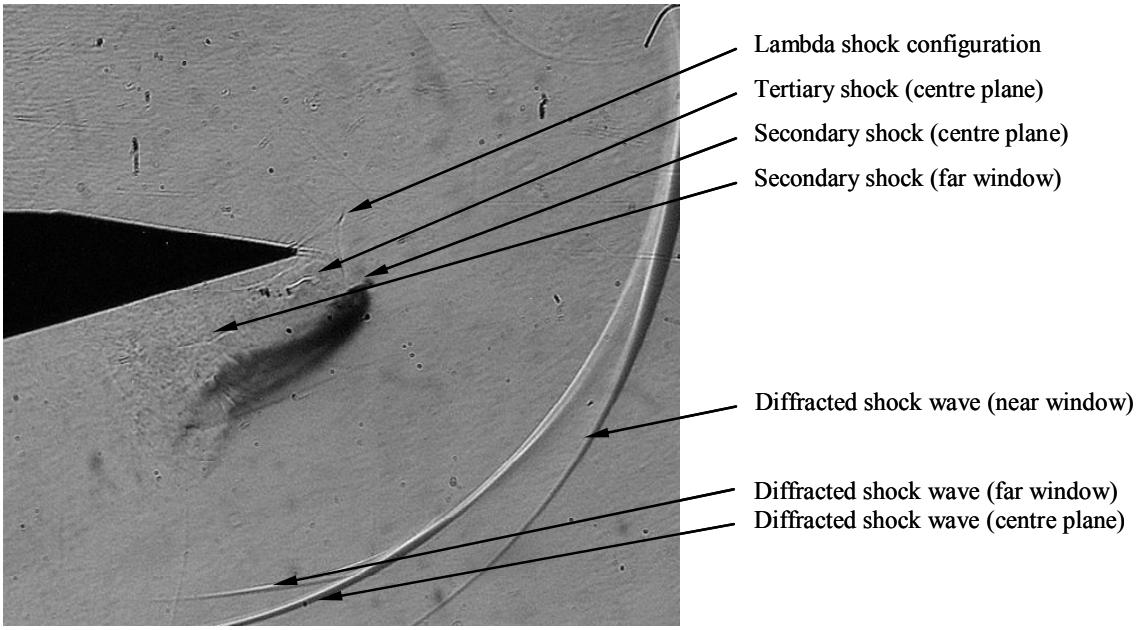

Figure 6.27: 'V' model, M_s=1.65, basic flow features, 10° optical roll.

Figure 6.28 shows a surface of constant density (ρ=0.8kg/m^3) obtained from numerical solution of the Euler equations at a similar time (140μs after the shock starts to diffract around the outer most extremity of the edge) to the experimental schlieren image in Figure 6.27. The black density line contours fall on a vertical plane taken through the centre of the flow domain, and the red contours fall on the boundary plane. The secondary shocks are represented by the dark blue surfaces in the figure. These are apparent in a region near the centre of the flow domain, and near the window. There is no evidence of the secondary shock in the region in between, where the vortex exhibits a conical profile. The tertiary shock was not extracted by the algorithm used, its presence in a region near the centre plane can however be seen in the density line plot given in Figure 6.30, discussed below.

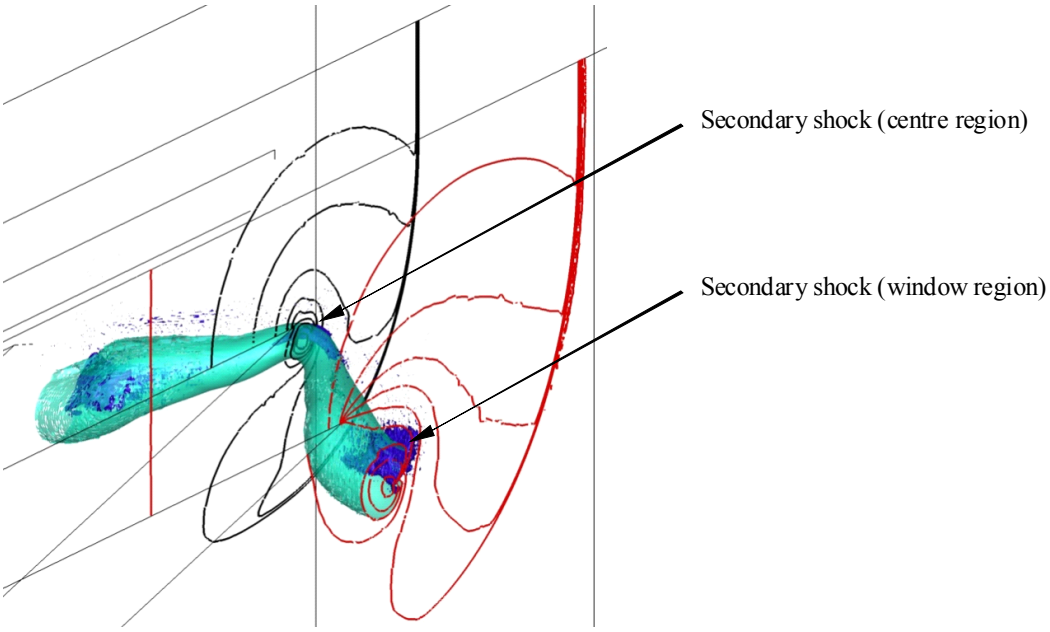

Figure 6.28: Line plots indicating locations of secondary and tertiary shocks

A series of images, similar to the ones presented for the M_s=1.42 case, showing the evolution of the free vortex from the top is given in Figure 6.29. Again, a density surface of 0.8kg/m^3 is plotted. The core of the vortex as extracted by Tecplot is indicated in the figures as a black line. The horizontal black line in the first few images indicates the position of the incident shock wave. The first image occurs 10μs after the shock starts to diffract around the edge. There is an interval of 22μs between each successive image. A non-dimensional scale is given so as to allow for comparison of the extent of the vortex distortion between different test cases. Again, the total length of the scale corresponds to 38 mm.

Initial inspection reveals very little difference in general vortex behaviour between the images in Figure 6.29 and those in Figure 6.6 (for an incident shock Mach number of 1.42). The vortex and core profiles appear very similar in general arrangement and shape. A more detailed comparison between the three incident shock Mach number cases is given after the results for the M_s=1.32 case are presented.

It appears from the images in Figure 6.29 that the presence of the secondary and tertiary shocks has little effect on the vortex geometry. The secondary shock is not apparent in the region between the distorted regions near the centre plane and wall (approximately 0.25 to 0.75 on the non-dimensionalised scale) in the numerical solutions. It would appear that discrepancies, arising from the flow not being perpendicular to the diffracting edge or vortex axis, between the three-dimensional and two-dimensional cases have prevented it from forming.

Line contour slices taken at various positions across the flow domain (where 0mm is the centre plane, and 38mm is the window), are shown in Figure 6.30, better illustrate the structure of the flow. These slices were taken at a time of t=162μs, corresponding to image h) in Figure 6.29.

The secondary and tertiary shocks can be seen in Figure 6.30 a). The tertiary shock seems to have disappeared by image e), 8mm from the centre plane. The secondary shock in the central region too, is apparent in images a) through e). In the region near the window, the secondary shock is apparent in images o) through t). There is no evidence in the numerical results of the tertiary shock in the region near the window. Images f) through l) suggest a degree of self similarity in the slipstream profile.

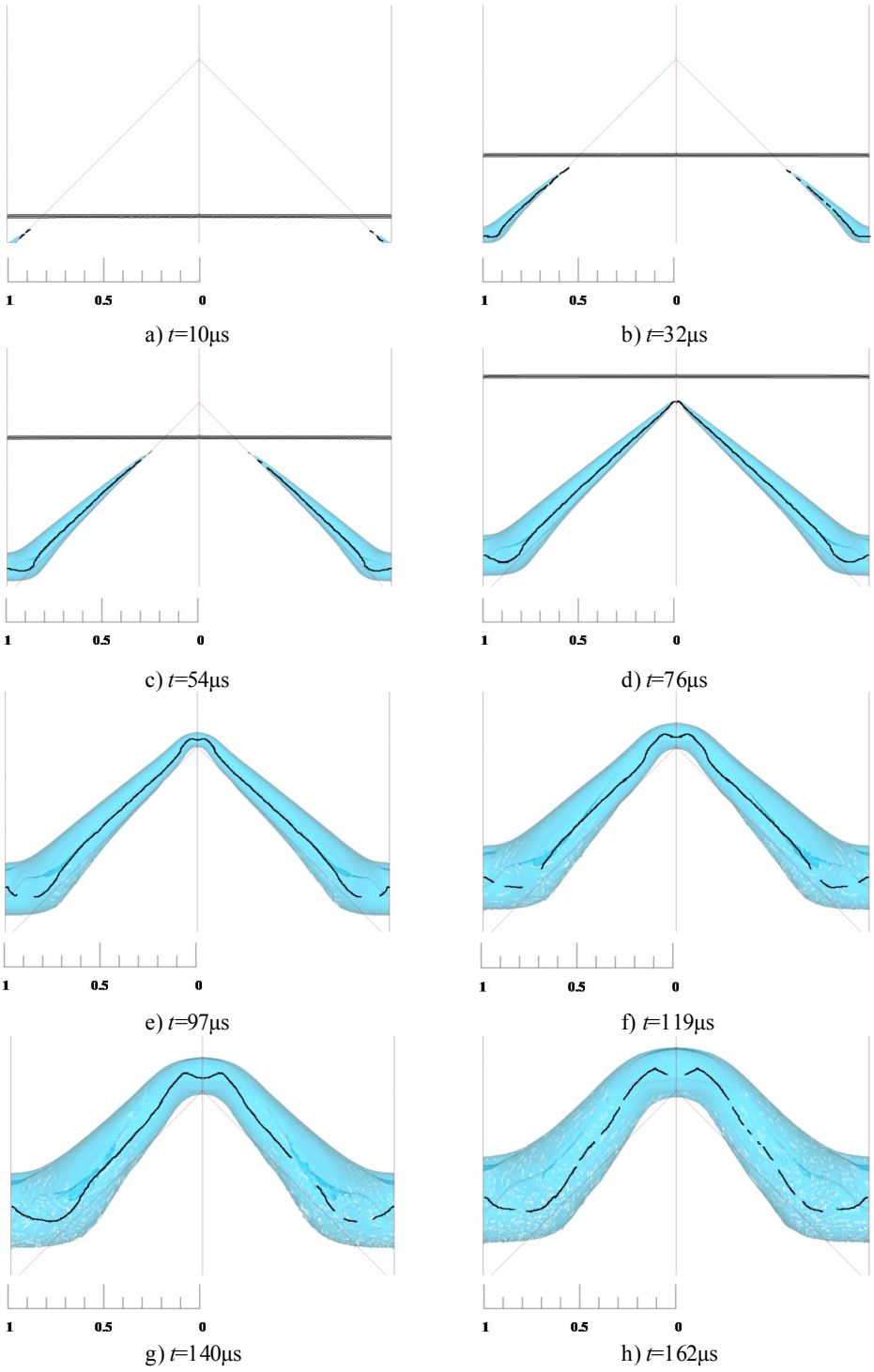

Figure 6.29: Top View of Vortex Bending ('V' Model M_s=1.65), surfaces of constant density (0.8kg/m^3) shown

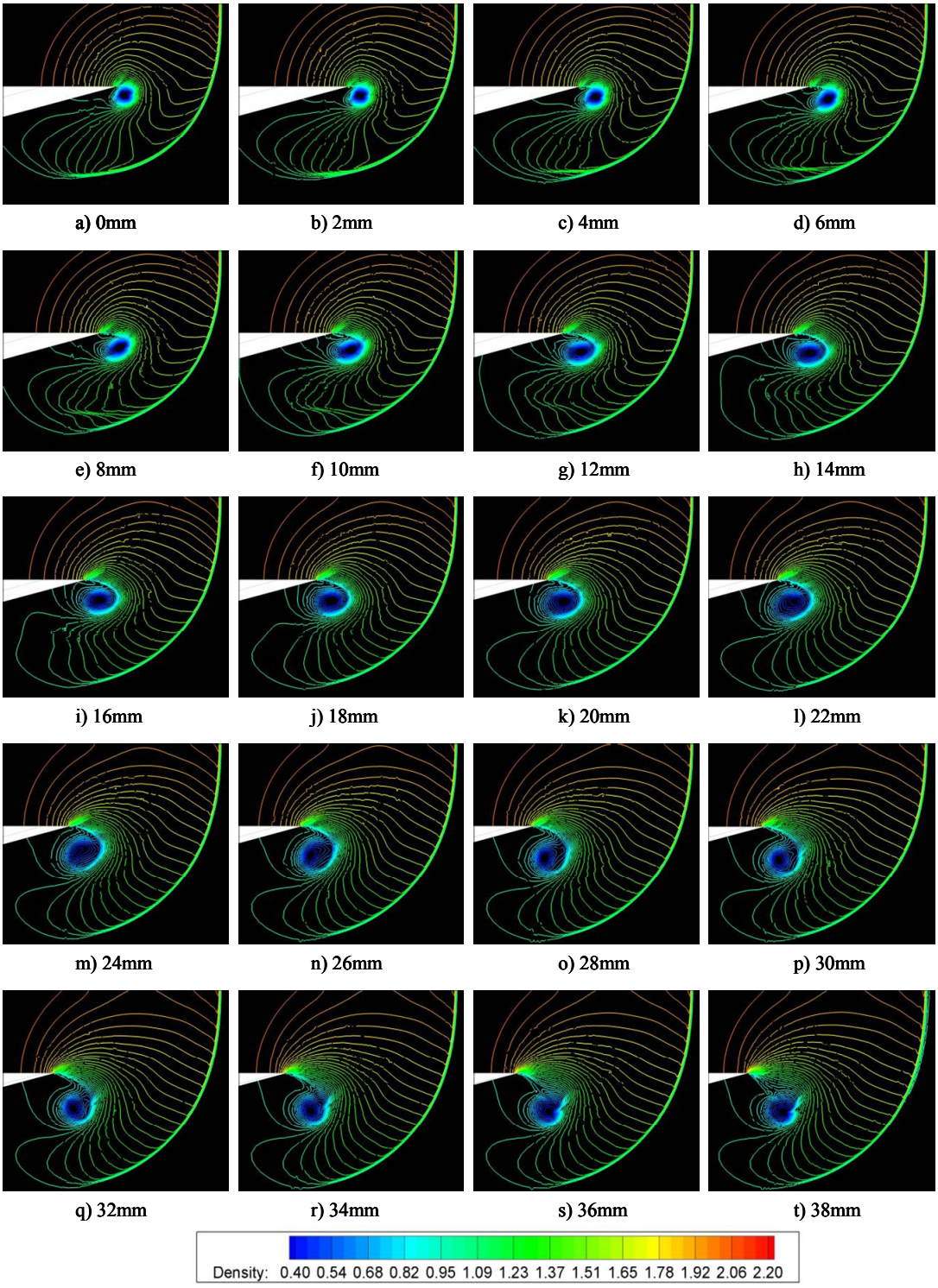

Figure 6.30: 'V' model density line slices, M_s=1.65

Structure of the vortex. Shown in Figure 6.31 is a streamline released from the centre plane on the vortex axis at a time of t=162μs. Whilst this does not indicate the actual path of that particle in flow would follow over time, as the streamline shown here is merely a visual representation of the velocity field at this specific time step in the solution, it does serve to illustrate the 'updraft' in the vortex.

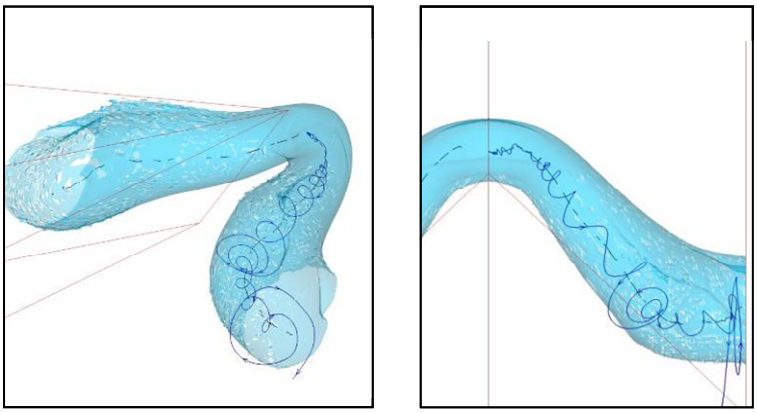

Figure 6.31: Streamline indicating flow inside vortex, M_s=1.65, t=162μs

Similar curves to those presented for the M_s=1.42 case, indicating the tangential, radial and updraft velocities, as well as the pressure, on various planes taken through the vortex are given below. Data is again taken on two planes, as is indicated on Figure 6.32. Data is presented for two time instants, t=119μs and t=162μs.

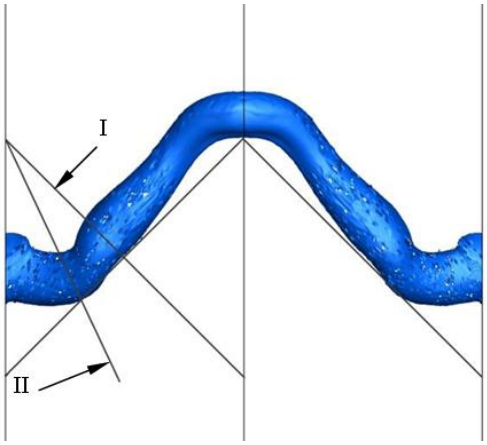

Figure 6.32: Vortex slice definitions (M_s=1.65)

Data taken on plane I is presented first, again, this corresponds to the 'conical' region, or the region of the vortex exhibiting a self-similar evolution. Figure 6.33 shows the profile of the vortex on plane I at t=119μs.

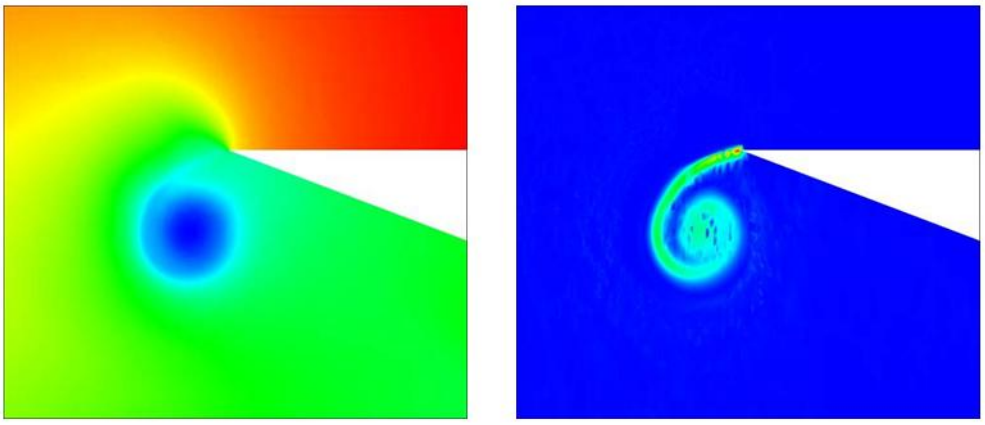

a) Density b) Vorticity Magnitude

Figure 6.33: Vortex profile, M_s=1.65, t=119μs

The plots given in Figure 6.34 through Figure 6.37 below contain data taken on a horizontal line through the vortex core. The data is taken from a reference point prior to the slipstream, and the spirals of the slipstream can clearly be identified in the plots. Data is presented in a similar manner as to that in §6.2.2 for the M_s=1.42 case, and exhibits the same general trends. General discussion of the plots will not be repeated here. The reader is referred to the explanation in that section if any further information is required.

Figure 6.34 and Figure 6.35 give the tangential and radial velocity profiles respectively.

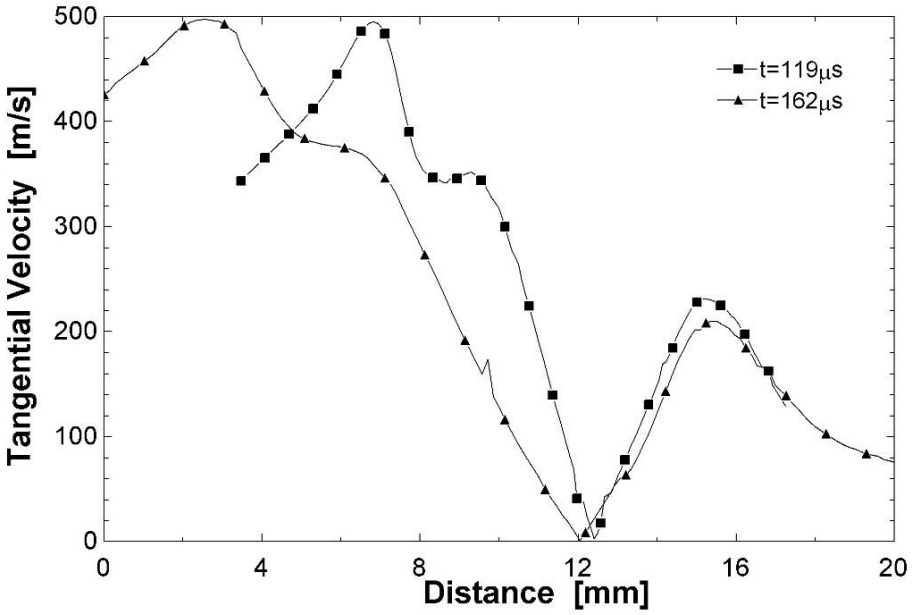

Figure 6.34: Tangential velocity profile, conical section, M_s=1.65

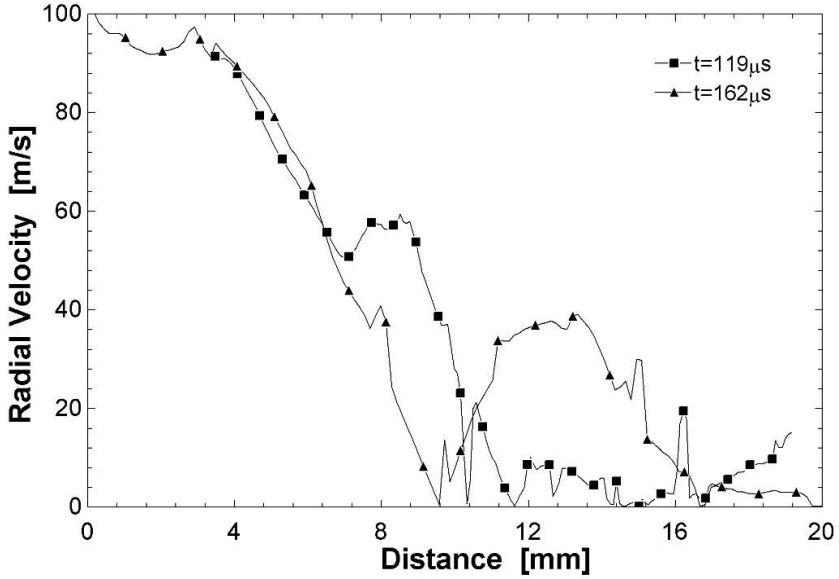

Figure 6.35: Radial velocity profile, conical section, M_s=1.65

Figure 6.36 and Figure 6.37 give plots of updraft velocity and normalised pressure respectively.

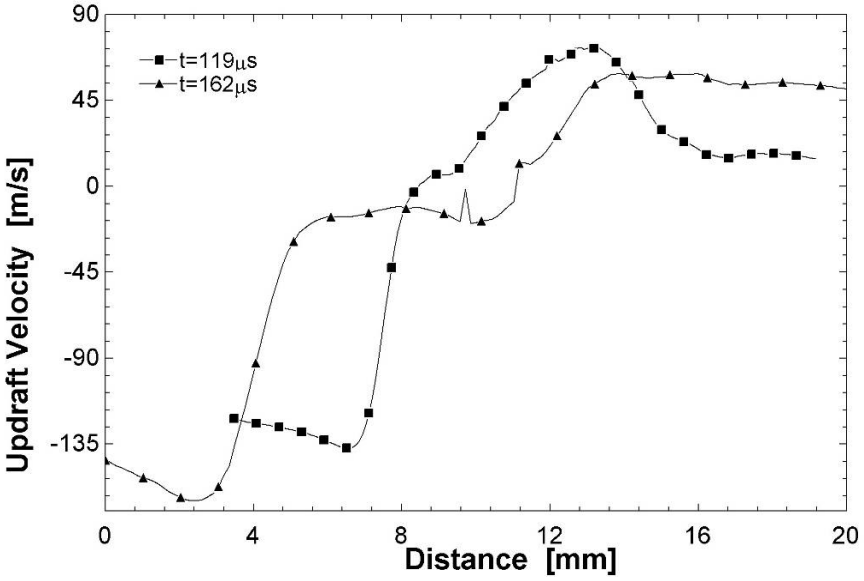

Figure 6.36: Updraft velocity profile, conical section, M_s=1.65

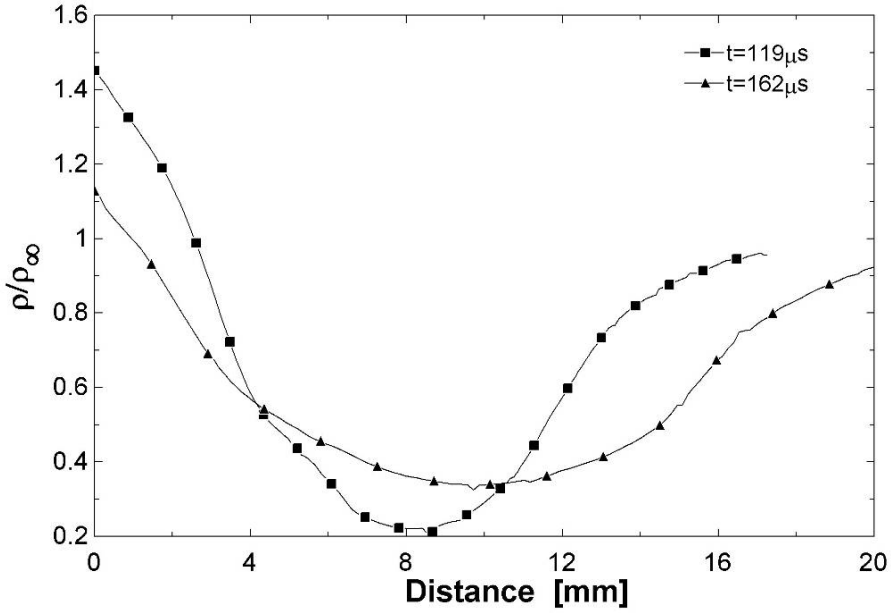

Figure 6.37: Pressure profile, conical section, M_s=1.65

The tangential velocity profile given in Figure 6.34 compares well with that in Figure 6.12 for the M_s=1.42 case in terms of general shape. The magnitudes of the rotational velocities are higher for the M_s=1.65 case, as one would expect. There is a slight difference, the region between the core and the peak at around 16mm exhibits a single linear trend, whereas in the data for the M_s=1.42 case this was not observed. Comparing Figure 6.33 b) and Figure 6.11 b) reveals that the slipstream joins the core region at the top (with reference to the figures) for M_s=1.42 and on the right for M_s=1.65, and that the discrepancy between the two curves is due to there being a region between the core and the outer portion of the slipstream in the M_s=1.42 case. The similarity between the two data sets taken at different time instants indicates a degree of self-similarity in the evolution of the vortex in this region.

Again, there is no describable trend in the plot of radial velocity, however, the general arrangement of the curve is consistent with that found for the M_s=1.42 case.

The curves of updraft velocity and pressure profile mimic those presented for the M_s=1.42 case. Here however, the maximum updraft velocity is around 80m/s for t=119µs, compared to that of 100m/s for M_s=1.42. The normalised pressure appears significantly lower for the M_s=1.65 case, with a minimum of 0.22 for t=119µs at the core, and a value of 0.35 at the core for an earlier time in the M_s=1.42 case.

Data taken on plane II, through the region of bending near the solid boundary, is presented in Figure 6.39 through Figure 6.42. Figure 6.38 shows the profile of the vortex in this region at t=119µs. Again, the centre of curvature of the bend lies to the left of the images in Figure 6.38.

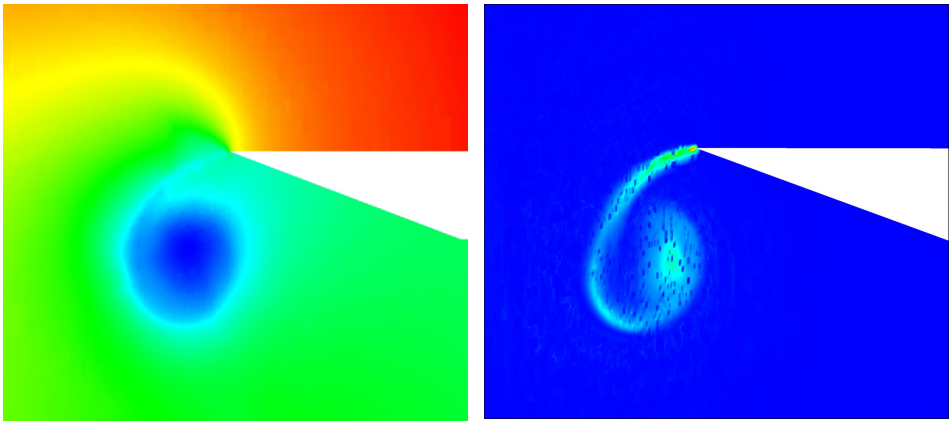

a) Density b) Vorticity Magnitude

Figure 6.38: Vortex profile, 'bend' section, M_s=1.65, t=162µs

Figure 6.39 and Figure 6.40 give the tangential and radial velocity profiles respectively. From the tangential velocity plot, it can be seen that outer portion of the spiral of the slipstream has ‘spread out’ significantly at t=162µs, when compared to the earlier time instant shown, and that there is a large gap between the outer slipstream spiral and the rest of the vortex on the side of the centre of curvature of the bend in the vortex.

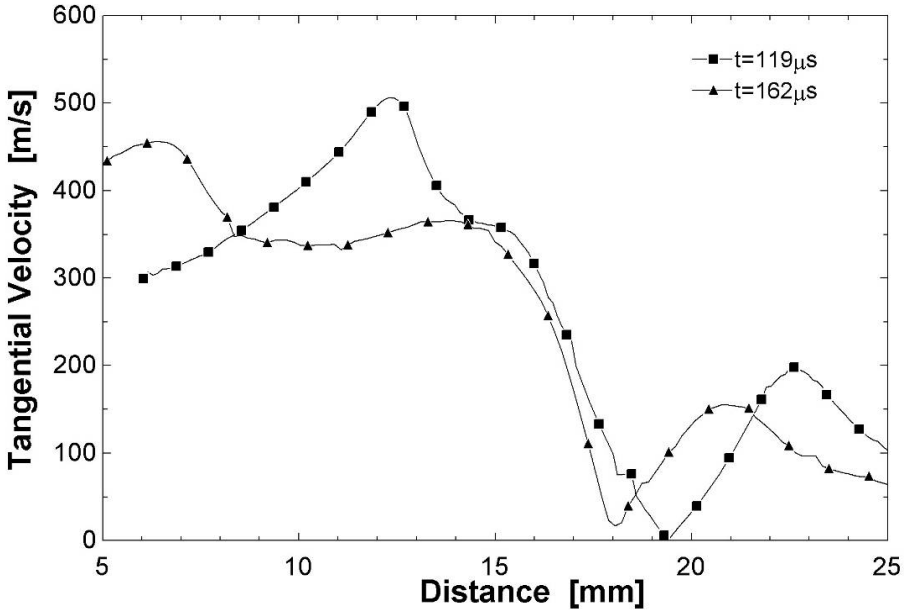

Figure 6.39: Tangential velocity profile, bend section, M_s=1.65

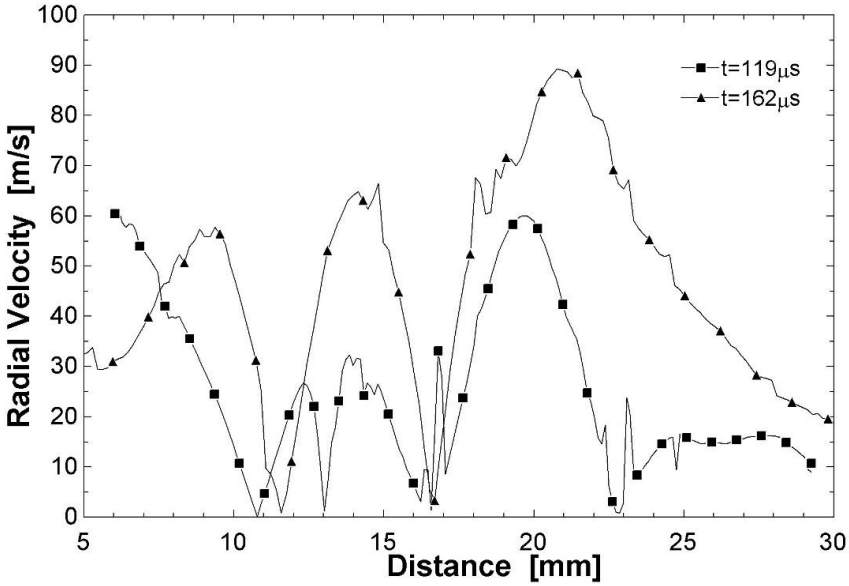

Figure 6.40: Radial velocity profile, bend section, M_s=1.65

Figure 6.41 and Figure 6.42 give plots of updraft velocity and normalised pressure respectively.

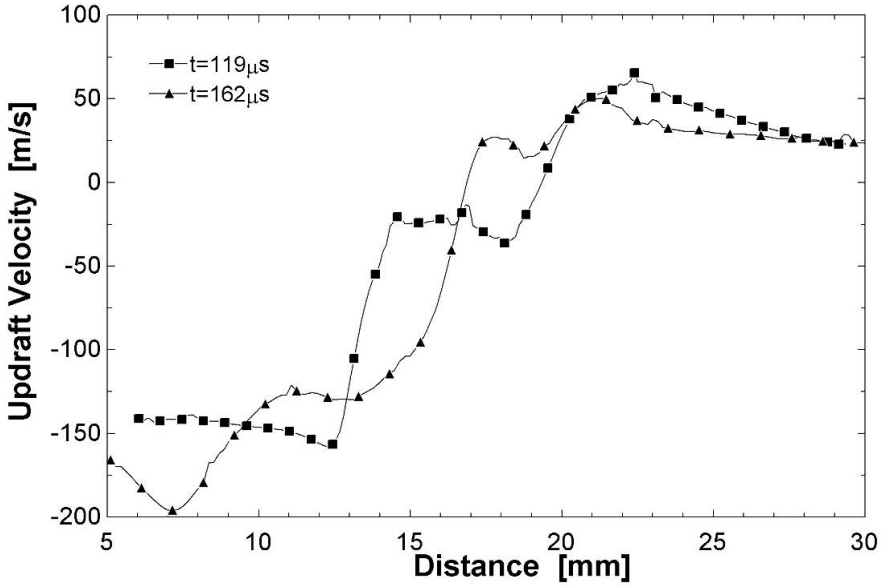

Figure 6.41: Updraft velocity profile, conical section, M_s=1.65

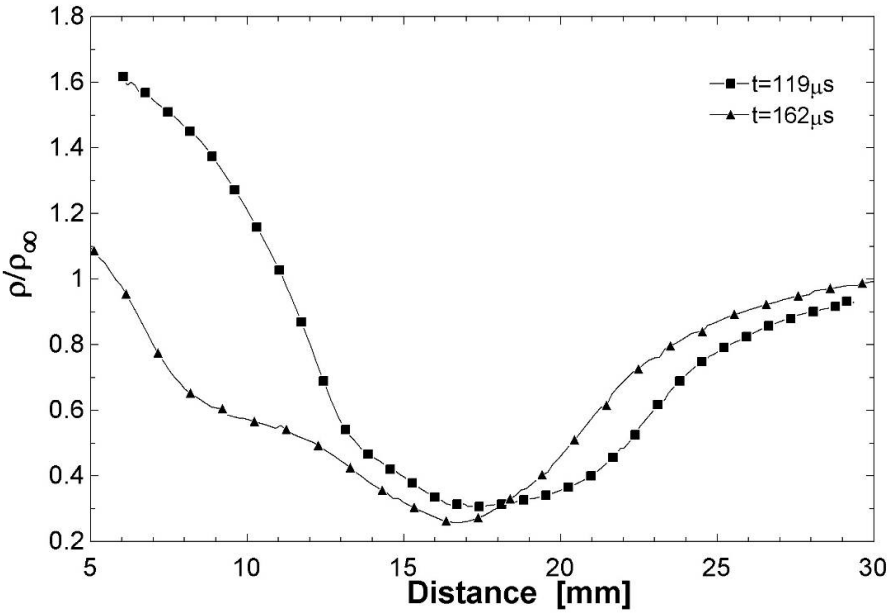

Figure 6.42: Pressure profile, conical section, M_s=1.65

The above plots tend to reinforce the observations made previously for the M_s=1.42 case. In the tangential velocity plot (Figure 6.39), the two peaks on the left-hand side of the core are more

spread out than in the 'conical' region. The difference between the tangential velocity on the left and right of the vortex is greater than in the 'conical' region, as was noted in the discussion concerning the M_s=1.42 case.

The plot of updraft velocity reveals the same trend in the results as that observed for the M_s=1.42 case. I.e. a large negative velocity on the left side of the vortex and a large positive velocity on the right side of the vortex.

M_s=1.32

The resulting flow field for the diffraction of an incident shock wave of Mach 1.32 is qualitatively similar to that obtained for the case of an incident shock of Mach 1.42, as one would expect. As was outlined in section §2.2, for incident shock Mach numbers of less than approximately 1.5, the resulting flow field exhibits the same features. For increasing Mach numbers, the slipstream is lengthened, and the vortex becomes slightly more elliptical in profile.

As a result of the similarities present between the M_s=1.32 and M_s=1.42 cases, the results for the M_s=1.32 case will not be discussed in as much detail as those obtained for the M_s=1.42 case. Instead, presented below are selected results highlighting the similarities, and differences between the flows for all three incident shock Mach numbers tested. Mention of the vorticity production for the M_s=1.32 case is made in §6.6.

Comparisons of the flow fields for the three incident shock Mach numbers of 1.32, 1.42 and 1.65 with shock wave at the same position are given in Figure 6.43. It can clearly be seen that a) and b) in figure 6.20 are qualitatively similar. These two sets of images contrast with c), where the secondary and tertiary shocks have developed.

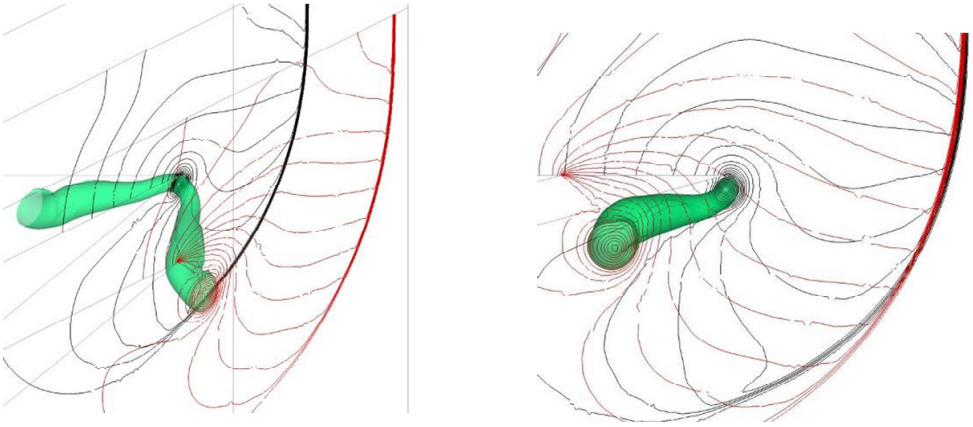

a) Incident shock of Mach 1.32

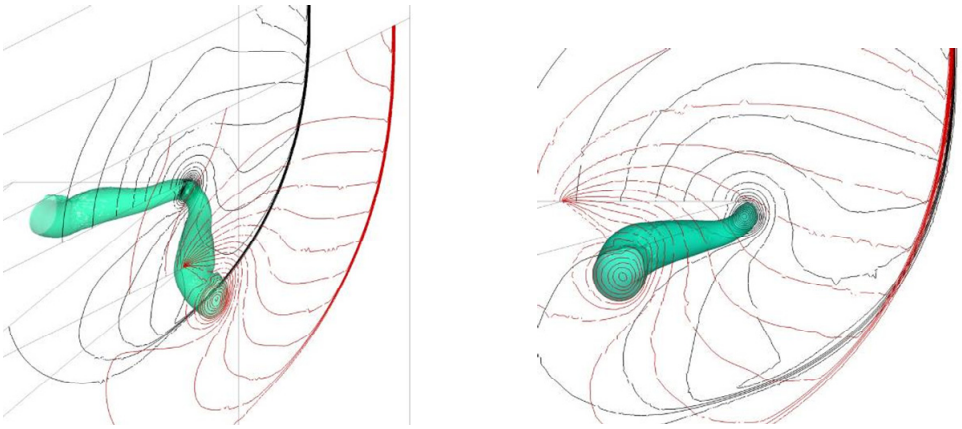

b) Incident shock of Mach 1.42

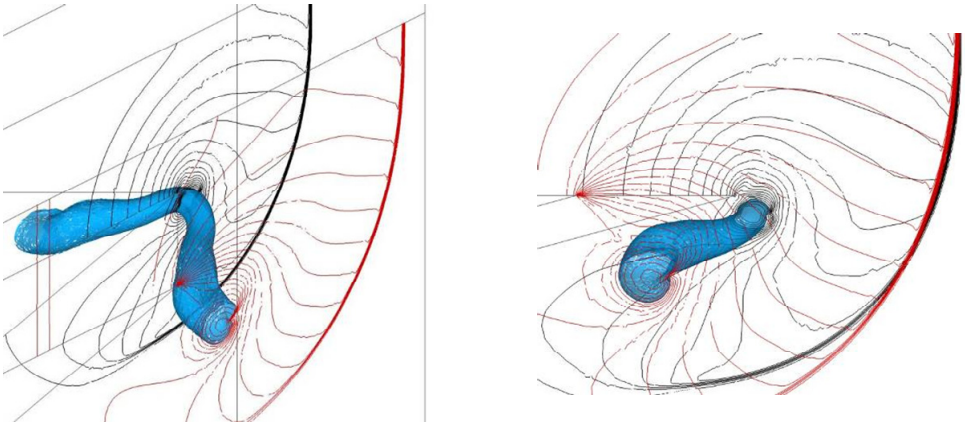

c) Incident shock of Mach 1.65

Figure 6.43: 'V' model diffraction pattern comparison, density contour lines plotted

6.2.6 Accuracy considerations

It should be borne in mind that in the numerical results presented above, the meshes used are significantly coarser than those used in work published in the literature concerning comparable two-dimensional cases (Sun & Takayama (2003a) and Tseng & Yang (2006)). Whilst simulations were run for different base meshes, in an effort to show that the results are mesh independent, the adaptive mesh refinement scheme that was used generated refined meshes that were similar, despite the use of different base meshes. Any anomalies that could have arisen due to mesh effects appeared negligible.

6.2.7 Summary

The evolution of the free vortex with time was shown and discussed through the use of experimental and numerical studies. The general arrangement and structure of the vortex was consistent across the three incident shock Mach numbers tested (1.32, 1.42, and 1.65).

The vortex core was shown to bend so as to meet the solid boundary at an angle of 90°, as was expected from theoretical relations. As the two vortices on generated on either side of the 'V' diffracting edge meet, their cores bend so as to join and form a continuous curve. The process is similar to that observed as the vortex bends so as to meet the solid boundary. Solutions of both the Euler and Navier-Stokes equations showed no noticeable difference in the evolution and bending behaviour of the free vortex.

Properties of the vortex (tangential, radial, and updraft velocities, and the pressure profile) were plotted for a conical region of the vortex, apparently unaffected by distortions to the vortex, and for the region where the vortex is distorted and bends. These results showed a fair indication of

self-similar vortex development with time in the region away from the distortions. The plots were distorted in the region of bending, where it was found that a larger velocity magnitude existed on the side of the vortex towards the centre of curvature of the bend. The vortex was found to contract in the region, as if it had been stretched.

For M_s=1.65, the secondary and tertiary shocks were only present in a region around the centre of the flow domain, at the tip of the 'V' diffracting edge. A secondary shock was also apparent in a region near the solid boundary.

The meshes used in the three-dimensional simulations presented were significantly coarser than those that were used in published works, dealing with two-dimensional simulations. In order to perform simulations with a mesh density comparable to published data on two-dimensional cases, a significant increase in computing power and memory would be required.

6.3 'Inverted-V' Model Tests

Presented in this section are the results of the tests for the 'inverted-V' model. These results are presented more briefly than those in the previous section, as similar flow phenomena are observed. The reader is referred to the relevant section in §6.2 for a more detailed discussion on the flow features presented here. The model tested is shown in Figure 4.8 b), with the tip or apex of the 'v' now being the initial point of shock diffraction.

6.3.1 Overview & description of flow field

M_s=1.42

The flow fields observed for the 'inverted-V' model appear to exhibit similar properties to those obtained for the 'V' model, on inspection of the experimental photographs. Experimental photographs for M_s=1.42 are given in Figure 6.44 and Figure 6.45. Figure 6.44 shows images at an optical roll of 0°, and Figure 6.45 at an optical roll of 10°. Both sequences have an initial time of t=1675μs, and δt=25μs.

The vortex is well defined in the series of images shown below, and the general evolution and development of the vortex appears consistent with that for the 'V' model presented in the previous section. Secondary shocklets are apparent on the slipstream in image h) of both Figure 6.44 and Figure 6.45. These secondary shocklets are apparent against both the near and far windows. There is no evidence in the schlieren photographs of secondary shocks forming in other regions of the flow domain.

Schlieren images for M_s=1.32 were also taken. These are however not presented here, as they reveal little that is not shown in Figure 6.44 and Figure 6.45, for the Mach 1.42 case. Further insight is to be gained from the numerical results, presented later in this section.

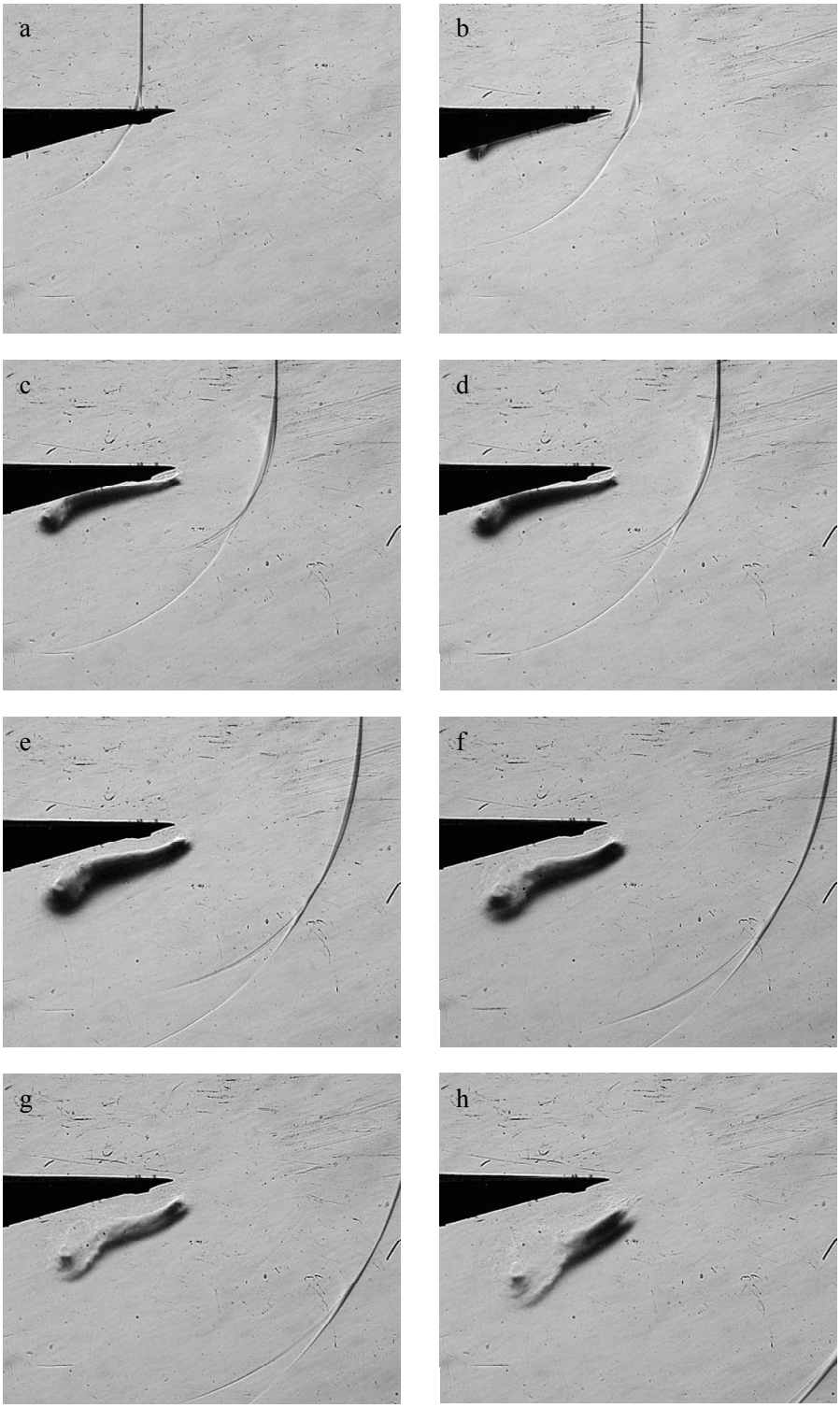

Figure 6.44: ‘Inverted-V' schlieren photographs, M_s=1.42, optical roll 0°, δt=25μs

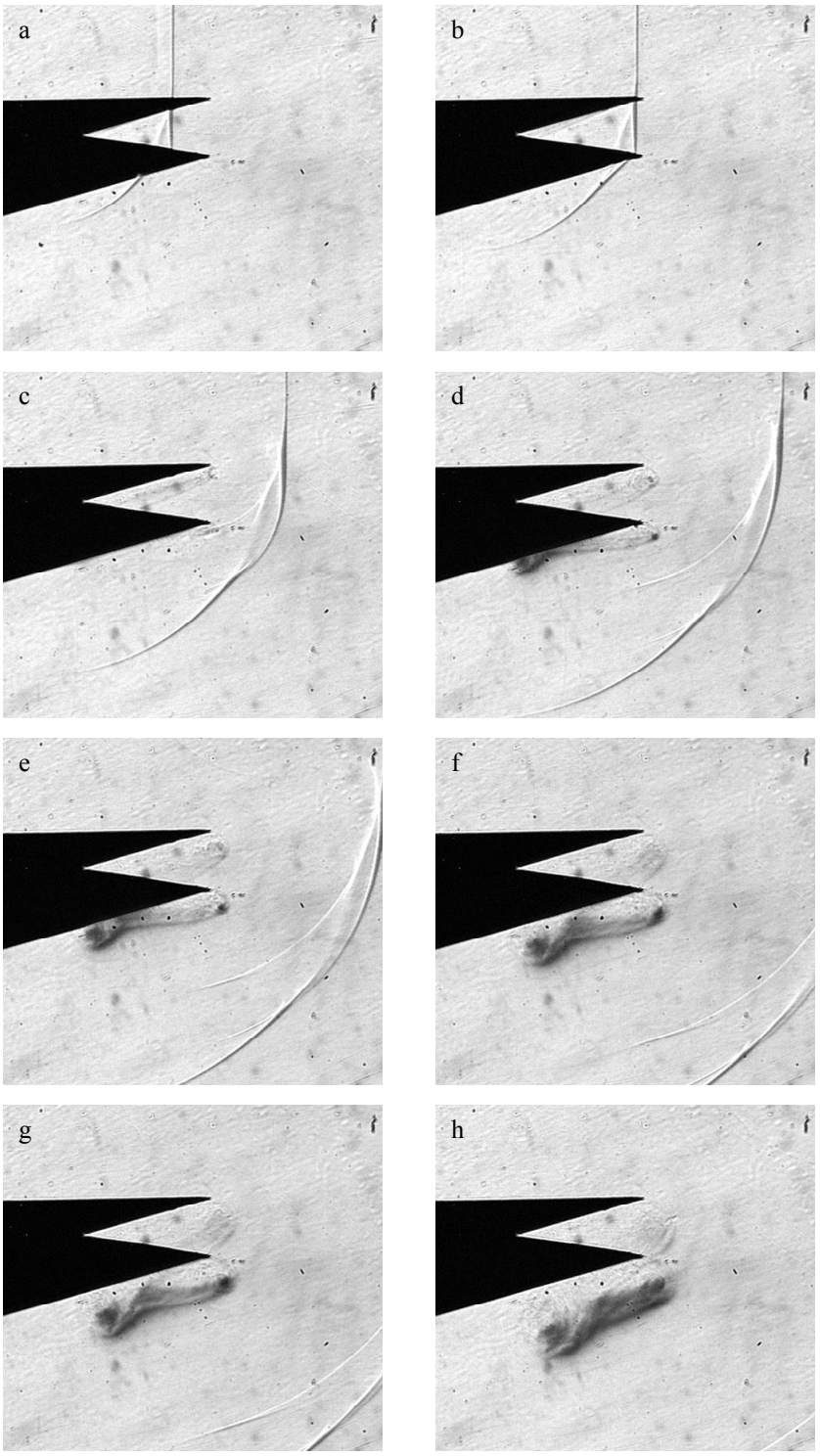

Figure 6.45: ‘Inverted V’ schlieren photographs, M_s=1.42, optical roll 10°, δt=25μs

M_s=1.65

Experimental photographs for M_s=1.65 are given in Figure 6.46 and Figure 6.47. Figure 6.46 shows images at an optical roll of 0°, and Figure 6.47 at an optical roll of 10°. Both sequences have an initial time of t=1425μs, and δt=25μs between successive images.

The secondary shocks are clearly visible in Figure 6.46, from image c) and onwards, in the region close to the tip of the diffracting edge. These are the shocks in the region close to the windows on either side of the test section. This can be more clearly seen in the images taken at an optical roll of 10° (Figure 6.47), where evidence of a tertiary shock in the same region is apparent. In both sets of images, one can seen a lighter 'patch' in the left-most portion of the vortex, caused by the density gradients across the secondary shock in the region near the centre plane of the test section. These flow features are all pointed out explicitly and discussed further in §6.3.2.

It appears that the secondary shocks against the windows are at slightly different angles to each other. This can be seen clearly in image h) of Figure 6.46, where the secondary shocks against the near and far windows do not lie on top of each other in the image. This anomaly was either caused by slight inconsistencies in the test specimen, or due to the effects of the sealing tape placed between the model and the windows of the test section.

The appearance of these secondary and tertiary shocks appears consistent with the descriptions presented in §6.2, for the 'V' model geometry, above: They are apparent in a region close to the window and centre of the flow domain. Investigation of the numerical results is however required to confirm this, and is presented in the sections that follow.

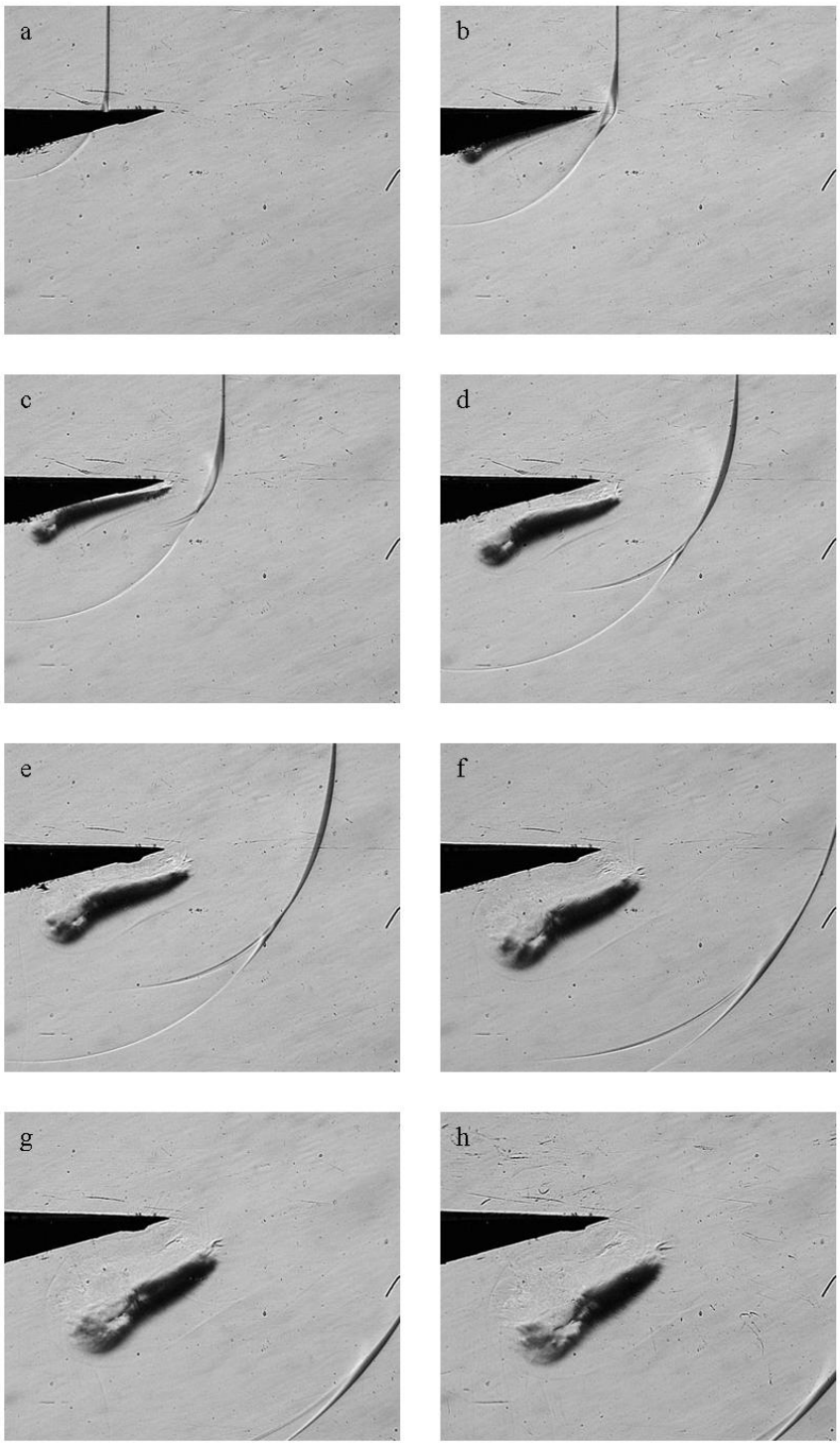

Figure 6.46: ‘Inverted-V’ schlieren photographs, M_s=1.65, optical roll 0°, δt=25μs

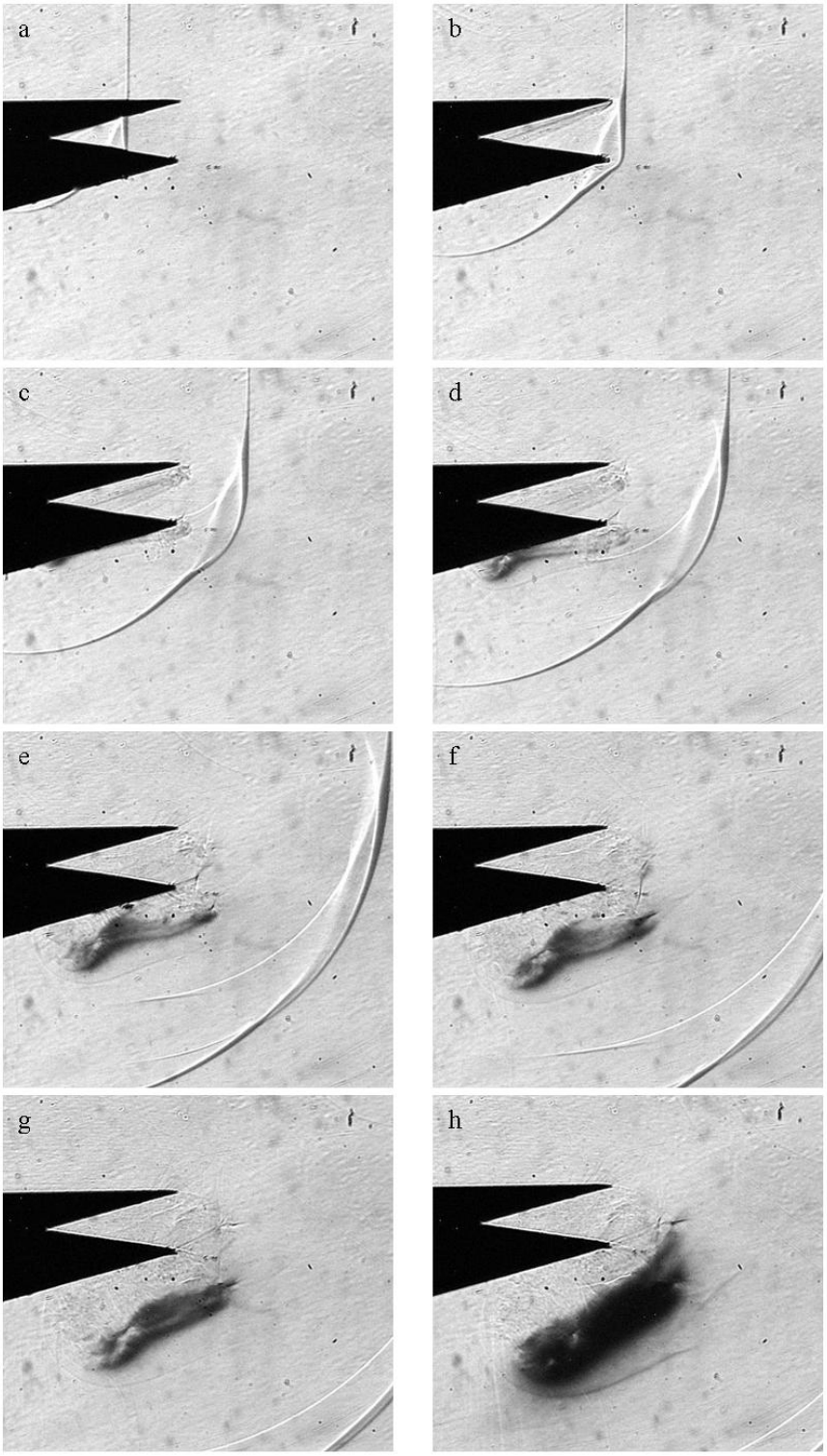

Figure 6.47: ‘Inverted-V’ schlieren photographs, M_s=1.65, optical roll 10°, δt=25μs

6.3.2 Comparison of experimental & numerical results for 'inverted-V' models and further description of flow field

Figure 6.48 shows the development of the numerical simulation with time for an incident shock Mach number of 1.42. The green surface is one of constant density (0.85kg.m^3), and the black lines represent isopycnals (lines of constant density) taken on three separate planes across the width of the test section (the near wall, centre, and far wall respectively). The time instant t_0 coincides with the initial point of diffraction, as the shock reaches the tip of the 'V'-shaped edge. As in previous sections, the correlation between the numerical results and experimental photographs is very good at the time instances tested. Figure 6.49 gives an overlay of the experimental and numerical results at a similar time instant and highlights the basic features of the flow field. This also serves to highlight the correlation between the two sets of results.

Figure 6.50 shows the development of the numerical simulation with time for an incident shock Mach number of 1.65. Again, the green surface is one of constant density (0.75kg/m^3 in this case), and isopycnals are shown at the near wall, centre, and far wall of the flow domain. An overlay of the experimental and numerical results is given in Figure 6.51, along with a description of the features of the flow field. Note that there is a slight time discrepancy between the numerical and experimental results shown in Figure 6.51.

Further discussion of these images is given after they are presented.

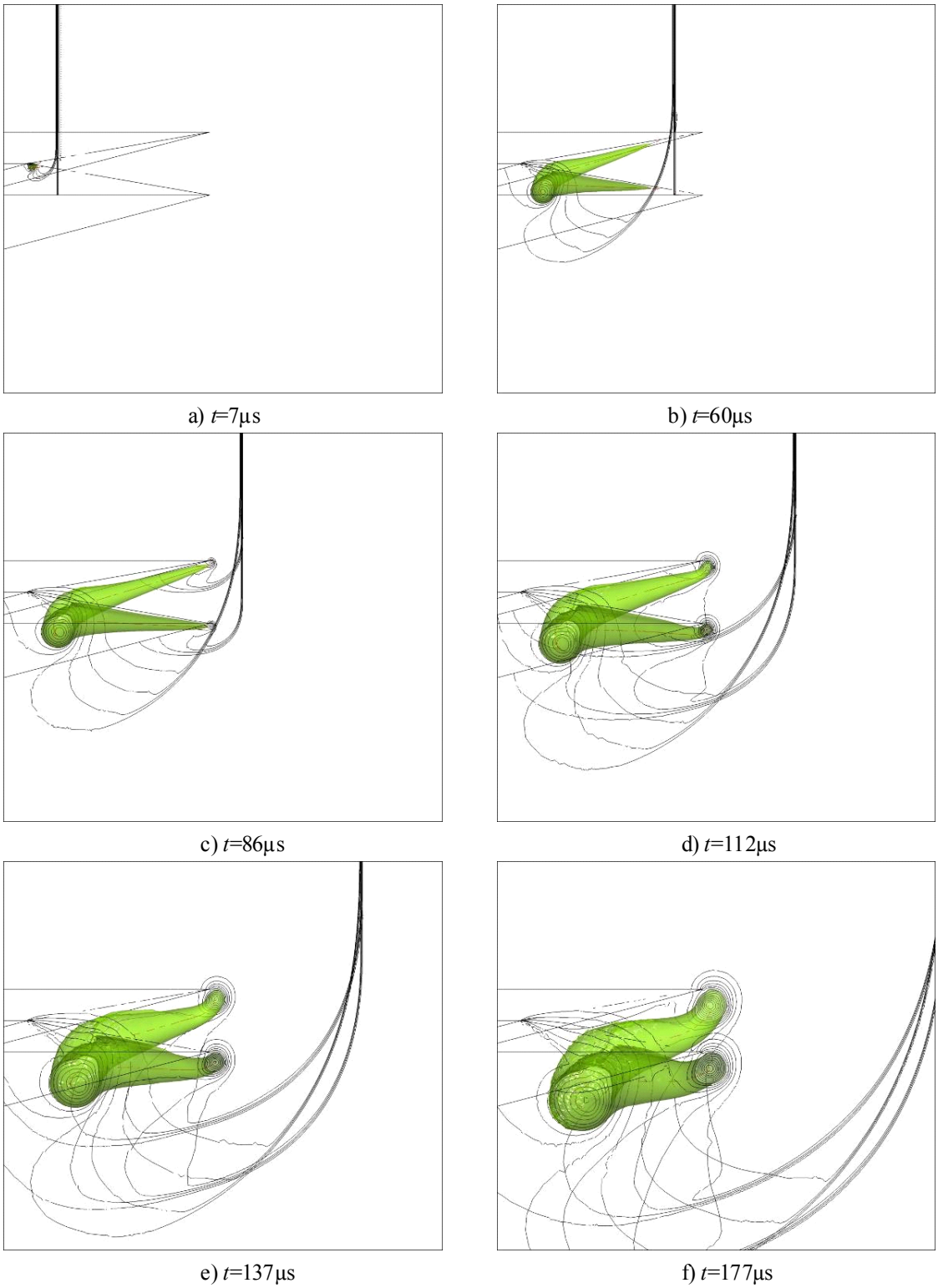

a) t=7μs b) t=60μs

c) t=86μs d) t=112μs

e) t=137μs f) t=177μs

Figure 6.48: 'Inverted-V' model, M_s=1.42, density lines and surface plots

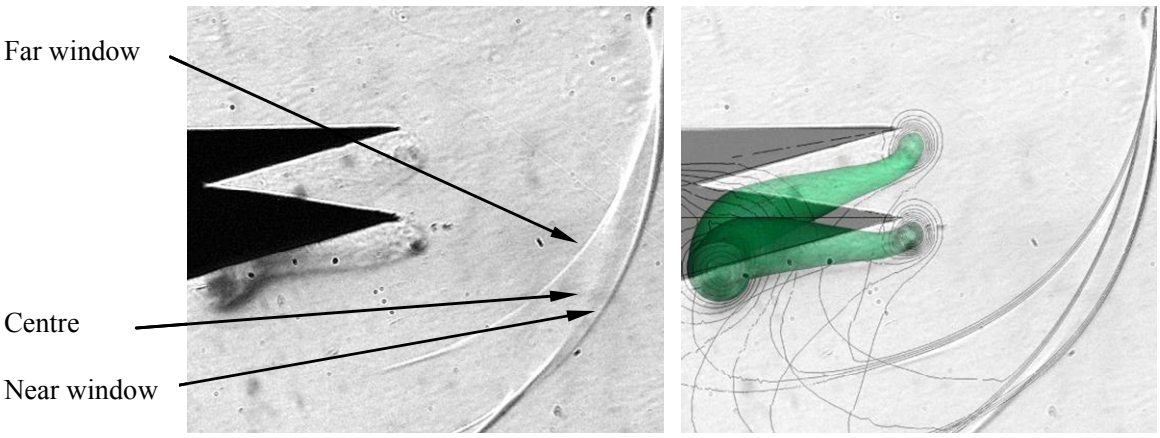

Figure 6.49: 'Inverted-V', M_s=1.42, experimental and numerical results overlay, indicating locations of visible shock wave

As mentioned previously, the development of the solution for the 'inverted-V' model is similar to that of the 'V' model. As Euler solutions are presented and due to the symmetry of the test models, ideally, identical solutions would be expected for the 'V' and 'inverted-V' cases, if one was to consider half of the flow domain. However it is expected that slight discrepancies may be present due to different initial meshes being used for the two solutions, and the relative coarseness of the final adapted meshes. As with the 'V' case, the numerical simulation for the 'inverted-V' case appears to have mimicked the experimental results very well.

Figure 6.51 gives expanded views of the experimental photographs for the flow region around the tips of the diffracting edges (Figure 6.51 image b)) and the flow in the centre of the flow domain (Figure 6.51 image c)), along with corresponding overlays of the numerical results. The red dashed line in the numerical images represents the location of the vortex cores as calculated by Tecplot 360. From image b), it can be seen that the numerical simulation has predicted the appearance of the secondary shocks against the boundaries of the flow domain. The slight distortion to the circular contours between the vortex and the wall (on the left-hand side of the vortex profile against the boundary in image b)) correspond to the location of the tertiary shock. However, the tertiary shock is poorly resolved in the solution, due to the coarseness of the meshes

used. For reasons mentioned in previous sections, the numerical results presented here do not capture the front leg of the lambda shock configuration.

Image c) shows the flow in the centre of the flow domain. Here the secondary shock can be seen clearly in the numerical results. It is obscured slightly in the numerical results, but is nevertheless present and its location is well represented in the numerical results. There is no evidence in either the numerical or experimental results of a tertiary shock at this location. Also visible is the contact surface. Further discussion pertaining to the extent to which these shocks extended across the flow domain is given in the sub-sections that follow.

The flow features are captured remarkably well for the M_s=1.65, and good correlation is found between the experimental and numerical results for the portion of the evolution of the flow field studied. Further discussion of the results and the structure of the flow field is contained in the sub-sections that follow.

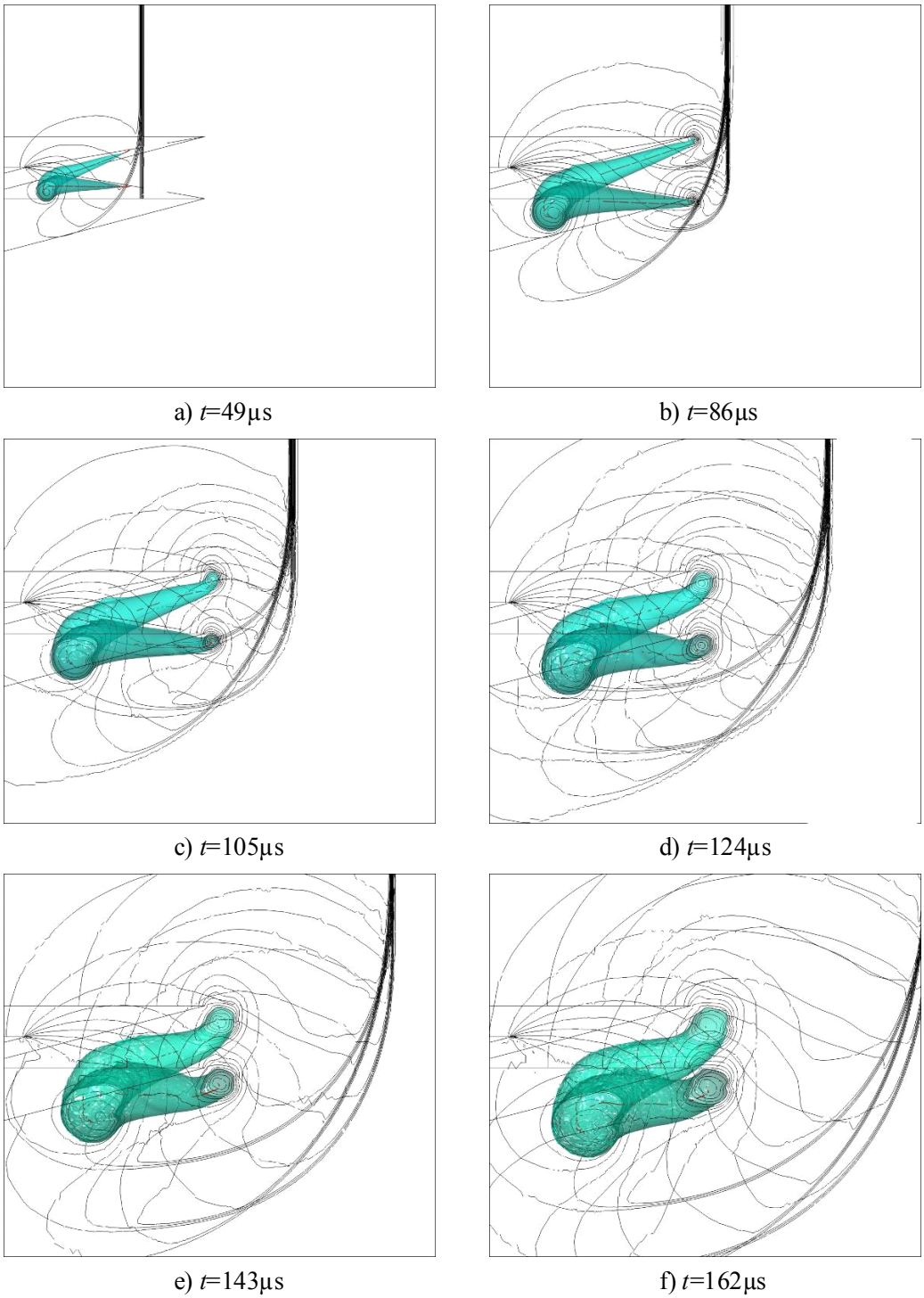

a) t=49μs b) t=86μs

c) t=105μs d) t=124μs

e) t=143μs f) t=162μs

Figure 6.50: 'Inverted-V' model, M_s=1.65, density lines and surface plots

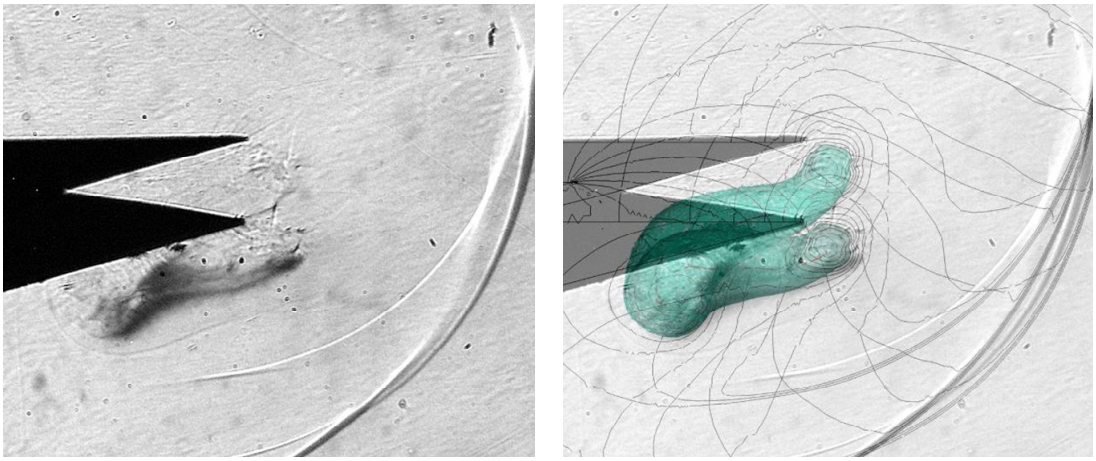

a) General overlay

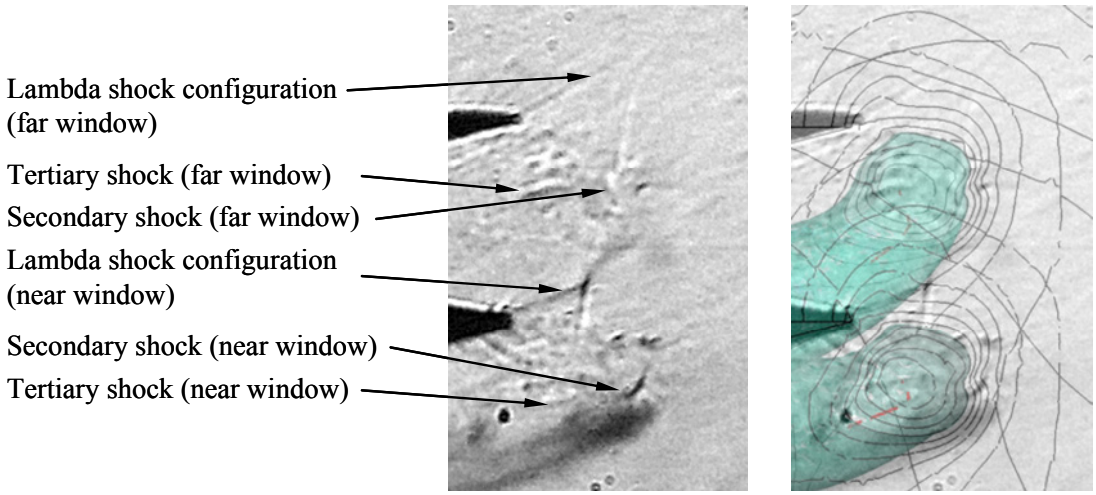

b) Expanded view of tip

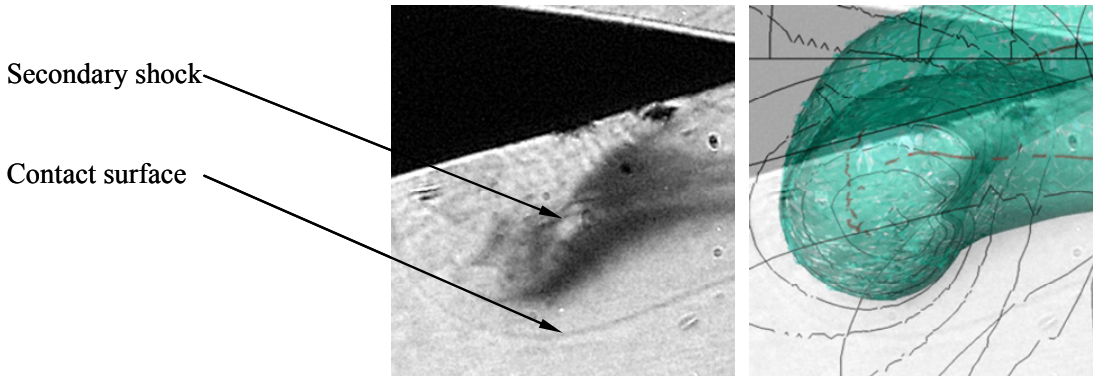

c) Expanded view of centre

Figure 6.51: Numerical and experimental results comparison, 'inverted-V' model, M_s=1.65, t=162μs

6.3.3 Vortex behaviour

In this sub-section, further details on the structure and behaviour of the free vortex for the 'inverted-V' model are given. Further details as to the structure of the flow fields for the cases of incident shock Mach numbers of 1.42 and 1.65 are presented. As mentioned previously, the M_s=1.32 case is qualitatively similar to the M_s=1.42, and for the sake of brevity, is not presented in detail here.

M_s=1.42

The evolution of the free vortex for the M_s=1.42 case is described in this section. Firstly, the evolution of the vortex with time is described. Figure 6.52 shows top views of the vortex at different time instants. The blue line indicates the position of the planar portion of the diffracting shock wave. The diffracting edge and boundaries of the flow domain are shown in black, and the red line indicates the location of the vortex core. Again, t_0 corresponds to the instant that the shock wave reaches the tip of the 'V'; the initial point of diffraction.

From this sequence of images, the bending of the vortex core so as to meet the solid boundaries at a right angle, and to form a continuous curve at the centre of the flow domain, is more clearly illustrated. The reader is referred to §6.2.2 for a discussion of these flow phenomena, as identical effects are observed here.

A comparison between the numerical solution for the two cases is given in Figure 6.53, where top views of the vortex in half of the flow domain are given for similar time instances. The similarity between the two sets of results is further emphasized through the vorticity production plots

presented in §6.6. This similarity also demonstrates the mesh independence of the solutions obtained.

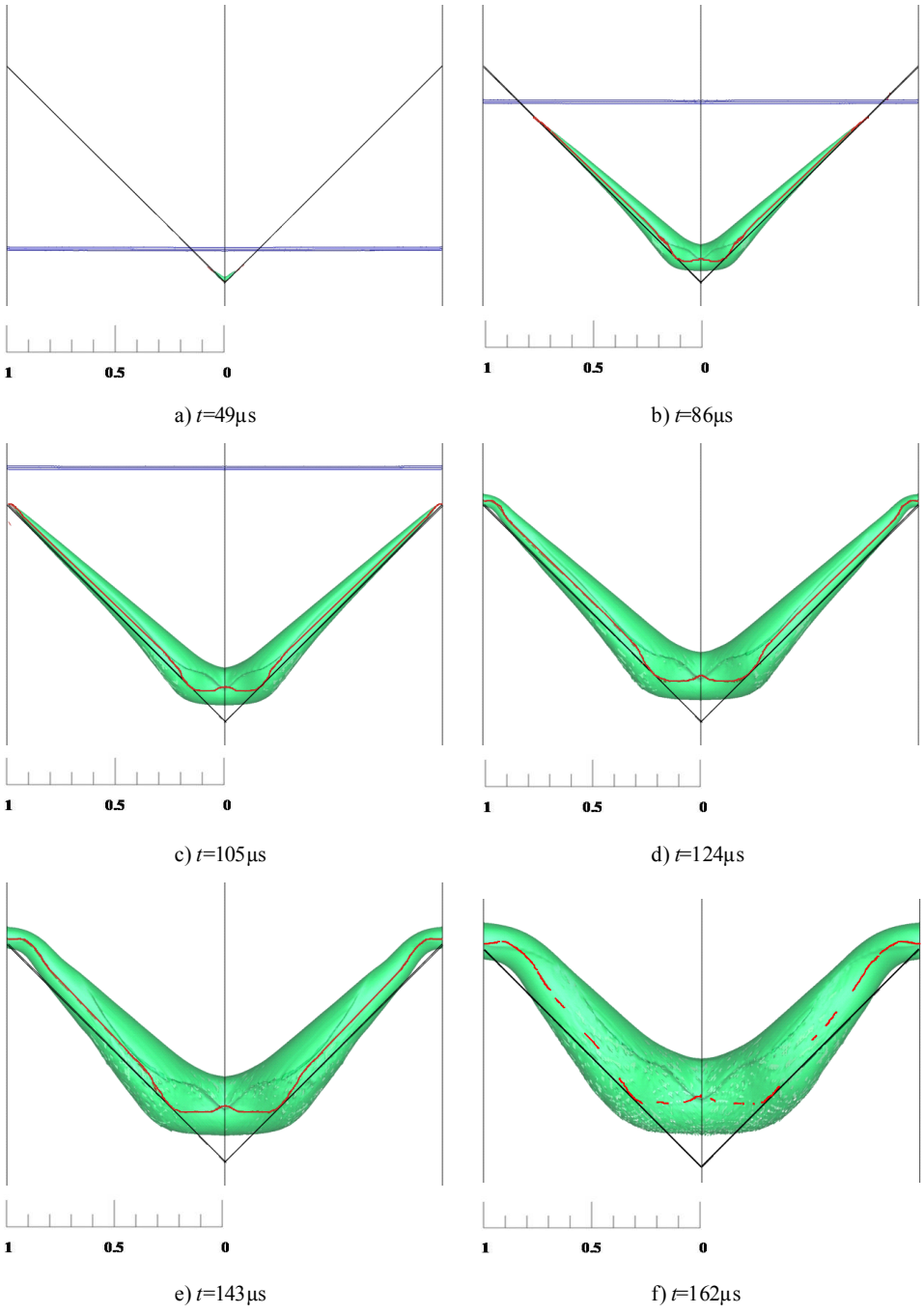

Figure 6.52: Top View of Vortex Bending ('Inverted-V' Model, M_s=1.42), surfaces of constant density (0.75kg/m^3) shown

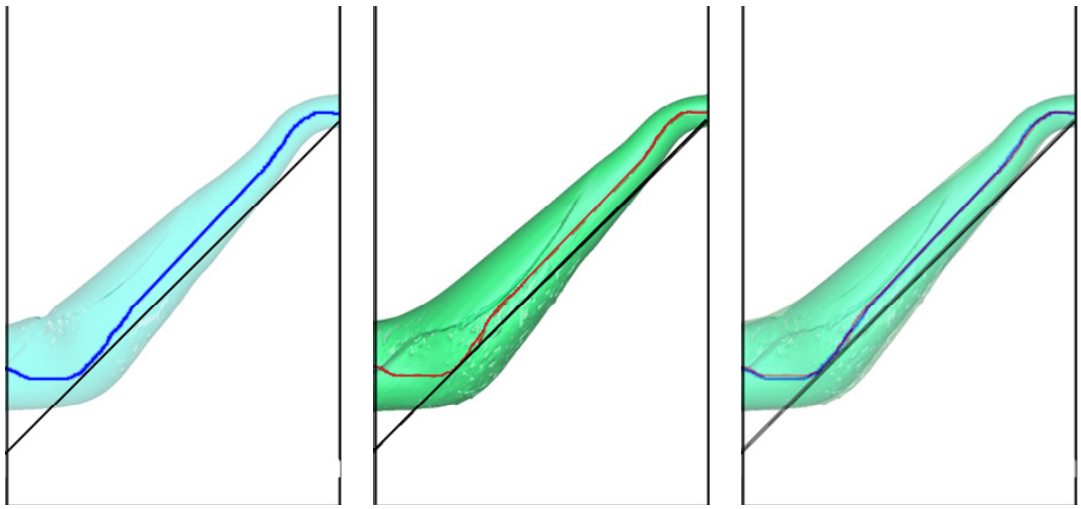

a) ‘V’ case b) ‘Inverted-V’ case c) Overlay

Figure 6.53: 'V' & ‘Inverted-V’ solution comparison, t=137μs

M_s=1.65

Top views of the evolution of the vortex for an incident shock Mach number of 1.65 are given in Figure 6.54. As expected, the results are similar to those for the shock M_s=1.42, and those presented in §6.2.5 for the ‘V’ model.

Figure 6.55 contains a sequence of density line plots taken on slices at various locations across the flow domain. 0mm corresponds to the centre of the flow domain, and 38mm is at the boundary. Also shown on these images is the vortex core (solid white line). This data is taken for t=143μs. The secondary shock in the vortex can clearly be seen in images a) through to e), starting from the centre of the flow domain and extending approximately 8mm away from the centre plane in both directions. The secondary shock is again apparent close to the window, in images q) through t), extending from the window approximately 8mm into the flow domain. A tertiary shock is apparent in the numerical results in a small region near the window. This can be

seen in images s) and t). However, due to the coarseness of the meshes used, these are not resolved properly in the numerical simulation.

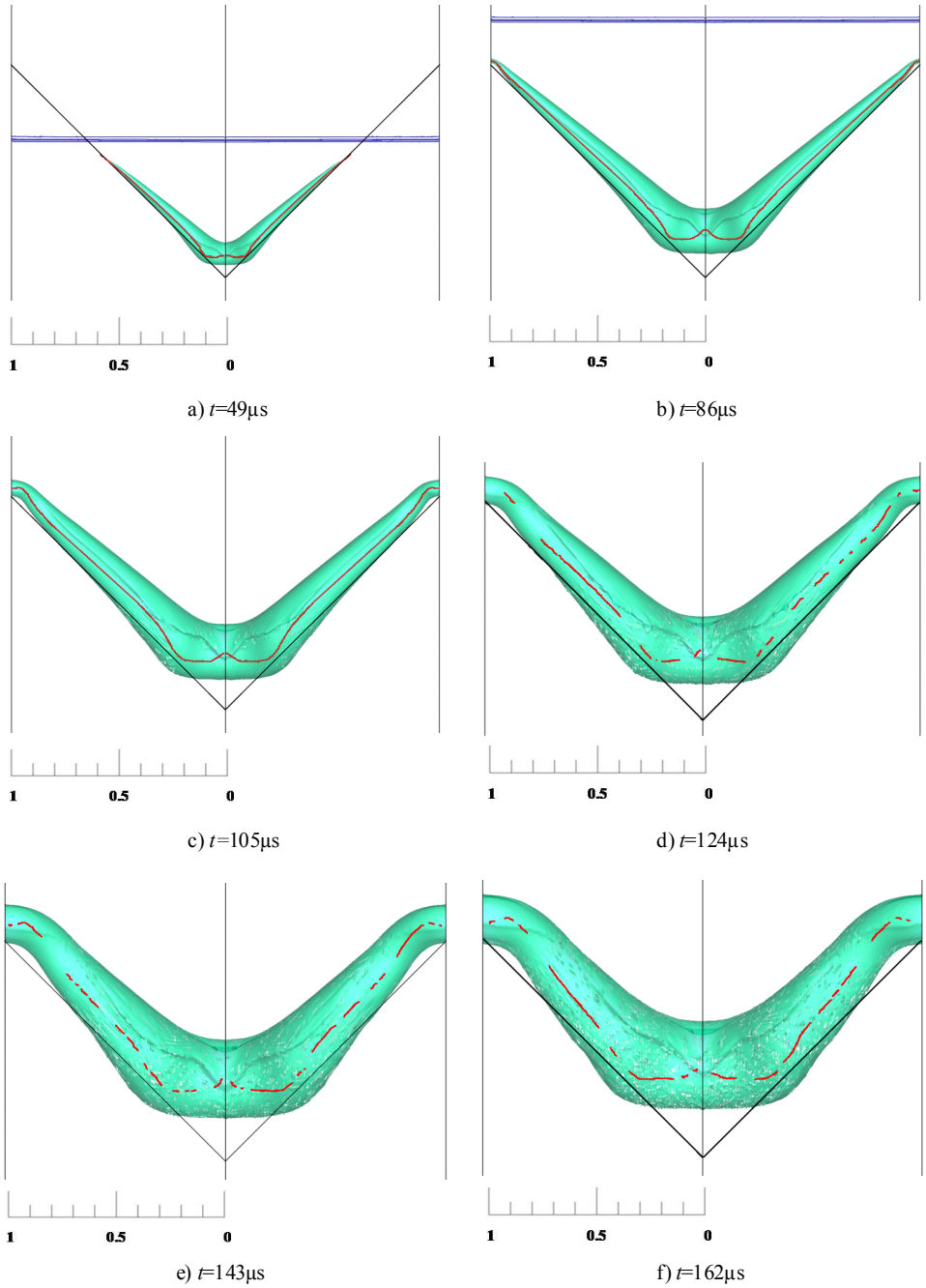

Figure 6.54: Top View of Vortex Bending ('Inverted-V' Model, M_s=1.65), surfaces of constant density (0.8kg/m^3) shown

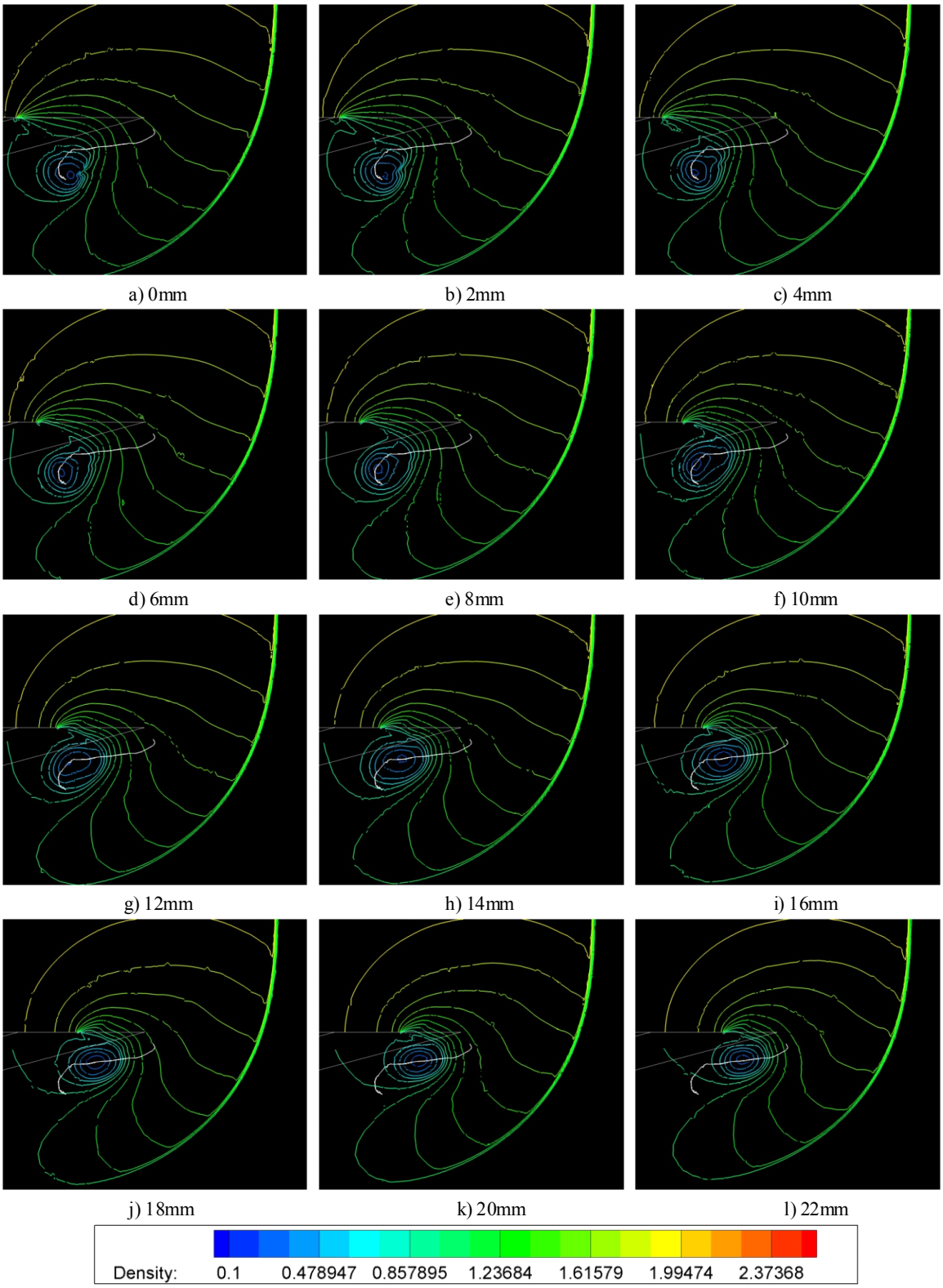
a) 0mm
b) 2mm
c) 4mm
d) 6mm
e) 8mm
f) 10mm
g) 12mm
h) 14mm
i) 16mm
j) 18mm
k) 20mm
l) 22mm
Density:
0.1
0.478947
0.857895
1.23684
1.61579
1.99474
2.37368

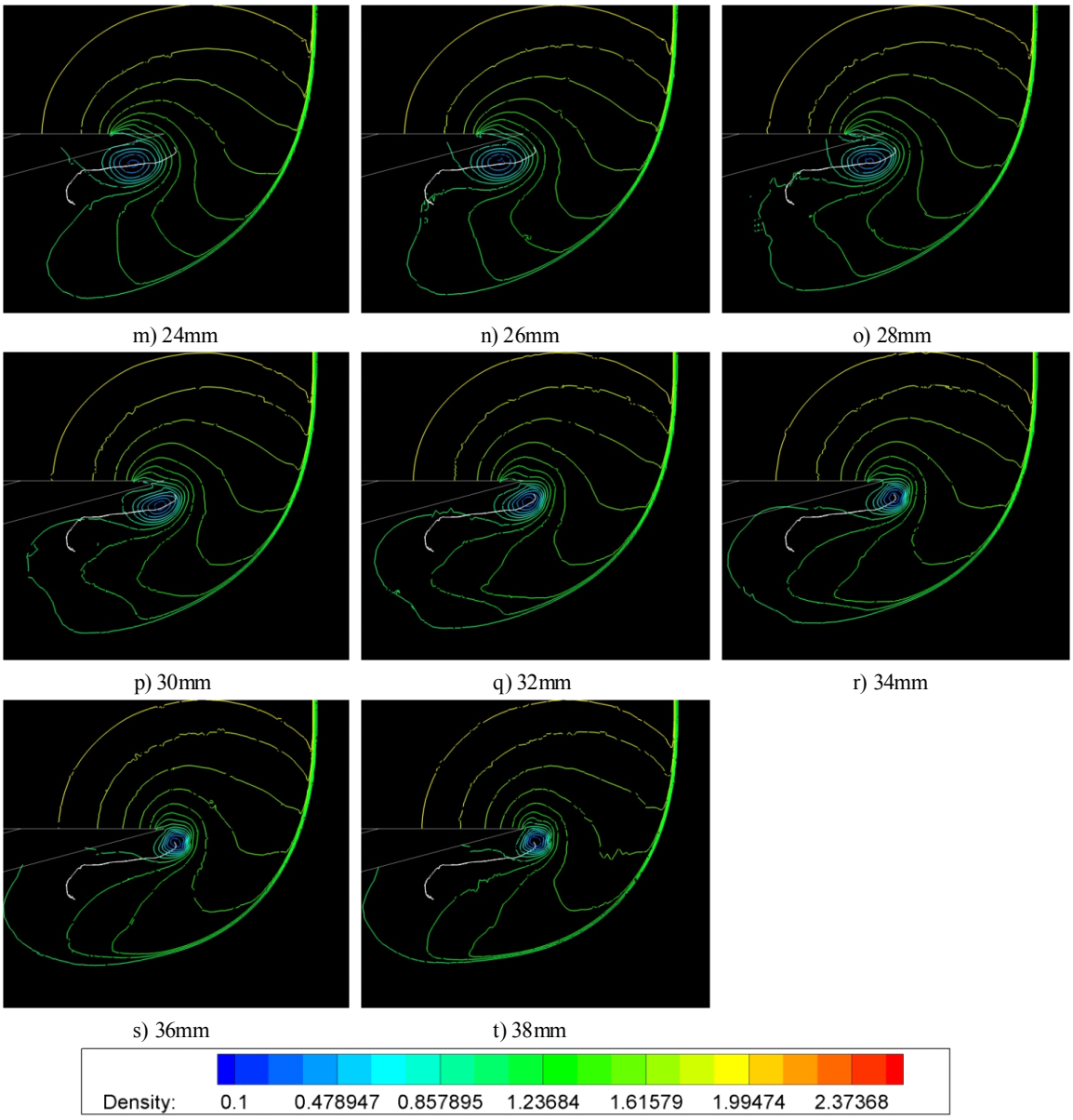

Figure 6.55: 'Inverted-V' model density line slices, M_s=1.65, t=143µs

Figure 6.56 shows an isometric view of the flow field at t=143µs, and indicates the vortex and the extent to which the secondary shocks extended throughout the flow domain.

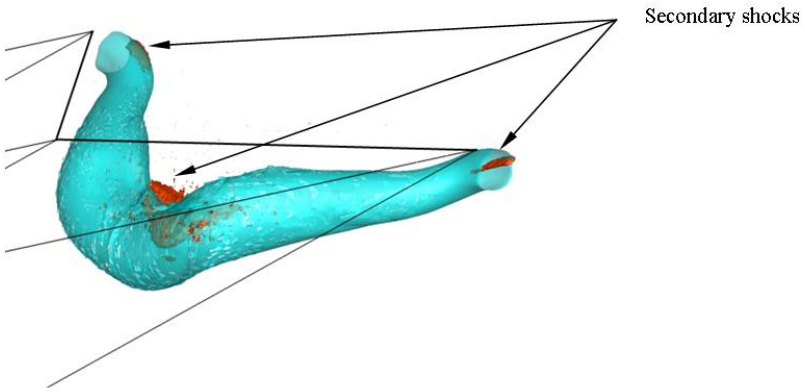

Figure 6.56: 'Inverted-V', M_s=1.65, t=143μs, shock features

As with the M_s=1.42 case, the 'V' and 'inverted-V' solutions are similar at equivalent time steps. The similarity between the two solutions is further emphasized by the vorticity plots in §6.6.

For further discussion, the reader is referred to the discussion in §6.2, as the results and processes involved are essentially the same here. Shown in Figure 6.57 are the flow fields, indicating the vortex and density line plots at the near boundary (red) and the centre of the domain (black), for the M_s=1.42 and M_s=1.65 cases. The secondary shocks are clearly visible from the line plots against the solid boundary and at the centre of the flow domain for the M_s=1.65 case.

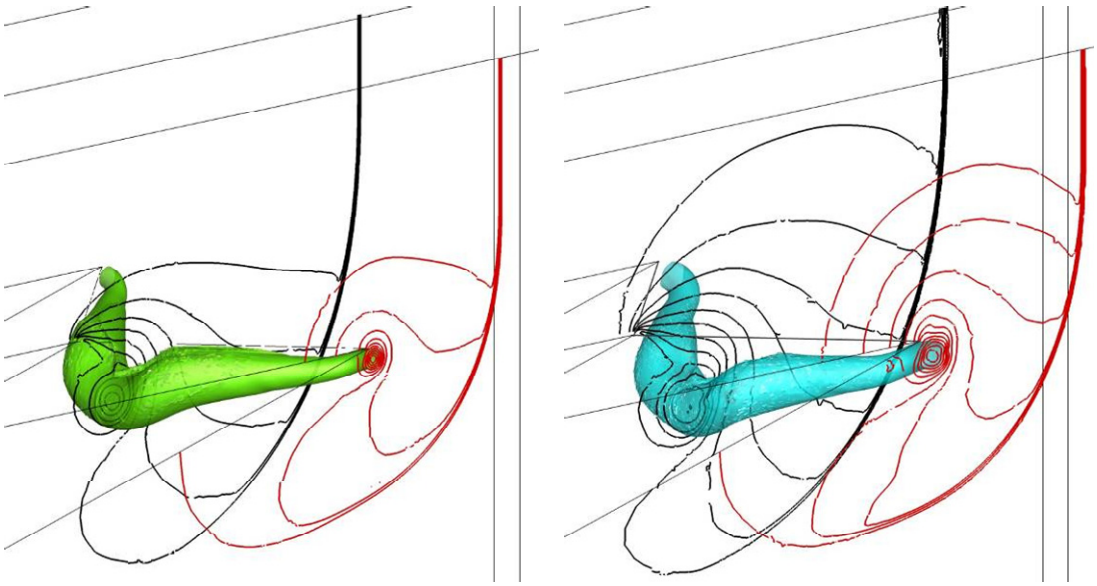

a) M_s=1.42 b) M_s=1.65

Figure 6.57: View of flow field, ‘inverted-V’ model

6.3.4 Summary

The evolution of the flow field for the ‘inverted-V’ model was described and discussed. The numerical results compared favourably with the experimental results, and captured the flow features very well. The numerical results are similar to the ‘V’ model, and confirm that the results are mesh independent.

6.4 Parabolic Edge Test Model

Two further test models, incorporating curved diffraction edges (of parabolic profile) were manufactured. These were to produce curved vortices, with the curvature varying along the length

of the vortex, for analysis. The two models are referred to as the parabolic and inverted parabolic models, in line with the convention used previously for the 'V' and 'inverted-V' models. These models can be seen in Figure 4.10.

The angle between these edges and the wall of the test section was shallower than that for the 'V' models, meaning that the vortex would have to bend through a greater angle to meet the wall at a right angle in these cases. This angle was 25° and 155° for the parabolic and inverted parabolic edged models respectively, and 45° for the straight edged models.

The experimental and numerical results for the parabolic edged model are presented in the following sub-sections. The results for the inverted parabolic test models are presented in §6.5.

6.4.1 Overview and experimental photographs

M_s=1.42

Schlieren images obtained from experiment for M_s=1.42 are presented in Figure 6.58. These images were taken at an optical roll of 10°, with δt=25μs between successive images.

The images in Figure 6.58 show that the shock diffraction process is consistent with that observed in the previous sections. Here, there are no discontinuities in the diffracting edge, as at the tip of the 'V' in the two models discussed previously. The free vortex has assumed a parabolic shape similar to the shape of diffracting edge away from the windows. There is significant distortion to the vortex in the region of the windows. In the latter two images, g) and h), the vortex is barely

discernable. Further discussion of the flow field and its evolution with time is given in the sections below.

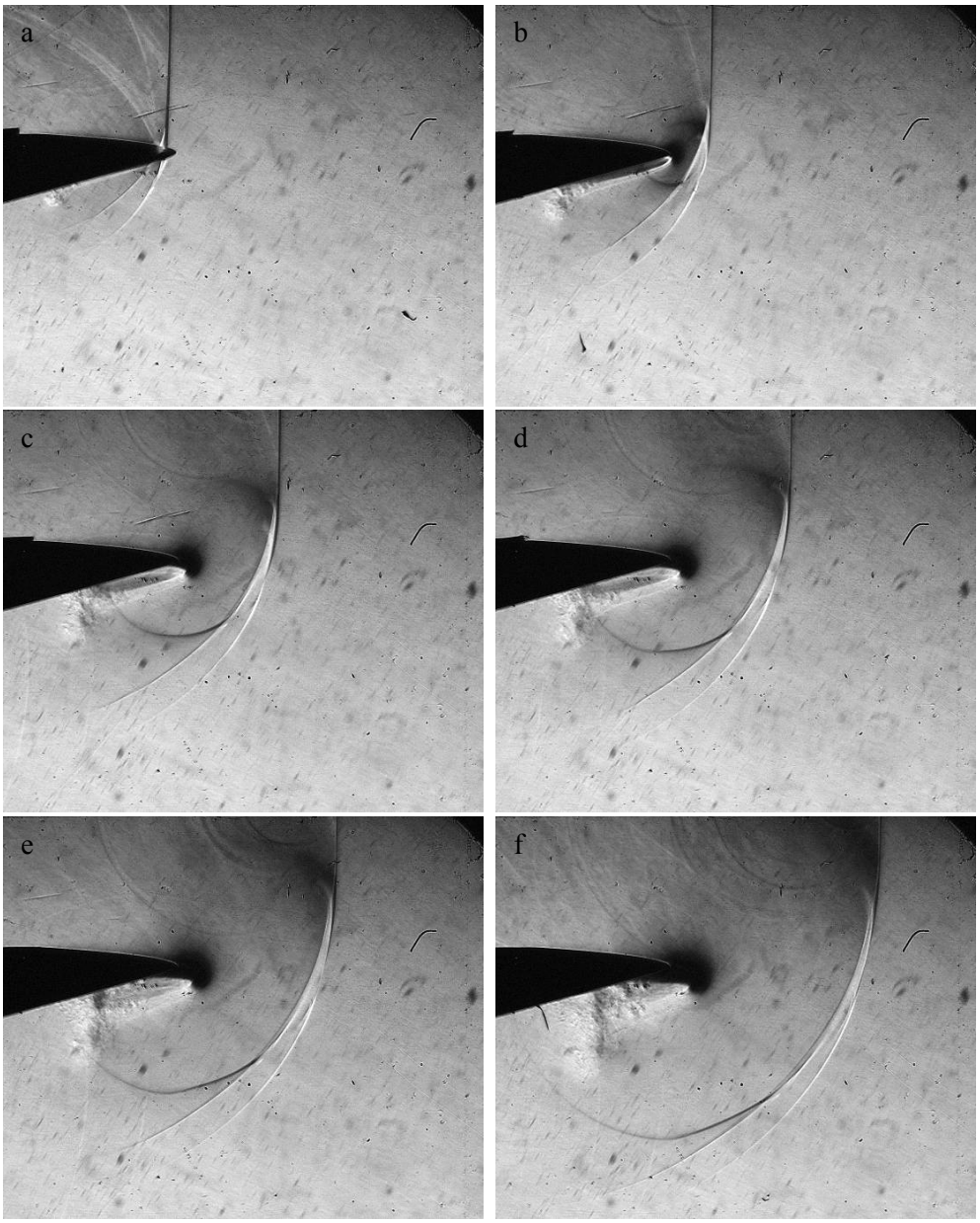

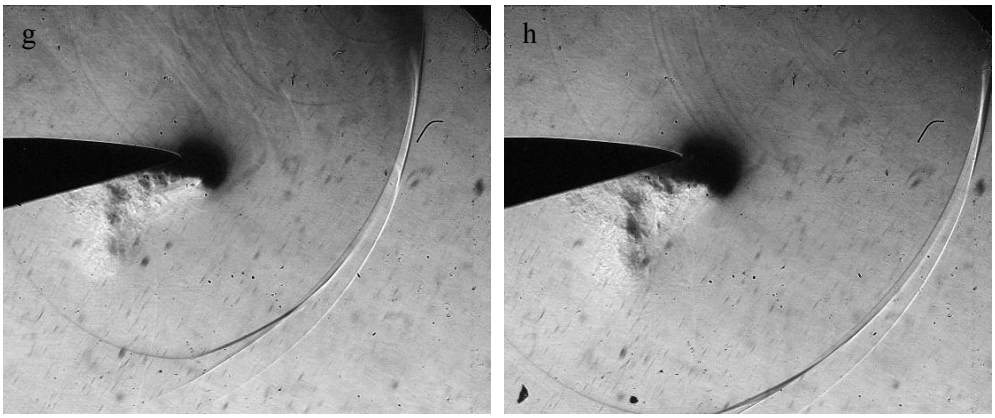

Figure 6.58: Parabolic model schlieren photographs, M_s=1.42, 10° optical roll, t=25μs

M_s=1.65

Experimental photographs for M_s=1.65 are given in Figure 6.59. Again, these images were taken at an optical roll of 10°, and the time between each successive image is given by δt=25μs.

Again, the flow field appears consistent with what one would expect, based on previous discussion. The secondary shocks are apparent against both the near and far windows in image c) and onwards. The secondary shock is apparent from image f) onwards, on the boundary of the dark region to the right of the rightmost part of the diffracting edge. The contact surface can clearly be seen just below the vortex in images g) and h). It is masked by the vortex in earlier images. Further discussion of the flow field and the evolution of it with time are given in the sections that follow.

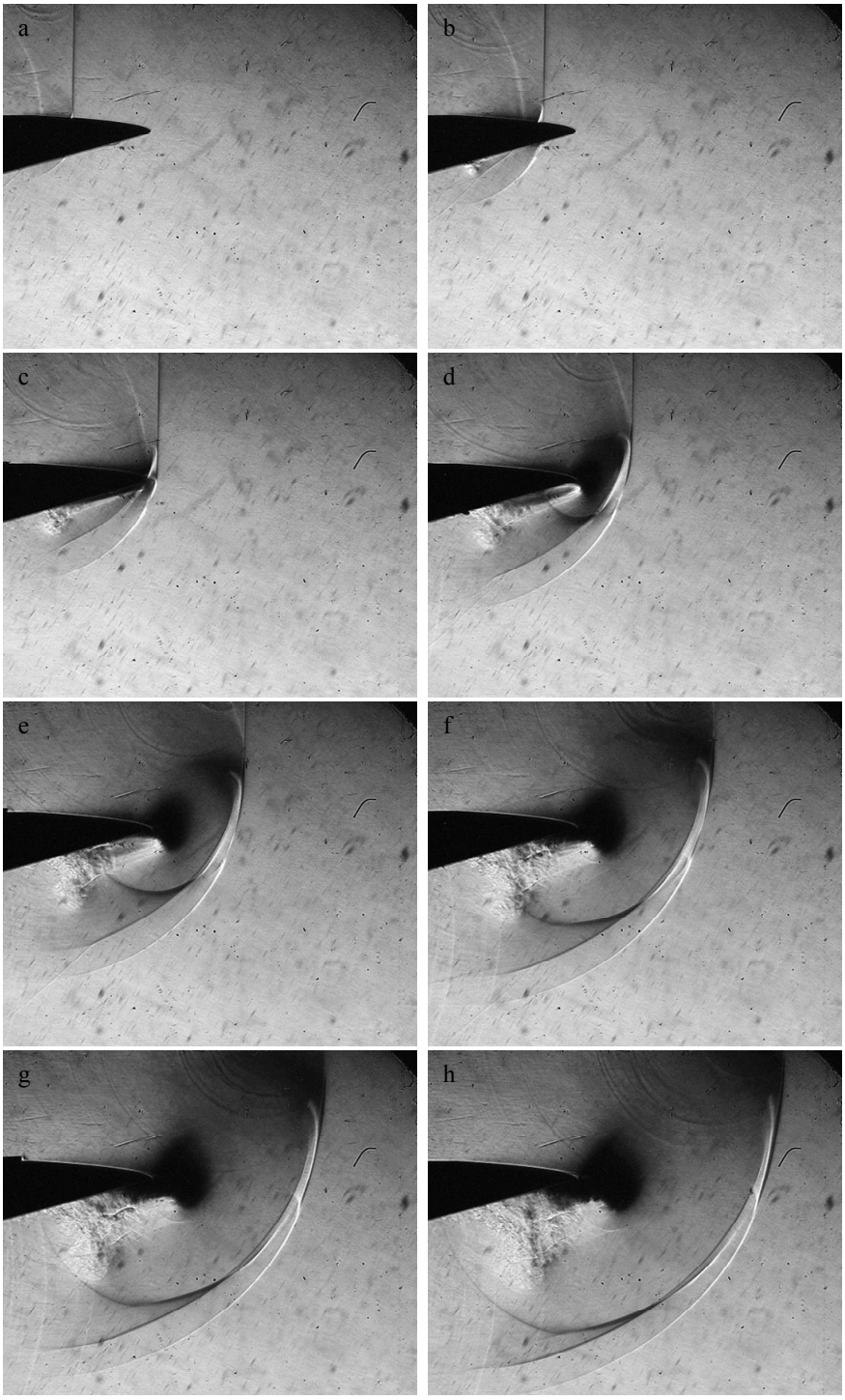

Figure 6.59: Parabolic model schlieren photographs, M_s=1.65, 10° optical roll, t=25μs

6.4.2 Overview of numerical results for parabolic edged test model

In this sub-section, further investigation of the flow field obtained for the parabolic edged model is presented, through analysis of the numerical results. A sequence of numerically generated plots is given for both incident shock Mach numbers (1.42 and 1.65), and this data is compared to the experimental schlieren photographs. Further numerically generated plots are presented in the sub-sections that follow, in an effort to describe the evolution of the free vortex.

Figure 6.60 shows the development of the numerical simulation with time for M_s=1.42. These images are taken at an optical roll of 10°, so as to match the schlieren images shown in the previous section. A constant density surface is shown (ρ=0.8kg/m^3) along with isopycnals taken on two slices across the flow domain (at the near boundary, and the centre plane). The time instant t_0 coincides with the initial point of diffraction. As with the results presented in previous sections, the correlation between the numerical results and experimental photographs is very good at the time instances investigated. Figure 6.61 gives an overlay of the experimental and numerical results at a similar time instant and highlights the basic features of the flow field. This also serves to highlight the correlation between the two sets of results. It should be noted that in this particular instance there is a slight discrepancy between the time at which the experimental and numerical images were taken. Indicated on the experimental image are the locations of the diffracted incident shock against the near and far boundaries, and on the centre plane.

Figure 6.62 shows a side view of the flow domain, again at an optical roll angle of 10°, with a constant density surface of 0.6kg/m^3 shown, for t=303μs. From this image, the bending and contraction of the free vortex in the region of bending is more evident. The slight ‘kink’ evident in the density lines taken on the centre plane to the right of the vortex would indicate the formation of a secondary shock at this location at later flow times. There is no evidence of this shock at the time instances shown in Figure 6.60. This behaviour is in line with what was

observed for the ‘V’ and ‘inverted-V’ M_s=1.42 cases. This feature is hard to identify in the schlieren images shown in Figure 6.58, as the feature is masked due to the higher sensitivity of the schlieren system used in obtaining these images.

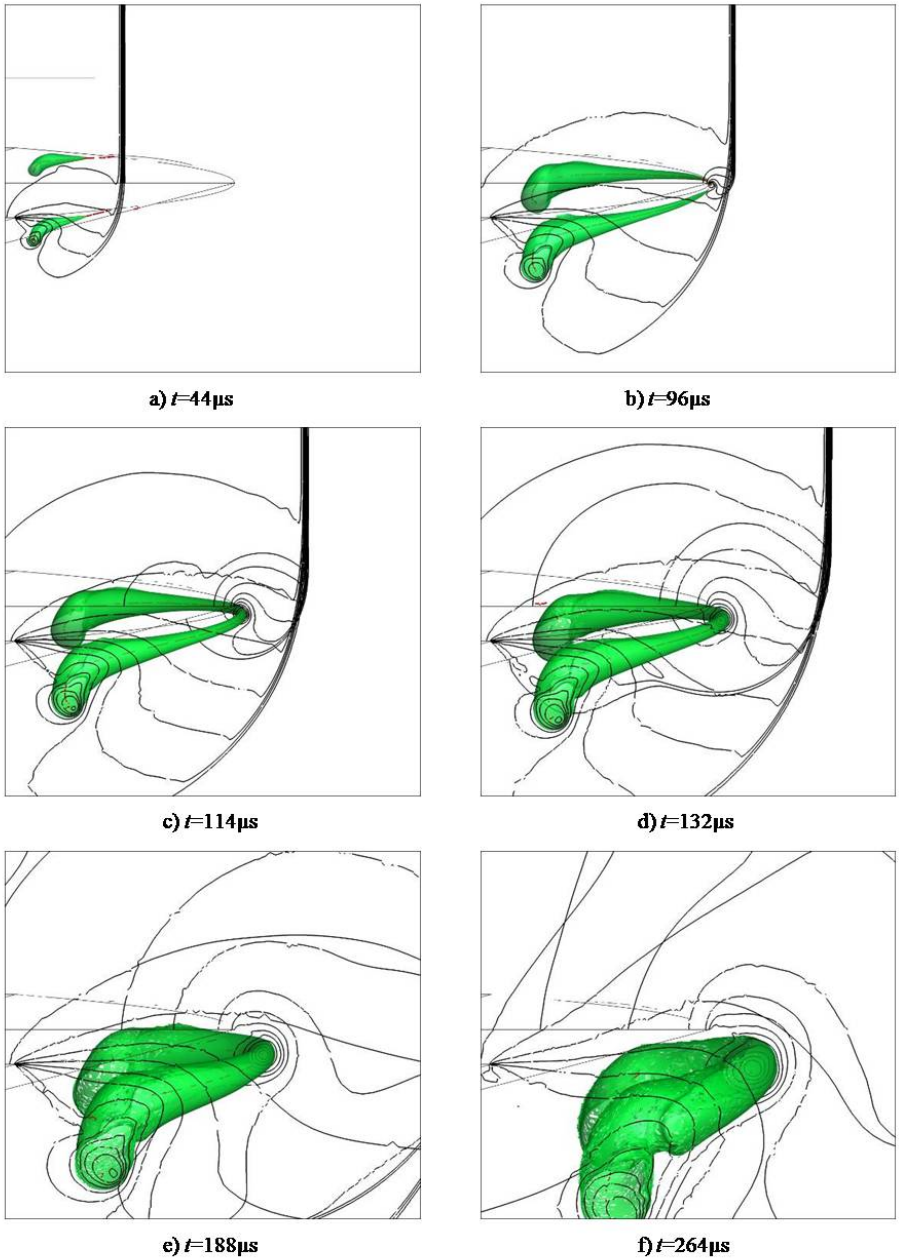

Figure 6.60: Parabolic model, M_s=1.42, density lines and surface plots

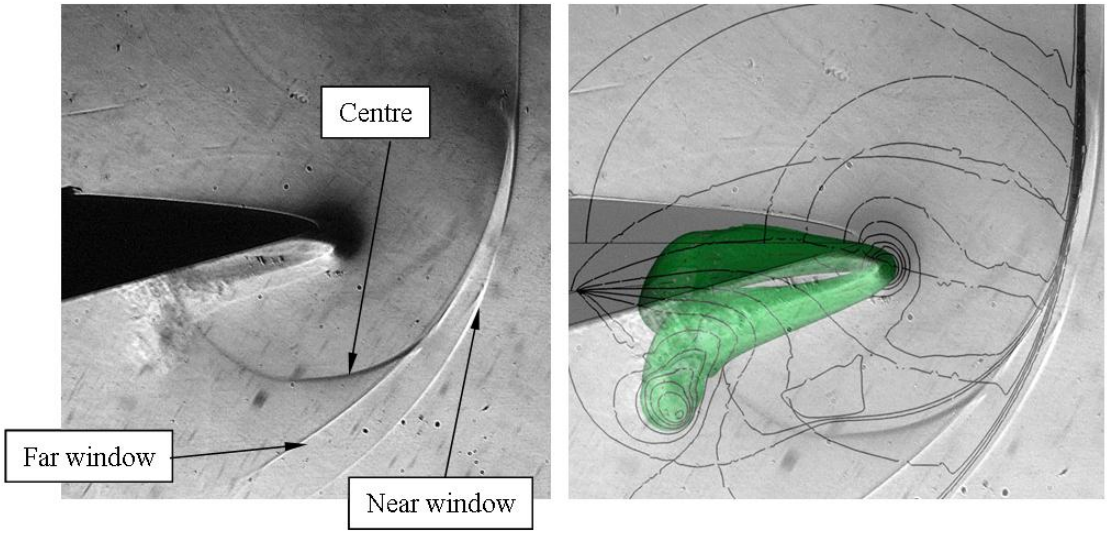

Figure 6.61: Parabolic model, M_s=1.42, experimental and numerical results overlay, incident shock wave location indicated

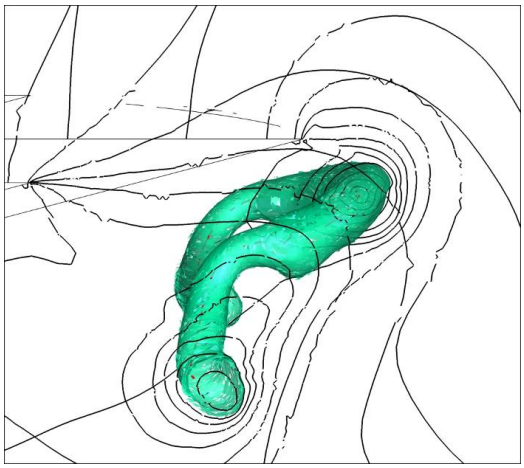

Figure 6.62: Parabolic model vortex side view, M_s=1.42, t=303µs

Figure 6.63 shows the evolution of the numerical simulation with time for M_s=1.65. Again, density surfaces of ρ=0.8kg/m^3 are shown.

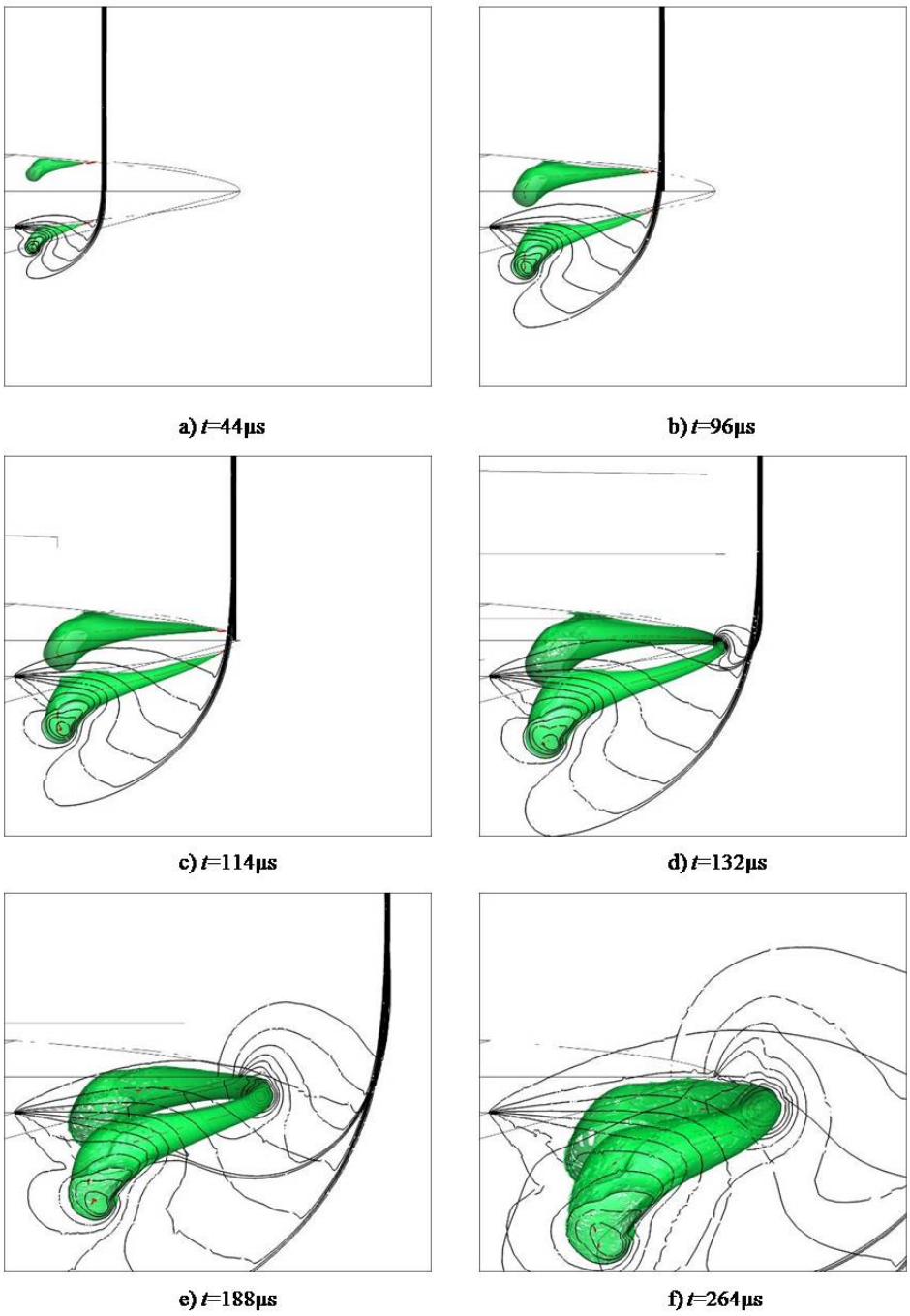

Figure 6.63: Parabolic model, M_s=1.65, density lines and surface plots

The secondary shock is clearly visible against the near boundary in Figure 6.63. It can also be seen in the density lines taken at the centre of the flow domain. A comparison of the numerical and experimental results is given in Figure 6.64, along with identification of the prominent flow features. It should be noted that the experimental and numerical images represent the flow at slightly different time instances. The secondary shocks are clearly visible against the near and far boundaries, and at the centre of the flow domain.

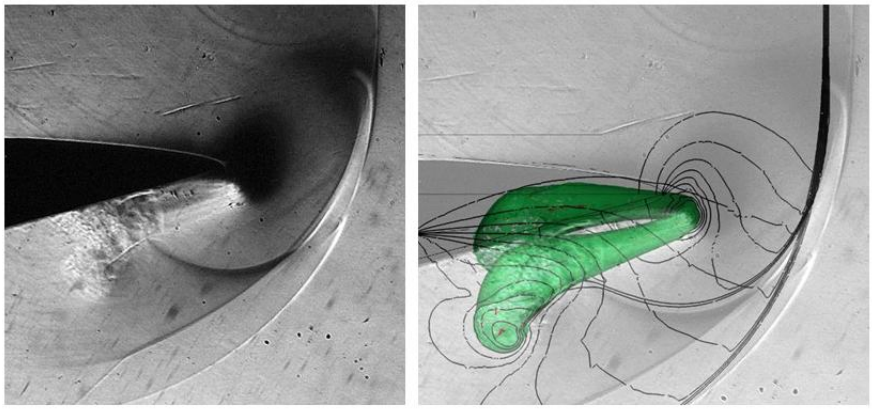

a) General overlay

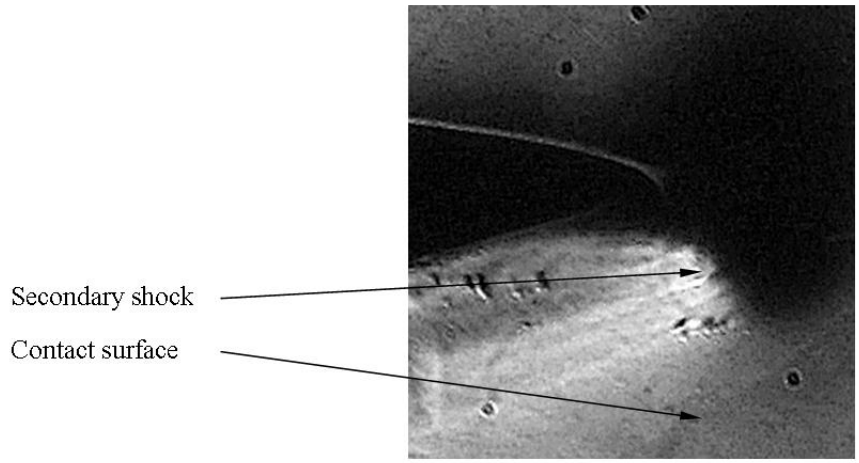

b) Zoomed view of central region

Figure 6.64: Parabolic model, M_s=1.65, experimental and numerical results overlay

Figure 6.65 gives a view of the numerical results for t=238μs, with a density surface of ρ=0.5kg/m^3 shown. This figure clearly demonstrates the presence of a secondary and tertiary shock on the centre plane, and a secondary shock against the near boundary of the flow domain. The general arrangement, in terms of bending, distortion and contraction of the vortex, is consistent with that shown for the case of M_s=1.42.

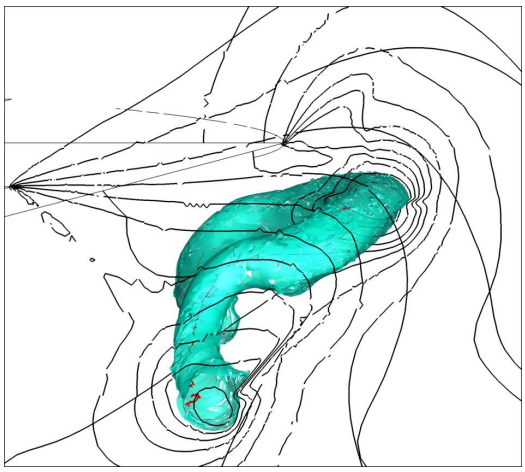

Figure 6.65: Parabolic model side view, M_s=1.65, t=238μs

Further discussion of the results and the structure of the flow fields is given in the sub-sections that follow.

6.4.3 Parabolic model vortex behaviour

In this sub-section, further details on the structure and evolution of the free vortex and the flow field are given.

M_s=1.42

A top down view of the diffraction process illustrating the evolution of the vortex is given in Figure 6.66. Here, a constant density surface of ρ=0.8kg/m^3 is shown, except where noted. The incident shock wave is represented by the blue horizontal line, and the vortex cores as extracted by Tecplot 360 2009 are shown as a red line. The core extraction did not seem to perform as well for the curved edged models, nevertheless, a reasonable idea of the core geometry can be obtained from the images in Figure 6.66.

Again, the general flow behaviour here is in accordance with the discussion presented in §6.2. The vortex core assumes a shape similar to that of the diffracting edge away from the walls. From images e) and f), we can clearly see the contraction of the vortex as it distorts and bends, where the vortex seems to have adopted a more complex arrangement in the vicinity of the walls than in the previously discussed cases.

Considering image f), at approximately 0.5 on the scale, the vortex core turns so as to point almost directly against the direction of propagation of the initial incident shock. It then turns through approximately 90°, and a small almost linear portion of the curve perpendicular to the wall exists between 0.6 and 0.85. It should be noted that in this region the vortex drops into the plane of the page below the diffracting edge, this is illustrated best by Figure 6.62. The core then bends again so as to meet the wall at a 90° angle, with the portion in the region immediately against the boundary slightly more downstream than the short and nearly linear section. This is more clearly shown in image e), where the core was more clearly calculated in this region.

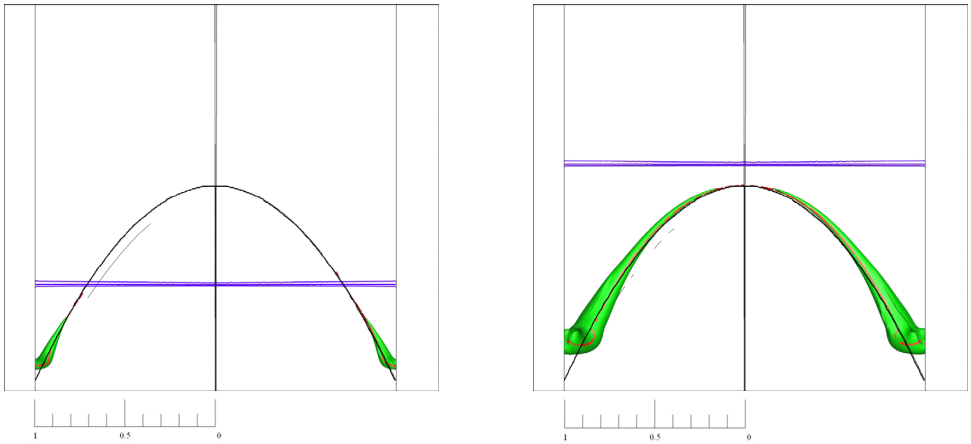

a) t=44μs

b) t=96μs

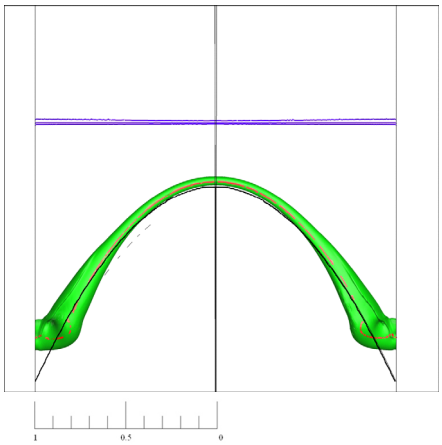

c) t=114μs

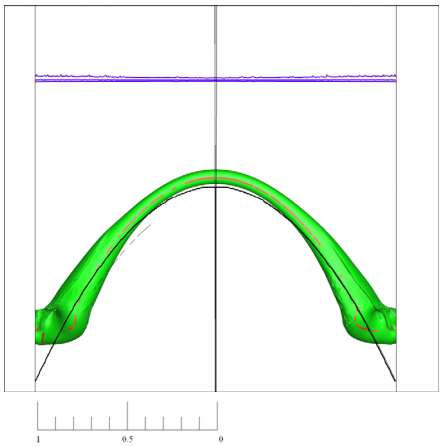

d) t=132μs

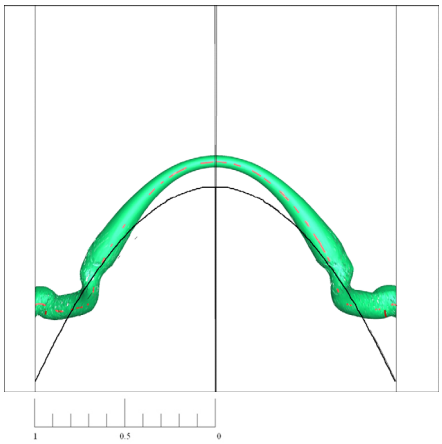

e) t=188μs (0.6kg/m^3)

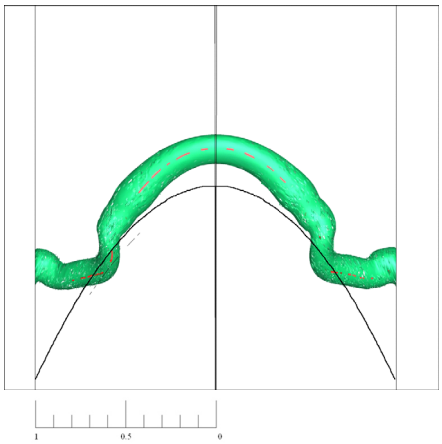

f) t=264μs (0.6kg/m^3)

Figure 6.66: Top view of vortex bending (parabolic model, M_s=1.42), surfaces of constant density (0.8kg/m^3) shown unless otherwise noted

Similar to the discussion in §6.2, various parameters were taken on slices taken through the vortex, in an effort to describe the flow and the effects on the flow that the distortion to the vortex have. Data presented here was taken on the two planes indicated in Figure 6.67 for two time instances.

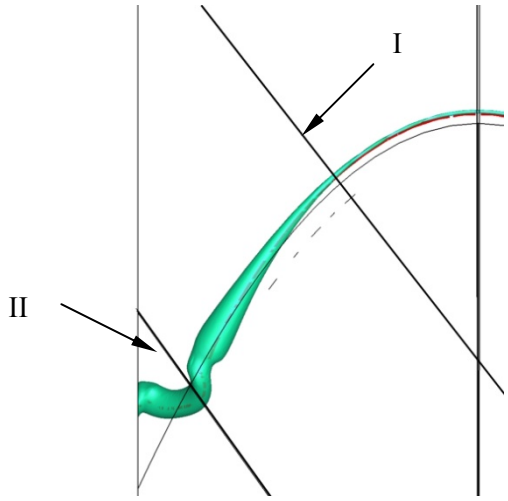

Figure 6.67: Vortex plane definitions (parabolic model, M_s=1.42)

Data is presented for plane I first. This region is away from the distortions caused by the presence of the solid boundaries. Figure 6.68 shows the profile of the vortex on plane I for the two time instants for which data is presented.

We can see from image d) that the slipstream has assumed a similar profile to that shown in Figure 6.11 for the 'V' model case.

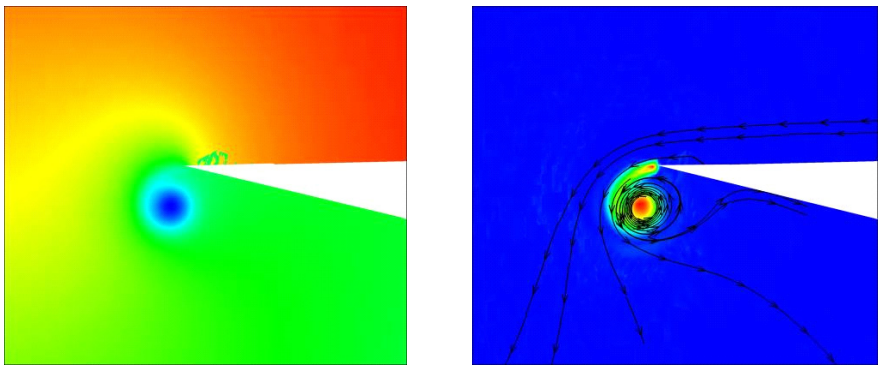

a) Density, t=114μs b) Vorticity & stream lines, t=114μs

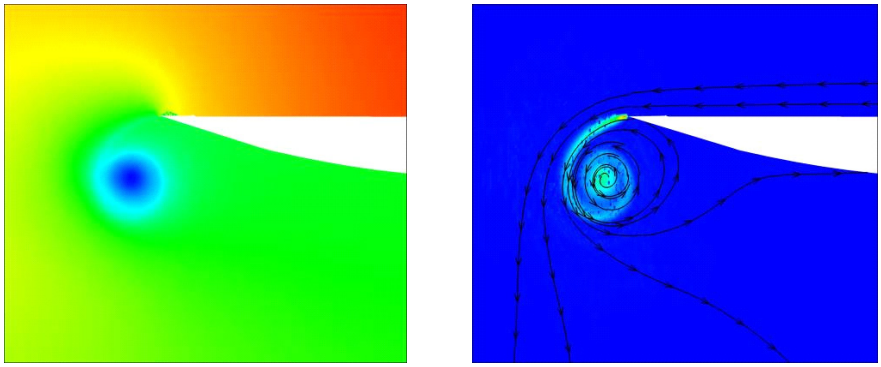

c) Density, t=264μs d) Vorticity & stream lines, t=264μs

Figure 6.68: Vortex profile, parabolic model, M_s=1.42, regular section

The plots given in Figure 6.69 through Figure 6.72 give data taken on a horizontal cut through the vortex core. The data is presented in a similar manner to that in §6.2.1. Figure 6.69 and Figure 6.70 give the tangential and radial velocities respectively.

In the data for t=114μs, insufficient time has elapsed for the slipstream to fully 'spread'. Thus, there are no peaks in the tangential velocity plot, signifying the portions of the slipstream inside the vortex.

These plots are similar to those presented in §6.2.2, and their basic features will not be discussed again here.

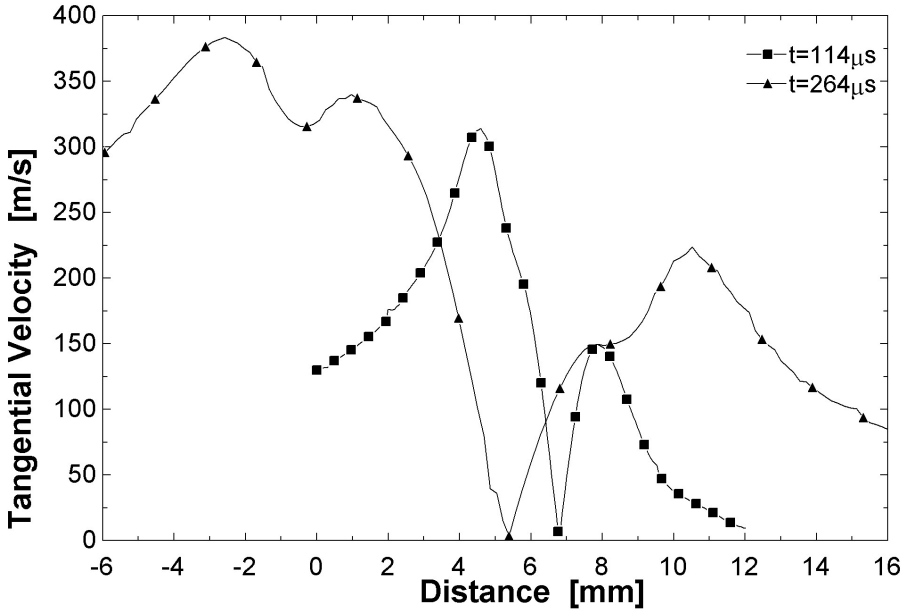

Figure 6.69: Tangential velocity profile, parabolic model, plane I, M_s=1.42

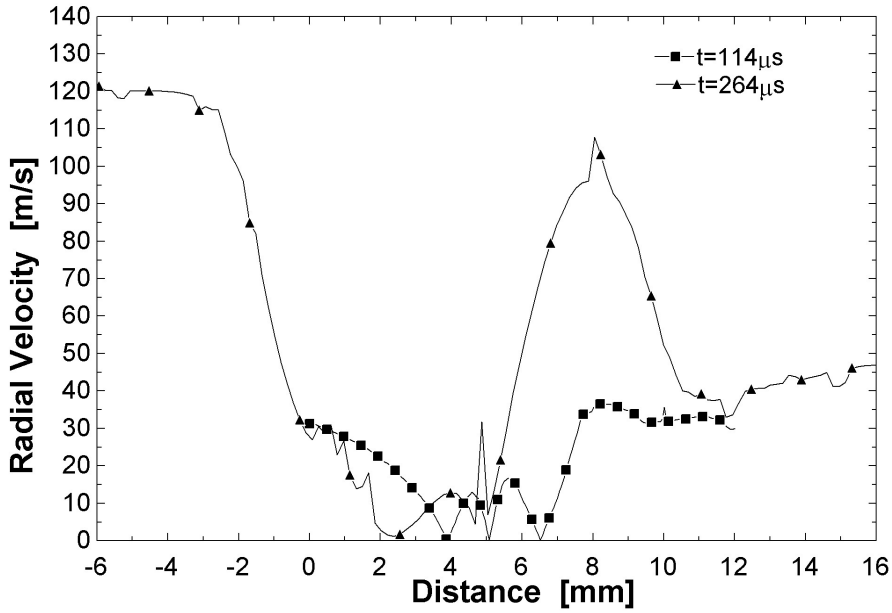

Figure 6.70: Radial velocity profile, parabolic model, plane I, M_s=1.42

Figures 6.73 and 6.74 give plots of the updraft velocity and normalised pressure respectively.

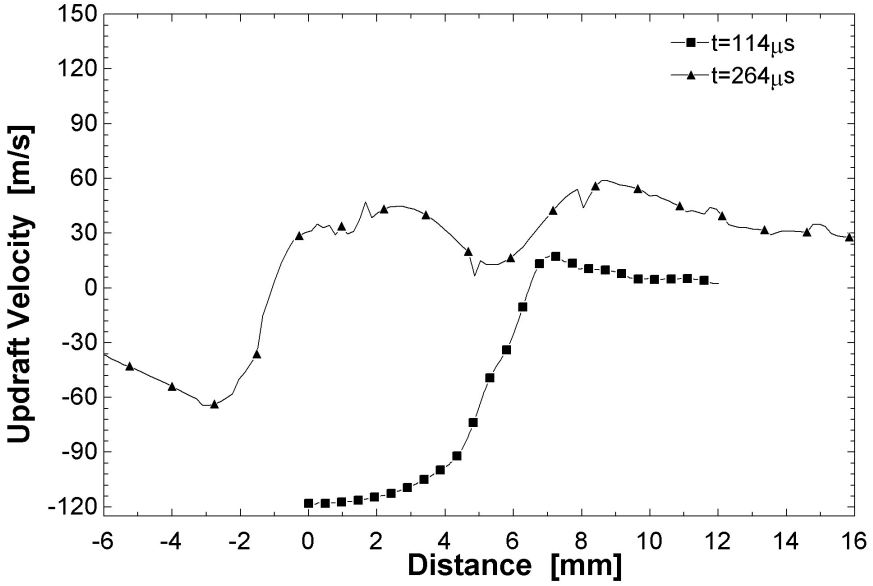

Figure 6.71: Updraft velocity profile, parabolic model, plane I, M_s=1.42

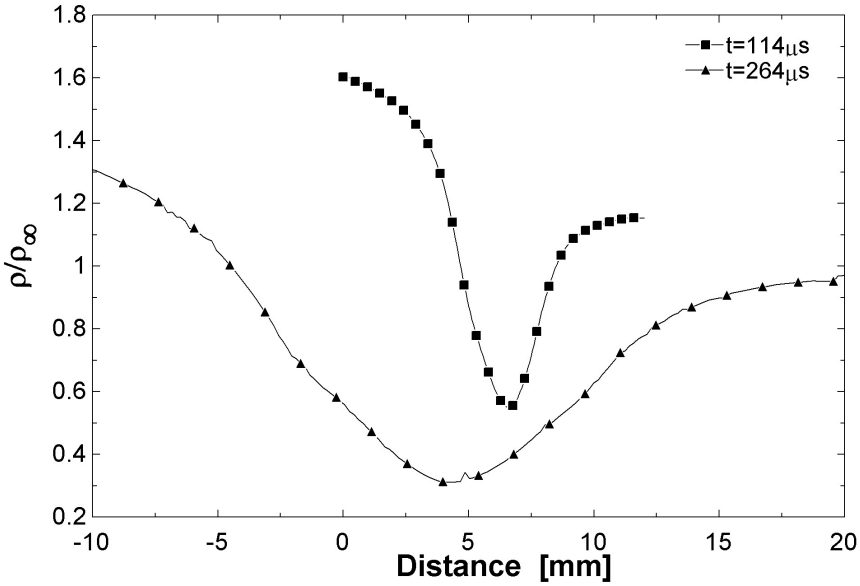

Figure 6.72: Pressure profile, parabolic model, Plane I, M_s=1.42

Figure 6.73 shows the profile of the vortex taken on plane II in Figure 6.67. It can be seen that significant distortion to the spiral pattern evident in Figure 6.68 has occurred. The slipstream has assumed a similar pattern at both time instances, as is indicated by images b) and d) in Figure 6.73.

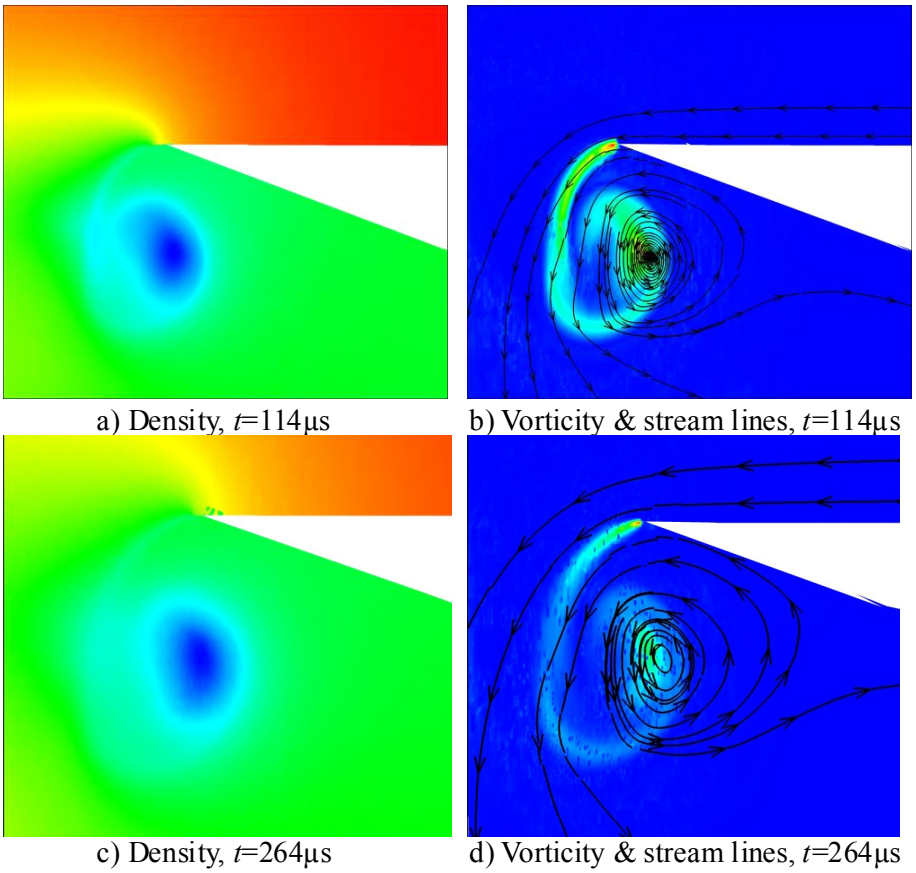

a) Density, t=114μs b) Vorticity & stream lines, t=114μs

c) Density, t=264μs d) Vorticity & stream lines, t=264μs

Figure 6.73: Vortex profile, parabolic model, M_s=1.42, bend section

Plots of the flow properties taken on a horizontal cut through the vortex core are given in Figure 6.74 through Figure 6.77.

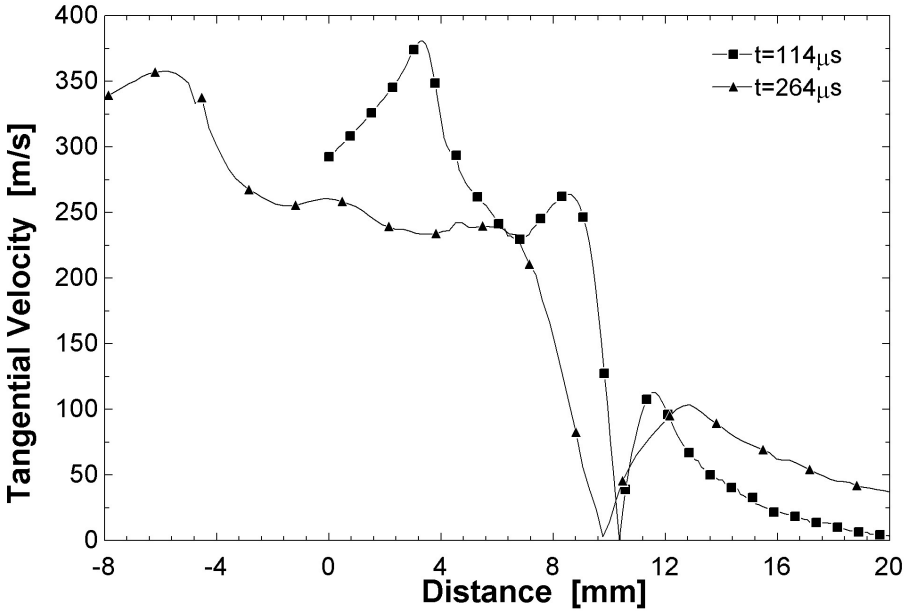

Figure 6.74: Tangential velocity profile, parabolic model, plane II, M_s=1.42

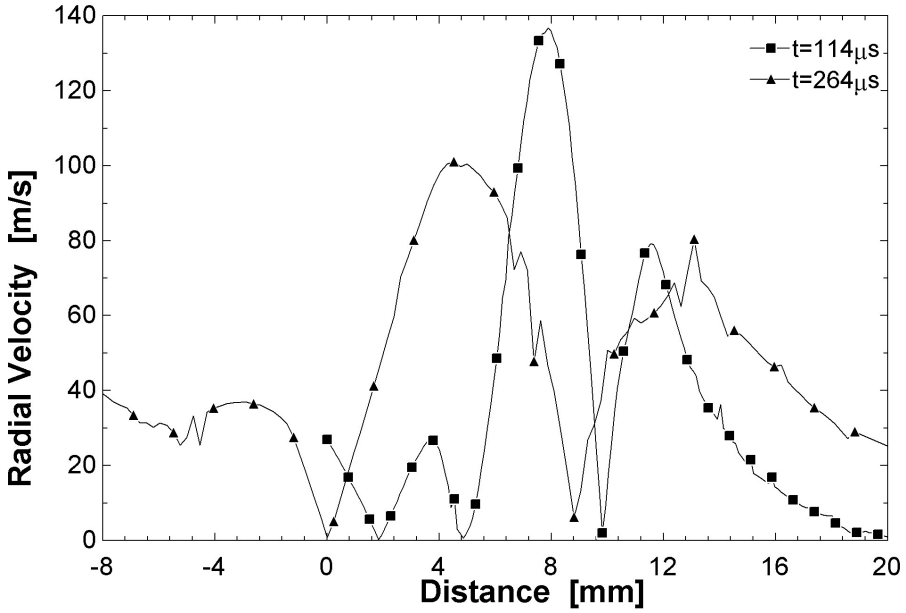

Figure 6.75: Radial velocity profile, parabolic model, plane II, M_s=1.42

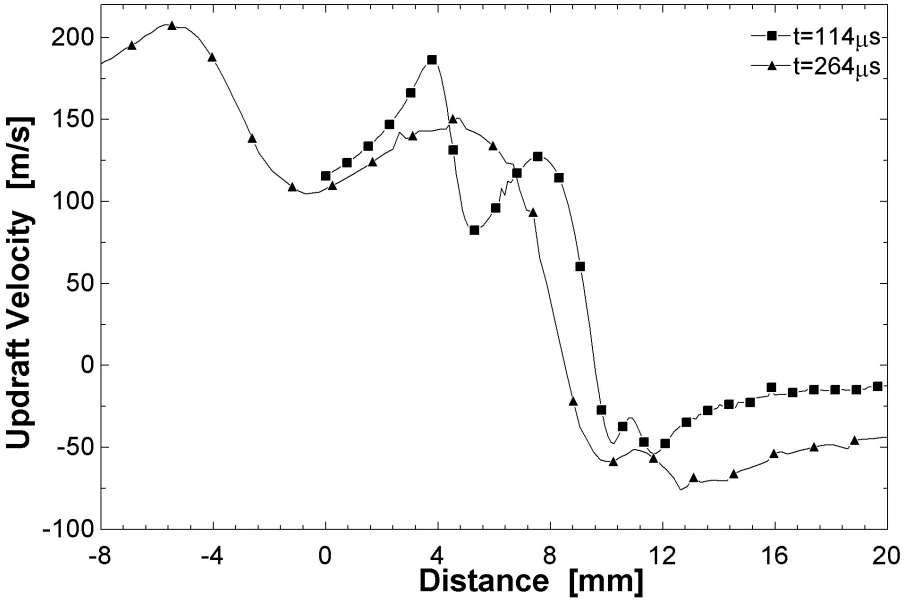

Figure 6.76: Updraft velocity profile, parabolic model, plane II, M_s=1.42

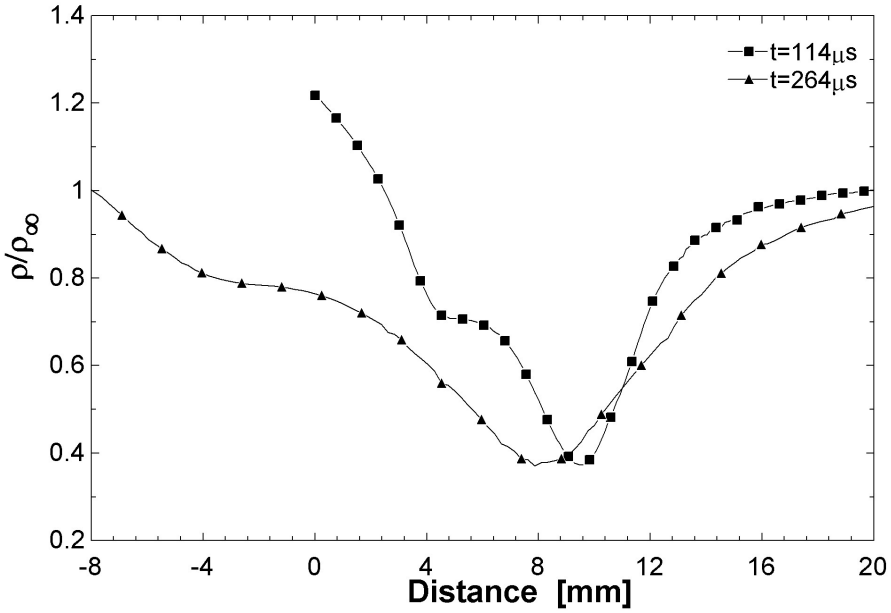

Figure 6.77: Pressure profile, parabolic model, plane II, M_s=1.42

The effects of vortex bending on the plots have been discussed in §6.2. This will not be repeated here.

Figure 6.78 contains a sequence of vorticity flood plots taken on various slices across the flow domain. These are shown for t=264μs, and show how the shape of the slipstream changes with position across the flow domain. Similar behaviour was observed for other time instances. 0mm corresponds to the slice taken on the centre plane of the flow domain, and 38mm the boundary. The black line represents the location of the vortex core, and as mentioned previously, is not as well captured in this case as it was in the results of the previous models. Here, we see that the slipstream exhibits the expected spiral pattern in the region near the centre of the flow domain. The distance between the outer and inner arms of the spiral grows as the vortex bends, in the region around image p), 30mm away from the centre of the flow domain. In the region between image p) and image t), the slipstream is compacted and distorted from its usual spiral shape. These observations are in line with what was observed in the previous sets of results for the other modes that were tested. It should be noted here that the vortex axis is generally not perpendicular to the plane on which these image are taken, and that in regions where there is a large angle between the vortex axis and the image plane (particularly between image g) 12mm and image m) 24mm), a distorted representation of the slipstream is given by these images.

Figure 6.78: Parabolic model, vorticity plots, M_s=1.42, t=264μs

M_s=1.65

Top views of the evolution of the free vortex for M_s=1.65 are given in Figure 6.79. The development of the flow and vortex follows a similar trend as for the M_s=1.42 case. Here, constant density surfaces of ρ=0.5kg/m^3 are shown, and the blue horizontal line represents the location of the incident shock wave. The evolution and arrangement of the free vortex is consistent with the discussion in the previous section on the M_s=1.42 case.

As in the previous discussion for the M_s=1.42 case, images and plots describing the properties of the free vortex on different planes perpendicular to the vortex axis are given here. The data is taken on the planes shown in Figure 6.67, with plane I corresponding to a region away from any distortions caused due to the presence of the solid boundary, and plane II through the region of bending of the vortex.

Figure 6.80 shows the arrangement of the vortex on plane I, for t=86μs and t=170μs. Data taken on a horizontal cut through the vortex core is presented in Figure 6.81 through Figure 6.84. The data given here is very similar to the M_s=1.42 case, as is evidenced in the similarity of the plots.

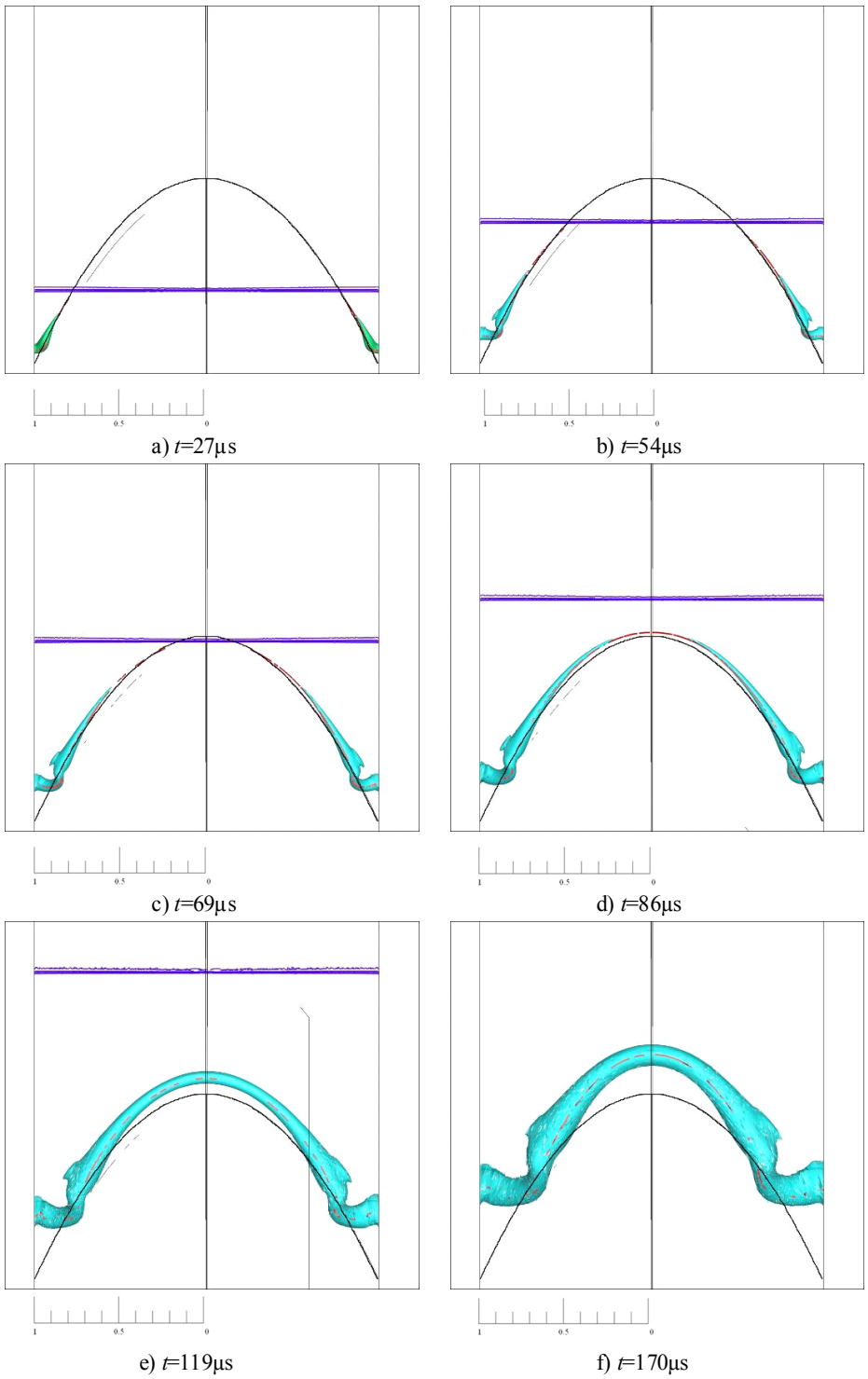

Figure 6.79: Top view of vortex bending (parabolic model, M_s=1.65), surfaces of constant density (0.5kg/m^3)

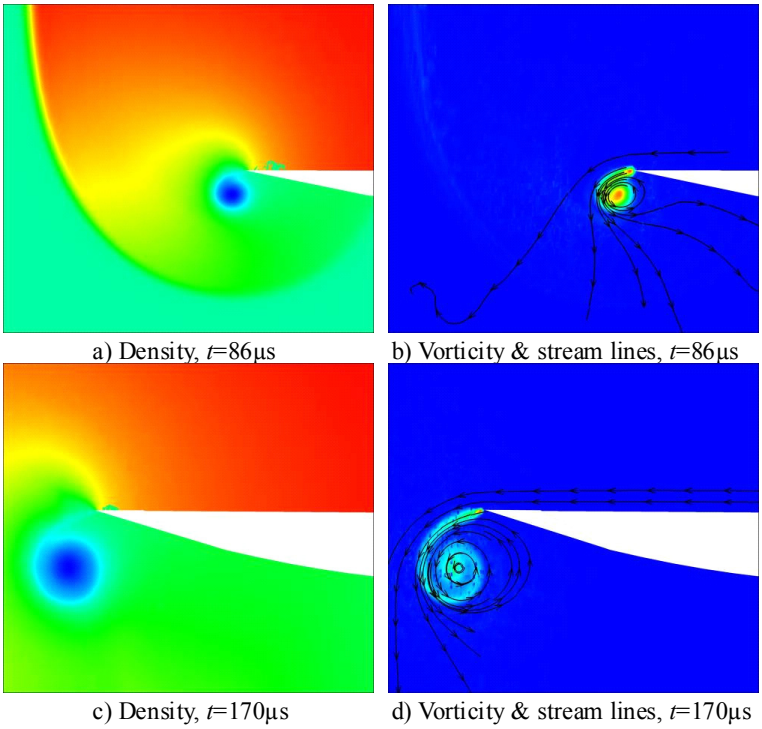

a) Density, t=86μs b) Vorticity & stream lines, t=86μs

c) Density, t=170μs d) Vorticity & stream lines, t=170μs

Figure 6.80: Vortex profile, parabolic model, M_s=1.65, regular section

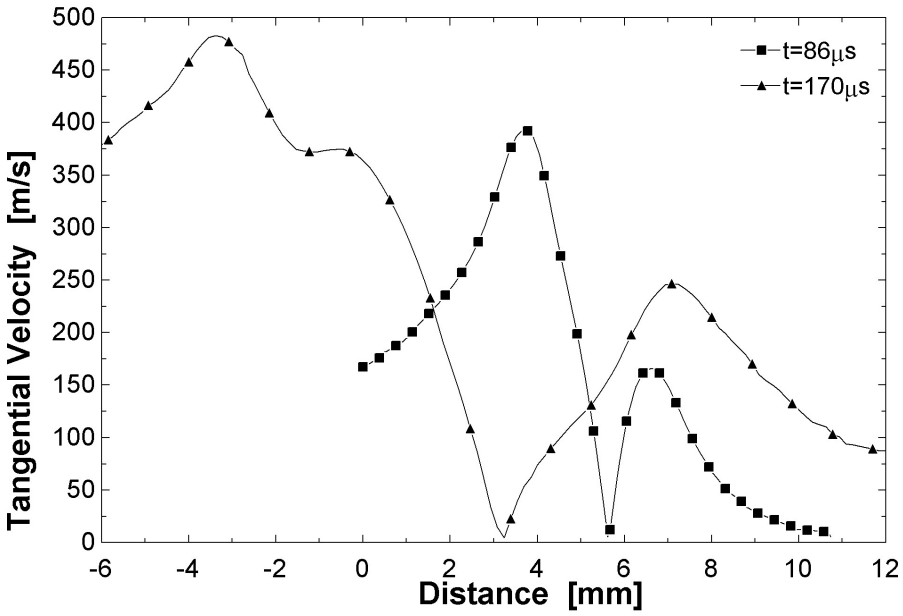

Figure 6.81: Tangential velocity profile, parabolic model, plane I, M_s=1.65

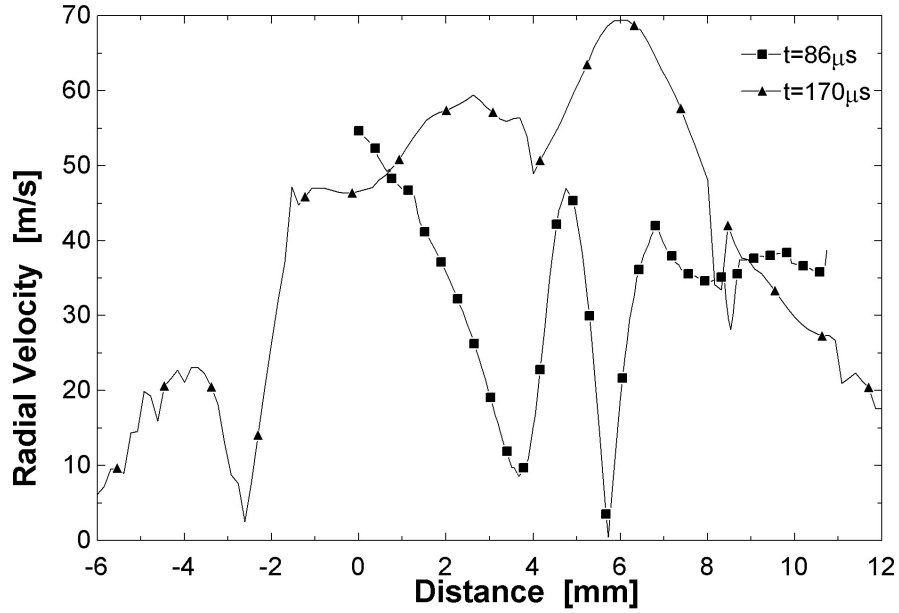

Figure 6.82: Radial velocity profile, parabolic model, plane I, M_s=1.65

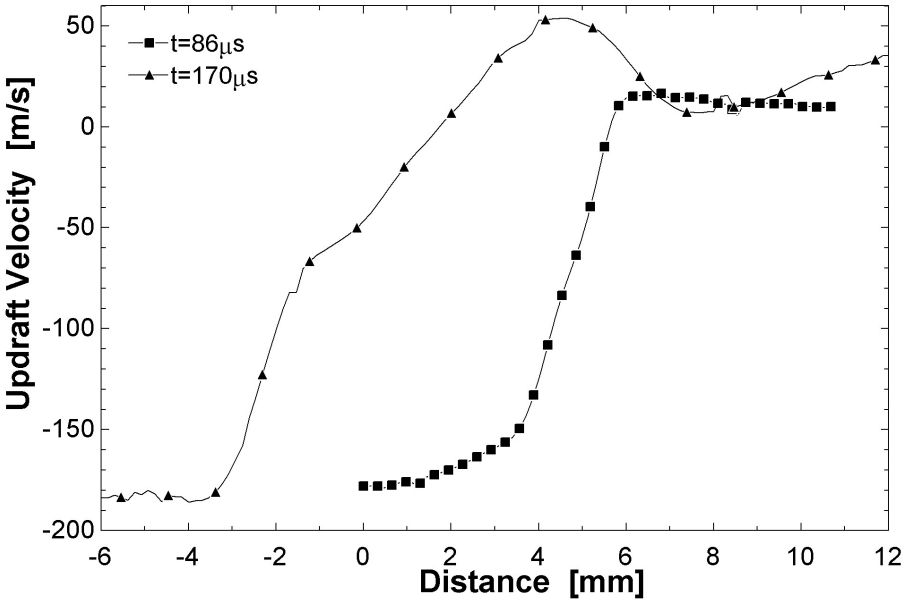

Figure 6.83: Updraft velocity profile, parabolic model, plane I, M_s=1.65

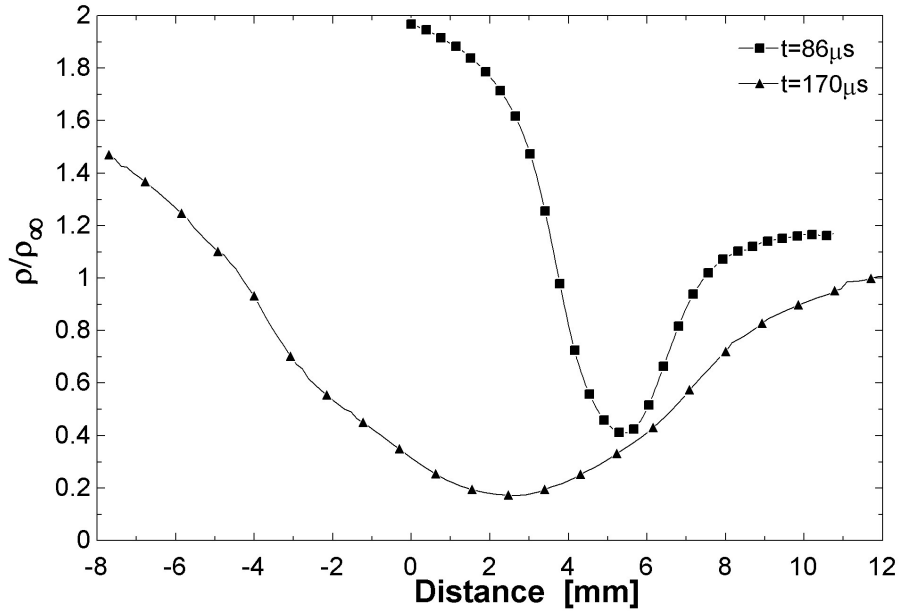

Figure 6.84: Pressure profile, parabolic model, plane I, M_s=1.65

Data taken on plane II is presented next. Figure 6.85 gives density and vorticity flood plots taken on plane I and II at two time instants. The density plots reveal the location of the secondary shock, the bump on the left of the vortex. The vorticity plots reveal that the secondary shock has caused a kink in the slipstream. It can also been seen from images b) and d) that the streamlines are compacted on the side of the vortex that is towards the centre of curvature of the bend, and that they are more spaced on the outside of the bend. This would imply that there is a higher velocity magnitude on the side of the vortex towards the centre of curvature of the bend. This effect has been demonstrated in previous sections.

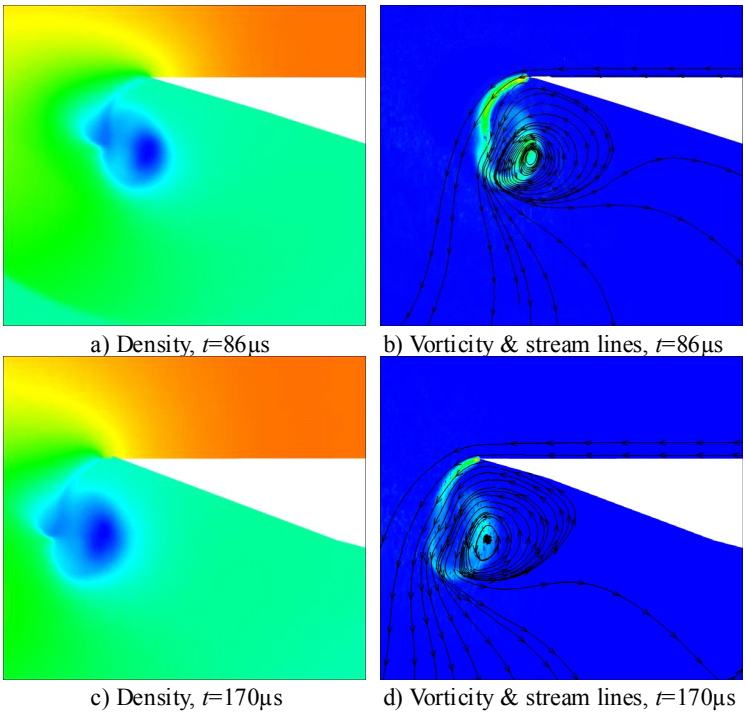

Figure 6.85: Vortex profile, parabolic model, M_s=1.65, bend section

Flow properties taken on a horizontal cut through the vortex core are presented in Figure 6.86 through Figure 6.89. Discussion of these plots is not presented here, as the features are similar to those presented in §6.2.2.

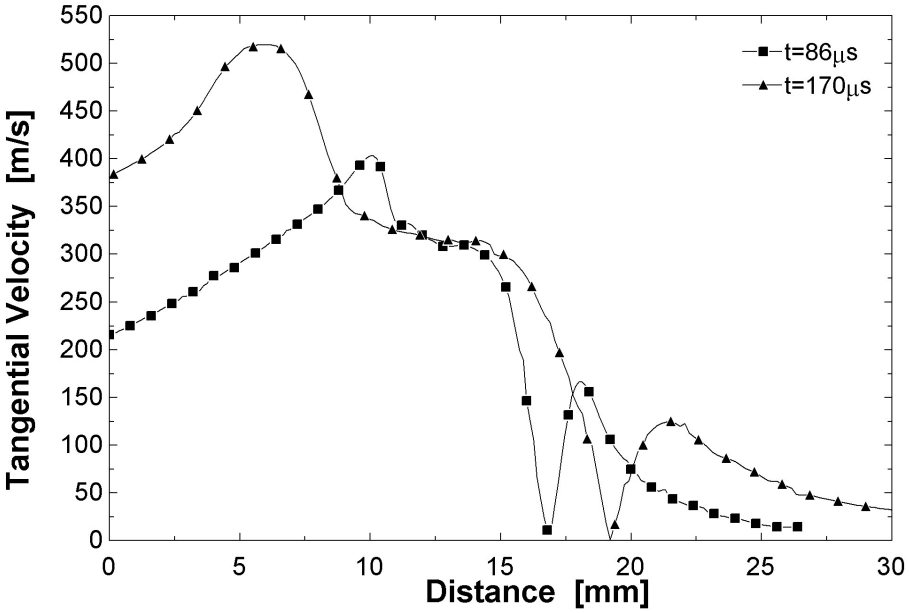

Figure 6.86: Tangential velocity profile, parabolic model, plane II, M_s=1.65

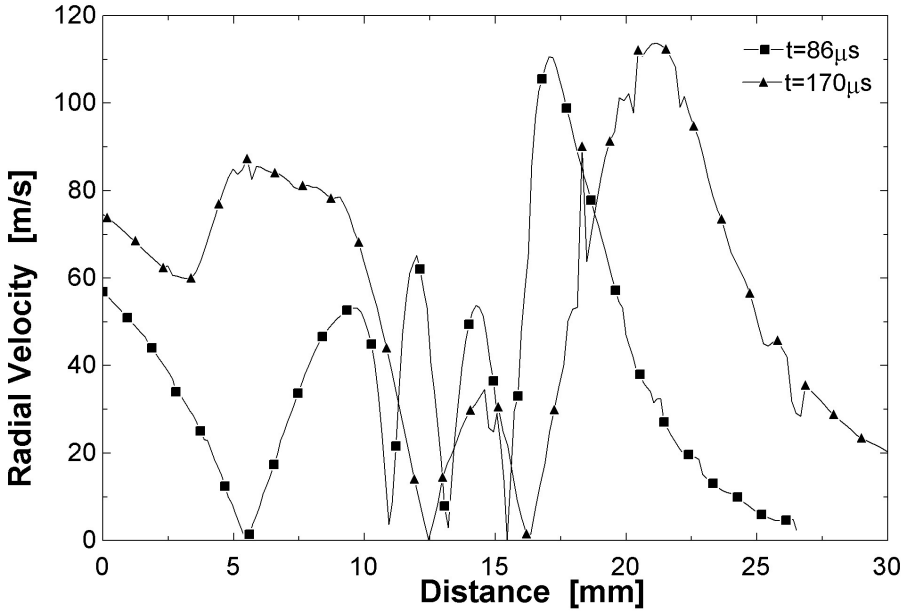

Figure 6.87: Radial velocity profile, parabolic model, plane II, M_s=1.65

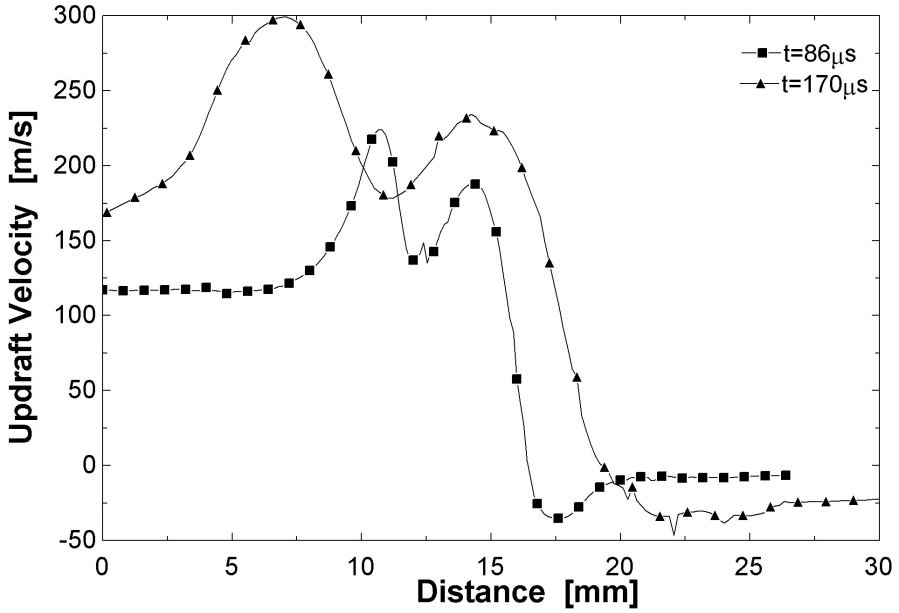

Figure 6.88: Updraft velocity profile, parabolic model, plane II, M_s=1.65

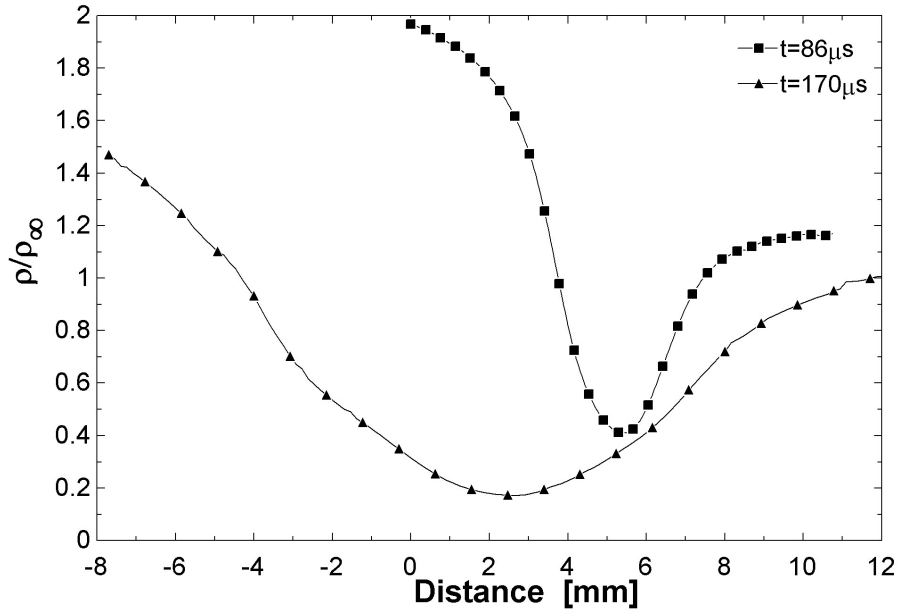

Figure 6.89: Pressure profile, parabolic model, plane II, M_s=1.65

Figure 6.91 gives a series of vorticity flood plots taken on various slices across the flow domain. The presentation of and observations derived from these images are similar to those mentioned in the discussion associated with Figure 6.78 above, and hence will not be repeated here. We do notice a difference in image t) between the M_s=1.42 and M_s=1.65 cases, where the secondary shock is apparent above the slipstream, against the solid boundary for the M_s=1.65 case. It should be noted that this secondary shock is present in regions near the centre and boundary of the domain, and that it is only revealed against the window with the display settings used to generate the images in Figure 6.91.

The extent to which the secondary shocks exist across the flow domain is shown in Figure 6.90. Here, the back leg of the lambda shock configuration is apparent in the numerical solution. The tertiary shock is not represented in the following images. It is however present in a region near the centre plane, as is shown in §6.4.2.

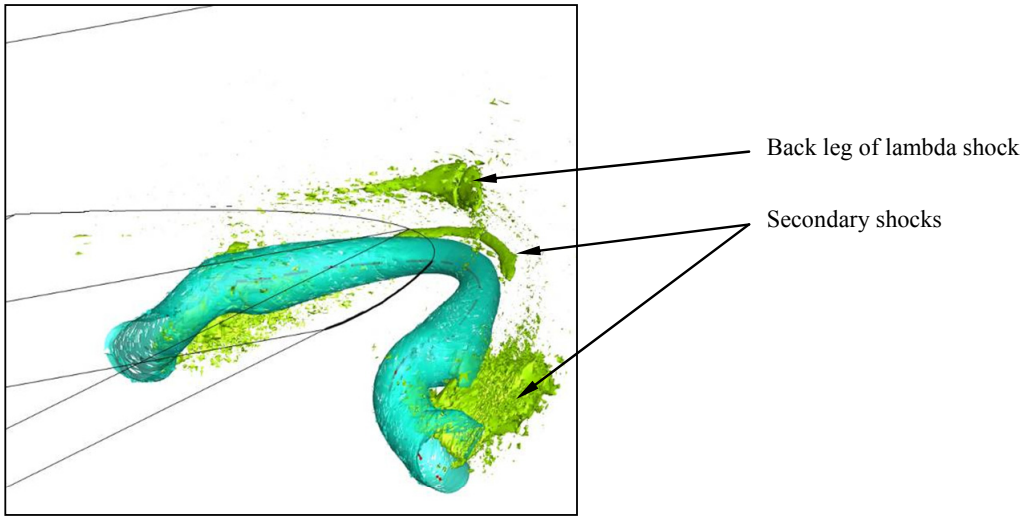

Figure 6.90: View of flow field, parabolic model, M_s=1.65

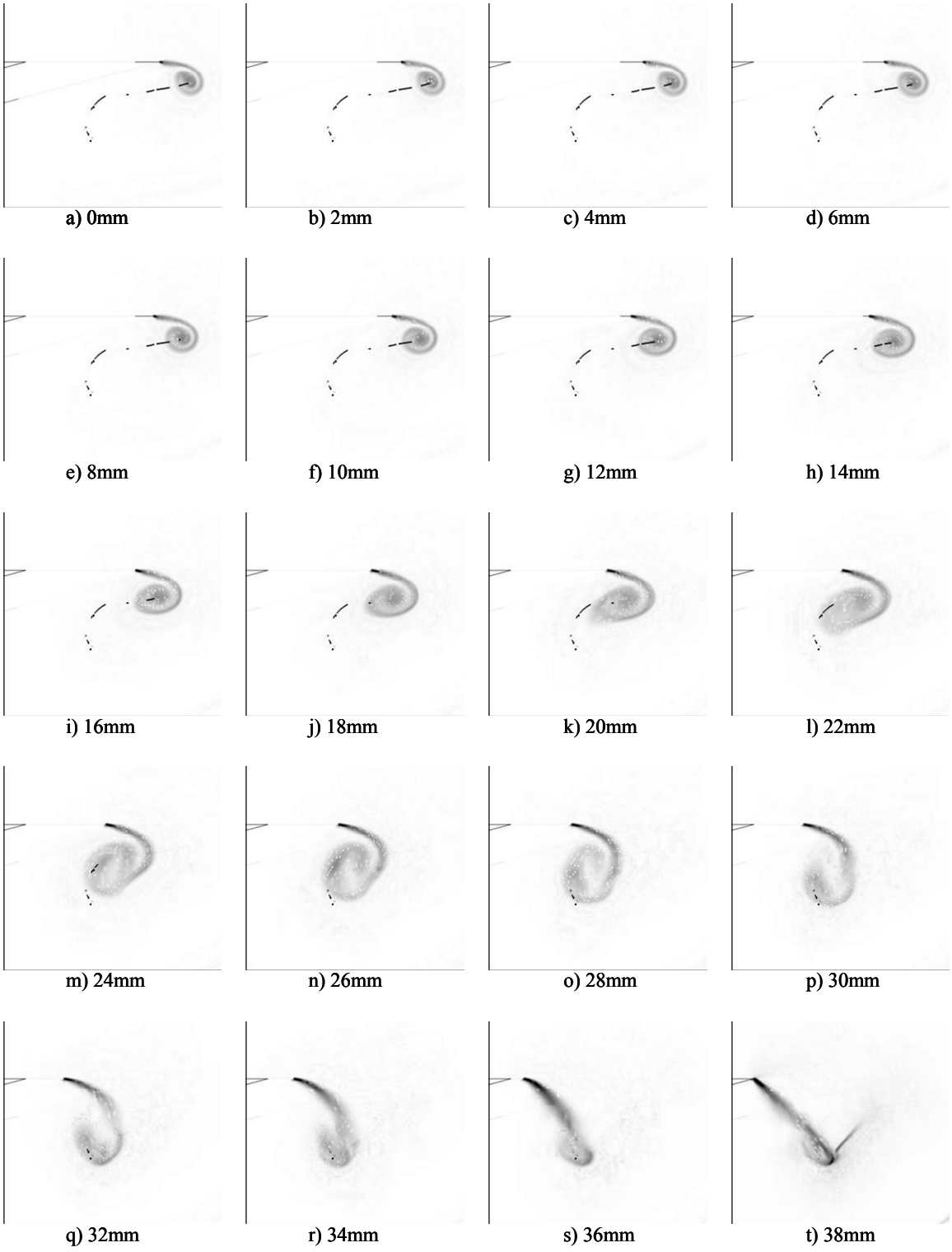

Figure 6.91: Parabolic model, vorticity plots, M_s=1.65, t=170μs

6.4.4 Summary

The evolution of the free vortex was observed and described both experimentally and numerically for the diffraction of a shock wave over a three-dimensional edge of parabolic definition. The strength of the incident shock wave had little effect on the arrangement of the free vortex. Similar to the results discussed in previous sections, secondary and tertiary shocks were evident in a region near the centre plane of the flow domain, and a secondary shock was evident in a region near the solid boundary of the domain, for M_s=1.65.

The axis of the free vortex assumes a complicated arrangement in the region affected by the presence of the boundary. Again, the vortex is found to contract in this region, as the axis is in effect 'extended' as it bends. No effects were observed where the two vortices from either side of the diffracting edge met at the centre plane, as the diffracting edge formed a continuous curve in this region. The vortex axes did not need to bend or distort in order to meet each other and form a continuous curve.

6.5 Inverted Parabolic Edge Test Model

Results for the inverted parabolic model are presented in this section. For the sake of brevity, these results are presented in less detail than those in previous sections. The results for this model show little that is not evident in those for the test models mentioned previously, and as such, the reader is referred to the discussions contained in the previous sections for more detail.

A comparison between the experimental and numerical results for the two incident shock Mach numbers (Mach 1.42 and 1.65) tested follows in §6.5.1, where the features specific to these flow cases are discussed. The vorticity and vorticity production calculations and results for both the parabolic and inverted parabolic test specimens are presented in section §6.6.

6.5.1 Discussion of experimental and numerical results

The experimental schlieren photographs for the inverted parabolic model are perhaps the most difficult to interpret. These, and a brief comparison with the numerical results are present below, first for the case of M_s=1.42, and then for M_s=1.65.

M_s=1.42

A sequence of schlieren photographs showing the development of the flow field, taken at an optical roll angle of 10°, is given in Figure 6.92. It can be seen, particularly by comparing images e) and f), that the vortex appears to move backwards (to the left in the photographs) at the windows. This effect was observed in previous sets of results, for example, at the tip of the 'V' for the case of the 'V' model tested, and presented in §6.2., and is mirrored in the numerical results.

The numerical results, shown in Figure 6.93, show the vortex expanding and moving to the left in the region against the wall. A surface of constant density (ρ=0.75kg.m^3) is shown, along with lines of constant density, taken at the near boundary (red) and on the centre plane of the domain (black).

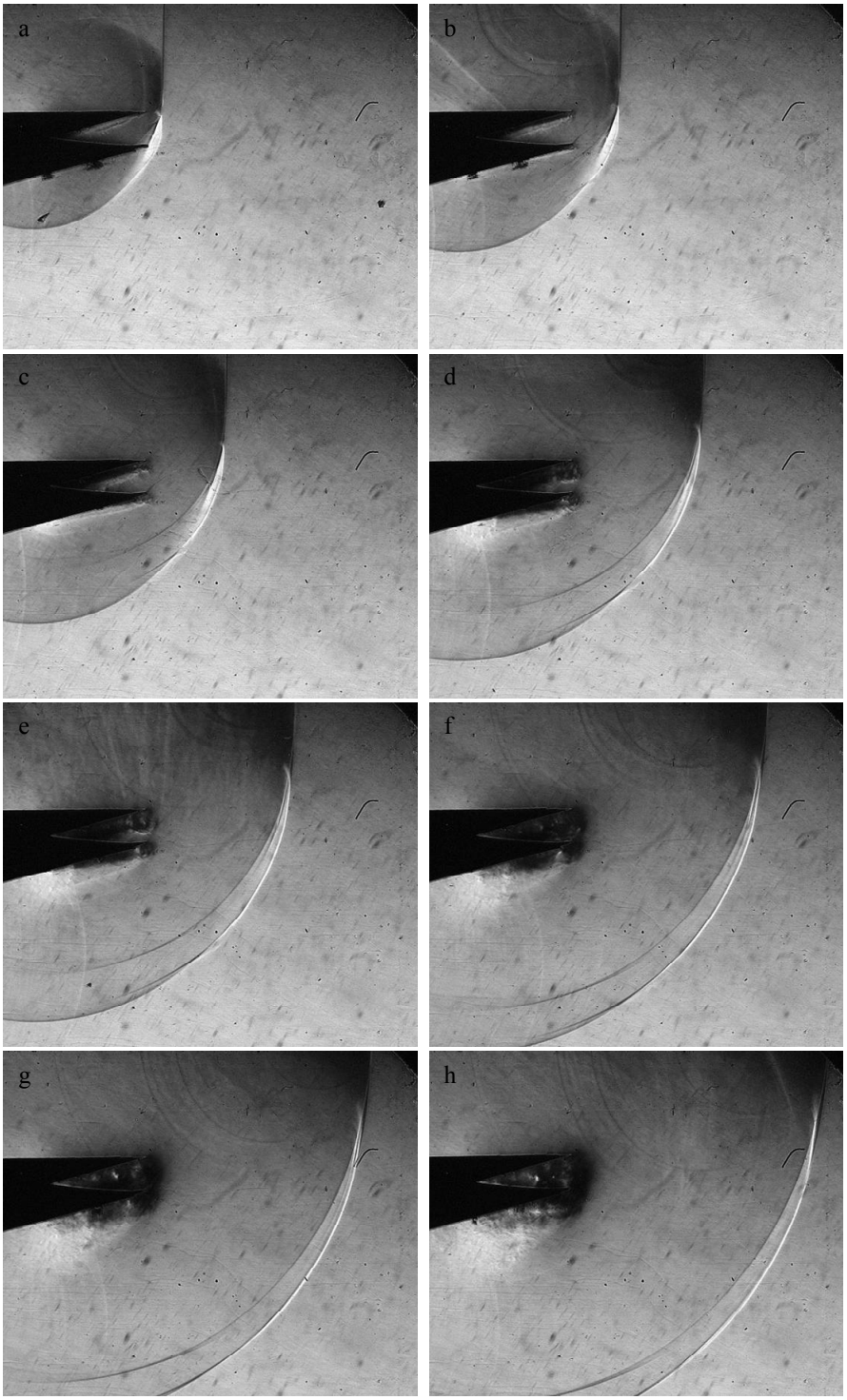

Figure 6.92: Inverted parabolic schlieren photographs, M_s=1.42, 10° optical roll, δt=25μs

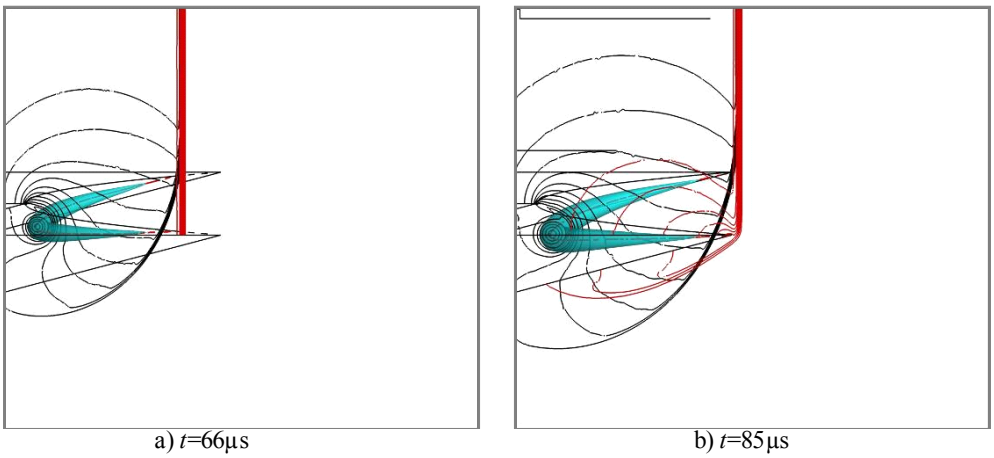

a) t=66μs

b) t=85μs

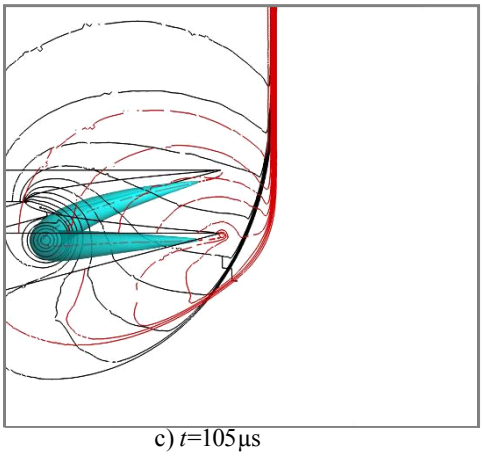

c) t=105μs

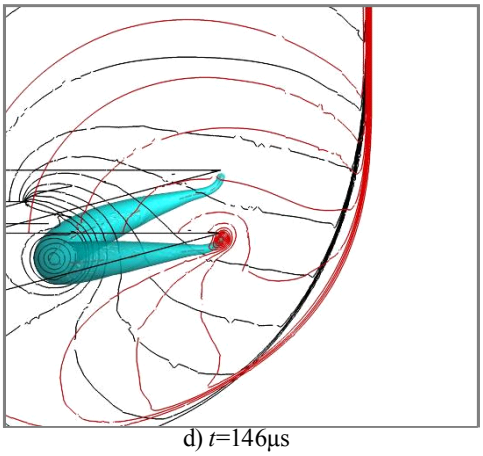

d) t=146μs

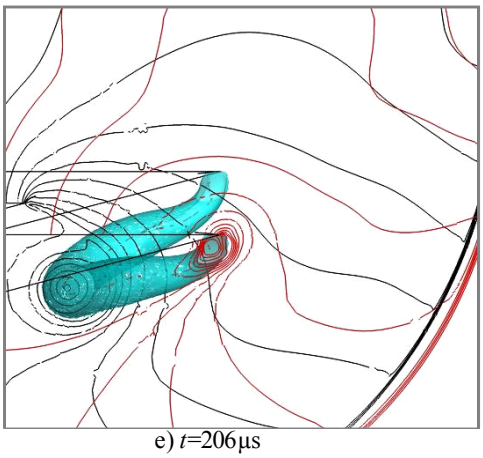

e) t=206μs

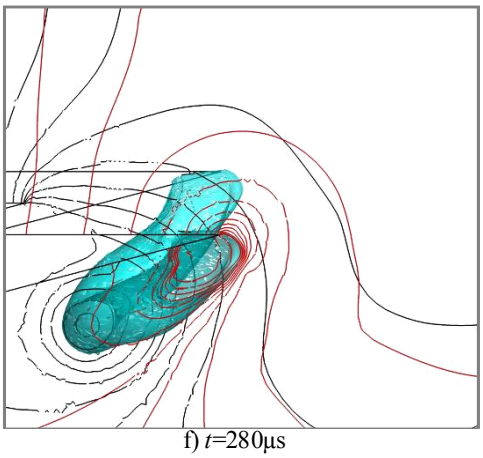

f) t=280μs

Figure 6.93: Inverted parabolic model, M_s=1.42, density lines and surface plots

M_s=1.65

Schlieren photographs of the development of the M_s=1.65 case are given in Figure 6.94. The vortex is hard to discern in these images, it does however appear to exhibit the same behaviour as the M_s=1.42 case in the region close to the boundaries, i.e., the vortex moves to the left in the photographs, the opposite direction to the incident shock propagation direction.

Images c) through f) in Figure 6.94 show a number of shocklets forming above the slipstream in the region near the centre plane of the flow domain. Exploded views of both images c) and e) are given in Figure 6.95, highlighting these features. These are not apparent in the numerical results, a sample of which is shown in Figure 6.97. It is however suspected that the mesh was too coarse to capture these flow features. These features were not apparent in any of the other schlieren photographs for the other models tested.

Secondary and tertiary shocks are clearly apparent in the numerical results, as is evidenced by images e) and f) in Figure 6.97. These can be most clearly seen in image d) of the set of schlieren photographs (Figure 6.94).

A further view of the flow field is given in Figure 6.96, for a time instant of t=160μs. An extraction of the shock surfaces is shown in the figure, and the secondary and tertiary shocks can clearly be seen in the region near the boundaries of the flow. The secondary shock is also evident in the region near the centre of the flow domain.

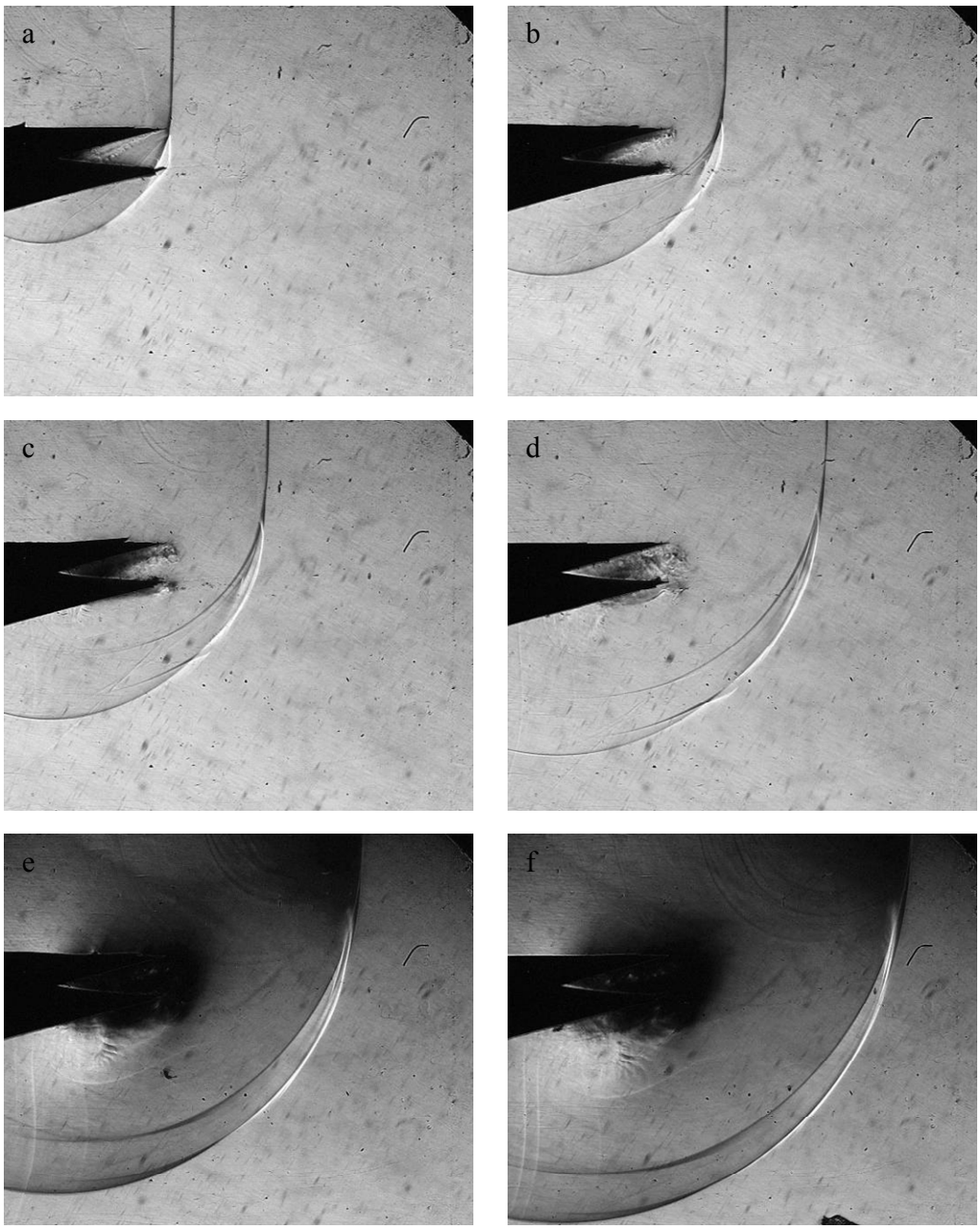

Figure 6.94: Inverted parabolic schlieren photographs, M_s=1.65, 10° optical roll, δt=25μs

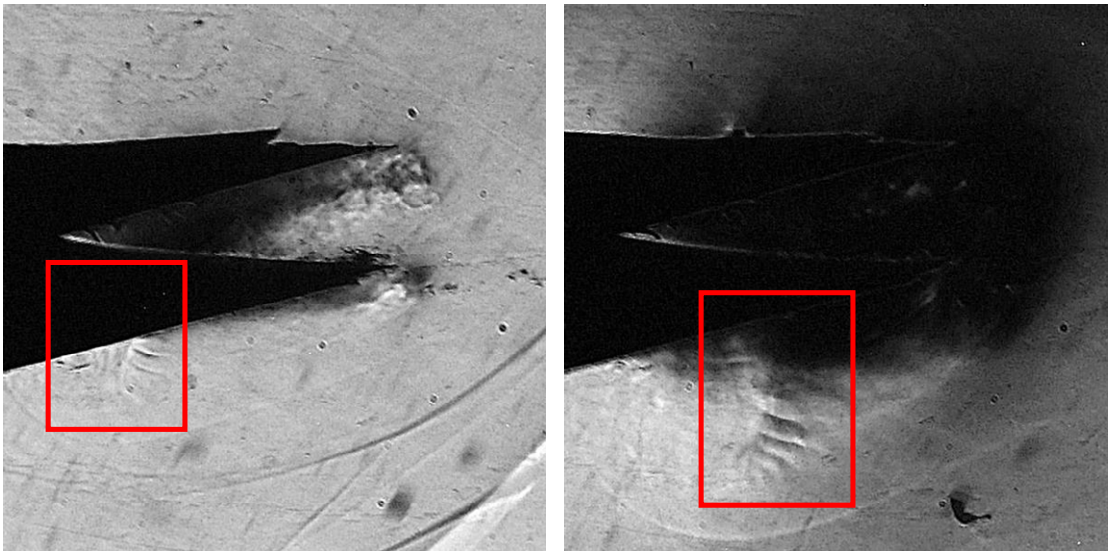

Figure 6.95: Enlarged view of images c) and e) from Figure 6.94

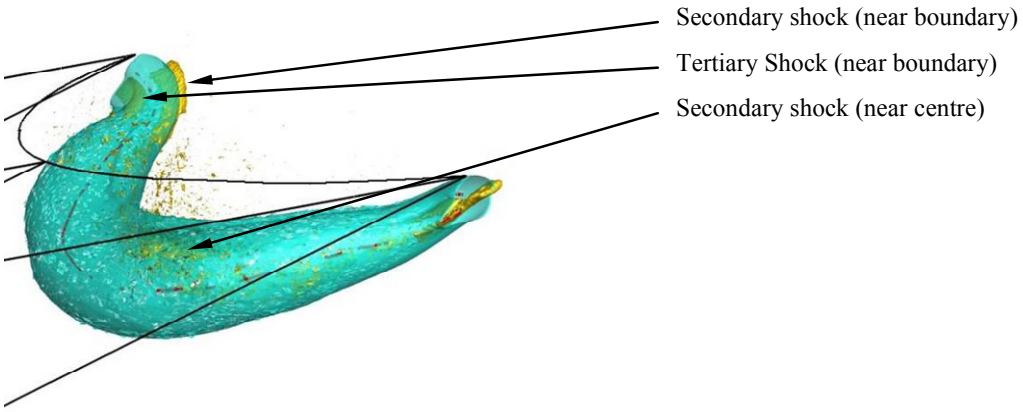

Figure 6.96: View of flow field, inverted parabolic model, M_s=1.65, t=160μs

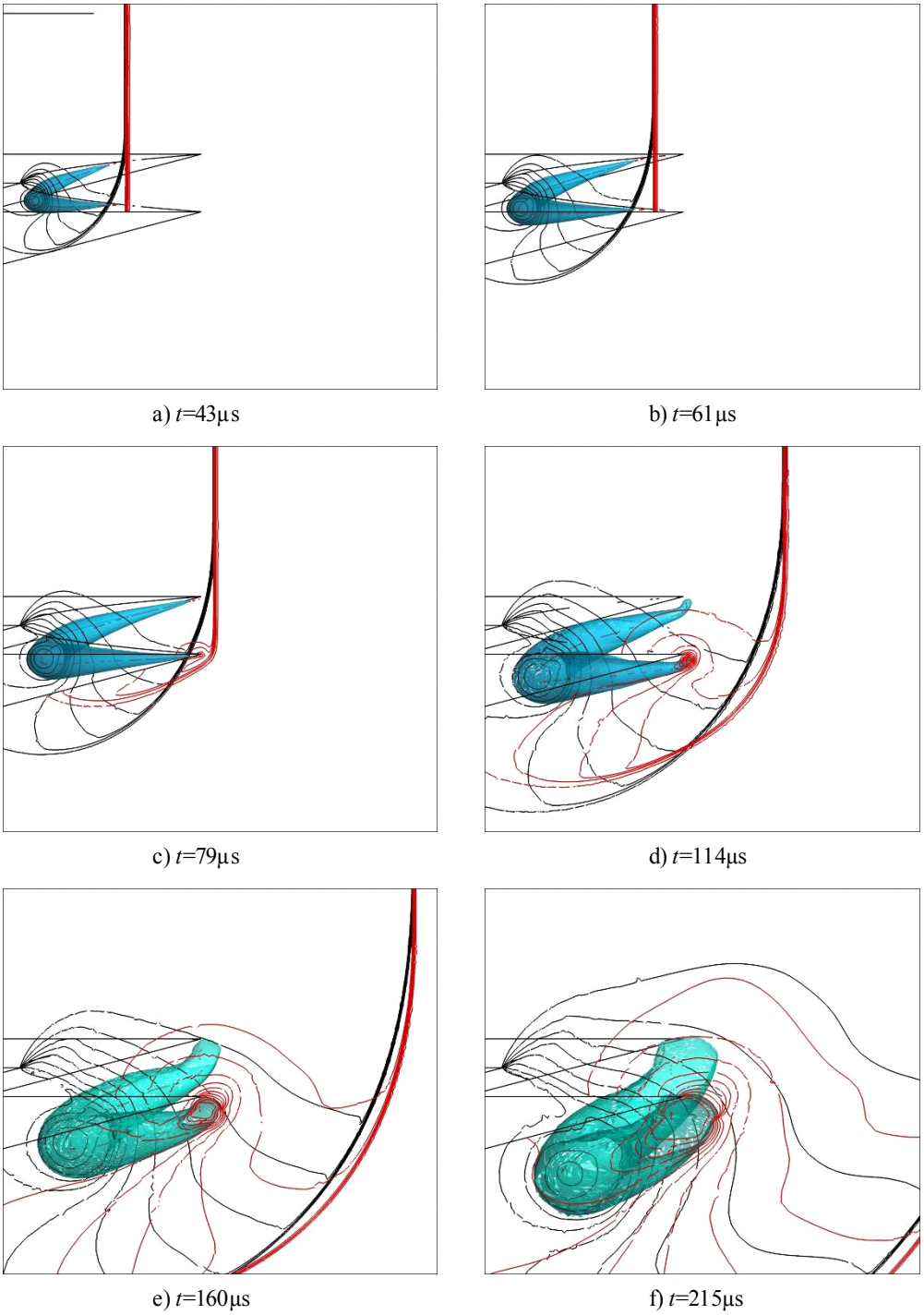

a) t=43μs b) t=61μs

c) t=79μs d) t=114μs

e) t=160μs f) t=215μs

Figure 6.97: Inverted parabolic model, M_s=1.65, density lines and surface plots

6.6 Vorticity Production

6.6.1 Introduction

Sun & Takayama (2003a) performed numerous experiments with the aim of quantifying the circulation produced during shock wave diffraction. A vast array of incident shock Mach numbers and wedge angles were tested, for two-dimensional flow cases, using an Euler solver. For the self-similar development of the two-dimensional vortex, it was found that the circulation produced was linearly proportional to time, and thus the rate of circulation production was a constant value (aside from discrepancies in the very early stages of diffraction, where the vortex had not fully formed). The rate of circulation production is proportional to the incident shock strength, and increases for increasing wedge angles, and approaches a constant value as the wedge angle is increased beyond 90°.

The circulation (Γ) is given by equation (2.15). For the two-dimensional case,

$$\Gamma = \int_S \omega.ds$$

In the studies of Sun & Takayama (2003a), the magnitude of the vorticity was integrated across the whole computational domain, so as to avoid ambiguities with specifying the boundaries of the perturbed region behind the incident shock wave. This was acceptable as the unperturbed flow regions (in front of the incident shock) were uniform, and made no contribution to the total vorticity, as did the region of uniform flow behind the incident shock wave away from the diffracting region.

The vorticity production results for the three dimensional shock diffraction cases presented in the preceding sections are presented here. A brief overview of the method of analysis and a comparison of the results it yields for the two-dimensional cases published by Sun & Takayama (2003a) against their results is given in §6.6.2. The results are presented in §6.6.3.

6.6.2 Method & verification

For the three-dimensional cases presented in this dissertation, the vorticity vector was calculated in Tecplot 360, in accordance with equation (2.14). A three-dimensional circulation was calculated by integrating the magnitude of the vorticity vector over the entire flow volume. As mentioned previously, the unperturbed region in front of the incident shock wave, and the region of uniform flow not affected by the diffraction process behind the shock wave make no contribution to the vorticity vector. Values of the circulation were calculated at various time instants throughout the evolution of the numerical solutions, and from this data, the rate of circulation production was determined.

A brief comparison between the methods adopted for the present study and the results presented by Sun & Takayama (2003a) was conducted. It should be noted that the results presented by Sun & Takayama (2003a) were for nitrogen as the test gas at an ambient temperature of T=298 K, and were only two dimensional.

A plot of normalized circulation (Γ') against time is given in Figure 6.98 for a two-dimensional diffraction case, a test gas of nitrogen at T=298K, wedge angle of 165°, and incident shock Mach number of 1.42. Circulation is normalised by RT_0, where R is the universal gas constant divided by the molecular mass of the gas (for nitrogen R=296.8 J/kg/K) and T_0 is the temperature of the gas in front of the incident shock wave (298K).

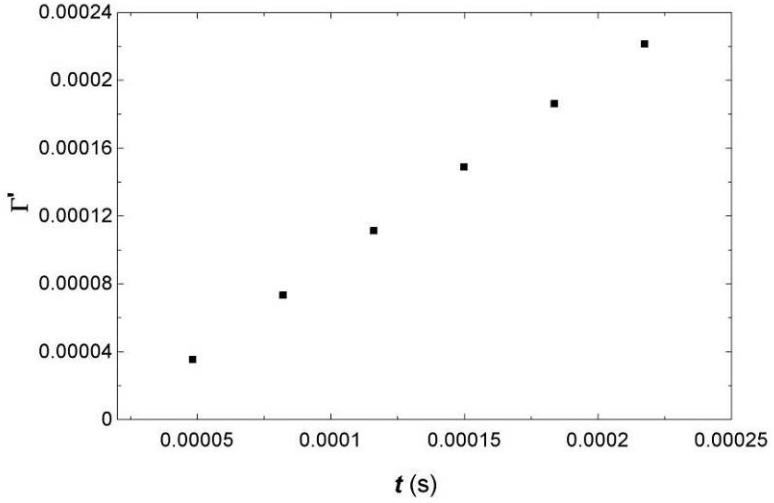

Figure 6.98: Γ' vs. t, M_s=1.42, two-dimensional with nitrogen as test gas

This data was obtained during the course of this investigation, using the same solver and solver settings and calculation method as the results presented in §6.2 through §6.5, save for a two-dimensional flow domain and nitrogen as the test gas.

The rate of circulation production (gradient of the curve) for the above set of data is 1.101. A curve fit to the data obtained and presented by Sun & Takayama (2003a), gives the relationship

$$\frac{\Gamma'}{t} = 1.82\left(M_s - 1\right) + 1.92\left(M_s - 1\right)^2$$

for a wedge angle of greater than 90°, which yields a value of (Γ'/t)=1.103. Tests for different shock strengths revealed similar correlation with the results of Sun & Takayama (2003a).

6.6.3 Summary of Results

Figure 6.99 gives a plot of normalized circulation against time for the three-dimensional 'V' case for M_s=1.32, M_s=1.42, and M_s=1.65. Considering the M_s=1.42 case, from the figure, it can be seen that the rate of circulation production increases in value initially, corresponding to the non-linear portion of curve for t less than 78μs. This is the time taken for the incident shock wave to reach the tip of the 'V', once it has started diffracting around the outer portions of the edge. It then appears to approach a constant value, and a linear relationship is observed between the circulation and time once the shock has propagated over the edge entirely. The rate of circulation production for the linear region is 0.177. These observations are in line with the findings of Sun & Takayama (2003a).

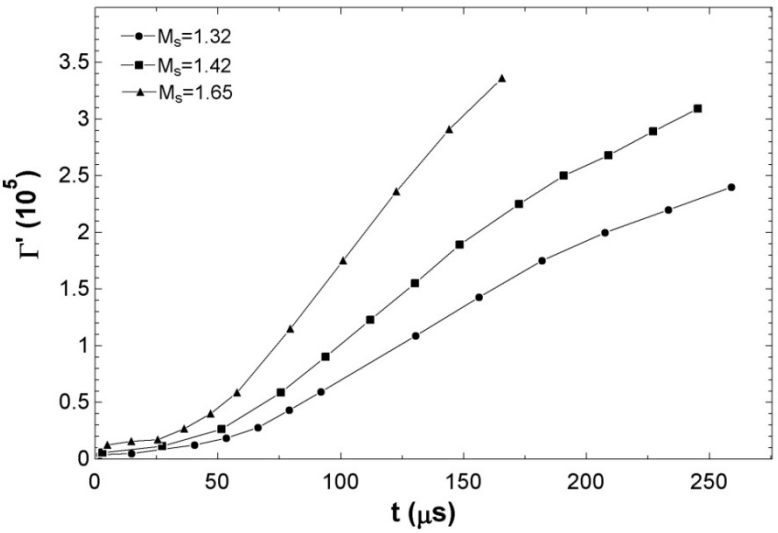

Figure 6.99: Circulation vs. Time, 'V' model

Considering the M_s=1.42 case, at around t=150μs, a slight change in gradient is apparent in the linear portion of the curve, with a second linear portion of slightly lower gradient apparent from approximately t=200μs onwards. A similar effect was observed in the results of Tseng & Yang (2006). In their study, this occurred as a result of the diffracted shock wave reflecting off of the wall underneath the diffracting edge. This was not the case in the studies documented in this

dissertation, as the bottom wall was sufficiently far away for the diffracting edge, and the diffracting shock wave does not reach it in the time range analysed. This is seen to occur at approximately t=135μs for the M_s=1.65 case, and t=175μs for M_s=1.32. This anomaly is discussed in more detail later.

Plots of the circulation production for all the models tested for both M_s=1.42 and M_s=1.65 are given in Figure 6.100. The data for each incident shock Mach number tested tends to the same linear trend, after the initial curved portion of the plot, during which the shock wave is still in the process of diffracting over the edge. This data shows that total rate of circulation production is independent of the diffracting edge profile, and that the fact that the edge is continuous or not (i.e. the parabolic edges verses the 'V' edges) has little effect on it. The wedge angle for all models tested was constant at 165°, and it is expected, based on the two-dimensional work by Sun & Takayama (2003a), that varying the wedge angle would affect the rate of circulation production in a similar manner as reported in that work.

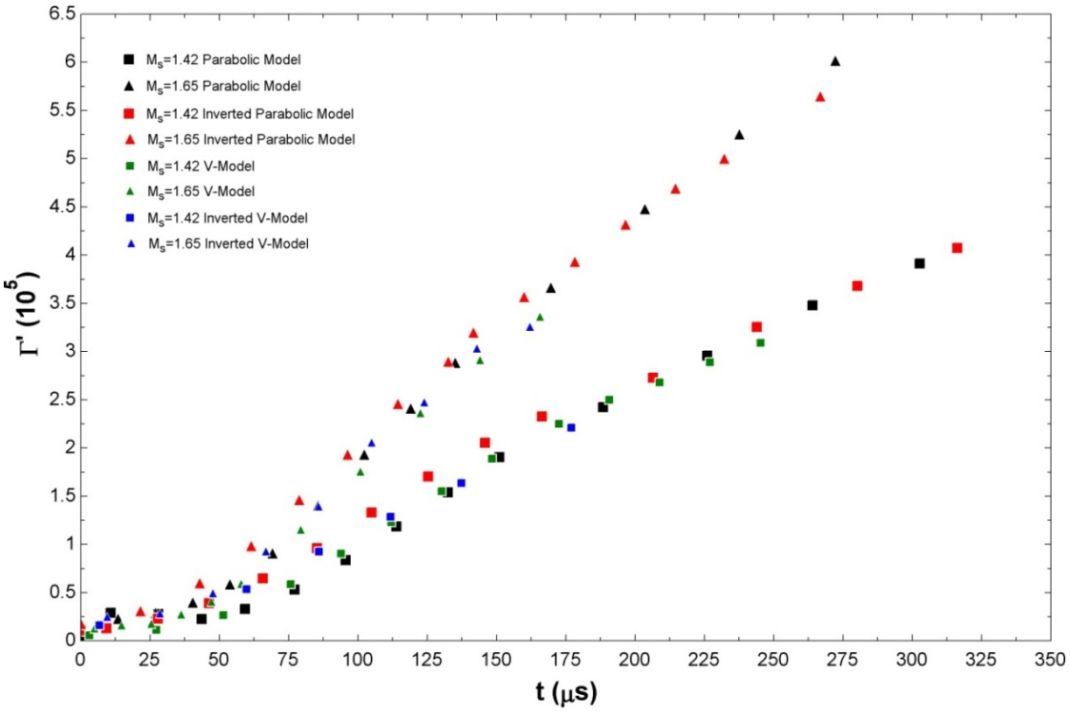

Figure 6.100: Circulation production for all models tested, M_s=1.42 & M_s=1.65

There are some slight discrepancies in the plot presented in Figure 6.100. Due to the number and size of the case and data files generated during the numerical computations, it was not possible to store the data calculated at every time step. Data was recorded at every 100^{th} time step, and as such, pin-pointing the exact time instant at which the incident shock wave began to diffract was difficult in some cases. This was done by interpolation. Thus, there would be a slight horizontal spread in the data presented in Figure 6.100.

As is mentioned numerous times throughout the preceding discussion, the meshes used, whilst as fine as was possible with the computer equipment used, were relatively coarse. It is difficult to say what effect this would have had on the results, but the data obtained for the different models displays a consistent trend, which would infer that this had little effect. It is possible that the coarseness of the meshes would have had the effect of introducing slight numerical noise into the results.

The slight gradient change in the linear portion of the curve is consistent across all models and incident shock Mach numbers. This begins to occur at around t=150μs and t=135μs in the data for M_s=1.42 and M_s=1.65 respectively.

This anomaly is caused by the reflection of the expansion wave off of the top wall of the flow domain. The expansion wave first starts to reflect off of the top wall at approximately t=142μs for M_s=1.42, and approximately t=135μs for M_s=1.65. This process appears to induce a slight downward curve in the data, until the expansion wave across the flow domain has fully reflected off of the top wall. The data then appears to approach another almost linear trend.

The gradients of the initial linear portions of the curves are given in Table 6.2.

Table 6.2: Gradient of linear portion of circulation production curve for all models tested

Model	Incident Shock Mach Number	Gradient
V'	1.42	0.180
	1.65	0.272
Inverted-'V'	1.42	0.142
	1.65	0.256
Parabolic	1.42	0.218
	1.65	0.285
Inverted parabolic	1.42	0.181
	1.65	0.273

6.6.4 Vorticity production for Navier-Stokes solution

A comparison of the Euler and Navier-Stokes solution circulation production for the 'V' model at an incident shock of M_s=1.42 is given in Figure 6.101. It can be seen that the Navier-Stokes solution has a large magnitude of circulation at t_0. Both curves exhibit the same general trend, approaching a similar linear curve.

The results of Tseng & Yang (2006) showed there to be little difference between the rate of circulation production for both solutions. The rate of circulation production (or gradient of the curve) for the initial linear portion of the Navier-Stokes solution is 0.165.

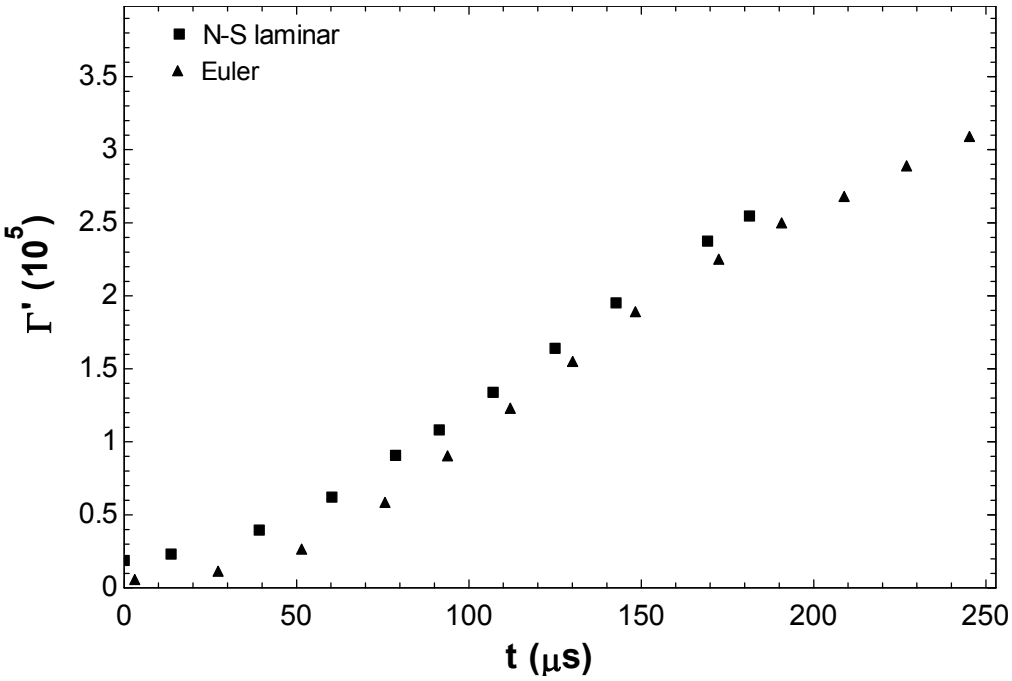

Figure 6.101: Circulation production, 'V' model, M_s=1.42, Euler and Navier-Stokes comparison

6.7 Diffracting Shock Shape

Skews (1967a) gave the results for the shape of a diffracting shock wave (in two-dimensional tests) in a non-dimensional plane. The shape of the diffracted shock wave was measured from experimental photographs, and non-dimensionalised with respect to time. This was done for numerous incident shock Mach numbers and wedge angles. As the two-dimensional diffraction

case is self-similar with time, the non-dimensionalised plots taken at different time instances of the shock shape form one curve, for constant shock Mach number and wedge angle.

Results of the shape of the diffracting shock wave for the three-dimensional cases presented in the previous sections are given here. The shape of the diffracting shock, non-dimensionalised by α ($\alpha=at$), is plotted in the figures that follow. This is done for the 'V' and parabolic edged test models, for both incident shock Mach numbers of 1.42 and 1.65. The data is taken from the results of the numerical simulations. It has been shown throughout the previous sections that the numerical simulations correlate very closely with the experimental photographs.

The data presented in this section is taken on three vertical slices through the flow domain, at three time instances. The centre plane, the wall plane, and a plane mid-way between the centre and the wall, referred to as the mid plane in the following discussion. The data is presented in the form of graphs of the non-dimensionalised shock profile on the three planes at a single time instant, and comparisons of the shock profile on a single plane for the three time instants. This allows us to investigate as to whether the shock shape is self-similar across the flow domain at a single time instant, and self-similar with the evolution of time at a single location.

The incident shock wave becomes vanishingly weak as the angle through which it is diffracted increases (in the region close to the bottom surface of the wedge). This can be seen in the various schlieren and numerical results images presented in the previous sections. Figure 6.26 gives an example of schlieren images, where the diffracted shock is indistinguishable at later time instants in the region underneath the diffracting wedge. For the parabolic model cases, a slightly more sensitive schlieren set up was used, and the diffracted shock can be seen under the wedge in those schlieren images near the centre plane of the domain. Interestingly, there is a discontinuity in the shock profile near the centre plane in the parabolic model schlieren images for both incident shock Mach numbers investigated. This can be seen in Figure 6.102, and in the sequences of schlieren images presented in §6.4.1. This is not observed in any of the other cases investigated.

Figure 6.102: Parabolic model shock profile schlieren illustration, M_s=1.42

In the numerical simulations, the mesh was not refined in the region under the diffracting edge to capture these portions of the diffracting shock accurately. An illustration of can be seen in Figure 5.2. This was due to the limited number of cells available, and the mesh adaption scheme being set up with a bias towards refining the grid in the region of the free vortex.

6.7.1 'V' test model

Plots of the non-dimensionalised shock wave profile are given for M_s=1.42 in Figure 6.103 through Figure 6.105, and M_s=1.65 in Figure 6.106 through Figure 6.108. Each figure gives the shape of the shock wave on three planes at a single time instant. Note that in Figure 6.103 and Figure 6.106, the shock has yet to reach and diffract over the tip of 'V'.

A consistent pattern is apparent in Figure 6.103 through Figure 6.108. It is apparent that the shape of the diffracted shock wave is not totally self-similar across the breadth of the flow domain. In all of the plots it can be seen that for values of greater than approximately 1 on the x axis, the three curves lie on top of each other. For values of less than approximately 1, the shock has a tighter curve at the wall, with that portion of the black curve lying above the other two curves. The profiles of the shock on the centre and mid planes are consistent with each other, indicating that the shock evolution appears self similar away from the solid boundary. This is particularly evident for the case of M_s=1.65. For the M_s=1.42 case. Figure 6.105 shows that the shock profiles on the centre and mid plane deviate from each other towards the end of the measured region (around 0.5 on the x-axis). This is probably just an anomaly in the results, as in all other plots the two curves show good agreement. The data represented in Figure 6.105 is taken late in the solution, and as mentioned previously, the mesh was not refined for values of less than approximately 0.5 on the x-axis, and as the solution evolved and shock front grew, this value would have increased slightly, due to the limited number of cells available to the refinement algorithm.

For x values of less than approximately 0, the diffracted shock became vanishingly weak, except for at very early time instants. These regions are hence not plotted on the curves. These weaker portions of the shock are not captured very well in the numerical simulations, and due to the limited number of cells available to the refinement algorithm, the mesh in these regions was generally not refined at all. The points describing the shock profile were extracted through investigating density contour plots and a Mach number contour equal to the incident shock strength.

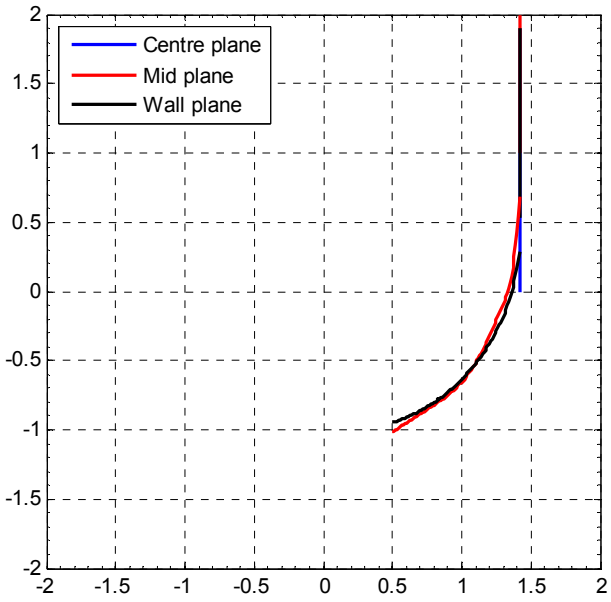

Figure 6.103: Non-dimensionalised shock profile, M_s=1.42, t=76μs

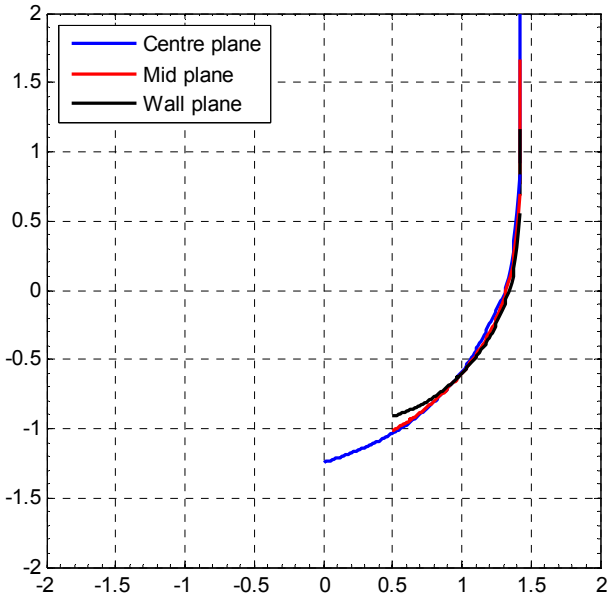

Figure 6.104: Non-dimensionalised shock profile, M_s=1.42, t=126μs

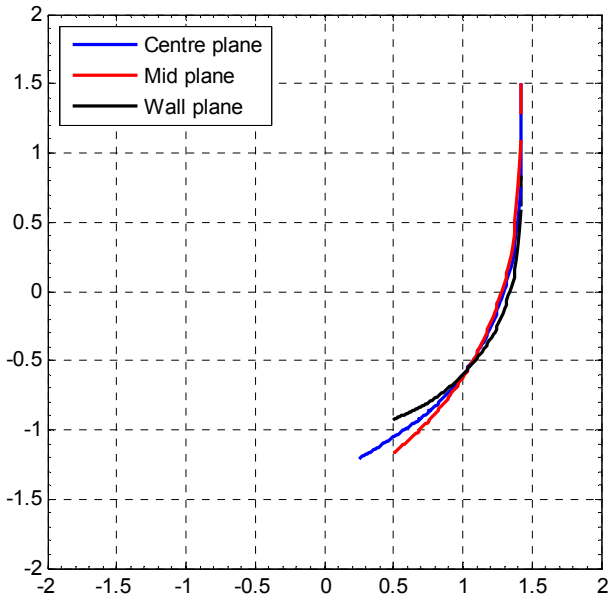

Figure 6.105: Non-dimensionalised shock profile, M_s=1.42, t=172μs

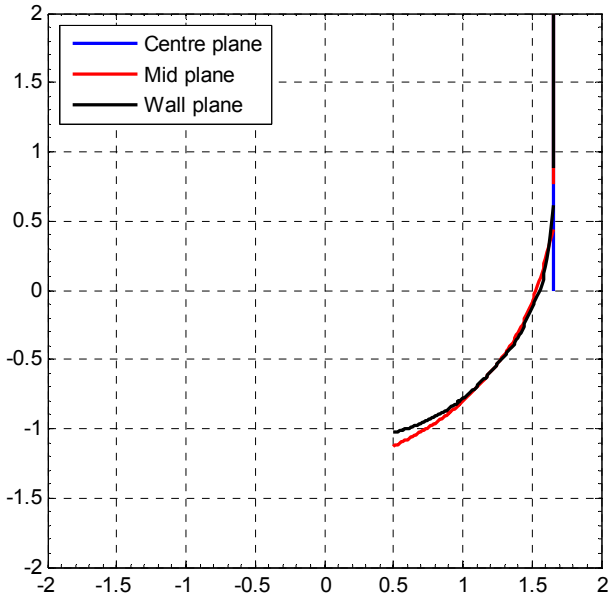

Figure 6.106: Non-dimensionalised shock profile, M_s=1.65, t=56μs

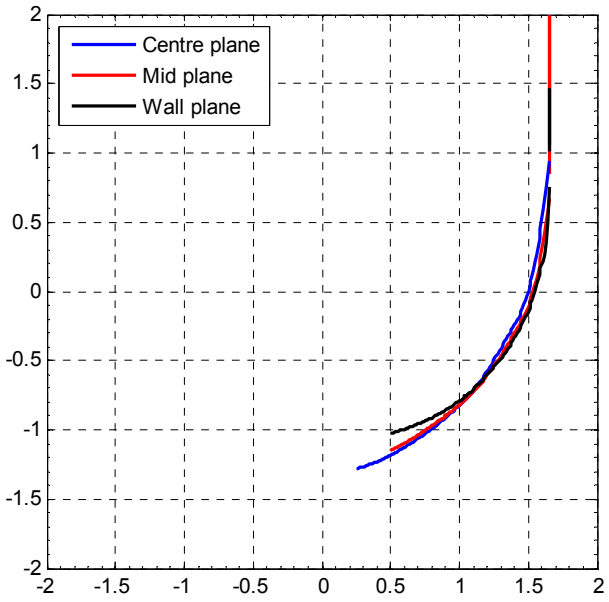

Figure 6.107: Non-dimensionalised shock profile, M_s=1.65, t=98μs

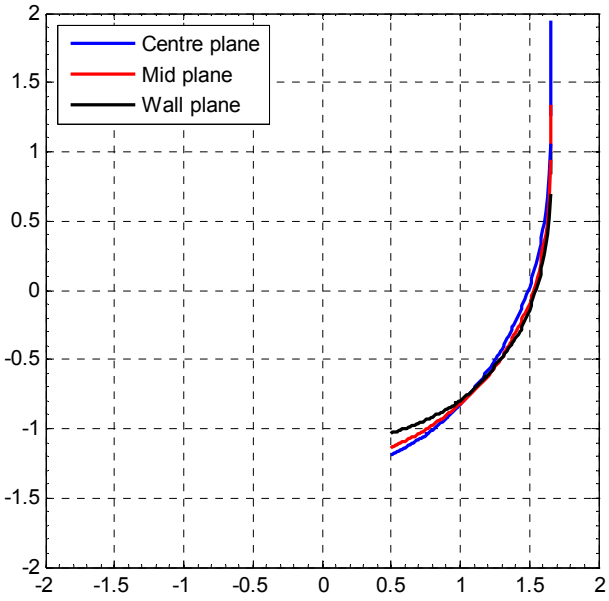

Figure 6.108: Non-dimensionalised shock profile, M_s=1.65, t=141μs

The series of plots given below give the non-dimensionalised shock shape plotted on a single plane (the same centre, mid, and wall planes as previously) at the three time instants investigated. The plots give an indication of whether the non-dimensionalised shock shape is consistent with time at a single location in the flow field. Also plotted on the curves is the non-dimensionalised shock shape for the two-dimensional diffraction case. This is represented by the dashed black line on the plots. Again, both the M_s=1.42 and M_s=1.65 cases are given. Note that the plots are labeled according to the time elapsed since the shock diffracted over the edge on the plane on which the data is taken, and not t_0, as is the case for all other data presented in this dissertation.

Figure 6.109 through Figure 6.111 give this data for M_s=1.42 and Figure 6.112 through Figure 6.114 give this data for M_s=1.65. These plots show that the evolution of the diffracted shock wave is self-similar with time on a plane with normal perpendicular to the shock propagation direction. Aside from the one anomaly in Figure 6.110, all curves lie on top of each other. When comparing the data to the two-dimensional curve, it can be seen that the data taken at the wall lies above the two-dimensional curve, and the other data sets. The two data sets for the centre and mid plane are similar to each other, as was highlighted in the previous set of plots, and again here. These curves appear consistent with the two-dimensional plot.

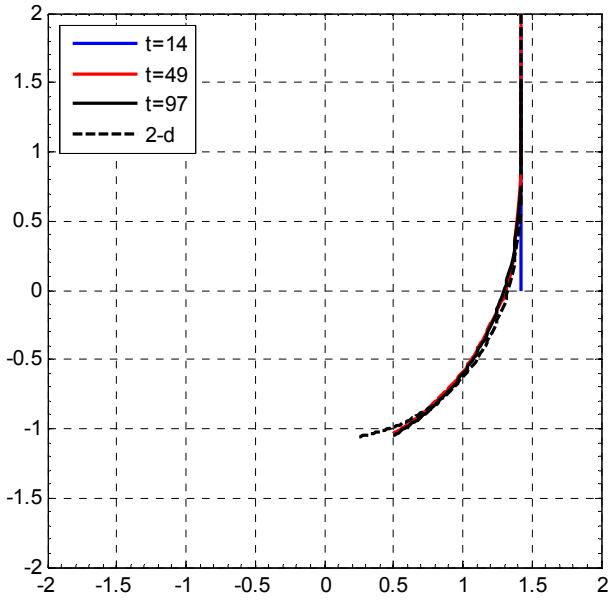

Figure 6.109: Non-dimensionalised shock profile, M_s=1.42, centre plane

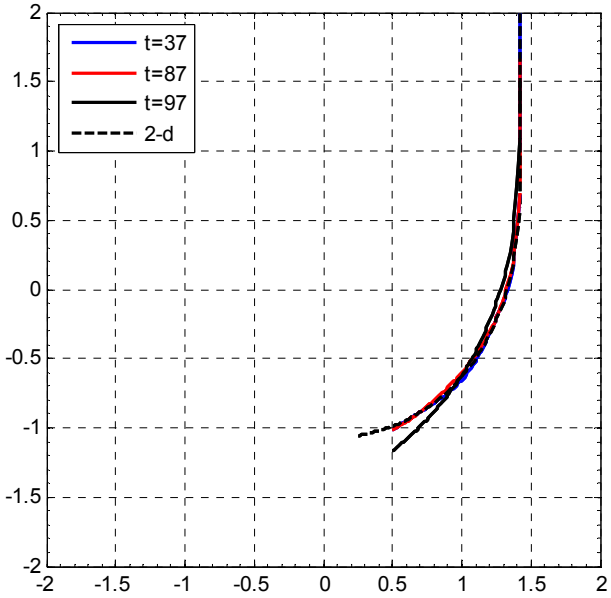

Figure 6.110: Non-dimensional shock profile, M_s=1.42, mid plane

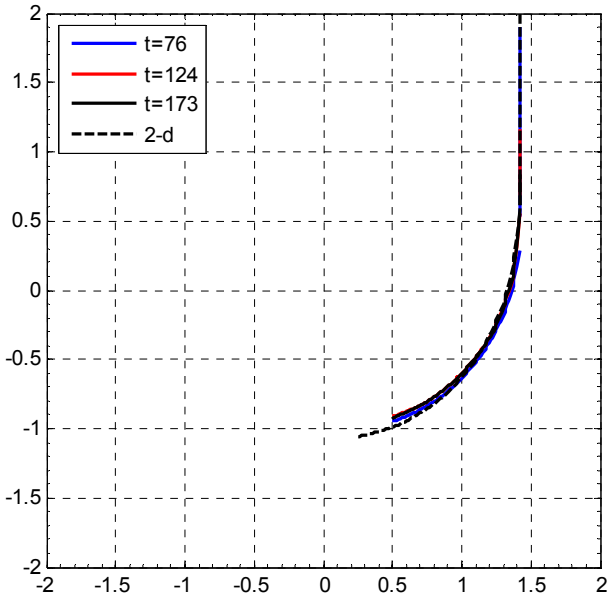

Figure 6.111: Non-dimensionalised shock profile, M_s=1.42, wall plane

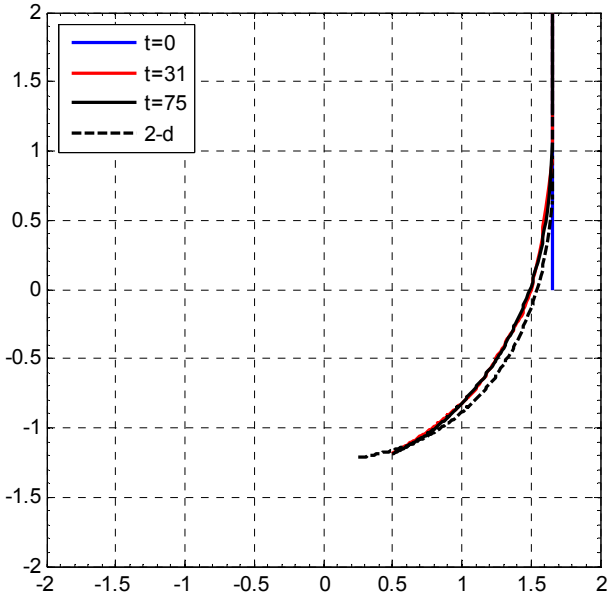

Figure 6.112: Non-dimensionalised shock profile, M_s=1.65, centre plane

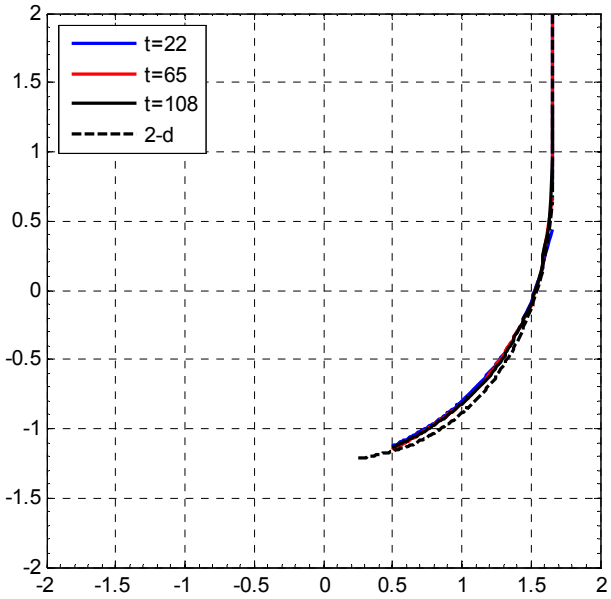

Figure 6.113: Non-dimensionalised shock profile, M_s=1.65, mid plane

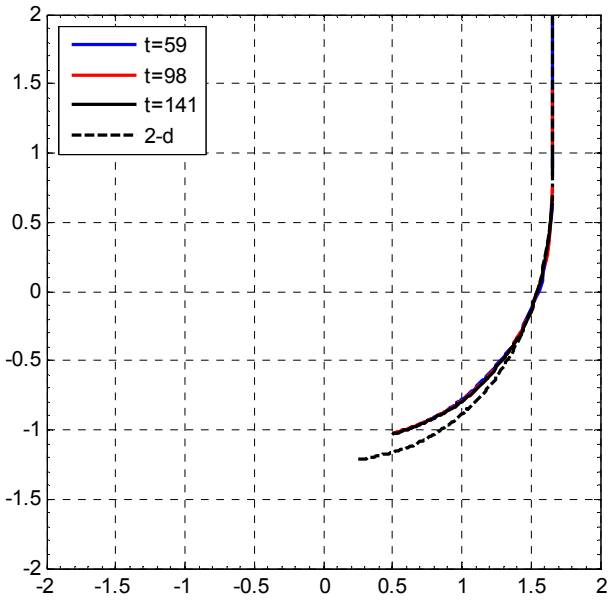

Figure 6.114: Non-dimensionalised shock profile, M_s=1.65, wall plane

6.7.2 Parabolic test model

Much of the discussion given in §6.6.1 applies to the results for the parabolic test model. For the sake of brevity, it will not be repeated here. The same trends present in the results for the 'V' model tests are evident in the results for the parabolic edged test model. Plots of the diffracted shock shape for the parabolic edged model are presented in Appendix A, in a similar manner to those presented in §6.6.1.

6.7.3 Further discussion

The results of this section would tend to indicate that the evolution of the diffracted shock wave with time appears self similar and consistent with the two dimensional case, away from the solid

boundary. However, this study only considered one wedge angle, and was based on numerical solutions that were optimised for investigation of the free vortex. Good correlation between the numerical and experimental results was obtained. A comparison of the non-dimensionalised shock profile obtained from the numerical and measured off of an experimental photograph is given in Figure 6.115. It should be noted that, due to motion blur and the three dimensional nature of the flow field, measured data from experimental photograph would likely include some inaccuracies that would be hard to quantify.

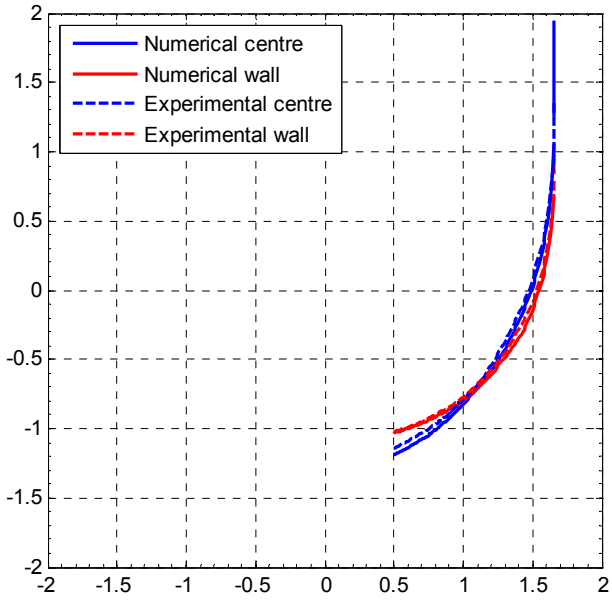

Figure 6.115: Shock diffraction profile, numerical and experimental results comparison, M_s=1.65, 'V' model, t=141μs

7 Conclusions

The three-dimensional shock diffraction case was investigated numerically and experimentally, with particular attention paid to the development and behaviour of the free vortex. The results of the numerical simulations correlated well with the experimentally obtained schlieren images across all of the test models and time instances investigated.

The free vortex was found to obey the laws of vortex motion and Hemholtz's laws, as described in the literature. The vortex core bends so as to meet the solid boundaries at a 90° angle. The meeting of two vortices generated by a 'V' shaped diffracting edge was investigated, and the vortex cores were found to bend so as to form a continuous curve where the two vortices meet. The process and vortex behaviour were consistent with the bending in the region of a solid boundary. The vortex development and behaviour was, in general, consistent across the different incident shock Mach numbers tested (Mach 1.32, 1.42, and 1.65) and four models tested. As would be expected, based on previous two-dimensional shock diffraction studies, secondary and tertiary shocks appeared in the vortex for an incident shock Mach number of 1.65. These were only apparent in a region near the centre plane of the flow domain (all models tested were symmetrical about the centre plane) and the regions near the solid boundaries. They did not extend across the entire flow domain.

Flow properties (tangential, radial, and updraft velocities, and the pressure profile) at different locations along the length of the vortex were presented, so as to investigate the effect that bending has on the structure of the vortex. Data were plotted for a conical region of the vortex, apparently unaffected by distortions to the vortex, and for the region where the vortex is distorted and bends

in the region near the solid boundary. The results showed a fair indication of self-similar vortex development with time in the region away from the distortions. The plots were distorted in the region of bending, where it was found that a larger velocity magnitude existed on the side of the vortex towards the centre of curvature of the bend. The vortex was found to contract in the region of the bend, as if the core had been stretched.

The vorticity production was calculated and the data for all test models compared. Plots for each incident shock Mach number across the four models tested approached the same linear trend once the incident shock had fully diffracted. Increasing the incident shock Mach number increased the rate of circulation production. The sets of results correlated quite closely, with the shape of the diffracting edge having no discernible impact on them.

The solution of the laminar Navier-Stokes equations yielded little difference to the Euler solutions with regard to the evolution and behaviour of the free vortex. However, in order to obtain more representative Navier-Stokes solutions, significantly more computer power and memory would be required.

Although the numerical simulations performed were not done so with the specific aim of investigating the diffracted shock shape, a brief analysis of this was performed and presented. The non-dimensionalised shock shape was compared at different locations and time instances, and against the results obtained from two-dimensional cases. It was found that the non-dimensionalised shock shape is very close to that of the two-dimensional case away from the solid boundaries. The results obtained and presented here tended to indicate that at the boundary, the curved portion of the diffracted shock is slightly tighter, and lies above the two-dimensional case on the plots. It is however recommended that further work be performed on this topic, in order to provide more definitive conclusions.

This work represents one of the first investigating an arbitrary three-dimensional compressible vortex. The work presented in this dissertation aimed to provide an initial investigation into the dynamics and behaviour of such three-dimensional vortices, and demonstrate the ability of modern numerical software at capturing the behaviour of such complex flow fields. It is believed that both of these objectives have been met.

Scope for further research exists, and could possibly involve the use of non-symmetric diffracting models, with ‘jump’ discontinuities in the diffracting edge, which would allow one to investigate as to how the vortices behave in order to join or terminate at a boundary. Due to the vast quantities of numerical data generated during this research, it was impossible to present and analyse all areas of interest in detail, and further investigation into areas of interest in this data may be performed.

More detailed calculations would require substantially more computing resources, and would perhaps best be saved for work in the future. Such calculations could comprise full Navier-Stokes solutions on substantially finer meshes. This would allow for much more detail to be captured in the slipstream, and in the regions where the secondary and tertiary shocks are present in the free vortex.

References

Bershader, B. W. (1995). Compressible Vortices. In S. I. Green, *Fluid Vortices.* Dordrecht: Kulwer Academic Publishers.

Church, C. R., Snow, J. T., Baker, G. L., & Agee, E. M. (1979). Characteristics of Tornado-Like Vortices as a Function of Swirl Ratio: A Laboratory Investigation. *Journal of Atmospheric Sciences , Vol. 36*, 1755-1776.

Glass, I. I. (1959). *Shock Tubes, Part I: Theory and Performance of Simple Shock Tubes.* UTIA Review, No. 12, Institute of Astrophysics, University of Toronto.

Green, S. I. (1995). Introduction to Vorticity. In S. I. Green, *Fluid Vortices.* Dordrecht: Kulwer Academic Publishers.

Howard, L. N., & Matthews, J. (1956). On the Vortices Produced in Shock Diffraction. *J. Appl. Phys. , 27*, 223-231.

Kliene, H., Yu, Q., Ritzerfeld, E., & Gröning, H. (1995). An Experimental/Numerical Approach to Shock Wave Diffraction. *Proc. 20th International Symposium on Shock Waves*, *Vol. 1*, pp. 501-506. Pasadena, California, USA.

Lee, S., & Bershader, D. (1994). The Structure of Compressible Starting Vortices. *Experiments in Fluids , No. 16*, 248-254.

Lugt, H. J. (1983). *Vortex Flow in Nature and Technology.* New York: John Wiley & Sons.

Mayer, E. W., & Powell, K. G. (1992). Similarity Solutions for Viscous Vortex Cores. *J. Fluid Mech. , 238*, 487-507.

National Instruments Corporation. (2009b). *National Instruments - NI PCI-6224 Technical Brochure.*

National Instruments Corporation. (2009a). *National Instruments, NI PCI-6110 Technical Brochure.*

Nolan, D. S., & Farrel, B. F. (1998). The Structure and Dynamics of Tornado-Like Vortices. *Journal of Atmospheric Sciences , Vol. 56*, 2908-2936.

Saffman, P. G. (1997). *Vortex Dynamics.* Cambridge University Press.

Seitz, M. W. (2001). *Ph.D Thesis - Shock Wave Interactions with Porous, Compressible Foams.* Johannesburg: University of the Witwatersrand.

Settles, G. S. (2001). *Schlieren and Shadowgraph Techniques: Visualizing Phenomena in Transparent Media.* Springer-Verlag.

Skews, B. W. (2007). *Compressible Flow - Course Notes.* Johannesburg: School of Mechanical Engineering, University of the Witwatersrand.

Skews, B. W. (1967b). The Perturbed Region Behind a Diffracting Shock Wave. *J. Fluid Mechanics* , 705-719.

Skews, B. W. (1967a). The Shape of a Diffracting Shock Wave. *J Fluid Mechanics , 29*, 297-305.

Skews, B. W., & Crosbie, E. C. (2008). Unsteady Three-Dimensional Compressible Vortex Flows. *6th South African Conference on Computational and Applied Mechanics.* Cape Town.

Sun, M., & Takayama, K. (2003b). A Note on the Numerical Simulation of Vortical Structures in Shock Diffraction. *Shock Waves* (13), 25-32.

Sun, M., & Takayama, K. (1997). The Formation of a Secondary Shock Wave Behind a Shock Wave Diffracting at a Convex Corner. *Shock Waves* , 287-295.

Sun, M., & Takayama, K. (2003a). Vorticity Production in Shock Diffraction. *J. Fluid Mech.* , 237-256.

Takayama, K., & Inoue, O. (1991). Shockwave Diffraction Over 90° Sharp Corner - Poster Presented at 18th ISSW. *Shock Waves , Vol. 1*, 301-312.

Thompson, P. A. (1972). *Compressible Fluid Dynamics.* McGraw-Hill Inc.

Tseng, T. I., & Yang, R. J. (2006). Numerical Simulation of Vorticity Production in Shock Diffraction. *AIAA Journal , Vol. 45* (No. 5), 1040-1047.

Yang, J. M., Takayama, K., & Han, Z. Y. (1997). Some Behaviours of Weak Shock Wave Diffraction Over a Convex Corner. *21st International Symposium on Shock Waves*, *vol. 2*, pp. 1445-1450. Great Keppel Island, Australia.

Zucrow, M. J., & Hoffman, J. D. (1976). *Gas Dynamics.* John Wiley & Sons Inc.

Appendix A – Diffracted Shock Shape For Parabolic Edged Test Model

The curves given below show plots of the non-dimensionalised shock shape for the parabolic test model. The first set of figure show the show shape taken at a single time instant on three planes taken across the flow domain (the centre, mid, and wall planes). Figures A-1 through A-3 show data for M_s=1.42 and figures A-4 through A-6 are for M_s=1.65. These plots are presented in accordance with section 6.6.2.

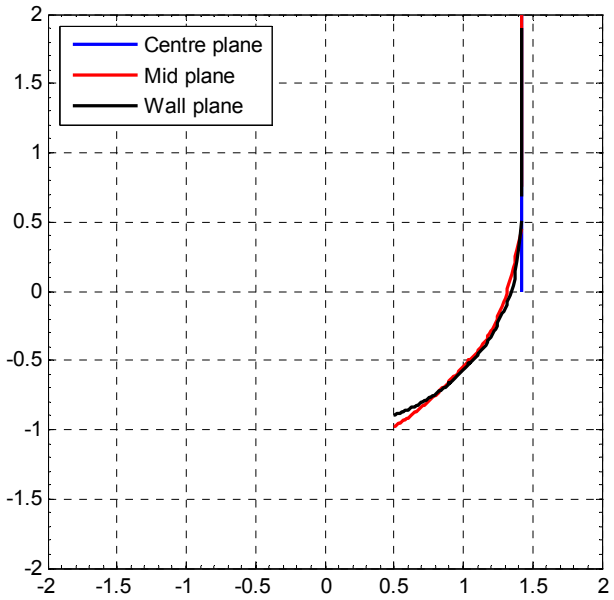

Figure A.1: Non-dimensionalised shock profile, M_s=1.42, t=76μs

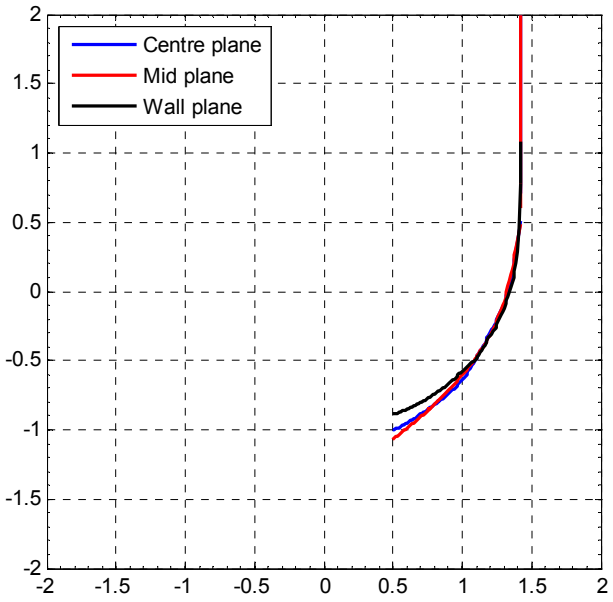

Figure A.2: Non-dimensionalised shock profile, M_s=1.42, t=131μs

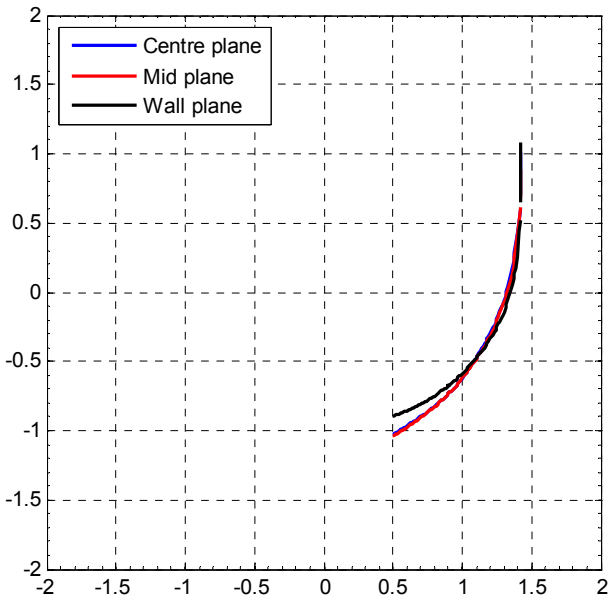

Figure A.3: Non-dimensionalised shock profile, M_s=1.42, t=224μs

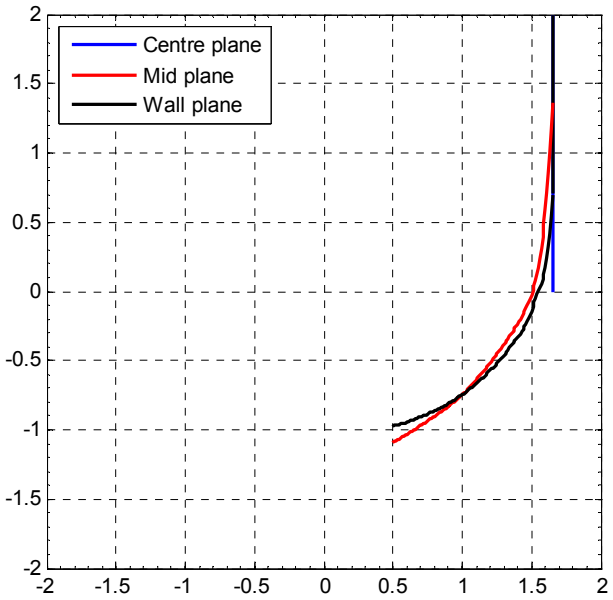

Figure A.4: Non-dimensionalised shock profile, M_s=1.65, t=71μs

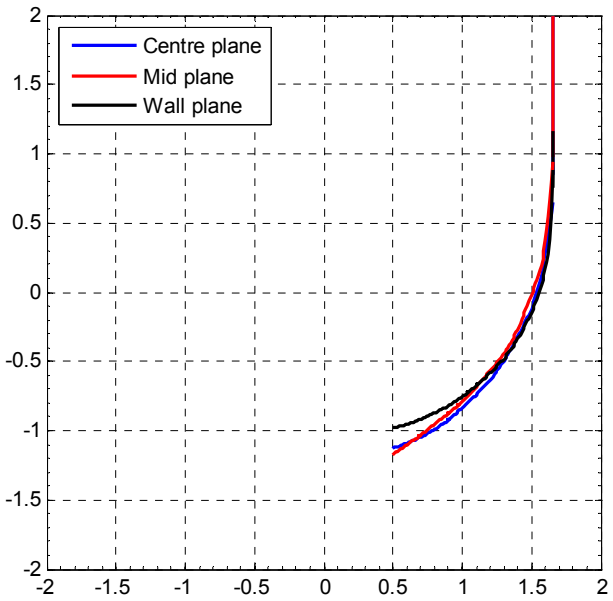

Figure A.5: Non-dimensionalised shock profile, M_s=1.65, t=120μs

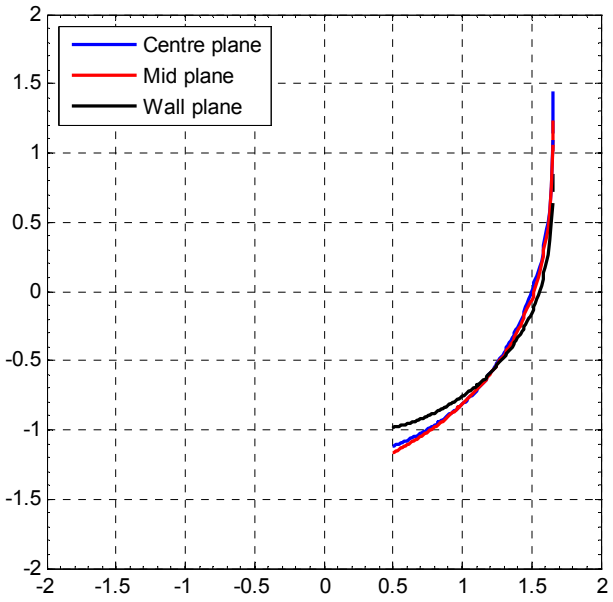

Figure A.6: Non-dimensionalised shock profile, M_s=1.65, t=170μs

The set of figures given below show the non dimensionalised shock shape on a single plane at multiple time instances. Also show on the curves is the two dimensional shock profile.

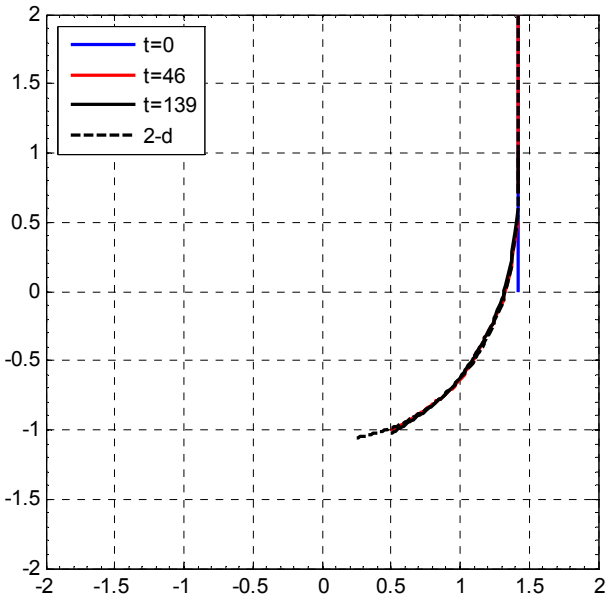

Figure A.7: Non-dimensionalised shock profile, M_s=1.42, centre plane

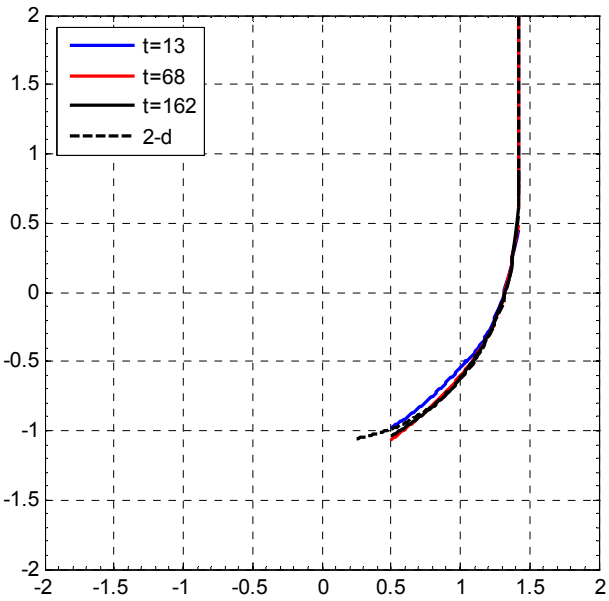

Figure A.8: Non-dimensionalised shock profile, M_s=1.42, mid plane

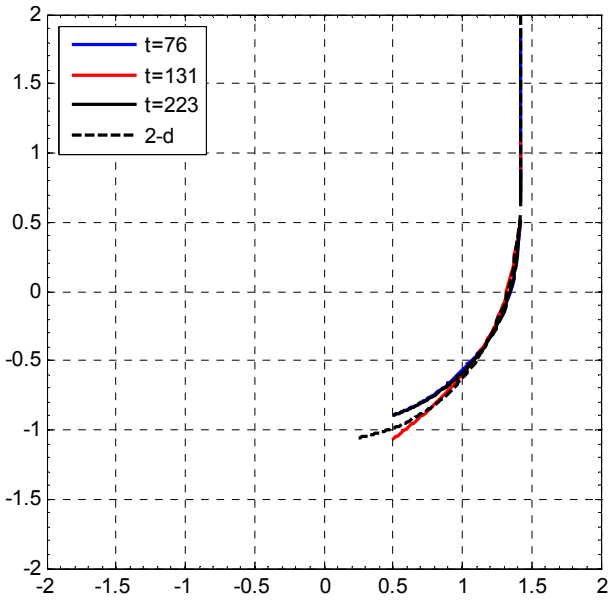

Figure A.9: Non-dimensionalised shock profile, M_s=1.42, wall plane

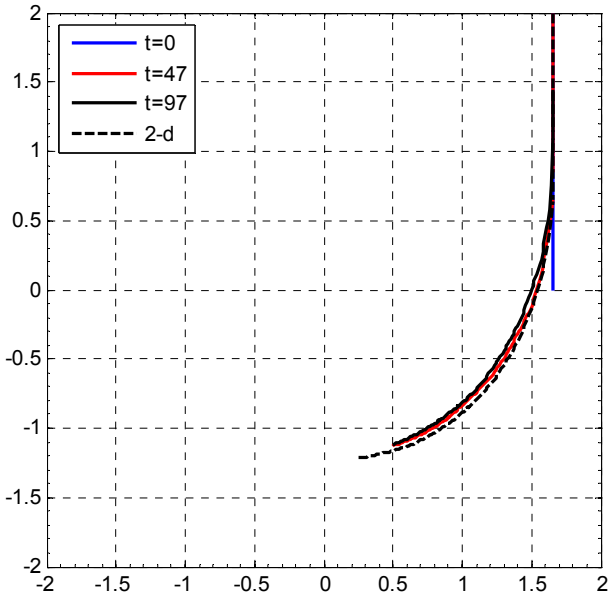

Figure A.10: Non-dimensionalised shock profile, M_s=1.65, centre plane

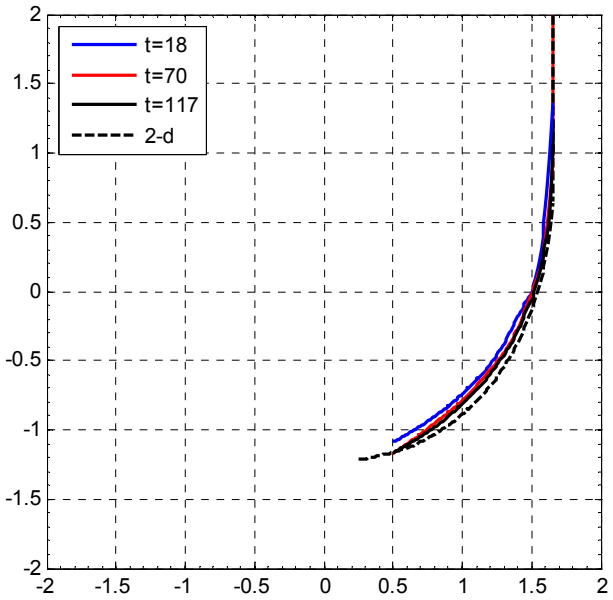

Figure A.11: Non-dimensionalised shock profile, M_s=1.65, mid plane

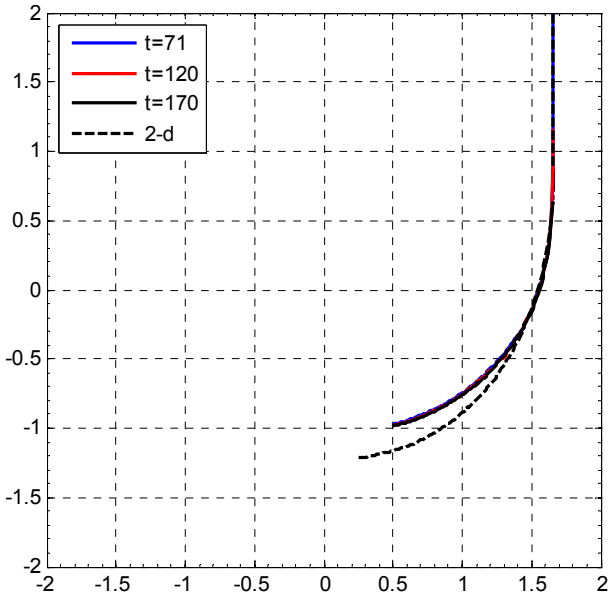

Figure A.12: Non-dimensionalised shock profile, M_s=1.65, wall plane